

Modelling pulsar emission in the high-energy and very-high-energy regimes

M Barnard

 **orcid.org 0000-0003-1720-7959**

Thesis accepted in fulfilment of the requirements for the degree
Doctor of Philosophy in Space Physics at the North-West
University

Promoter: Prof C Venter

Co-promoter: Dr AK Harding

Graduation June 2021

20574266

Acknowledgements

I dedicate this work to my loving Father for his grace, guidance, and love. Special thanks to Him for providing me with the love and support from family, friends, and work colleagues at the Physics Department. Special thanks to my husband for his unwavering faith in me, and encouraging me to follow my dreams. It gives me great pleasure in acknowledging the support of my supervisor (Prof. Christo Venter) and co-supervisor (Dr. Alice Harding) for their guidance, patience, invaluable advice, and constantly challenging me. Your perseverance and ideas are truly inspirational. Special thanks goes to other collaborators, Constantinos Kalapotharakos, and Tyrel Johnson for their valuable contributions made to my PhD research.

“I would have lost heart, unless I had believed that I would see the goodness of the Lord in the land of the living. Wait on the Lord; be of good courage, and He shall strengthen your heart. Wait, I say, on the Lord!” — Psalm 27:13–14, NKJV

*“He counts the number of the stars;
He calls them all by name.
Great is our Lord, and mighty in power;
His understanding is infinite.” — Psalm 147:4–5, NKJV*

“When I consider Your heavens, the work of Your fingers, The moon and the stars, which You have ordained, What is man that You are mindful of him, And the son of man that You visit him?” — Psalm 8:3–4, NKJV

*“Now faith is the substance of things hoped for,
the evidence of things not seen.” — Hebrews 11:1, NKJV*

“Call to Me, and I will answer you, and show you great and mighty things, which you do not know.” — Jeremiah 33:3, NKJV

*“Fear not, for I am with you;
Be not dismayed, for I am your God.
I will strengthen you,
Yes, I will help you,
I will uphold you with My righteous right hand.” — Isaiah 41:10, NKJV*

Abstract

Modelling pulsar emission in the high-energy and very-high-energy regimes

The *Fermi* Large Area Telescope has revolutionised the γ -ray pulsar field, increasing the population to over 250 detected pulsars. The majority display spectra with exponential cutoffs in a narrow range around a few GeV. Models predicted cutoffs up to 100 GeV; it was therefore not expected that pulsars would be visible in the very-high-energy (>100 GeV) regime. Subsequent surprise discoveries by ground-based telescopes of pulsed emission from four pulsars above tens of GeV have marked the beginning of a new era, raising important questions about the electrodynamics and local environment of pulsar magnetospheres. I have performed geometric light curve modelling using static, retarded vacuum, and offset polar cap dipole B -fields, in conjunction with standard two-pole caustic and outer gap geometries. I also considered a slot gap E -field associated with the offset polar cap B -field and found that its inclusion leads to qualitatively different light curves. Solving the particle transport equation shows that the particle energy only becomes large enough to yield significant curvature radiation at large altitudes above the stellar surface, given this relatively low E -field. Therefore, particles do not always attain the radiation-reaction limit. Increasing the slot gap E -field by a factor of 100 led to improved light curve fits, as well as curvature radiation reaction at lower altitudes. The overall optimal light curve fit was for the retarded vacuum dipole field and outer gap model. Recent kinetic simulations sparked a debate regarding the emission mechanism of pulsed γ -ray emission from pulsars. Some models invoke curvature radiation, while others assume synchrotron radiation in the current sheet. Detection of the Vela pulsar by H.E.S.S. (20 – 120 GeV) and *Fermi* provides evidence for a curved spectrum. We posit this to result from curvature radiation via primary particles in the pulsar magnetosphere and current sheet. We present energy-dependent light curves using an extended slot gap and current sheet model and invoking a two-step accelerating E -field as motivated by kinetic simulations. I include a refined calculation of the curvature radius of particle trajectories, impacting the particle transport, predicted light curves, and spectra. The model reproduces the decrease of flux of the first light-curve peak relative to the second one, evolution of the bridge emission, near constant phase positions of peaks, and narrowing of pulses with increasing energy. We can fundamentally explain the first of these trends, since I found that the curvature radii of the particle trajectories in regions where the second γ -ray light curve peak originates are systematically larger than those associated with the first peak, implying a correspondingly larger cutoff for the second peak. An unknown azimuthal dependence of the E -field as well as uncertainty in the precise emission locale preclude a simplistic discrimination of emission mechanisms. Finally, H.E.S.S. recently announced the detection of pulsed emission from the Vela pulsar up to 7 TeV, constraining particle energies to exceed several TeV. I contributed to a paper invoking synchrotron self-Compton emission to model this new radiation component, thus providing a consistent framework to describe the TeV emission from Vela.

Keywords: Gamma rays — Pulsars — Vela pulsar (PSR J0835–4510) — Magnetic fields — *Fermi* Large Area Telescope.

Contents

1	Introduction	1
1.1	Recent developments in γ -ray pulsar astronomy	1
1.1.1	Historical perspective of γ -ray pulsar detections and theoretical expectations	1
1.1.2	Observational revolution	2
1.1.3	Debate regarding high-energy radiation mechanisms	2
1.1.4	Latest <i>NICER</i> results	3
1.1.5	Upcoming developments	3
1.2	Problem identification and research aims	4
1.3	Publications	5
1.3.1	Peer-reviewed conference proceedings	5
1.3.2	Journal articles	5
1.4	Thesis outline	5
2	Pulsar astrophysics	7
2.1	Pulsar discovery, formation and classes	7
2.1.1	A survey of pulsar history	7
2.1.2	Pulsar formation	9
2.1.3	Pulsar classes	11
2.2	Standard braking model for rotation-powered pulsars	12
2.3	The Goldreich-Julian model	14
2.4	High-energy radiation mechanisms and pair creation processes	15
2.4.1	Particle acceleration	15
2.4.2	Synchrotron radiation	16
2.4.3	Curvature radiation	18
2.4.4	Inverse Compton scattering and synchrotron self-Compton scattering	19
2.4.5	Pair production	20
2.5	Traditional pulsar models	22
2.5.1	Polar cap model	22
2.5.2	Slot gap model	23
2.5.3	Outer gap model	24
2.5.4	Pair-starved polar cap model	25
2.6	Developments in the magnetic field structure calculations	26
2.6.1	Static dipole magnetic field	26
2.6.2	Retarded vacuum dipole magnetic field	27
2.6.3	Offset-dipole magnetic field	28
2.6.4	A force-free field	29
2.7	Recent theoretical developments	30
2.7.1	A dissipative field	30

2.7.2	Kinetic models	30
2.7.3	Striped-wind models	32
2.8	Summary	33
3	The effect of an offset-PC B-field geometry on the predicted γ-ray light curves of the Vela pulsar	34
3.1	Introduction	35
3.2	Offset-dipole B -field structure	36
3.3	Geometric models	38
3.4	Transformation of a B -field from the magnetic to the rotational frame	39
3.5	Finding the PC rim and extending the range of ϵ	40
3.6	Incorporating an SG E -field	41
3.6.1	Approximate expressions of the associated E -field	41
3.6.2	Determining the matching parameter η_c	42
3.7	Chi-squared fitting method	44
3.8	Results	46
3.8.1	Particle transport and testing for curvature radiation reaction	46
3.8.2	Light curves in different wavebands	48
3.8.3	$\chi^2(\alpha, \zeta)$ contours and best-fit light curves	50
3.9	Comparison of best-fit parameters for different models	50
3.10	Conclusion	55
4	Model description: code setup and refinements	57
4.1	An SSC emission modelling code	57
4.2	Calibration of the code	58
4.3	Running the code on a cluster	59
4.4	Recalculating the curvature radius ρ_c	63
4.5	Conclusion	65
5	Probing the γ-ray pulsar emission mechanism	66
5.1	Introduction	66
5.2	Isolating the origin of emission for each of the light curve peaks	68
5.3	Results	69
5.3.1	Finding optimal fitting parameters	69
5.3.2	Optimal model fit	74
5.3.3	Testing the attainment of the CRR limit	76
5.3.4	Local environment of emission regions connected to each light curve peak	77
5.4	Conclusion	82
6	Modelling the emission from the Vela pulsar in the TeV band	86
6.1	Overview	86
6.2	The effect of the refined ρ_c on the model output	87
6.3	Conclusion	89
7	Conclusions	90
7.1	Significant contributions and results	90
7.1.1	Offset-dipole studies	90
7.1.2	Energy-dependent CR light curves and spectral modelling	91
7.1.3	SSC modelling	92
7.2	Research implications	92
7.2.1	Offset-dipole studies	92

<i>CONTENTS</i>	v
7.2.2 Energy-dependent CR light curves and spectral modelling	93
7.2.3 SSC modelling	93
7.3 Future prospects	94
Appendix A Refined calculation of the curvature radius ρ_c	95

List of Figures

2.1	Schematic representation of a massive star's interior	9
2.2	The “lighthouse” pulsar model	10
2.3	A $P\dot{P}$ -diagram representing the canonical and millisecond pulsar populations	13
2.4	The pulsar magnetosphere as envisioned by Goldreich & Julian (1969)	14
2.5	Illustration of a photon pair cascade	20
2.6	Schematic view of the different traditional pulsar emission models	22
2.7	Illustration of the two types of PC accelerators, including the SCLF and vacuum gap	23
2.8	A schematic view of an SG geometry	24
2.9	Representation of particle acceleration and pair production inside an OG geometry	25
2.10	Comparison between the static and RVD B -field structures	28
2.11	An example of the distortions in an RVD B -field for $\alpha = 65^\circ$	28
2.12	Snapshots of time-dependent FF simulations of the (a) aligned and (b) oblique rotators.	29
2.13	The observed and predicted light curves, and phase-resolved spectra for a FIDO model	31
2.14	The electron and positron components of the current density as predicted by the PIC model	32
2.15	Current sheet model	33
3.1	Symmetric offset-PC dipole B -field	37
3.2	Asymmetric offset-PC dipole B -field	37
3.3	PC shapes of the offset-PC dipole B -field for a few cases of α and ϵ in the $x' - y'$ plane	41
3.4	Examples of the general SG E -field ($E_{\parallel, \text{new}}$) we obtained by matching $E_{\parallel, \text{low}}$ and $E_{\parallel, \text{high}}$	43
3.5	Plot of \log_{10} of $-E_{\parallel, \text{high}}$, $-E_{\parallel, \text{low}}$, the general $-E_{\parallel, \text{SG}}$ -field (using η_c as the matching parameter; $-E_{\parallel, \text{old}}$) and a corrected E -field, $-E_{\parallel, \text{new}}$, gain rate $\dot{\gamma}_{\text{gain}}$, loss rate $\dot{\gamma}_{\text{loss}}$, and the Lorentz factor γ as a function of s/R	46
3.6	Phase plots and light curves for the SG model assuming an offset-PC dipole field, for $\epsilon = 0.18$ and a variable ϵ_γ	47
3.7	Phase plots and light curves for the SG model assuming an offset-PC dipole field, for $\epsilon = 0.18$, variable ϵ_γ , and a lower $E_{\gamma, \text{min}}$ of 1 MeV.	48
3.8	Phase plots and light curves for the SG model assuming an offset-PC dipole field, for $\epsilon = 0.18$, variable ϵ_γ , and a higher E -field.	49
3.9	Contour plots and best-fit light curves for each of the best-fit solutions we obtained for the offset-PC dipole B -field and SG model solution, for the two separate cases.	51
3.10	Comparison of the relative goodness of the fit of solutions obtained for each B -field and geometric model combination, including the case of $100E_{\parallel}$	52
3.11	Comparison between the best-fit α and ζ , with errors, obtained from this and other studies.	54
4.1	An example of the phase-averaged CR spectra for the Crab pulsar assuming $\alpha = 45^\circ$ and $\zeta_{\text{cut}} = 50^\circ$	59
4.2	An example of the phase plots for the Vela pulsar assuming $\alpha = 75^\circ$ and $\zeta_{\text{cut}} = 65^\circ$	60

4.3	An example of the newly calculated ρ_c as a function of normalised arclength s/R_{LC} before and after smoothing and matching	61
4.4	A comparison of electron position $x(s), y(s), z(s)$, trajectory direction $x'(s), y'(s), z'(s)$ and $\log_{10}(\rho_c)$, as calculated previously and now being refined	62
4.5	Phase plots and pulse profiles for $\alpha = 60^\circ$, $\zeta_{cut} = 65^\circ$, and $0.1 < E_\gamma < 50.0$ GeV	63
4.6	Phase plots and pulse profiles for $\alpha = 75^\circ$, $\zeta_{cut} = 65^\circ$, and $0.1 < E_\gamma < 50.0$ GeV	64
5.1	Example phase plots with (ϕ_L, ζ) -“blocks”(or 2D bins) and their associated light curves for $\alpha = 75^\circ$, $\zeta_{cut} = 65^\circ$, $R_{acc} = 0.25$ cm $^{-1}$, and $0.1 < E_\gamma < 50$ GeV	67
5.2	Energy-dependent light curves for $\alpha = 75^\circ$ and $\zeta_{cut} = 65^\circ$ for several different combinations of R_{acc} for both scenarios	70
5.3	Model phase-averaged and phase-resolved spectra associated with Figure 5.2	71
5.4	Energy-dependent light curves for $\alpha = 75^\circ$ and different ζ_{cut} for the optimal values of $E_{ }$ -field for both scenarios	72
5.5	Model phase-averaged and phase-resolved spectra associated with Figure 5.4	73
5.6	Energy-dependent phase plots and light curves for $\alpha = 75^\circ$ and $\zeta_{cut} = 65^\circ$ and for the optimal R_{acc} for both scenarios	75
5.7	The same as Figure 5.6 but for $\zeta_{cut} = 40^\circ$ and $\delta = -0.2$	77
5.8	Phase-averaged and phase-resolved spectra for the refined ρ_c calculation, for $\alpha = 60^\circ$ and $\zeta_{cut} = 65^\circ$, for both scenarios	78
5.9	The same as Figure 5.8, but for $\alpha = 75^\circ$ and $\zeta_{cut} = 65^\circ$	78
5.10	The particle dynamics, along the same B -field lines as in Figure 4.4, are shown for the refined ρ_c calculation, for $\alpha = 75^\circ$	79
5.11	Energy-dependent histograms for $\log_{10}(E_{\gamma,CR}/\text{GeV})$ for P1 and P2, for both scenarios	80
5.12	The same as Figure 5.11 but for $\log_{10}(\rho_c)$	81
5.13	The same as Figure 5.11 but for $\log_{10}(\gamma)$	82
5.14	Energy-dependent histograms of $\log_{10}(E_{\gamma,CR}/\text{GeV})$, $\log_{10}(\rho_c)$, and $\log_{10}(\gamma)$, for P1 and P2. All three cases are for scenario 1 at altitudes equal to and beyond R_{LC}	83
5.15	The same as in Figure 5.14 but for scenario 2	84
6.1	E_γ -dependent light curves for emission from Vela in the IR/optical band, and three different γ -ray energy bands, assuming $\alpha = 75^\circ$ and $\zeta_{cut} = 65^\circ$	88
6.2	Model phase-averaged spectra for the Vela pulsar assuming $\alpha = 75^\circ$ and $\zeta_{cut} = 65^\circ$	88

List of Tables

3.1	Best-fit parameters for each B -field and geometric model combination	53
-----	---	----

Chapter 1

Introduction

1.1 Recent developments in γ -ray pulsar astronomy

1.1.1 Historical perspective of γ -ray pulsar detections and theoretical expectations

Since the launch in June 2008 of the *Fermi* Large Area Telescope (LAT; Atwood et al., 2009), a high-energy (HE) satellite measuring γ -rays in the 20 MeV to > 300 GeV range, there has been a consistent discovery rate of new pulsars. The *Fermi* LAT Collaboration has already released two pulsar catalogues (1PC, Abdo et al., 2010c; 2PC, Abdo et al., 2013) discussing the light curve and spectral properties of these (117 in 2PC) pulsars. Prior to *Fermi*, only 7 γ -ray pulsars were known (Thompson et al., 1997). The bulk of the *Fermi*-detected pulsars display exponentially cutoff spectra with cutoffs falling in a narrow range around a few GeV. During this time (early 2000s), there was no detection of TeV pulsed emission.

Earlier pulsar models mostly expected HE emission at tens of GeV, while some made predictions of TeV emission, but this was rather uncertain. For example, pulsar models (see Chapter 2 for more details), assuming the standard outer gap (OG) scenario, predicted spectral components in the very-high-energy (VHE; > 100 GeV) regime when estimating the inverse Compton scattering (ICS) flux of primary electrons on synchrotron radiation (SR) or other soft photons (Cheng et al. 1986; Romani 1996; Hirotani 2001). This resulted in a natural bump around a few TeV (involving ~ 10 TeV particles) in the extreme Klein-Nishina limit. However, these components may not survive up to the light cylinder¹ and beyond, since magnetic pair creation leads to absorption of the TeV γ -ray flux (Hirotani, 2001). Other studies assumed standard pulsar models and curvature radiation (CR) to be the dominant radiation mechanism producing γ -ray emission and found spectral cutoffs of up to 100 GeV. For example, Bulik et al. (2000) modelled the cutoffs of millisecond pulsars (MSPs) that possess relatively low B -fields and short periods. Their model assumed a static dipole B -field and a polar cap (PC) geometry, and predicted CR from the primary electrons that are released from the PC and accelerated along curved B -field lines. Their predicted spectrum cut off at ~ 100 GeV. The CR photons may undergo magnetic pair production in the intense low-altitude B -fields, and the newly formed electron-positron secondaries will emit SR in the optical and X-ray band. Harding et al. (2002a) also found CR spectral cutoffs at energies between 50–100 GeV. Harding et al. (2005) investigated the X-ray and γ -ray spectrum of rotation-powered MSPs using a pair-starved polar cap (PSPC) model, and found CR cutoffs of ~ 10 –50 GeV (see also Frackowiak & Rudak, 2005; Venter & De Jager, 2005). Harding et al. (2008) modelled the optical to γ -ray emission from a slot gap (SG) accelerator and applied it to the Crab pulsar (assuming a retarded vacuum dipole (RVD) B -field), finding spectral cutoffs of up to a few GeV. Hirotani (2008a) modelled phase-resolved spectra of the Crab pulsar using the OG and SG models, and found HE cutoffs of up to ~ 25 GeV (see also Tang et al. (2008) who used the RVD B -field to model phase-resolved spectra of the Crab, finding HE cutoffs around ~ 10 GeV). *Therefore, it was*

¹The radius R_{LC} where the co-rotation speed equals the speed of light c .

more or less the consensus of the field prior to 2008 that the HE emission from pulsars occurred in an energy band that was perhaps above the detection range of satellite detectors like the Energetic Gamma-Ray Experiment Telescope (EGRET) in some cases, and below that of ground-based Cherenkov detectors that had energy thresholds above 100 GeV, unless there were TeV spectral components (but the older OG predictions of the latter had been scaled down based on available upper limits at the time, so this was not a strong expectation).

1.1.2 Observational revolution

In view of the above, it was not strongly expected that pulsars should be visible in the VHE regime. It was therefore surprising when the Major Atmospheric Gamma-ray Imaging Cherenkov Telescope (MAGIC) detected pulsed emission from the Crab pulsar at energies up to ~ 25 GeV (Aliu et al., 2008; Aleksić et al., 2011, 2012), and even more surprising when the Very Energetic Radiation Imaging Telescope Array System (VERITAS) announced the detection of the same, but up to ~ 400 GeV (Aliu et al., 2011). The Crab pulsar is thus the first source from which pulsations have been detected over almost all energies ranging from radio to VHE γ -rays.

The detection of the Crab pulsar above several GeV prompted *Fermi* to search for pulsed emission at HEs. They detected significant pulsations above 10 GeV from 20 pulsars and above 25 GeV from 12 pulsars (Ackermann et al., 2013). A stacking analysis involving 115 *Fermi*-detected pulsars (excluding the Crab pulsar) was performed by McCann (2015). However, no emission above 50 GeV was detected, implying that VHE pulsar detections may be rare, given current telescope sensitivities. Notably, pulsed emission was also detected from the Vela pulsar up to 80 GeV with the *Fermi* LAT (Leung et al., 2014).

Ground-based Cherenkov telescopes are now searching for more examples of VHE pulsars, and they have had some success in recent years. In the VHE band, MAGIC detected pulsations from the Crab pulsar at energies up to 1 TeV (Ansoldi et al., 2016). Pulsed emission from the Vela pulsar was detected in the sub-20 GeV to 100 GeV range with H.E.S.S. (Abdalla et al., 2018). New observations by H.E.S.S. reveal pulsed emission from Vela up to several TeV (H.E.S.S. Collaboration, in preparation). VERITAS furthermore detected no emission from Geminga above 100 GeV (Aliu et al., 2015). However, pulsed emission from the Geminga pulsar between 15 GeV and 75 GeV at a significance of 6.3σ was recently announced by MAGIC, although only the second light curve peak is visible at these energies. The MAGIC spectrum is an extension of the *Fermi* LAT spectrum, ruling out the possibility of a sub-exponential cutoff in the same energy range at the 3.6σ level (Acciari et al., 2020). H.E.S.S. II furthermore detected pulsed emission from PSR B1706–44 in the sub-100 GeV energy range (Spir-Jacob et al., 2019).

From these VHE observations, four trends in the energy-dependent pulse profiles seem to emerge: as the photon energy E_γ is increased (above several GeV), the main light curve peaks of Crab, Vela and Geminga seem to remain at the same phase positions, the intensity ratio of the first to second peak (P1/P2) decreases with an increase of E_γ for Vela and Geminga, the inter-peak “bridge” emission evolves for Vela, and the peak widths decrease for Crab (Aliu et al., 2011), Vela (Abdo et al., 2010d) and Geminga (Abdo et al., 2010b). The second peak of Crab for MAGIC is harder and extends to a bit higher energy (~ 2 TeV) than the first peak. The P1/P2 vs. E_γ effect was also seen by *Fermi* for a number of pulsars (Abdo et al., 2010c, 2013).

1.1.3 Debate regarding high-energy radiation mechanisms

In general, multi-wavelength pulsar light curves exhibit an intricate structure that evolves with E_γ (e.g., Bühler & Blandford, 2014), reflecting the various underlying emitting particle populations and spectral radiation components that contribute to this emission, as well as the local B -field geometry and E -field spatial distribution. In addition, Special Relativistic effects modify the emission beam, given the fact that the co-rotation speeds may reach close to the speed of light c in the outer magnetosphere.

Some traditional physical emission models invoke CR from extended regions within the magnetosphere to explain the HE spectra and light curves. These include the SG (Arons, 1983; Harding & Muslimov, 2003) and OG (Romani & Yadigaroglu 1995; Cheng et al. 1986) models. However, they fall short of fully addressing

global magnetospheric characteristics, e.g., the particle acceleration and pair production, current closure, and radiation of a complex multi-wavelength spectrum. Geometric light curve modelling (Dyks et al., 2004a; Venter et al., 2009; Watters et al., 2009; Johnson et al., 2014; Pierbattista et al., 2015) presented an important interim avenue for probing the pulsar magnetosphere in the context of traditional pulsar models, focusing on the spatial rather than physical origin of HE photons. More recent developments include global magnetospheric models such as the force-free (FF) inside and dissipative outside (FIDO) model (Brambilla et al., 2015; Kalapotharakos & Contopoulos, 2009; Kalapotharakos et al., 2014), equatorial current sheet models (e.g., Bai & Spitkovsky 2010a; Pétri 2012), the striped-wind models (e.g., Pétri & Dubus 2011), and kinetic / particle-in-cell simulations (PIC; Brambilla et al. 2018; Cerutti et al. 2016a,b, 2020; Kalapotharakos et al. 2018; Philippov & Spitkovsky 2018). Some studies using the FIDO models assume that particles are accelerated by induced E -fields in dissipative magnetospheres and produce GeV emission via CR (e.g., Kalapotharakos et al. 2014). Conversely, in some of the wind or current-sheet models, HE emission originates beyond the light cylinder via SR by relativistic, hot particles that have been accelerated via magnetic reconnection inside the current sheet (e.g., Pétri & Dubus, 2011; Philippov & Spitkovsky, 2018). Other studies assume ICS to be the dominant emission mechanism of HE γ -rays in an OG scenario (see Lyutikov et al. 2012; Lyutikov 2013 who modelled the broadband spectrum of the Crab pulsar). There is thus an ongoing debate regarding pulsar emission mechanisms, and it is hoped that future observations will help discriminate between models.

1.1.4 Latest *NICER* results

The Neutron star Interior Composition Explorer (*NICER*; Gendreau et al. 2016)² is an instrument that is dedicated to study thermal and non-thermal emission from neutron stars (NS) in the soft X-ray band (0.2 – 12 keV) through soft X-ray timing and a spectroscopy instrument on-board the International Space Station, with exceptional sensitivity. *NICER* has a star-tracker-based pointing system that allows the X-ray timing instrument to target and track celestial objects over nearly the full hemisphere.

Earlier modelling have long expected multipolar B -fields in MSPs (Ruderman & Sutherland 1975; Arons 1983; Asseo & Khechinashvili 2002). For example, Harding & Muslimov (2011a,b) used a generalised solution of an offset dipole of which the PCs are assumed to be offset from the dipole axis and applied it to MSPs. Since MSPs such as PSR J0437–4715 and PSR J0030+0451 are too old to suffer significant cooling, their thermal X-ray emission is believed to be from hot spots on the PCs. These hotspots may not be strictly antipodal, given a non-dipolar B -field structure.

Since the launch of *NICER* in June 2017, the rotation-powered MSPs such as PSR J0030+0451 and PSR J0437–4715, have been studied in much detail. Modelling of the observed thermal X-ray pulsations from these sources gave valuable insight into the global B -field structures associated with MSPs. These studies support the existence of a multi-polar B -field, including offset-dipole plus quadrupole components, that deviates from a centred dipole (e.g., Miller et al., 2019; Riley et al., 2019; see Section 2.6.1) after modelling *NICER* X-ray waveforms from PSR J0030+0451. Kalapotharakos et al. (2020) investigated the B -field structure that includes offset dipole plus quadrupole components using a static vacuum field and FF global magnetosphere models. They modelled the γ -ray and X-ray emission and compared it to the *Fermi* data (see also Chen et al. 2020). These observations thus confirm earlier expectations of more complicated, multi-polar B -field structures in pulsars, the effect of which are particularly evident near the stellar surface.

1.1.5 Upcoming developments

The population of pulsars detected by the *Fermi* LAT has increased to over 250, leading to the preparation of the *Fermi*’s Third Pulsar Catalogue (3PC). This catalogue builds on the 2PC, and will include updated timing solutions, pulse profiles, spectra, and ancillary data. In addition to an increase in the number of pulsars, the 3PC also includes novel pulsars, e.g., the first radio-quiet MSP and first extra-Galactic γ -ray pulsar (Limyansky,

²<https://heasarc.gsfc.nasa.gov/docs/nicer/>

2019). The All-sky Medium Energy Gamma-ray Observatory (*AMEGO*; McEnery et al. 2019) is a proposed MeV γ -ray surveyor probe that fills the gap between hard X-ray instruments, e.g., NuSTAR and the HE γ -ray telescopes, e.g., *Fermi* LAT and the Astro-Rivelatore Gamma a Immagini Leggero (*AGILE*), and is planned to launch in 2029. Current and future missions (including the Square Kilometre Array, SKA) are dedicated to search for more pulsars over the entire electromagnetic spectrum. More pulsars emitting VHE emission may be found by present and future ground-based telescopes, e.g., the Cherenkov Telescope Array (CTA), which will have a ten-fold increase in sensitivity compared to present-day Cherenkov telescopes.

1.2 Problem identification and research aims

The *NICER* mission shows evidence of MSPs possessing offset-dipole structures. These studies pave the way for investigating new B -field structures, similar to our study done in Chapter 3. As a first approach, we will study the effect of the B -field structure on the predicted GeV light curves of the Vela pulsar by developing a geometric modelling code (Dyks et al., 2004a) based on different B -field solutions, i.e., static dipole, RVD, and an offset-PC dipole (the latter is additionally implemented; Harding & Muslimov 2011a,b), assuming constant emissivity ϵ_ν . Also, we implement an SG E -field to modulate ϵ_ν for such an offset-PC dipole and examine the effect thereof on the GeV light curves. Since this E -field is relatively low, we will multiply it by a factor 100 and illustrate the effective change in the light curves as well as the best fits of the *Fermi* data to the model, and compare our fits to multi-wavelength fits from independent studies.

As we have seen, a few major developments have shaped the field of pulsar science over the past decade. One of these include the increase in pulsar detections by the *Fermi* LAT. The light curves and phase-resolved spectra exhibit unique trends and different cutoffs for each emission peak in the different energy bands. The phase-resolved spectral cutoff for the second peak appears larger than that for the first peak in many cases, as well as the trends pointed out earlier. Our main goal for this study is to explain these trends and the spectral cutoffs for the Vela pulsar in the GeV range (see Chapter 5). Additionally, the more advanced kinetic and global models led to the debate between emission mechanisms. Given this ongoing debate between the emission mechanisms of HE emission, our motivation in this study is to explain the curved GeV spectrum and light curves of Vela as measured by *Fermi* and H.E.S.S. that result from primary particles emitting CR. Specifically, by modelling the E_γ -dependent light curves (and P1/P2 signature) and phase-resolved spectra in the CR regime of synchro-curvature (SC) radiation, we hope to probe whether this effect can serve as a potential discriminator between emission mechanisms and models (see also the reviews of Harding 2016; Venter 2016; Venter et al. 2017 on using pulsar light curves to scrutinise magnetospheric structure and emission distribution).

To date, four VHE pulsars have been detected, i.e., Crab, Vela, Geminga and PSR B1706–44, being some of the brightest γ -ray sources. To explain the measured VHE pulsed emission as seen from these pulsars leads to motivation for updating existing or implementing new spectral components. Harding & Kalapotharakos (2015) implemented a synchrotron self-Compton (SSC) radiation component that can explain the VHE emission seen from the Crab pulsar. A follow up paper (Harding et al., 2018) extended the SSC emission code and modelled the emission for Vela in this same energy range, and will be discussed in greater detail in Chapter 6. The immense rise in the number of pulsars detected makes population studies possible in order to better understand pulsar physics.

We have access to an SSC emission code that predicts light curves and spectra, and already includes the SG current sheet model, FF B -field solution, a constant E_\parallel (as motivated by the kinetic models), standard radiation processes including CR, SR, ICS, and SSC, as well as pair cascades (associated with magnetic pair production and calculated in a separate code) that originate near the PC (Harding & Kalapotharakos, 2015). In order to model emission pulse profiles as a function of energy, as well as predicting phase-resolved spectra for Vela, we will apply this SSC emission code assuming emission from primary particles that emit only CR. Since particles that emit CR radiation mostly follow the curved B -field lines in the rotating frame, our proposed project involves implementing a refined calculation of the curvature radius ρ_c of the particle trajectory. We will investigate the

behaviour of the light curve peaks as well as the light curve trends as a function of ρ_c . For the optimal light curve and spectral fits, we will study the local environment of the peaks' emission regions, finding a systematic difference in ρ_c , particle Lorentz factor γ , and spectral cutoff energy $E_{\gamma,CR}$ for the two peaks. Lastly we will compare our results to measurements of *Fermi* and H.E.S.S. for the Vela pulsar (see Chapter 5). Our improved ρ_c was also one of the adaptations made by Harding et al. (2018), therefore the results we obtained in this study accompany theirs (see Chapter 6).

1.3 Publications

The publications that emanated directly from this study are listed below.

1.3.1 Peer-reviewed conference proceedings

1. Breed, M.; Venter, C.; Harding, A. K., 2016, *Very-high energy emission from pulsars*, in Conf. Proc. of SAIP2015: Proc. of the 60th Ann. Conf. of the South African Inst. of Phys., ed. by M. Chithambo & A. Venter, pp. 278–283.
2. Barnard, M., Venter, C., & Harding, A. K., 2017, *High-energy pulsar light curves in an offset polar cap B-field geometry*, in Conf. Proc. of HEASA2016: the 4th Ann. Conf. on High Energy Astrophys. in Southern Africa, ed. by M. Boettcher, D. Buckley, S. Colafrancesco, P. Meintjes, & S. Razzaque, id. 42.
3. Barnard, M., Venter, C., Harding, A. K., & Kalapotharakos, C., 2017, *Modelling energy-dependent pulsar light curves due to curvature radiation*, in Conf. Proc. of HEASA2017: the 5th Ann. Conf. on High Energy Astrophys. in Southern Africa, ed. by M. Boettcher, D. Buckley, S. Colafrancesco, P. Meintjes, & S. Razzaque, id. 22.
4. Venter, C., Barnard, M., Harding, A. K., & Kalapotharakos, C., 2018, *Modelling energy-dependent pulsar light curves*, in Conf. Proc. of IAUS No. 337: Pulsar Astrophysics - The Next 50 Years, ed. Weltevrede, P., Perera, B. B. P., Preston, L. L., & Sanidas, S., 337, 120–123.

1.3.2 Journal articles

1. Barnard, M., Venter, C., & Harding, A. K., 2016, *The Effect of an Offset Polar Cap Dipolar Magnetic Field on the Modeling of the Vela Pulsar's γ -Ray Light Curves*, ApJ, 832, 107.
2. Harding, A. K., Kalapotharakos, C., Barnard, M., & Venter, C., 2018, *Multi-TeV Emission from the Vela Pulsar*, ApJ, 869, L18.
My contribution is the calculation of a refined curvature radius ρ_c as discussed in Chapter 4.
3. Barnard, M., Venter, C., Harding, A. K., & Kalapotharakos, C., 2020, *Probing the γ -ray Pulsar Emission Mechanism via Energy-dependent Light Curve Modeling*, in preparation.

1.4 Thesis outline

Chapter 2: This Chapter gives an overview of various topics related to pulsar science, and more specifically, those that are relevant to this study on pulsar emission modelling, e.g., the history of pulsars, their formation, different pulsar classes, standard models of pulsar electrodynamics, important radiation mechanisms, later pulsar emission models, and models of pulsar magnetospheres.

Chapter 3: A summary of a published journal article investigating the implication of magnetospheric structures on pulsar model light curves. Additionally, I studied an offset-PC dipole B -field structure and an SG E -field solution, and the effect on light curve predictions when I increased such an E -field.

Chapter 4: In this Chapter, I describe the emission modelling code I used to study pulsar emission and explain the implementation of a more refined ρ_c calculation. I also discuss additional technical details that this study entails, such as the calibration of the code and getting the parallelised version thereof running on the local cluster.

Chapter 5: This Chapter describes first results that followed from the implementations discussed in Chapter 4 for the Vela pulsar, and include the energy-dependent light curve and spectral modelling (Barnard et al., in prep.). This Chapter highlights the main results of my PhD thesis work, in accordance with the aims set earlier. The results also accompany those discussed in Chapter 6.

Chapter 6: Here I emphasise my main contribution to the accompanying VHE paper for the Vela pulsar (Harding et al., 2018).

Chapter 7: Summarises the conclusions drawn from this study.

Chapter 2

Pulsar astrophysics

I give an overview of several relevant pulsar topics in order to provide context for the present study. I briefly describe the historical development of the pulsar field (Section 2.1.1), the mechanism of pulsar formation (Section 2.1.2), different classes of pulsars (Section 2.1.3), the standard braking model that explains the conversion of rotational energy of pulsars into radiation and particle acceleration (Section 2.2), the traditional Goldreich-Julian model (Section 2.3), some relevant radiation mechanisms and pair production (Section 2.4), and pulsar emission models (Section 2.5). Given the fact that this project mainly deals with pulsar magnetospheres and the HE and VHE γ -ray light curves of the Vela pulsar as measured by the *Fermi* and ground-based telescopes, I lastly describe developments in B -field structures and models (Sections 2.6 and 2.7). This Chapter represents an update on what was presented in Breed (2015).

2.1 Pulsar discovery, formation and classes

2.1.1 A survey of pulsar history

The neutron was discovered by James Chadwick in 1932 (Chadwick, 1932). The concept of a neutron star (NS) originated more or less at the same time. Chandrasekhar studied stellar evolution and discovered that a collapsing stellar core consisting of a mass larger than $1.4 M_{\odot}$ (the well-known Chandrasekhar limit, applicable to white dwarf stars) should continue collapsing, since it can not balance its own gravity after all its nuclear fuel has been exhausted (Chandrasekhar, 1931). Landau (1932) also studied white dwarf stars and speculated on the existence of a star that could be more dense than white dwarf stars, and is described as a gigantic atom. Walter Baade and Fritz Zwicky analysed observations of supernova explosions and discovered that supernovae appeared to be less frequent than common novae, and to emit enormous amounts of energy during each explosion (Baade & Zwicky, 1934b). They also observed that supernovae explode faster than novae. Their calculations implied that a supernova remnant can not have a larger radius than a nova. Baade and Zwicky proposed that NSs could form in supernova explosions, since a supernova represents a transition from an ordinary star into a very dense object with a small radius and mass (Baade & Zwicky, 1934a). In 1939, Oppenheimer and Volkoff constructed the first models that could describe the structure of an NS, also incorporating general relativity. They stated that NSs are so dense that spacetime is curved around and within them, motivating the importance of general relativistic effects (Haensel et al., 2007). They calculated that stars reaching a mass larger than $3 M_{\odot}$ (known as the Oppenheimer-Volkoff limit) would undergo gravitational collapse to form a black hole. The concept of NSs was not taken too seriously until the late 1960s when new discoveries were made in high-energy (HE) and radio astronomy (Becker & Pavlov, 2002).

Results from HE cosmic-ray experiments implied that there could be astrophysical objects, e.g., supernova remnants, which could produce high-energy cosmic rays as well as X-rays and γ -rays (Morrison et al., 1954;

Morrison, 1958). In 1962, Rossi and Giacconi confirmed these notions when they detected X-rays from Sco X-1 (a source located in the constellation Scorpio), the brightest X-ray source in the sky (Giacconi et al., 1962). These X-rays were believed to be the result of SR by cosmic electrons carrying energies of the order of tens of keV. Bowyer et al. (1964) detected a second X-ray source Tau X-1, situated in the constellation Taurus. This source coincided with the Crab supernova remnant. Among all the different theories and processes proposed for the origin of these X-rays, Chiu & Salpeter (1964) proposed that this was due to thermal radiation emitted from the surface of a hot NS. Since NSs are expected to appear as point sources and the X-radiation from the Crab supernova remnant had a finite angular size of $\sim 1'$, the existence of an actual NS still remained uncertain. Hoyle et al. (1964) made the visionary prediction that there could be an NS with a strong B -field of $\sim 10^{10}$ G at the centre of the Crab Nebula.

In 1967, Anthony Hewish directed the construction of a radio telescope at the Mullard Radio Astronomy Observatory, which was designed to detect interplanetary scintillation from cosmic sources (Hewish et al., 1968). The first discovery made with this new radio telescope was by Jocelyn Bell, a graduate student from Cambridge University supervised by Hewish. She detected a weak, variable radio source displaying a series of stable periodic pulses (Hewish et al., 1968; Hewish, 1975). These radio pulses arrived at a precise period of 1.3373012 s. They jestingly called this source “Little Green Man 1”. After three more similar pulsating radio sources were detected (PSR B1133+16, PSR B0834+06, PSR B0950+08), it became clear that a new kind of natural phenomenon was discovered. Another faster pulsar – the Vela pulsar – was discovered in 1968 by the Molonglo group, possessing a pulse period of 0.089 s and situated near the centre of the Vela X supernova remnant (Large et al., 1968). Staelin and Reifenstein discovered two more pulsars in 1968, one of which (the Crab pulsar) was located within $5'$ from the centre of the famous Crab Nebula, having a period of 33 ms (Staelin & Reifenstein, 1968). In the same year that the first known pulsar (PSR B1919+21) was discovered, over 100 theoretical papers were published proposing interpretations or models for pulsars (Will, 1994). During this time, Wheeler (1966) and Pacini (1967) proposed that the energy source in the Crab Nebula could possibly be a rapidly rotating, and highly magnetised NS. Gold (1968; 1969) suggested that since supernova remnants are associated with fast rotating NSs, a pulsar is none other than a rotating NS. Therefore, it is believed that NSs are born in core-collapsed supernovae of highly evolved massive stars. Cocke et al. (1969) next discovered strong optical pulses from the Crab pulsar. This important discovery that the “remnant star” that survived the Crab supernova explosion (Minkowski, 1942) was in fact a pulsar, a rapidly rotating NS, therefore solidified the link between supernovae, NSs, and pulsars. Soon after, Bradt et al. (1969) and Fritz et al. (1969) detected X-ray pulsations from the Crab pulsar in the 1.5 – 10 keV range, and Hillier et al. (1970) detected γ -ray pulsations at energies > 0.6 MeV with a significance of $\sim 3.5\sigma$.

During the mid-seventies γ -ray astronomy expanded with the launch of two satellites: *Small Astronomy Satellite 2* (SAS-2) in 1972 (Fichtel et al., 1975), which confirmed the existence of γ -ray emission from the Crab pulsar (Kniffen et al., 1974) and the Vela pulsar (Thompson et al., 1975), and *Cosmic Ray Satellite-B* (COS-B) in 1975, which provided a complete detailed map of the γ -ray sky (Schönfelder, 2001). The number of detected radio pulsars also increased rapidly in this era. The idea that pulsars have high B -fields ($\sim 10^{12}$ G) was confirmed by the *Uhuru* (i.e., *Small Astronomy Satellite 1* (SAS-1)) observation of an accreting X-ray binary pulsar Her X-1 in the constellation Hercules (Tananbaum et al., 1972). A spectral feature at 58 keV was interpreted as resonant electron cyclotron emission or absorption in the hot polar plasma of the NS, implying a B -field of $\sim 6 \times 10^{12}$ G (Truemper et al., 1978).

The launch of other satellite missions that made important contributions to HE astrophysics, especially isolated NSs, include *High Energy Astrophysical Observatories* (HEAO 1, HEAO 2, and HEAO 3), *Chandra X-ray Observatory*, and *X-ray Multi-Mirror Mission* (XMM-Newton; Rudak et al., 2002). The field of γ -ray pulsars has been revolutionised by the launch of *Astro-rivelatore Gamma a Immagini LEggero* (AGILE) and the *Fermi* LAT, which is much more sensitive than its predecessor, *EGRET* (Atwood et al., 2009). Very recently, the ground-based imaging atmospheric Cherenkov telescopes, *Major Atmospheric Gamma-Ray Imaging Cherenkov* (MAGIC; Aleksić et al., 2011, 2012, 2015; Aliu et al., 2008) and *Very Energetic Radiation Imaging Telescope Array System* (VERITAS; Aliu et al., 2011) detected γ -ray pulsations from the Crab pulsar up to sev-

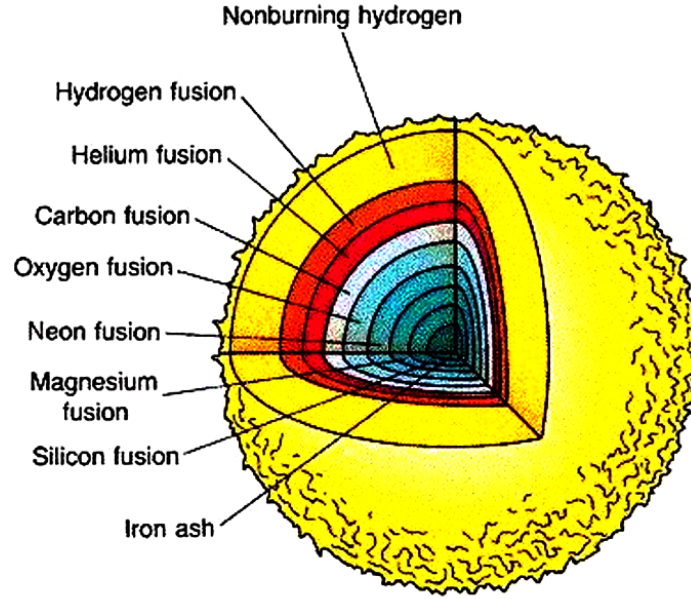


Figure 2.1: Illustration of the chemical composition of a highly evolved massive star, with each layer representing a different element, and an iron core at the centre. From Chaisson & McMillan (2002).

eral hundred GeV. Furthermore, the H.E.S.S.-II has earlier detected pulsed emission from the Vela pulsar above 20 GeV (Abdalla et al., 2018), and recently up to 7 TeV (Djannati-Ataï et al., 2017). Pulsed emission was also detected from Geminga between 15 GeV and 75 GeV by MAGIC (Acciari et al., 2020), and PSR B1706–44 in the sub-100 GeV energy range by H.E.S.S. II (Spir-Jacob et al., 2019).

2.1.2 Pulsar formation

The formation of pulsars is initiated by the death of high-mass ($M > 8M_{\odot}$) stars (Chaisson & McMillan, 2002). A high-mass star is made up of various layers of elements, starting with the hydrogen surface, then helium, carbon, oxygen, and other heavier elements at the core, as illustrated in Figure 2.1. There are two mechanisms operating during the burning and evolutionary stages of such stars, namely fusion and fission. Fusion takes place during the burning process. Each element (from the outer layers down to the inner layers) burns its nuclei, causing an increase in temperature with depth. The released nuclear energy produces gas and radiation pressure which counteracts the star's gravity. Once a particular element is exhausted, the burning of a heavier one is initiated by gravitational contraction (Chaisson & McMillan, 2002).

The burning process continues until an iron core is established. Since iron is the most stable element, it serves as the division between operation of the fusion and fission processes. The iron core becomes unstable when the star attempts to contract again and the nuclear reactions (which have been supplying energy) cease, so that all equilibrium is destroyed (Tayler, 1994). The gravity exceeds the gas pressure and the core collapses in on itself, causing the central regions to reach high densities and extremely high temperatures. After the collapse, fission takes place and the thermal energy from the core is absorbed to enable the photons to break the iron up into lighter nuclei, which in turn dissociate into protons and neutrons (a process known as photo-disintegration, Chaisson & McMillan, 2002). As the temperature and pressure of the core (now consisting of elementary particles) decrease, the gravitational force becomes stronger and the density increases even more, allowing the collapse to continue. The compression inside the core causes the protons and electrons to combine, producing neutrons and neutrinos (the process is known as neutronisation, Tayler, 1994). These neutrinos escape from the star, carrying energy with them. The pressure decreases again, so that the core collapses to

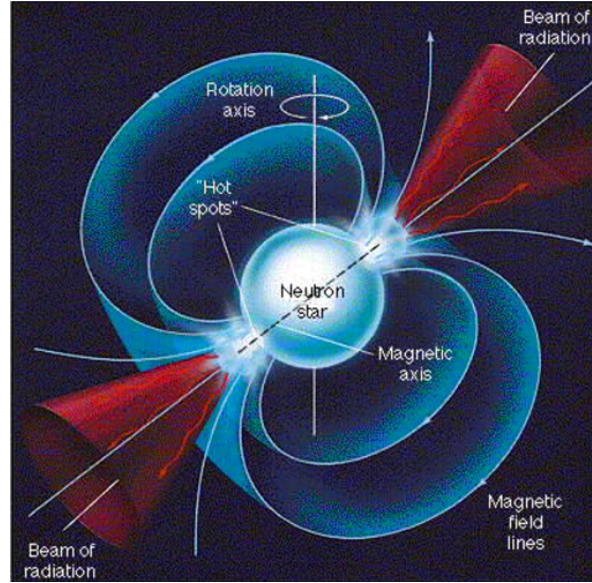


Figure 2.2: A pulsar may be compared to a lighthouse. The charged particles are accelerated along the B -field lines of the rotating NS, producing radiation in the form of beams. Figure from Chaisson & McMillan (2002).

a point where the neutrons make contact with each other, reaching stellar core densities of $\sim 10^{15} \text{ kg m}^{-3}$. Neutron degeneracy pressure now opposes further gravitational collapse, slowing it down. The core contracts, exceeding the equilibrium point, and is accompanied by the release of gravitational binding energy and emission of neutrinos and gravitational waves (Bowers & Deeming, 1984). A “hydrodynamic bounce” may occur as the core rebounds and a shock wave will sweep through the star at high speed, outward into the mantle, and may lead to a spectacular supernova explosion (Bowers & Deeming, 1984; Tayler, 1994).

Historically supernovae have been divided into two classes, i.e., core-collapse and thermal runaway supernova, from a physical point of view of their mechanism of explosion. Type I supernovae occur in binary systems (Palen, 2002) involving white dwarfs, and Type II supernovae involve isolated, highly evolved massive stars. When a massive star explodes as a Type II supernova, the remains of the star are carried outward into space by the shock wave. These remains may form a nebula, sometimes observed as being surrounded by a supernova remnant shell. Nebulae are regions of glowing, ionised gas with the brightness of these clouds depending on the brightness of the central degenerate NS (Chaisson & McMillan, 2002).

The maximum predicted mass of an NS is between $1.5M_{\odot}$ and $2.7M_{\odot}$ (Palen, 2002). The highest mass observed so far is $2.01 \pm 0.04M_{\odot}$, for PSR J0348+0431 (Antoniadis et al., 2013)¹. For somewhat higher stellar masses, it is believed that a black hole will be formed after gravitational collapse (Kanbach, 2001). NSs are small, very dense objects. According to the law of conservation of angular momentum, a rigidly rotating object will spin faster as it shrinks, implying that the NS rotates very rapidly, with millisecond to subsecond periods, and having strong B -fields, e.g., $B \sim 10^{8-13} \text{ G}$. Such a rapidly, highly magnetised NS is known as a (rotation-powered) pulsar that radiates energy into space. The simplest analogy of a pulsar is a lighthouse, as shown in Figure 2.2.

The magnetic poles of the pulsar are known as polar caps (PCs), from where charged particles may be accelerated more or less steadily along the B -field lines to very high energies (although newer models prefer the dominant site of acceleration to be the equatorial current sheet - see Section 2.7). The radio radiation is emitted in a searchlight pattern, and as the radio beam sweeps past Earth, a pulse is observed. All pulsars are NSs but not all NSs are (observable as) pulsars, for two reasons. First, an NS only pulses because of a

¹<https://greenbankobservatory.org/most-massive-neutron-star-ever-detected/>

strong B -field and rapid rotation, which diminish with time, causing the radio pulses to weaken and occur less frequently. Second, young pulsars are not always visible from Earth because the radio beam is very narrow, and may miss Earth (Chaisson & McMillan, 2002).

2.1.3 Pulsar classes

Pulsars are generally divided into two categories according to the B -field and age. Canonical pulsars are young ($\tau \sim 10^3 - 10^6$ yr) and have high B -fields ($B \sim 10^{12} - 10^{13}$ G), while MSPs are old ($\tau \sim 10^8 - 10^9$ yr) and are characterised by low B -fields ($B \sim 10^8 - 10^9$ G). Since the launch of several satellite observatories, for instance *Röntgensatellit* (ROSAT), *Extreme Ultraviolet Explorer* (EUVE), *Advanced Satellite for Cosmology and Astrophysics* (ASCA), *Rossi X-ray Timing Explorer* (RXTE), *Chandra*, *XMM-Newton*, and the *Fermi* LAT, the number of detections of rotation-powered pulsars (RPPs, pulsars driven by the rotational energy of the NS) has increased dramatically (Becker & Pavlov, 2002). These RPPs have been detected in various energy bands including radio, X-ray, γ -ray, and optical, enabling the study of multi-wavelength pulsar emission.

The Crab pulsar is a famous canonical pulsar. Its light curves have been detected in radio, optical, X-ray, and γ -ray bands, all being phase-aligned (Abdo et al., 2010a). Several other pulsars have similar emission properties as those of the Crab pulsar, including B0540–69, J0537–6909, and B1509–58 (Becker & Pavlov, 2002). Another well-known example is the Vela pulsar (PSR B0833–45), the brightest persistent GeV source in the sky (Abdo et al., 2009). It has a period $P = 0.089$ s, period derivative $\dot{P} = 1.24 \times 10^{-13}$ s s $^{-1}$, a characteristic age $\tau = P/2\dot{P} = 1.2 \times 10^4$ yr, and it is also one of the closest pulsars to Earth, lying at a distance of $d = 287^{+19}_{-17}$ pc (Dodson et al., 2003). Vela was first detected emitting HE pulses by *SAS-2* (Thompson et al., 1975), followed by phase-resolved studies with *COS-B* (Grenier et al., 1988) and *EGRET* (Kanbach et al., 1994; Fierro et al., 1998). Vela was the first source investigated by *AGILE* (Pellizzoni et al., 2009), and the *Fermi* LAT used the Vela pulsar as a calibration source. Vela-like pulsars (e.g., PSR B0833–45, PSR B1706–44, PSR B1046–58, and PSR B1951+32) possess spin-down ages in the range $\sim 10^4$ – 10^5 years and are detected in various wavebands. Another source detected by *SAS-2* and *COS-B* was Geminga, which was identified as a radio-quiet pulsar when the *ROSAT* satellite detected pulsed X-ray emission from it (Halpern & Holt, 1992). *SAS-2* and *COS-B* confirmed, using a timing solution from *ROSAT* data, that Geminga is also a bright γ -ray pulsar (Mattox et al., 1992).

A new class of radio pulsars was discovered in 1981 by Backer and his colleagues, following the detection of PSR B1937+21, which has a period of 1.56 ms (Backer et al., 1982). MSPs originate from ordinary pulsars that are in binary systems. These normal pulsars “switch off” due to continued rotational energy loss, but following angular momentum and mass transfer via accretion from their companion star, they “switch on” again and become visible as MSPs (Alpar et al., 1982). MSPs have relatively short spin periods ($P \lesssim 10$ ms), small period derivatives ($\dot{P} \sim 10^{-21} - 10^{-19}$, i.e., they are very stable rotators), large spin-down ages, and low B -field strengths compared to those of normal pulsars and magnetars (Alpar et al., 1982).

An interesting new class of pulsars has recently been discovered. These so-called rotating radio transients (RRATs) are associated with single, dispersed bursts of emission having durations in the range of 2 – 30 ms, with the average time interval between bursts ranging from a few minutes to hours. It is suggested that these sources originate from rotating NSs, since radio emission from these objects is usually detectable for < 1 s per day, with their periodicities ranging between 0.4 – 7.0 s (McLaughlin et al., 2006). RRATs may be examples of pulsars whose magnetospheres switch between several stable configurations (Keane et al., 2011).

Magnetars, including anomalous X-ray pulsars (AXPs) and soft γ -ray repeaters (SGRs), are NSs that have extremely strong surface B -fields of $B \sim 10^{14-15}$ G, increasing in strength from the surface down to the core (Duncan & Thompson, 1992). These sources are also characterised by burst-like emission. They exhibit very strong X-ray emission, which is too high and variable to be explained by conversion of rotational energy alone, but possibly involve the decay and instability of their enormous B -fields (Rea & Esposito, 2011). They have long rotation periods that range from 2 – 12 s (exceeding those of radio pulsars), as well as large period derivatives ($\dot{P} \sim 10^{-13} - 10^{-9}$ s s $^{-1}$; Mereghetti, 2008).

2.2 Standard braking model for rotation-powered pulsars

Let us consider the NS to be a rapidly rotating object possessing a dipolar B -field. This NS has an angular momentum $J \approx M_i R_i^2 \Omega_i$, which is assumed to be conserved during the collapse of the progenitor, with M_i , R_i , and $\Omega_i = 2\pi/P_i$ the initial mass, radius, angular velocity, and P_i the initial rotational period. The relation between the initial and final angular velocity is therefore (since $M_i \approx M_f$)

$$\Omega_f \sim \Omega_i \left(\frac{R_i}{R_f} \right)^2. \quad (2.1)$$

This relation states that for values $R_i > R_f$ the angular velocity increases so that the rotational period P_f becomes much shorter, ranging from milliseconds up to seconds. The interior of the NS is assumed to be fully conductive, implying conservation of the magnetic flux $\Phi = \oint \mathbf{B} \cdot d\mathbf{a} \sim B_i R_i^2$ during the collapse of the core. The magnitude of the final B -field is then given by

$$B_f \sim B_i \left(\frac{R_i}{R_f} \right)^2. \quad (2.2)$$

From this relation it follows that for $R_i > R_f$ the B -field will increase, yielding high values of $B_f \sim 10^{12}$ G. The collapse of a compact neutron core therefore leads to high magnetic strengths and short periods. The rotational energy of the pulsar will be converted into electromagnetic and particle energy, leading to a slower rotational rate. The basic outcome of this rotation-powered pulsar model is to predict the rate at which this slow-down occurs. The angular kinetic energy of the rotating NS is given by

$$E_{\text{rot}} = \frac{1}{2} I \Omega^2, \quad (2.3)$$

with $I \sim MR^2$ the moment of inertia. In this model the polar B -field strength at the stellar surface can be estimated by equating the rotational energy loss rate to the magnetic dipole radiation loss rate L_{md} (Ostriker & Gunn, 1969)

$$\dot{E}_{\text{rot}} = \frac{d}{dt} \left(\frac{1}{2} I \Omega^2 \right) = I \Omega \dot{\Omega} = -\frac{4\pi^2 I}{P^3} \dot{P} \approx L_{\text{md}} = -\frac{2}{3c^3} \mu^2 \Omega^4 \sin^2 \alpha, \quad (2.4)$$

with $\mu \equiv B_0 R^3/2$ the magnetic moment of the dipole, \dot{P} the time derivative of the period in s s^{-1} , B_0 the surface B -field strength (polar B -field strength in Gaussian units), R the stellar radius, α the inclination angle between the magnetic and spin axes of the NS, and c the speed of light. The magnitude of B_0 can now be estimated by inserting typical values of $I = 10^{45} \text{ g cm}^2$, $R = 10^6 \text{ cm}$ and $\alpha \sim 90^\circ$, giving

$$B_0 \approx 6.4 \times 10^{19} \sqrt{P \dot{P}}. \quad (2.5)$$

Later calculations by, e.g., Spitkovsky (2006); Li et al. (2012) resulted in $L_{\text{pf}} \propto (1 + \sin^2 \alpha)$, the Poynting flux. By equating this \dot{E}_{rot} yields a similar value for B_0 .

We can estimate the pulsar rotational (characteristic) age as follows. Assume that the change in $\dot{\Omega} = -K\Omega^{(n-1)}$ is due to magnetic dipole radiation losses (Bowers & Deeming 1984), where K is a positive constant, and the parameter $n = \ddot{\Omega}/\dot{\Omega}^2$ is the braking index, which comes from differentiating the equation for $\dot{\Omega}$. This expression for $\dot{\Omega}$ is motivated by Eq. (2.4), assuming that $\mu_\perp \equiv \sin \alpha$ stays constant. Next, integrate this expression and substitute $\Omega^2 = -\dot{\Omega}/k_1$ where k_1 is a constant (see Eq. [2.4]). The characteristic age is then given by (Manchester & Taylor, 1977)

$$\tau = -\frac{\Omega}{(n-1)\dot{\Omega}} \left[1 - \left(\frac{\Omega}{\Omega_0} \right)^{n-1} \right] \approx -\frac{\Omega}{(n-1)\dot{\Omega}} \equiv \frac{P}{(n-1)\dot{P}}, \quad (2.6)$$

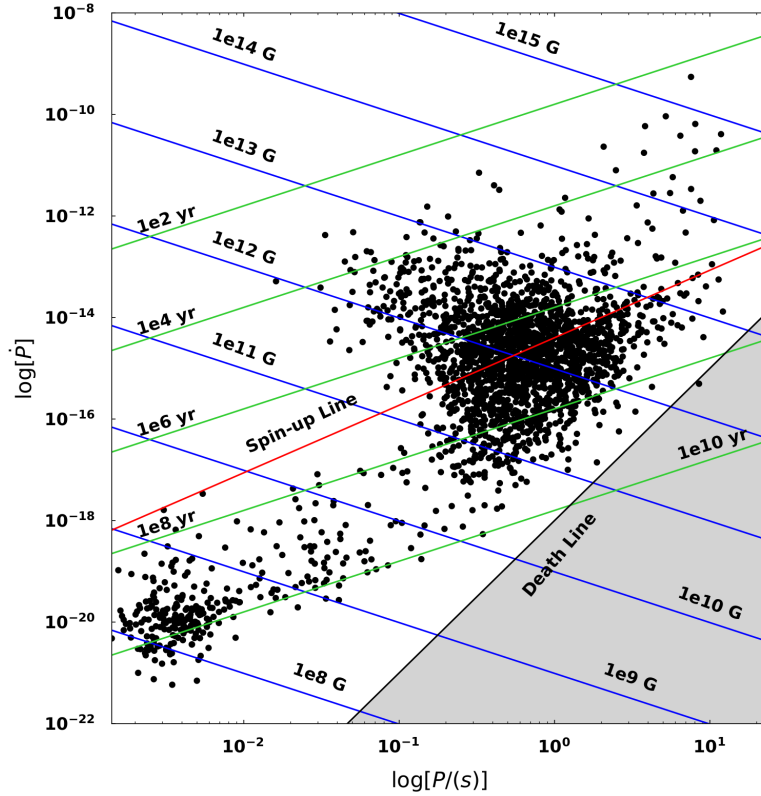


Figure 2.3: A $P\dot{P}$ -diagram indicating the two pulsar populations including the canonical pulsars (in the centre) and the MSPs (in the lower left corner). The black dots are radio pulsars from the Parkes Observatory *ATNF* Pulsar Catalogue for $\dot{P} > 0$ (Manchester et al., 2005). The blue solid lines represent constant surface magnetic field B_0 contours, while the green solid lines represent characteristic pulsar ages τ . The grey area is the “graveyard” where the canonical pulsars turn off and are spun up again so that they eventually enter the MSP region. The spin-up line (red line) is the equilibrium period of spin-up by accretion, which is the Keplerian orbital period at the Alfvén radius (Alpar et al., 1982).

with the assumptions $n \neq 1$ and $\Omega \ll \Omega_0$, with Ω_0 the angular velocity at time $t = 0$. This is approximately equal to

$$\tau \approx -\frac{\Omega}{2\dot{\Omega}} \equiv \frac{P}{2\dot{P}}, \quad (2.7)$$

when setting $n = 3$ for the case of magneto-dipole braking (Becker & Pavlov, 2002). This characteristic age serves as an upper limit for the true age of the pulsar, since the value for n is chosen to be a constant. However, when $\Omega \lesssim \Omega_0$, the true age of the pulsar will be smaller than τ .

The evolution and properties of different pulsar populations are best described by drawing a $P\dot{P}$ -diagram (Figure 2.3, the time derivative of the period \dot{P} versus P , using the pulsars from the Parkes Observatory *ATNF* Pulsar Catalogue for $\dot{P} > 0$; Manchester et al., 2005). Rotation-powered pulsars could also have $\dot{P} < 0$, e.g., when there is acceleration along the line of sight for such objects embedded in a globular cluster. As mentioned in Section 2.1.3, one can distinguish two pulsar populations: the canonical pulsars and MSPs. The canonical radio pulsar population is identified with the younger pulsars and is situated at the centre of the $P\dot{P}$ -diagram. The canonical pulsars typically have high surface magnetic fields of $B_0 \sim 10^{12} - 10^{13}$ G and rotational ages of $\tau \sim 10^3 - 10^6$ yr (as indicated by the contours of constant B_0 and τ). During the evolution of pulsars as they age, three things happen. First, the magnetic dipole field drops (although the timescale for this process is uncertain),

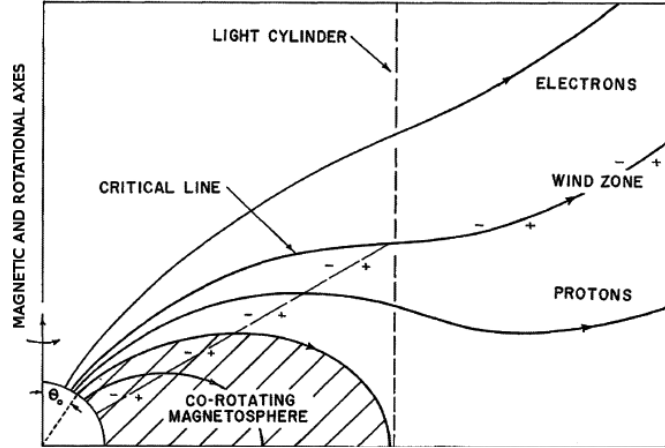


Figure 2.4: The pulsar magnetosphere as envisioned by Goldreich & Julian (1969). The corotating zone is represented by the shaded region within the light cylinder, where the particles corotate with the closed B -field lines. The B -field lines which go beyond the light cylinder are forced open and the particles escape along them. The electrons flow out near the PC along the higher-latitude lines, whereas the protons (or possibly iron nuclei) flow out near the PC angle (θ_{PC}) along the lower-latitude lines. These two magnetospheric regions are separated by the critical field line (which is at the same potential as the interstellar medium). The dashed line represents the condition where the charge density $\rho_{GJ} \propto -\mathbf{\Omega} \cdot \mathbf{B} = 0$. Above this dashed line $\mathbf{\Omega} \cdot \mathbf{B} > 0$ (negative ρ_{GJ}), and below it $\mathbf{\Omega} \cdot \mathbf{B} < 0$ (positive ρ_{GJ}).

second, the pulsar slows down due to energy losses (mostly by dipole radiation and particle loss), causing the pulse period to increase, and lastly the particles emitted by the pulsar form a pulsar wind. On the $P\dot{P}$ -diagram there is a “death valley” where the canonical pulsars turn off (Chen & Ruderman, 1993). This turn-off is due to the fact that the PC potential responsible for electron-positron (e^\pm) pair creation and subsequent radio emission becomes too low, inhibiting pair production (see Section 2.4.5), and leading to the “death” of canonical radio pulsars (i.e., they become invisible). Some pulsars inside the death valley are spun up again by the transfer of mass and angular momentum from a binary companion (Alpar et al., 1982), so that they enter the MSP region (lower left corner). These MSPs have relatively short periods ($P \lesssim 10$ ms) and lower surface B -fields ($B_0 \sim 10^8 - 10^9$ G) compared to the canonical pulsars. The spin-up line, representing the spin-up upper limit of MSPs (via accretion), is also indicated.

2.3 The Goldreich-Julian model

In 1969, Peter Goldreich and William Julian studied a simple model describing the properties of the magnetosphere around a highly magnetised, rotating pulsar. In this model, they considered an NS to be a uniformly magnetised, perfectly conducting sphere, with an internal magnetic field $\mathbf{B}_{in} = B_0 \hat{e}_z \parallel \boldsymbol{\mu}$, and with an external dipole B -field (e.g., Padmanabhan, 2001). They considered an aligned rotator, i.e., the rotation axis being aligned with a magnetic dipole vector ($\mathbf{\Omega} \parallel \boldsymbol{\mu}$; see Figure 2.4). Another assumption is that there are initially no charges filling the surrounding magnetosphere (Mészáros, 1992).

As the pulsar rotates with a velocity $\mathbf{v} = \mathbf{\Omega} \times \mathbf{r}$, the charged particles at the stellar surface will experience a Lorentz force $(q/c)(\mathbf{v} \times \mathbf{B}_{in})$, with q the particle charge. Since the NS is a perfect conductor ($\mathbf{E}_{in} \cdot \mathbf{B}_{in} = 0$, implying that the B -field lines are equipotentials) the charges will be redistributed in order for the electric force

to counter balance the magnetic force, leading to charge separation. This implies

$$\mathbf{E}_{\text{in}} = -\frac{(\boldsymbol{\Omega} \times \mathbf{r}) \times \mathbf{B}_{\text{in}}}{c} = -\frac{\Omega B_0 r \sin \theta}{c} (\sin \theta \vec{e}_r + \cos \theta \vec{e}_\theta). \quad (2.8)$$

Since $\nabla \times \mathbf{E}_{\text{in}} = 0$, we can write

$$\mathbf{E}_{\text{in}} = -\nabla \Phi_{\text{in}}(r, \theta), \quad (2.9)$$

with $\Phi_{\text{in}}(r, \theta)$ the electric potential. After integration, we find

$$\Phi_{\text{in}}(r, \theta) = \frac{\Omega B_0 r^2}{2c} \sin^2 \theta + \Phi_0, \quad (2.10)$$

with Φ_0 a constant. This implies a potential difference between the magnetic axis and PC angle (colatitude of the PC rim, $\theta_{\text{PC}} \sim \sqrt{\Omega R/c}$) of

$$\Delta \Phi_{\text{in}} = \frac{1}{2} \left(\frac{\Omega R}{c} \right)^2 B_0 R. \quad (2.11)$$

The external E -field now follows by solving the Laplace equation and requiring a continuous electric potential at the stellar surface:

$$E_{r,\text{out}} = -\frac{9Q}{r^4} \left(\cos^2 \theta - \frac{1}{3} \right), \quad (2.12)$$

$$E_{\theta,\text{out}} = -\frac{6Q}{r^4} \cos \theta \sin \theta, \quad (2.13)$$

with $Q = B_0 \Omega R^5 / 6c$. Using these expressions for E_{out} it follows that the electric force on surface charges vastly exceeds the gravitational force (by a factor of $\sim 5 \times 10^8 B_{12} P$ for a proton and $\sim 8 \times 10^{11} B_{12} P$ for an electron with $B_{12} = B_0 / 10^{12}$ G; Goldreich & Julian, 1969). This constitutes an existence proof for a plasma-filled pulsar magnetosphere, since the accelerating E -field parallel to the local B -field (E_{\parallel}) will extract particles from the stellar surface to fill the magnetosphere.

An expression for the charge density in the corotating magnetosphere follows from Eq. (2.8)

$$\rho_{\text{GJ}} = \frac{\nabla \cdot \mathbf{E}}{4\pi} \approx -\frac{\boldsymbol{\Omega} \cdot \mathbf{B}}{2\pi c}. \quad (2.14)$$

This implies a number density of

$$n_e = 7 \times 10^{-2} \frac{B_0}{P} \text{ cm}^{-3}, \quad (2.15)$$

at the stellar surface. Despite its success, the model has a few problems, most notably the question of the return current (charge neutrality) and its inherent instability, as well as the charge supply (which cannot be only from the NS surface).

2.4 High-energy radiation mechanisms and pair creation processes

2.4.1 Particle acceleration

Charged particles that are accelerated will emit electromagnetic radiation. If the speed v of the charged particle is much less than the speed of light in vacuum c , i.e., $v \ll c$, the particle is non-relativistic. The power radiated by such charged particles in the non-relativistic regime is calculated by using the Larmor formula (Jackson,

1999)

$$P_{\text{total}} = \frac{2q^2 a^2}{3c^3}, \quad (2.16)$$

with q the charge of the particle and a its acceleration.

However, when charged particles are accelerated to extremely high energies (GeV–TeV), they will emit HE γ -ray photons, e.g., those detected by *Fermi*. At these HEs the particle's speed becomes relativistic ($\beta \equiv v/c \approx 1$) with a Lorentz factor of $\gamma \equiv 1/\sqrt{1-\beta^2} \gg 1$. The relativistic Larmor formula (or Liénard formula, see Jackson, 1999) for these HE particles is as follows

$$P_{\text{total}} = \frac{2q^2}{3c^3} \gamma^4 (a_{\perp}^2 + \gamma^2 a_{\parallel}^2), \quad (2.17)$$

with a_{\perp} the perpendicular acceleration component and a_{\parallel} the parallel acceleration component (with respect to the particle's velocity direction). In the following subsections, radiation mechanisms including synchrotron radiation (SR), curvature radiation (CR), and inverse Compton scattering (ICS), which are relevant for HE pulsar emission models, are discussed. The first two are due to relativistic particles that are accelerated along curved paths inside the magnetosphere, whereas the latter occurs due to the interaction between photons and the relativistic particles. In the last subsection we discuss pair production, where an HE photon converts into an electron and positron pair.

2.4.2 Synchrotron radiation

SR (magneto-bremsstrahlung) occurs when relativistic charged particles gyrate about a B -field line. For non-relativistic particles, this is known as cyclotron radiation. When the particle's perpendicular momentum becomes relativistic, it is known as SR (Rybicki & Lightman, 1979). Neglecting radiation losses, the equation of motion for a relativistic particle reveals that the particle travels at a constant speed parallel to the B -field with an acceleration perpendicular to the B -field. This implies that the particle will follow a helical path as it gyrates along a B -field. The gyration angular frequency (rotation around a field line) is given by (Rybicki & Lightman, 1979)

$$\omega_B = \frac{qB}{\gamma mc}, \quad (2.18)$$

with m the particle's mass, and B the magnitude of the B -field. If $\mathbf{v} \cdot \mathbf{B} = 0$ the gyroradius is

$$r_B = \frac{v}{\omega_B}. \quad (2.19)$$

Since the particle is accelerated it will emit radiation and the assumption of no radiation losses will no longer be valid. The total SR energy loss rate is given by

$$\dot{E}_{\text{SR}} = \frac{2}{3c} (r_0 \gamma B v_{\perp})^2, \quad (2.20)$$

with v_{\perp} the charged particle's speed perpendicular to the B -field (Blumenthal & Gould, 1970) and $r_0 \equiv e^2/m_e c^2$ the classical electron radius (with m_e the electron mass and $m_e c^2$ its rest-mass energy). For the gyrating component we assume $a_{\perp} = \omega_B v_{\perp}$ and $a_{\parallel} = 0$, then Eq. (2.17) is the total emitted radiation

$$P_{\text{total}} = \frac{2q^2}{3c^3} \gamma^4 \left(\frac{qB}{\gamma mc} \right)^2 v_{\perp}^2. \quad (2.21)$$

When Eq. (2.21) is averaged over all angles, for an isotropic distribution of velocities, the SR power emitted is (Padmanabhan, 2000)

$$P_{\text{SR,total}} = \frac{4}{3} \sigma_{\text{T}} (c\beta^2 \gamma^2) U_{\text{B}} \propto E_{\text{e}}^2 B^2, \quad (2.22)$$

with $\sigma_{\text{T}} \equiv 8\pi r_0^2/3$ the Thomson cross section, E_{e} the particle energy, and $U_{\text{B}} = B^2/8\pi$ the magnetic energy density.

The radiation emitted by these relativistic particles will be beamed into a cone with an angular width $\sim 1/\gamma$ around the velocity direction. Since the particle's acceleration and velocity are perpendicular for SR, the observed pulses are a factor of γ^3 shorter in time than the gyration period, leading to a broader spectrum with a maximum characterised by a critical frequency

$$\omega_{\text{c}} = \frac{3}{2} \gamma^3 \omega_{\text{B}} \sin \alpha^{\text{P}}, \quad (2.23)$$

with $\alpha^{\text{P}} = \arctan(v_{\perp}/v_{\parallel})$ the pitch angle (Rybicki & Lightman, 1979). The total SR power per unit frequency emitted by a single electron is

$$P_{\text{SR}}(\omega) = \frac{\sqrt{3}}{2\pi} \frac{q^3 B}{m c^2} \sin \alpha^{\text{P}} F\left(\frac{\omega}{\omega_{\text{c}}}\right), \quad (2.24)$$

with

$$F(x) \equiv x \int_x^{\infty} K_{5/3}(\xi) d\xi, \quad (2.25)$$

where $K_{5/3}$ is the modified Bessel function of order 5/3, and

$$F(x) \sim \begin{cases} \frac{4\pi}{\sqrt{3}\Gamma(\frac{5}{3})} \left(\frac{x}{2}\right)^{1/3} & x \ll 1 \\ (\frac{\pi}{2})^{1/2} e^{-x} x^{1/2} & x \gg 1, \end{cases} \quad (2.26)$$

with $x = \omega/\omega_{\text{c}}$. For $\omega \ll \omega_{\text{c}}$, $F \propto \omega^{1/3}$, while for $\omega \gg \omega_{\text{c}}$, $F \propto e^{-(\omega/\omega_{\text{c}})} \omega^{1/2}$.

In many astrophysical sources, the photon spectra reveal a power law distribution of energies. Assume that the number density $N(E_{\gamma})$ of particles over some energy range $(E_{\text{e}}, E_{\text{e}} + dE_{\text{e}})$ can be described by a power law $N(E_{\text{e}})dE_{\text{e}} = C E_{\text{e}}^{-p} dE_{\text{e}}$, with C a constant and p the power-law index of the emitting particles. Following Rybicki & Lightman (1979), the total SR power radiated per unit volume per unit frequency can be shown to be a power-law spectrum

$$P_{\text{SR}}(\omega) \propto \omega^{-s}, \quad (2.27)$$

and is only valid between the minimum and the maximum cutoff frequencies depending on the minimum and maximum values for γ , and with $s = (p - 1)/2$ the index of the energy spectrum. The latter relation implies that the injection and radiation spectral indices are related in this case.

SR is an important process for pulsars. For example, in PC and SG models primary photons are emitted via CR and undergo magnetic photon absorption (see Section 2.4.5) to create e^{\pm} pairs. The perpendicular energy from these secondary pairs is converted to HE radiation via SR. It is possible that radio photons are absorbed by charged particles present in the B -field via the process of synchrotron self-absorption (Harding et al., 2008). The above discussion is only valid for B -field strengths $B < 4 \times 10^{12}$ G. For larger B -fields, a quantum SR approach is necessary (e.g., Sokolov & Ternov, 1968; Harding & Preece, 1987; Harding & Lai, 2006).

2.4.3 Curvature radiation

CR is the radiation process associated with relativistic particles that are constrained to move along a curved B -field line. This implies that its perpendicular velocity component $v_{\perp} = 0$, and $\alpha^P = 0$ (see above Sections for definitions). CR is therefore linked to a change in longitudinal kinetic energy with respect to the B -field, as opposed to SR, where there is change in transverse energy (see Figure 2.5). These two processes in fact represent two limits of the more general synchro-curvature (SC) process (Torres, 2018). In some pulsar models, primary particles are accelerated from the stellar surface along the open field lines. The kinetic energy longitudinal to the B -field will exceed the transverse energy (which will be radiated away very rapidly via SR), and therefore CR will be more important than SR regarding energy loss of primary particles (Sturrock, 1971). The curvature radius is the instantaneous radius of curvature of the particle trajectory, i.e., $\rho = \rho_c$. The critical frequency is then defined as (Daugherty & Harding, 1982; Story et al., 2007; Venter et al., 2009)

$$\omega_{\text{CR}} = \frac{3c}{2\rho_c} \gamma^3, \quad (2.28)$$

and the critical energy

$$E_{\text{CR}} = \hbar\omega_{\text{CR}} = \frac{3\hbar c \gamma^3}{2\rho_c} = \frac{3\lambda_c \gamma^3}{2\rho_c} m_e c^2, \quad (2.29)$$

where $h = 6.626 \times 10^{-27}$ erg s⁻¹ is Planck's constant, $\lambda_c \equiv \hbar/m_e c$ (with $\hbar = h/2\pi$ and $\lambda_c = \lambda_c/2\pi$), and λ_c the Compton wavelength. The instantaneous power spectrum (in units of erg s⁻¹ erg⁻¹) is given by (e.g., Venter & De Jager, 2010)

$$\left(\frac{dP}{dE}\right)_{\text{CR}} = \frac{\sqrt{3}\alpha_f \gamma c}{2\pi\rho_c} F\left(\frac{E_{\gamma}}{E_{\text{CR}}}\right), \quad (2.30)$$

with α_f the fine structure constant, $K_{5/3}$ the modified Bessel function of order 5/3, $x = E_{\gamma}/E_{\text{CR}}$, with E_{γ} the photon energy and F given by Eq. (2.25). Similar to SR, for $E_{\gamma} \ll E_{\text{CR}}$, $F \propto E_{\gamma}^{1/3}$, while for $E_{\gamma} \gg E_{\text{CR}}$, $F \propto e^{-(E_{\gamma}/E_{\text{CR}})} E_{\gamma}^{1/2}$ (see Eq. [2.26], Erber, 1966). The total power radiated by the electron primary can be determined by integrating Eq. (2.30) over energy. The latter is equal to the total CR loss rate of electrons,

$$\dot{E}_{\text{CR}} = \frac{2e^2 c \gamma^4}{3\rho_c^2}, \quad (2.31)$$

with e the electron charge.

Traditionally, HE emission in standard pulsar models is believed to be from CR of primary electrons accelerated tangentially to the B -field in the radiation-reaction regime. The curvature radiation reaction (CRR) limit is reached when the energy gained via acceleration of relativistic electrons (by an E -field parallel to the B -field) is equal to the energy loss via radiation, and can be expressed as follows (e.g., Harding et al., 2005)

$$c|E_{\parallel}| \sim \frac{2ce\gamma^4}{3\rho_c^2}, \quad (2.32)$$

yielding $\gamma = (1.5E_{\parallel}/e)^{1/4} \rho_c^{1/2}$, the Lorentz factor corresponding to radiation reaction. For pulsars with surface magnetic field strengths $B_0 \sim 10^{12}$ G and electric potentials $\Phi \sim 10^{13}$ V, the E -field strength is $E_{\parallel} \sim 10^4$ statvolts/cm (for young pulsars $E_{\parallel} > 10^4$ statvolts/cm) and depends on B and P . In these strong fields, the CR spectral cutoffs are therefore around a few GeV for emitting particles with Lorentz factors of $\gamma \sim 10^7$ (Yadigaroglu, 1997). These high Lorentz factors are connected to beamed radiation in the form of a cone with an opening angle $\sim 1/\gamma \ll 1$, implying emission tangentially to the B -field lines. We used this approximation to simplify the geometric models described in Section 2.5 and Chapter 3. Given the fact that we expect spectral

cutoffs in the GeV range for typical pulsar parameters, as well as rather hard power-law low-energy tails, this process has become the standard explanation for HE pulsar spectra such as those observed by the *Fermi* LAT satellite (e.g., Abdo et al., 2013).

2.4.4 Inverse Compton scattering and synchrotron self-Compton scattering

Compton scattering involves the collision between HE photons and low-energy electrons, where the photons transfer some of their momentum $p = hf/c = h/\lambda$ (with h Planck's constant, f the frequency and λ the wavelength) and energy to the electrons. This transfer leads to an increase in photon wavelength, implying a lower photon energy. The inverse case of Compton scattering is ICS, where the HE electrons scatter the low-energy photons, resulting in photons with very high energies (i.e., “boosting” of photon energies).

When a relativistic electron with Lorentz factor γ upscatters a photon from a low energy to a high energy, the energy E_γ of the Compton-boosted photon, with an initial energy ϵ , may be approximated as (Ramana Murthy & Wolfendale, 1986)

$$E_\gamma \sim \epsilon\gamma^2, \quad \gamma\epsilon \ll m_e c^2 \quad - \text{Thomson limit} \quad (2.33)$$

$$E_\gamma \sim \gamma m_e c^2, \quad \gamma\epsilon \gg m_e c^2 \quad - \text{Extreme Klein-Nishina limit.} \quad (2.34)$$

The total power lost due to ICS by an electron in an isotropic radiation field of low-energy photons, in the Thomson limit, is given by

$$P_{\text{ICS,total}} = \frac{4}{3} \sigma_T (c\beta^2 \gamma^2) U_{\text{rad}}, \quad (2.35)$$

which has the same form as Eq. (2.22), but with U_{rad} the soft-photon energy density, and σ_T the classical Thomson scattering cross section (see Section 2.4.2). In order to obtain the total radiated Compton spectrum, we need to integrate the production rate $dN'(\epsilon, \gamma)/dE_\gamma$, valid for a single electron, over the soft-photon energy ϵ and the electron energy γ (Blumenthal & Gould, 1970):

$$\left(\frac{dN}{dE_\gamma} \right)_{\text{total}} = \iint N_e(\gamma) \left(\frac{dN'(\epsilon, \gamma)}{dE_\gamma} \right) d\gamma d\epsilon, \quad (2.36)$$

with $dN_e = N_e(\gamma)d\gamma$ the differential number of electrons in the interval $(\gamma, \gamma+d\gamma)$. Similar to SR (see Eq. [2.27]), if we assume that the electron spectral energy distribution is a power law, $N_e \sim \gamma^{-p}$ with index p , and a blackbody soft-photon distribution, then it follows from Eq. (2.36) that the ICS spectrum is also power law:

$$\left(\frac{dN}{dE_\gamma} \right)_{\text{total}} \propto \begin{cases} E_\gamma^{-(p+1)/2} & - \text{Thomson limit} \\ E_\gamma^{-(p+1)} & - \text{Extreme Klein-Nishina limit,} \end{cases} \quad (2.37)$$

and is valid only in a specified energy range between the minimum and maximum cutoff energy similar to SR. In the Thomson limit, we follow a classical approach for photon energies $\gamma\epsilon \lesssim 100$ keV for which σ_T is valid. However, when we consider target soft photons of higher energies, quantum effects become important and σ_T should be replaced by the Klein-Nishina cross section σ_{KN} (Rybicki & Lightman, 1979). As the photon energy increases, the cross section reduces, leading to a steeper photon spectrum (reduced loss rate) in the extreme Klein-Nishina limit (with $\sigma_T > \sigma_{\text{KN}}$) and eventually a rapid spectral cutoff.

The ICS process is important for pulsars. One example is MSPs such as PSR J0437–4715 from which thermal and non-thermal (possibly SR) X-ray emission have been observed (see e.g., Zavlin et al., 2002). These energetic photons provide a background field that may be upscattered to TeV energies by relativistic particles in the magnetosphere. Another example is afforded by the pulsed very-high-energy (VHE) emission recently observed from the Crab pulsar. This has been explained using a revised OG model (Hirotani, 2008a,b) that produces IC radiation of up to ~ 400 GeV when secondary and tertiary pairs upscatter infrared to ultraviolet

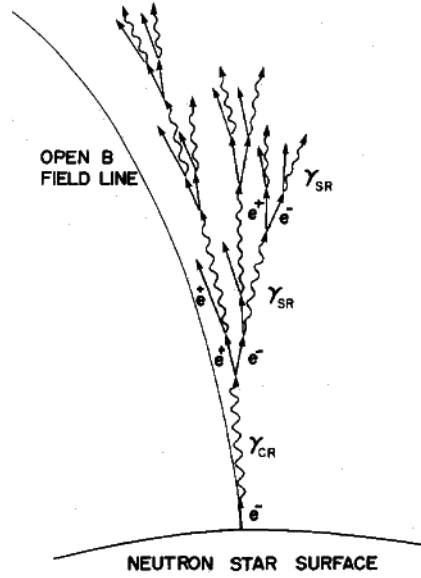


Figure 2.5: Schematic illustration by Daugherty & Harding (1982) of a photon pair cascade emerging from the acceleration of a primary electron above the PC along the curved B -field of an NS. Four generations of photons, including both CR photons γ_{CR} and SR photons γ_{SR} , are shown.

photons (Aleksić et al., 2012).

Other astrophysical examples include pulsar wind nebulae (PWNe, see e.g., De Jager et al., 1996) and many other VHE sources which display typical spectral components corresponding to SR and IC radiation as part of their broadband emission spectrum.

Another suggestion to explain the Crab pulsar’s VHE emission is proposed by Lyutikov et al. (2012), invoking the SSC radiation process where relativistic pairs upscatter the SR photons emitted previously by the same particle population. In the SSC process, one needs to calculate the SR from primaries and pairs at each step along all particle trajectories in the open field volume, since the SR photon density is needed to compute the SSC radiation. The SR emission is recorded at each location and photon emission direction in the inertial observers frame. Second, once the SR photon density in all directions at a certain position is determined, the SSC flux at a certain position and velocity can be calculated (see Harding & Kalapotharakos 2015 and references therein). In essence, the soft-photon energy density is basically replaced by the SR photon energy density.

2.4.5 Pair production

Pulsar magnetospheres contain of strong B -fields and E -fields, especially near the NS surface, and the latter fields can accelerate particles to relativistic energies. Efficient radiation processes (see Sections 2.4.2 to 2.4.4) and a pair creation mechanism, necessary for particle-photon cascades to ensue, also operate in these extreme environments (Daugherty & Harding, 1982). There are two different pair creation processes that may occur, namely single photon (magnetic) and two-photon pair production.

Magnetic (one-photon) pair creation

Magnetic pair production can only occur in the presence of a strong B -field ($B_{\perp} > 10^9$ G, perpendicular to the photon’s direction of motion) with which the photons, if they have a high enough energy, can interact to produce e^{\pm} -pairs. The probability that e^{\pm} -pairs will be produced via this process is expressed by the photon

attenuation coefficient given by

$$\alpha'(\chi) = \frac{1}{2} \left(\frac{\alpha_f}{\lambda_c} \right) \left(\frac{B_\perp}{B_{\text{cr}}} \right) T(\chi), \quad (2.38)$$

which determines the number of pairs n_p created for each photon that travels a path length d through the B -field (Erber, 1966):

$$n_p = n_\gamma (1 - \exp[-\alpha'(\chi)d]) \simeq n_\gamma \alpha'(\chi)d, \quad (2.39)$$

with $\alpha_f = e^2/\hbar c \approx 1/137$ the fine structure constant, $\chi \equiv 0.5(h\nu/m_e c^2)(B_\perp/B_{\text{cr}})$ the Erber parameter, ν the photon frequency, $B_{\text{cr}} = m_e^2 c^3 / eh = 4.414 \times 10^{13}$ G the critical B -field value in which the electron's gyro-energy (cyclotron) equals its rest mass (Daugherty & Harding, 1983), $T(\chi)$ a dimensionless function, and n_γ is the photon number density. Sturrock (1971) approximated the threshold condition for magnetic pair production as

$$E_\gamma B \sin \theta_{\gamma B} = E_\gamma B_\perp \gtrsim 10^{11.9}, \quad (2.40)$$

with E_γ in units of $m_e c^2$, $\theta_{\gamma B}$ the photon propagation angle with respect to the B -field, and B_\perp measured in Gauss. In the PC model (see Section 2.5.1) primary particles are accelerated from the PC surface along the curved field lines and CR occurs. When the emitted CR photon energy and the local B -field are high enough or $\theta_{\gamma B} \gg 1$, magnetic pair production will occur, leading to a cascade of secondary e^\pm pairs that will screen the E_\parallel -field (E -field parallel to the local B -field). An E_\parallel -field develops because there is a deficit of negative charges and due to the backflow of the first generation of pair e^+ to the NS surface, a space charge accumulates that counteracts any charge imbalances and screens out the accelerated E_\parallel -field, significantly so above the so-called pair-formation front (PFF). ICS photons may also be converted into e^\pm pairs. The pair cascade is characterised by the so-called multiplicity, i.e., the number of pairs spawned by a single primary, as represented in Figure 2.5.

Two-Photon pair creation

Two-photon pair creation is due to a collision between two photons with high enough energies, where the minimum photon energy required is $E_\gamma = 2m_e c^2 \sim 1$ MeV (for a head-on collision), creating an e^\pm pair. The cross section for two-photon pair production (in a region devoid of a B -field) in terms of the photon energy in the centre-of-momentum frame, $\epsilon_{\text{cm}} = [\epsilon_1 \epsilon_2 (1 - \cos \theta_{12}) / 2]^{1/2}$, is (Svensson, 1982) (using dimensionless energies normalised to the electron rest-mass energy)

$$\sigma_{2\gamma} \simeq \frac{3}{8} \sigma_T \begin{cases} (\epsilon_{\text{cm}}^2 - 1)^{1/2} & (\epsilon_{\text{cm}} - 1) \ll 1 \\ [2 \ln(2\epsilon_{\text{cm}}) - 1] / \epsilon_{\text{cm}}^6 & \epsilon_{\text{cm}} \gg 1, \end{cases} \quad (2.41)$$

where ϵ_1 and ϵ_2 refer to the energies of the photons, and θ_{12} is the angle between the photon propagation directions. Two-photon pair production can also take place in the presence of a strong B -field. In this case, the resulting e^\pm pair will have non-zero velocity to ensure that the energy and parallel momentum are conserved. In a strong B -field, the requirement for producing a pair in the ground state, using the conservation equations, is given by (Harding & Lai, 2006):

$$(\epsilon_1 \sin \theta_1 + \epsilon_2 \sin \theta_2)^2 + 2\epsilon_1 \epsilon_2 [1 - \cos(\theta_{12})] > 4, \quad (2.42)$$

where θ_1 and θ_2 are the angles between the photon propagation directions and the B -field. The first term in the above equation is due to the non-conservation of perpendicular momentum, implying that pair production is possible when photons travel parallel to each other ($\theta_{12} = 0$, $\theta_1 = \theta_2 \neq 0$), an event not permitted in field-free space.

In the high-altitude SG model, electrons are accelerated away from the NS, such that the angle of each of the photons to the B -field is too small to tap the perpendicular momentum of the B -field and no pairs are

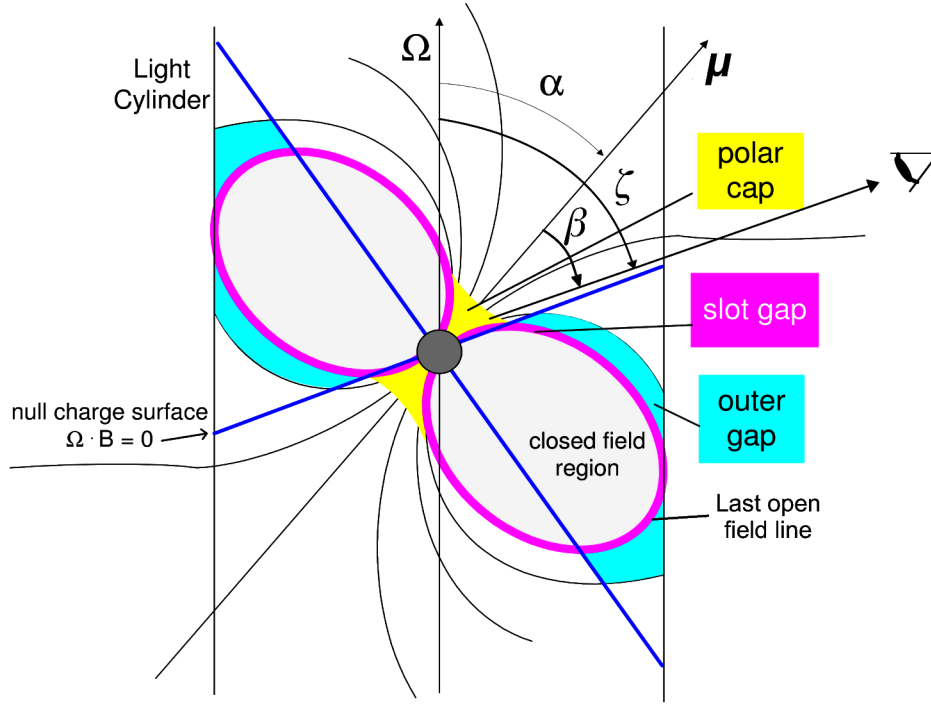


Figure 2.6: Schematic view of the different traditional pulsar emission models, with μ the magnetic axis inclined by an angle α with respect to the rotation axis Ω , and ζ the observer angle measured with respect to Ω . From Harding (2005).

produced. However, in high-altitude OG model, particles are also accelerated downward so that these particles (and therefore their emitted CR photons) have large angles with respect to soft photons originating at the hot stellar surface. The two-photon pair creation process is therefore expected to occur. The resulting pairs play an important role in gap closure (Hirotani, 2008a). Burns & Harding (1984) found that the one-photon pair creation process will generally dominate over the two-photon process in B -fields above $\approx 10^{12}$ G, since the first is a lower-order process than the second.

2.5 Traditional pulsar models

Several pulsar emission models have been developed over the last forty years, including the PC, SG, and OG models. These geometries are illustrated in Figure 2.6. Each model differs in its assumption of the geometry and location of the acceleration region where HE radiation takes place. To simulate the HE emission from these physical models, the assumed electrodynamics and B -field structures are important.

2.5.1 Polar cap model

In PC models (Ruderman & Sutherland, 1975; Daugherty & Harding, 1982) HE particles (e^\pm) are assumed to originate at the NS surface layer. These are then accelerated by large, rotation-induced E -fields at the magnetic poles (known as the magnetic PCs) up to heights just above the PC ($h \lesssim R$, see Figure 2.6). There exist two types of polar cap accelerators: the vacuum gaps with $\Omega \cdot \mathbf{B} < 0$ (Ruderman & Sutherland, 1975; Usov & Melrose, 1995) and space-charge-limited-flow (SCLF) gaps with $\Omega \cdot \mathbf{B} > 0$ (Arons & Scharlemann, 1979; Harding & Muslimov, 1998; see Figure 2.7). The formation of these gaps depends primarily on the surface temperature T_s of the NS, and the thermionic emission temperatures for the charges (electrons and ions) $T_{e,i}$.

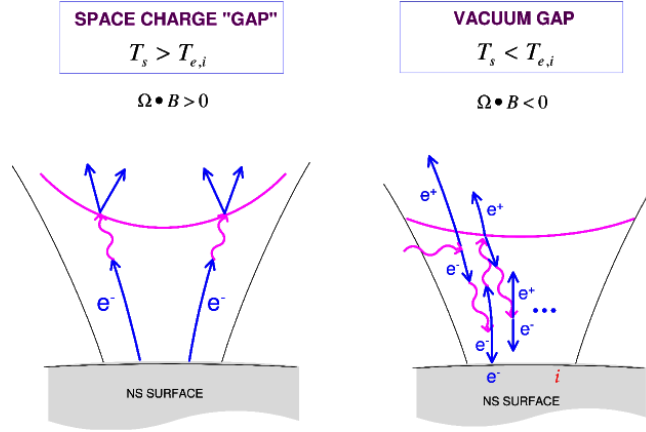


Figure 2.7: Illustration of the two types of PC accelerators, including the SCLF gap on the left (Daugherty & Harding, 1982), and the vacuum gap on the right (Ruderman & Sutherland, 1975). If the NS surface temperature T_s exceeds the ion or electron thermionic temperature $T_{i,e}$ then the SCLF gap will form, otherwise the vacuum gap will dominate. Figure from Harding (2007).

For the vacuum accelerator the surface temperature $T_s < T_{e,i}$, causing the charges to be trapped inside the NS surface and a full vacuum E -field (or potential drop) develops above the surface (Usov & Melrose, 1995). However, at high surface temperatures, $T_s > T_{e,i}$ the binding energy of the charges due to lattice structures in strong B -fields is exceeded (Medin & Lai, 2007) and the charges are “boiled off” the surface layers and flow freely along the open field lines in the SCLF regime. These two acceleration gaps differ primarily in their surface boundary conditions (at the stellar surface $r = R$) which state that for the vacuum gap the space charge $\rho(r) = 0$ and $E_{\parallel}(R) \neq 0$, whereas for the SCLF accelerator the full Goldreich-Julian charge can be provided, $\rho(r) = \rho_{GJ}$ (which may be modified by curvature of B -field lines as well as inertial frame dragging, Muslimov & Tsygan, 1992) and $E_{\parallel}(R) = 0$ (Harding, 2007). Both accelerators will be self-limited by the development of pair cascades (initiated by the conversion of radiated photons into e^{\pm} pairs; see Section 2.4.5), with the particles being accelerated to altitudes where they will reach high enough Lorentz factors to radiate γ -ray photons.

The pair production in the vacuum gap differs from that in the SCLF model. In the vacuum gap the potential breaks down when a random photon crosses the B -field and creates a pair. The resulting electron and positron are accelerated in opposite directions. This electron and positron can then initiate more pairs since they will radiate photons that may again be converted into pairs, causing a pair cascade and discharge of the vacuum gap. In contrast, in the SCLF model electrons and positrons are accelerated from the NS surface upwards until the radiated photons reach the pair creation threshold. A pair cascade ensues at the PFF. The E_{\parallel} is screened due to the polarisation of pairs above this front, halting any further acceleration (with the relativistic charges “coasting” outward, potentially emitting SR). Since these accelerators can maintain a steady current, there will be an upward current of electrons ($j_{\parallel}^{-} \approx c\rho_{GJ}$) and also a downward current of positrons ($j_{\parallel}^{+} \ll c\rho_{GJ}$), which will heat the PC. The height of the PFF determines the eventual potential of these accelerators. Simulations of time-dependent vacuum (Timokhin, 2010) and SCLF (Timokhin & Arons, 2013) gaps show that the pair cascades are non-steady.

2.5.2 Slot gap model

In SG models (Arons, 1983; see Figure 2.6) it is assumed that HE particles originate from the NS surface layer and are accelerated from the PCs along the last open field lines and up to high altitudes, comparable to the light cylinder radius $R_{LC} = c/\Omega$ (Harding & Grenier, 2011). This SG model is very similar to the SCLF accelerator of the PC model, except that the SG model extends up to high altitudes. The altitude of the PFF (Figure 2.8)

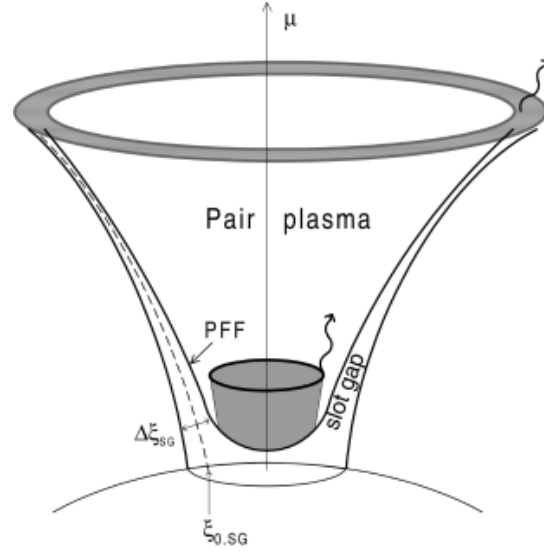


Figure 2.8: Schematic view of the SG, which is the region between the PFF and the outer boundary formed by the last open field lines (with μ the magnetic axis and $\Delta\xi_{\text{SG}}$ the gap width). The SG forms a hollow cone emitting HE radiation. From Muslimov & Harding (2003).

strongly varies with magnetic colatitude across the PC due to the B -field geometry and the boundary conditions ($E_{\parallel} = 0$ on the surface and last open B -field lines) assumed for the SG accelerator (Harding & Muslimov, 1998). The PFF will occur at higher and higher altitudes closer to the closed field line region boundary. This is because the mean free path for magnetic (one-photon) pair production increases as E_{\parallel} decreases toward this boundary. The radiating particle therefore needs to be accelerated over a longer distance before it can radiate photons of high enough energy so that pair formation can take place. The mean free path becomes infinite at and asymptotically tangent to the last open field line. The E_{\parallel} is screened above the PFF, and a narrow gap surrounded by two conducting walls will form, as represented in Figure 2.8 (Harding & Muslimov, 2003). The electrons accelerated in the SG will radiate CR, ICR and SR, although their Lorentz factors are constrained by the CR. We note that new solutions for the E_{\parallel} were determined by Muslimov & Harding (2003, 2004a), including the general relativistic effect of inertial frame-dragging near the NS surface, enhancing this field significantly.

2.5.3 Outer gap model

The OG model (Figure 2.6) was introduced by Cheng et al. (1986), initially assuming an inclined rotator with a charge density of ρ_{GJ} . They proposed that when the primary current passes through the neutral sheet (where $\mathbf{\Omega} \cdot \mathbf{B} = 0$ and thus $\rho_{GJ} = 0$) the negative charges above this sheet will escape beyond the light cylinder. A vacuum gap region is then formed (in which $E_{\parallel} \neq 0$). Charges will be accelerated in this gap region and will emit CR photons, the energy of which depends on the E -field strength. Therefore, as the vacuum region grows, E_{\parallel} will increase, and hence the energy of the CR photons will increase until the photons have enough energy to produce electron and positron pairs when they collide with the background soft photons via photon-photon (or two-photon) pair production (see Section 2.4.5, Cheng, 2011).

The outer magnetosphere is conceptually divided into three regions (see Figure 2.9). In region I the primary electrons and positrons are accelerated in opposite directions due to the E_{\parallel} present in the gap, with the acceleration limited by CR losses or ICS on infrared photons. Although some γ -rays undergo pair creation, most of them move over into region II, where the E_{\parallel} is small and secondary e^{\pm} pairs are produced, radiating secondary γ -rays and X-rays via SR. In region III, tertiary e^{\pm} pairs are created and are responsible for the emission of

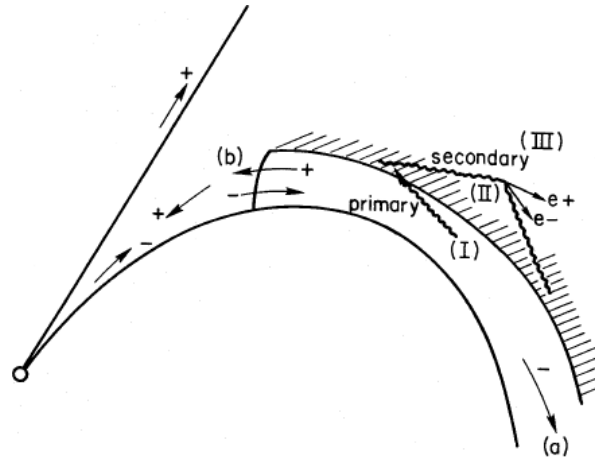


Figure 2.9: Schematic representation of the location of the three regions in an OG model, including the primary (I) (where primary particle acceleration and pair production occur), secondary (II) (where a small E_{\parallel} is present and secondary pair production as well as SR occur) and tertiary (III) regions (where tertiary pair production occurs, producing soft γ -rays). From Cheng et al. (1986).

softer radiation (Cheng et al., 1986). This is also the region where γ -rays are produced by ICS involving the primary pairs. The radiation in this region may furthermore interact with primary CR γ -rays to create pairs in region II. Romani (1996) investigated an OG model based on CRR-limited charges (see Section 2.4.3) in the outer magnetosphere, showing that photon-photon pair production may limit the gap width. He also demonstrated that radiation efficiency should increase with pulsar age, and discussed spectral variations in the optical and X-ray SR spectra. More modern approaches have solved the electrodynamic equations of the OG in a 2D and 3D geometry (e.g., Takata et al., 2004; Hirotani, 2006, 2008a).

2.5.4 Pair-starved polar cap model

The PSPC model for MSPs was first introduced by Harding et al. (2005). They studied X-ray and γ -ray emission emitted by rotation-powered MSPs (see Section 2.1.3). These MSPs have very low surface B -field strengths and short periods (compared to younger pulsars). The electrodynamics is based on a (young-pulsar) model that considers the acceleration of particles and pair production (see Section 2.4) on the open field lines above the PCs (Muslimov & Harding, 2004b). Harding et al. (2005) assumed a PC geometry (see Section 2.5.1) and a dipole field (see Section 2.6.1). They found that most MSPs are below the CR pair death line (i.e., the PP death line for creating pairs via CR, see Section 2.2), due to the low surface B -fields (see Eq. [2.40]), implying that pairs are rather produced by ICS radiation. Since the pair cascade multiplicity is very low in PSPC pulsars, the accelerating E -field is inefficiently screened by these pairs and no PFF is formed as in the case of young pulsars. This leads to a pair-starved PC. Therefore, the primary particles and possibly a few pairs continue to accelerate to high altitudes, up to the light cylinder, over the full open volume (in contrast to the traditional PC model where particles are only accelerated up to the PFF, and then coast along the field lines after which they escape from the magnetosphere). There exists a progression between models, depending on the pair multiplicity: the SG model has very narrow gaps for pulsars with high multiplicity, but these gaps increase in thickness and the model eventually tends toward a PSPC geometry as pair creation is more and more inhibited (Harding, 2007).

2.6 Developments in the magnetic field structure calculations

The B -field is one of the basic assumptions of the geometric models (others include the gap region's location, and the emissivity ϵ_ν profile in the gap). Several B -field structures have been studied, including the static dipole (Griffiths, 1995), the RVD (a rotating vacuum magnetosphere that can in principle accelerate particles but do not contain any charges or currents; Deutsch, 1955), the force-free field (FF; filled with charges and currents, but unable to accelerate particles, since the accelerating E -field is screened everywhere; Contopoulos et al., 1999), and the offset dipole (to mimic deviations from the static dipole near the stellar surface analytically; Harding & Muslimov, 2011a,b). A more realistic pulsar magnetosphere, i.e., a dissipative solution (Kalapotharakos et al., 2012c; Li et al., 2012; Tchekhovskoy et al., 2013; Li, 2014), would be one that is intermediate between the RVD and the FF fields. The dissipative B -field is characterised by the plasma conductivity σ_c (e.g., Lichnerowicz, 1967) which can be set in order to alternate between the limiting cases of vacuum ($\sigma_c \rightarrow 0$) and FF ($\sigma_c \rightarrow \infty$) magnetospheres (see Li et al., 2012).

2.6.1 Static dipole magnetic field

The static dipole field has been studied since the calculations are simpler for this B -field. We derive its form below. In order to obtain an approximate formula for a vector potential associated with a localised current distribution, valid at distant points, a multipole expansion can be used and the potential is written in the form of a power series in $1/r$, with r the radial distance to the point in question. If r is very large the power series is dominated by the lowest non-vanishing contribution and the higher-order terms can be ignored. The first term (which goes like $1/r$) in the multipole expansion is called a monopole term, the second term (which goes like $1/r^2$) the dipole term, and the third term (which goes like $1/r^3$) the quadrupole, etc. (Griffiths, 1995). The magnetic monopole term is zero (i.e., $\nabla \cdot \mathbf{B} = 0$). The next term is the magnetic dipole. The vector potential can be written as a function of position vector \mathbf{r} :

$$\mathbf{A}_{\text{dip}}(\mathbf{r}) = \frac{I}{r^2} \oint r' \cos \theta' d\mathbf{l}' = \frac{I}{r^2} \oint (\hat{\mathbf{r}} \cdot \mathbf{r}') d\mathbf{l}', \quad (2.43)$$

with $\hat{\mathbf{r}}$ the unit radial vector and I the current. By rewriting this integral, the vector potential becomes

$$\mathbf{A}_{\text{dip}}(\mathbf{r}) = \frac{\boldsymbol{\mu} \times \hat{\mathbf{r}}}{r^2}, \quad (2.44)$$

where $\boldsymbol{\mu}$ is the magnetic dipole moment (aligned with the magnetic axis, therefore sometimes defined by the same symbol) defined as

$$\boldsymbol{\mu} \equiv \frac{I}{c} \int d\mathbf{a} = \frac{Ia}{c}, \quad (2.45)$$

with a the enclosed area of the current loop, and c the speed of light. To calculate the B -field of a dipole, $\boldsymbol{\mu}$ may be set at the origin, pointing in the z -direction. The vector potential, Eq. (2.44) can then be written in spherical co-ordinates,

$$\mathbf{A}_{\text{dip}}(\mathbf{r}) = \frac{\mu \sin \theta}{r^2} \hat{\boldsymbol{\phi}}, \quad (2.46)$$

hence the dipole B -field is given by (Griffiths, 1995):

$$\mathbf{B}_{\text{static}}(\mathbf{r}) = \nabla \times \mathbf{A}_{\text{dip}}(\mathbf{r}) = \frac{\mu}{r^3} (2 \cos \theta \hat{\mathbf{r}} + \sin \theta \hat{\boldsymbol{\theta}}), \quad (2.47)$$

in the magnetic ($\boldsymbol{\mu}$) frame or where the inclination angle $\alpha = 0$ (the angle between the rotation $\boldsymbol{\Omega}$ and the $\boldsymbol{\mu}$ axes).

When the light curve shapes and features for the static dipole are compared to those for the other B -fields (see Chapter 3), the importance of the near- R_{LC} distortions in the B -fields for predicted radiation characteristics can be gauged (Dyks et al., 2004a). The static (non-rotating) dipole is a special case of the retarded (rotating) dipole which we consider next.

2.6.2 Retarded vacuum dipole magnetic field

The solution for a B -field surrounding a star rotating in vacuum was first derived by Deutsch (1955). Previous investigators (Yadigaroglu, 1997, Arendt & Eilek, 1998, Jackson, 1999, Cheng et al., 2000, Dyks et al., 2004a) implemented methods that considered distortions in the B -field structure due to sweepback of the field lines as the NS rotates with an angular frequency Ω about the $\hat{\mathbf{z}}$ -axis. The general expression for this RVD field is given by

$$\mathbf{B}_{\text{ret}} = -\left[\frac{\mu(t)}{r^3} + \frac{\dot{\mu}(t)}{cr^2} + \frac{\ddot{\mu}(t)}{c^2r}\right] + \hat{\mathbf{r}} \cdot \left[3\frac{\mu(t)}{r^3} + 3\frac{\dot{\mu}(t)}{cr^2} + \frac{\ddot{\mu}(t)}{c^2r}\right], \quad (2.48)$$

with

$$\mu(t) = \mu(\sin \alpha \cos \Omega t \hat{\mathbf{x}} + \sin \alpha \sin \Omega t \hat{\mathbf{y}} + \cos \alpha \hat{\mathbf{z}}), \quad (2.49)$$

the magnetic moment, with $\dot{\mu}(t)$ and $\ddot{\mu}(t)$ its first and second time-derivatives, and $\hat{\mathbf{r}} = \mathbf{r}/r$ the unit radial vector. The RVD solution can be described by the following B -field equations in spherical co-ordinates in the laboratory frame (where $\hat{\mathbf{z}} \parallel \boldsymbol{\Omega}$; Dyks & Harding, 2004):

$$B_{\text{ret},r} = \frac{2\mu}{r^3} [\cos \alpha \cos \theta + \sin \alpha \sin \theta (r_n \sin \lambda + \cos \lambda)], \quad (2.50)$$

$$B_{\text{ret},\theta} = \frac{\mu}{r^3} (\cos \alpha \sin \theta + \sin \alpha \cos \theta [-r_n \sin \lambda + (r_n^2 - 1) \cos \lambda]), \quad (2.51)$$

$$B_{\text{ret},\phi} = -\frac{\mu}{r^3} \sin \alpha [(r_n^2 - 1) \sin \lambda + r_n \cos \lambda], \quad (2.52)$$

with $\lambda = r_n + \phi_L - \Omega t$, $r_n = r/R_{\text{LC}}$, Ω the angular velocity, and ϕ_L the phase. These equations can be rewritten to give the B -field components in Cartesian co-ordinates (where $\hat{\mathbf{z}} \parallel \boldsymbol{\Omega}$; Dyks & Harding, 2004)

$$B_{\text{ret},x} = \frac{\mu}{r^5} (3xz \cos \alpha + \sin \alpha \{[(3x^2 - r^2) + 3xyr_n + (r^2 - x^2)r_n^2] \cos(\Omega t - r_n) + [3xy - (3x^2 - r^2)r_n - xyr_n^2] \sin(\Omega t - r_n)\}), \quad (2.53)$$

$$B_{\text{ret},y} = \frac{\mu}{r^5} (3yz \cos \alpha + \sin \alpha \{[3xy + (3y^2 - r^2)r_n - xyr_n^2] \cos(\Omega t - r_n) + [(3y^2 - r^2)r_n - 3xyr_n + (r^2 - y^2)r_n^2] \sin(\Omega t - r_n)\}), \quad (2.54)$$

$$B_{\text{ret},z} = \frac{\mu}{r^5} \{ (3z^2 - r^2) \cos \alpha + \sin \alpha [(3xz + 3yzr_n - xzr_n^2) \cos(\Omega t - r_n) + (3yz - 3xzr_n - yzr_n^2) \sin(\Omega t - r_n)] \}. \quad (2.55)$$

The above expressions are obtained when assuming the limit of the Deutsch solution where $R/R_{\text{LC}} \ll 1$, with R the stellar radius. By setting $r_n = 0$, the retarded field simplifies to the non-aligned static dipole ($\alpha \neq 0$).

The difference between the static dipole and RVD is illustrated in Figure 2.10 for $\alpha = 90^\circ$, i.e., field lines in the equatorial plane. For the static dipole (left) the field lines are symmetric, whereas in the RVD case (right) the field lines are distorted due to sweepback of the field lines as the NS rotates. This has implications for the definition of the PC. These distortions in the RVD B -field are illustrated in Figure 2.11 for an $\alpha = 65^\circ$ as seen

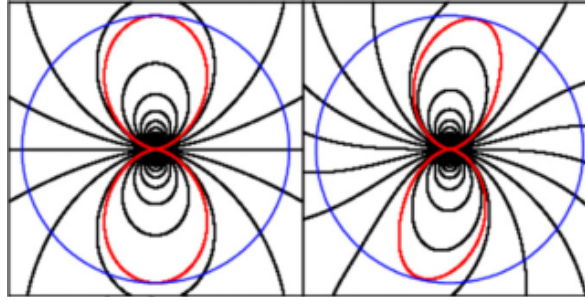


Figure 2.10: Illustration of the static dipole (left) and RVD (right) B -field structures in the equatorial plane, where $\alpha = 90^\circ$. The red curve indicates the last closed field line which closes at the light cylinder, where the corotation speed is equal to c . The sweepback of field lines is evident for the RVD case. The blue circle indicates a slice through the light cylinder. From Romani & Watters (2010).

from different points of view.

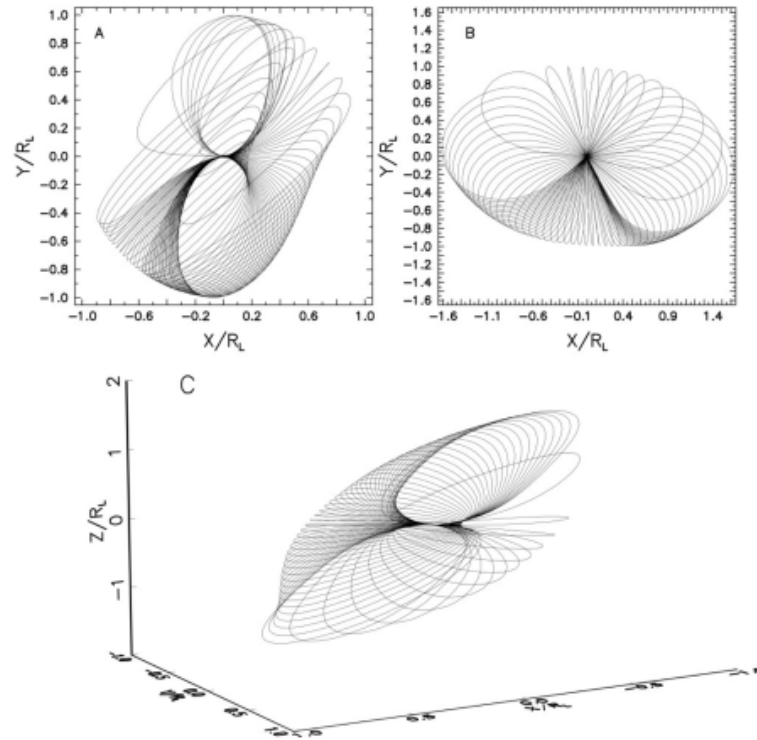


Figure 2.11: Illustration of an RVD B -field for the last closed field lines, inclined with respect to Ω by an angle $\alpha = 65^\circ$. Three projections are presented: (a) looking down Ω , (b) looking down μ , and (c) a 3D view. Strong distortions are visible as the inclination becomes larger (see Arendt & Eilek, 1998). From Cheng et al. (2000).

2.6.3 Offset-dipole magnetic field

The offset dipole is a heuristic model of a dipolar magnetic structure that is offset from the stellar centre, leading to PCs offset from the central μ -axis. The B -field lines of an offset dipole field are azimuthally asymmetric compared to those of a pure dipole field. This leads to field lines having a smaller curvature radius ρ_c over half of the PC compared to those of the other half. Such small distortions in the B -field structure are due

to retardation and asymmetric currents, thereby shifting the PCs by small amounts in different directions. A detailed study of the effects of this B -field structure on the predicted HE light curves of the Vela pulsar will be presented in Chapter 3.

2.6.4 A force-free field

The FF B -field structure assumes that the entire pulsar's magnetosphere is filled with highly conductive and dense plasma so that the E_{\parallel} is fully screened (i.e., $E_{\parallel} = 0$; Spitkovsky 2006). This implies that the ideal magnetohydrodynamic (MHD) condition $\mathbf{E} \cdot \mathbf{B} = 0$ is valid everywhere in the magnetosphere (Spitkovsky, 2011).

There are different analytic solutions that have been studied regarding the ideal MHD equation. Michel (1973b) obtained a split-monopole solution (representing the magnetospheric structure farther from the NS; see Petrova 2016), whereas Michel (1973a) (see also Michel 1982) found a solution for a corotating relativistic dipole magnetosphere with zero poloidal current, valid inside the light cylinder. Other solutions include a slightly perturbed monopole (Beskin et al., 1998), as well as an exact axisymmetric dipole with a differential rotational magnetospheric velocity distribution and general toroidal structure (Petrova, 2016, 2017).

However, the first numerical solution of the pulsar equation (valid for FF magnetospheres, relating current and magnetic flux) for a dipole B -field near the NS was found by Contopoulos et al. (1999), and permits a smooth transition of the field lines at and beyond the light cylinder as well as current closure (see Figure 2.12a). This solution is characterised by two zones where field lines are closed or open, respectively. Also, as the poloidal field lines move out to greater distances away from the NS these lines become monopolar at regions where torodial B -field components exist. There exist time-dependent numerical solutions as well, such as the oblique rotator (e.g., Spitkovsky 2006; Kalapotharakos & Contopoulos 2009; Contopoulos & Kalapotharakos 2010; Kalapotharakos et al. 2012a; see Figure 2.12b) with B -field lines similar to those of the solution by Contopoulos et al. (1999), but the current sheet thereof has the shape of a “ballerina skirt” about the rotational equator.

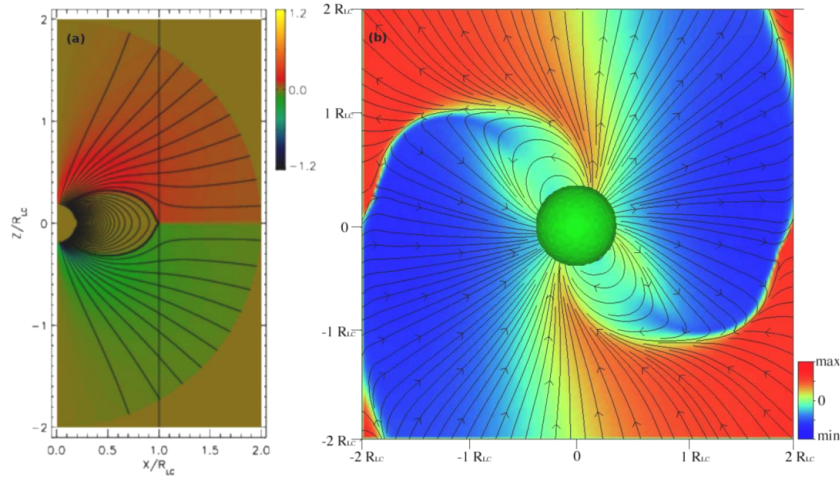


Figure 2.12: Snapshots of time-dependent FF simulations of the (a) aligned and (b) oblique rotators. In the first instance, poloidal field lines of the steady-state solution are shown. The thick black line indicates the boundary of the light cylinder, and the colour the normalised toroidal B -field component. In the second panel, for an $\alpha = 60^\circ$, the B -field lines are shown in the corotating frame where the colour indicates the field strength perpendicular to the plane (the toroidal field in the aligned rotator case). From Spitkovsky (2006).

2.7 Recent theoretical developments

2.7.1 A dissipative field

The dissipative B -field solution represents a transition from the vacuum to the FF case, and allows energy dissipation and therefore particle acceleration, which is not the case for the FF solution. Thus, the dissipative B -fields is characterised by a zero (in vacuum case) to infinite (FF case) macroscopic conductivity, σ (Kalapotharakos et al., 2012c; Li et al., 2012; Kalapotharakos et al., 2014). The dissipative FF was developed in order to probe the locations where particle acceleration may take place, as well as the effect of the deviations from ideal MHD conditions on the magnetosphere structure (Li et al., 2012; Kalapotharakos et al., 2012c). In these approaches, different methods led to a non-accelerating E -field, e.g., a finite σ alter the current density (Kalapotharakos et al., 2012c). For increasing σ , the regions containing large charge and current densities also increased in size and the current sheet became more pronounced, and B -field lines became more straight over farther distances.

Some studies modelled energy light curves as a function of σ . Kalapotharakos et al. (2012b) modelled light curves assuming a geometric approach and found that peak widths broadened accompanied by a phase lag to the right with increasing σ . This is ascribed to the effect of the magnetospheric structure on the light curves. Kalapotharakos et al. (2014) constructed a model assuming dissipative magnetospheres, and incorporating CR and a slightly new prescription for the current density, as well as different values for the σ based on the region in the magnetosphere. They studied the particle trajectories together with a self-consistent accelerated E -field, including CR energy losses. For lower σ values emission was noticed at lower altitudes inside the light cylinder, and as σ was increased the radiation occurred at higher altitudes near the current sheet where E_{\parallel} is higher. The latter implies that for a decrease in E_{\parallel} longer acceleration distances need to be followed for particles to acquire enough energy to emit CR. However, emission from the current sheet was enhanced. Also, small values of σ were associated with broad light curves, while those corresponding to large σ 's were narrower in some instances.

Another implementation of the dissipative models is the FIDO models and are defined as FF conditions existing inside the light cylinder and dissipative conditions outside (FIDO) beyond the light cylinder (into the current sheet). Thus, a large but finite σ is chosen for the dissipative regions. Brambilla et al. (2015) calculated phase-averaged and phase-resolved spectra, using a FIDO model, for a few very luminous pulsars (including Vela; see Figure 2.13) and assuming CR. They found that for a fixed α the spectral cutoff energy $E_{\gamma, \text{CR}}$ increased for larger ζ , but decreased for larger σ 's. The FIDO model also predicted that $E_{\gamma, \text{CR}}$ may increase near the second light curve peak's phase. However, this is not always the case. We also demonstrate that the P1/P2 effect can be explained within an CR emission model framework using a FF B -field and SG current sheet model (see Chapter 5).

The FIDO model still fails to replicate some trends of the light curve phenomenology as well as the phase-resolved spectral details. However, the FIDO model does provide good results regarding basic trends. Moreover, a model such as the FIDO is able to replicate the GeV light curve phenomenology relatively well and impacts future microphysical simulations.

2.7.2 Kinetic models

The kinetic particle-in-cell (PIC) codes model the pulsar magnetosphere from first principles and resolve both the temporal and spatial scales of the problem (plasma frequency and skin depth) to avoid numerical instabilities and numerical plasma heating (Brambilla et al., 2018). However, the assumed field values of the latter codes are unrealistically low. These codes follow a two-step process: first to calculate charge and current densities, and then the fields based on these; Lastly, the process is iterative, so the influence on of the B -fields and E -fields on the charges are taken into account, and updated currents and charge densities are calculated. Recent studies (e.g., Philippov & Spitkovsky 2014; Belyaev 2015; Cerutti & Philippov 2017; Kalapotharakos et al. 2018) concentrated on handling the pulsar electrodynamics self-consistently, including global current closure,

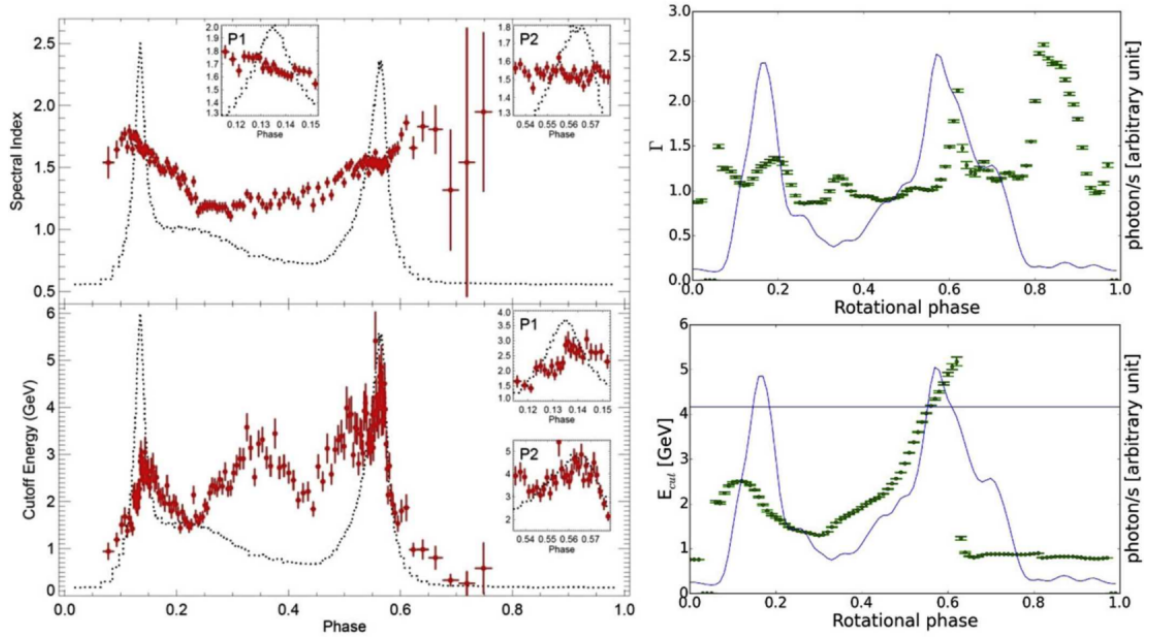


Figure 2.13: The observed (left) and predicted (right) light curves, and phase-resolved spectral index (top) and the cutoff energy (bottom) for the Vela pulsar using the FIDO model. From Brambilla et al. (2015).

the contribution of charges of different sign to the current, dissipative processes, electromagnetic emission, and the effects of pair production and general relativity (for a detailed review see Venter 2016; Cerutti et al. 2020).

Recent reviews, see Brambilla et al. (2018) investigated current composition and flow using a new PIC code (Kalapotharakos et al., 2018), and focused on the dependence of magnetospheric properties on particle injection rate. Larger injection rates are achieved by Brambilla et al. (2018) than in previous studies. They obtained a transition of the magnetospheric solutions from a vacuum to FF solution, invoking two scenarios of particle injection, e.g., from the NS surface and everywhere in the pulsar magnetosphere. They obtained the highest dissipation for intermediate injection rates. As they increased injection rate (i.e., equivalent to a macroscopic σ being increased), E_{\parallel} was gradually (but not fully) screened and the FF current structure was attained. The dissipation regions also mostly moved to the current sheet. However, these two particle injection scenarios differ in particle density distribution in the sense that higher multiplicities were reached at the NS surface in the surface-injection scenario. They also studied the particle trajectories, and could probe some details of the current composition, e.g., they found that electrons and positrons both flowed out in the PC regions (which may inhibit two-photon pair production; see Figure 2.14), and lower-energy electrons returned to the NS surface by crossing the B -field lines close to the return current sheet inside the light cylinder, thus making them good candidates for emitting SR in the MeV range.

The energetic particles flowing out along the current sheet correspond well to the FIDO model assumption (Kalapotharakos et al., 2017) that invokes dissipation regions beyond the light cylinder into the current sheet. This model generally provides a good description of the *Fermi* pulsar phenomenology. Thus, the latest PIC simulations are now elucidating and justifying the FIDO macroscopic assumptions and electrodynamic (or spatial accelerator) constraints derived from the GeV data when assuming CR from positrons in the current sheet (Kalapotharakos et al., 2018).

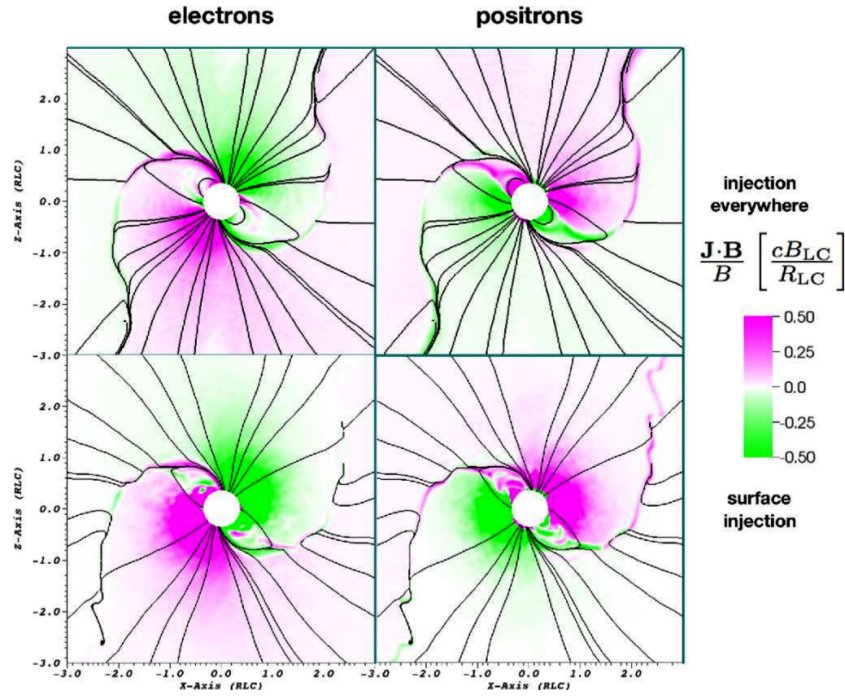


Figure 2.14: The electron and positron components of the current density for magnetospheres close to being FF, as predicted by the PIC model of Brambilla et al. (2018). One can see that the electrons and positrons both flowed out in the PC regions. The labels distinguish the cases where pair injection took place only at the surface vs. everywhere in the magnetosphere. From Brambilla et al. (2018).

2.7.3 Striped-wind models

In these models, the current sheet (equatorial region between B -field lines of different polarities) is considered to be the main region for the generation of HE pulsed emission (Beskin et al., 1983; Montgomery, 1999). There are still many open questions regarding the basic understanding of general concepts within the framework of the current sheet models, e.g., location of the magnetic reconnection, the formation plasmoids via the tearing instability, the nature of the dissipation, and the effect of internal thermal pressure on the current sheet thickness. Several studies attempted to answer these questions (e.g., Lyubarskii 1996; Pétri & Dubus 2011; Pétri 2012) in the context of the “striped-wind” models (Coroniti, 1990; Michel, 1994) (see Pétri 2016 for a more detailed review).

Some studies have contrasting ideas about the current sheet. Kalapotharakos et al. (2014) notice that the physical conditions present in the current sheet greatly modifies the global magnetosphere structure. Others, such as Uzdensky & Spitkovsky (2014), argue that the current sheet is part of a rotating pulsar magnetosphere, and that the magnetic reconnection dissipates a large fraction of the pulsar spin-down power there. The numerical FF codes cannot treat the current sheet properly, therefore they developed a near- R_{LC} reconnection model to constrain the local plasma conditions. They stated that reconnection takes place via the formation of plasmoids (growing “magnetic islands”; Figure 2.15b) of different sizes. These plasmoids are continuously formed and merging with each other, and are ejected quasi-periodically. The relativistically hot reconnection layers present in pulsars undergo strong SR cooling, which leads to plasma compression. The particles can indeed radiate pulsed GeV emission by SR as well as pulsed emission in the TeV-band via ICS of ultraviolet or X-ray emission from the pulsar (see Chapter 6).

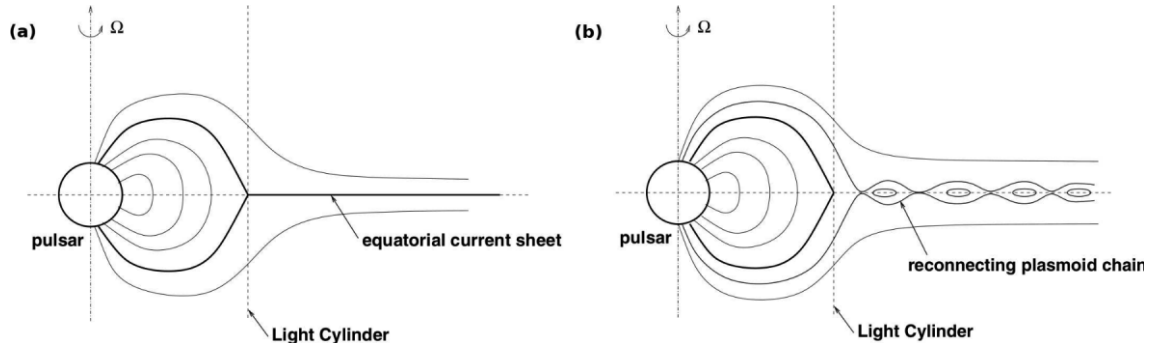


Figure 2.15: The (a) basic axisymmetric magnetosphere, and the (b) tearing of the equatorial current sheet (formation of plasmoids). From Uzdensky & Spitkovsky (2014).

2.8 Summary

This Chapter gave a broad overview of pulsar astrophysics such as the pulsar history, formation of pulsars, different pulsar classes, traditional models, etc. Harding & Kalapotharakos (2015) assumed a FF B -field structure (Section 2.6.4), in an SG and current sheet scenario, in their SSC emission model (Section 2.4) used in this study (see Chapters 4, 5, and 6). The trends observed using the FIDO model are also seen in the GeV to TeV light curves (see Chapters 5 and 6).

In Chapter 5 I investigate the P1/P2 effect seen in the light curves and also explain this by investigating the phase-resolved spectra. This effect is also noted in studies regarding the dissipative models (Section 2.7.1). Lastly the values chosen for the two-step E_{\parallel} used by Harding et al. (2018) are motivated by values obtained for the accelerating E -field in the PIC simulations, after suitable scaling of the particle energies to realistic values.

In the next Chapter I will discuss our study concerning the investigation of different B -field structures on the GeV light curves of Vela. This study deals with the offset-PC dipole field described in Section 2.6.3.

Chapter 3

The effect of an offset-PC B -field geometry on the predicted γ -ray light curves of the Vela pulsar

Recent studies using *NICER* (see Section 1.1.4) data point to pulsars having offset-PC B -field structures (Bilous et al. 2019; Lockhart et al. 2019; Kalapotharakos et al. 2020). These non-dipolar B -field geometries are also motivated by earlier observations of thermal X-ray emission, e.g., pulse profiles from MSPs such as PSR J0437–4715 (Bogdanov et al., 2007) and PSR J0030+0451 (Bogdanov & Grindlay, 2009), with the B -fields of NSs in low mass X-ray binaries even more distorted (Lamb et al., 2009).

Within the global modelling landscape, numerical magnetic fields such as the FF solution (characterised by different PC currents than those assumed in space-charge limited flow models; Contopoulos et al., 1999; Timokhin, 2006) will undergo larger sweepback of field lines near the light cylinder, and consequently display a larger offset of the PC toward the trailing side (opposite to the rotation direction) than in the RVD field (which has offset PCs due to rotation alone; see Section 2.6.2).

We investigated the impact of different magnetospheric structures on the predicted γ -ray pulsar light curves. Using a particular implementation of an offset-PC B -field (see Section 2.6.3 and Section 3.2), we wanted to constrain the amount of offset using GeV data of the Vela pulsar. We also considered a SG (see Section 2.5.2) E -field associated with this particular B -field and constrain the E -field magnitudes when multiplying it with a factor 100. We performed geometric pulsar light curve modelling using different B -field structures in conjunction with geometric models. Additionally, we incorporated an SG E -field into our geometric modelling code. The fact that we have an E -field solution enables us to solve the particle transport equation on each B -field line for the offset-PC dipole and SG model combination for both the relatively low SG E -field and the increased case.

This Chapter is a summary¹ of work presented in Barnard et al. (2016) and will focus on the implementation of an offset-PC B -field and the results obtained. In this chapter we will briefly describe the offset-PC dipole B -field structure we considered (Section 3.2) as well as the implementation thereof in our geometric modelling code, assuming certain geometric models (Section 3.3). This implementation involved a transformation of the B -field between the magnetic and rotational frames (Section 3.4), as well as finding the PC rim (Section 3.5). We also describe the calculation of the associated SG E -field and the matching of the low-altitude and high-altitude solutions using a matching parameter (scaled radius) η_c in Section 3.6. We briefly discuss the χ^2 method we applied in order to find best-fit (α, ζ) for the different model combinations (see Section 3.7). In Section 3.8,

¹This Chapter is based on research that was initiated during my MSc (Breed, 2015), as well as research done during the first year of my PhD.

we present our solution of the transport equation for the offset-PC dipole B -field for the usual and increased E -field solutions. This also includes our light curve predictions for two distinct cases: 1) the effect of lowering the minimum photon energy as well as 2) multiplying the E -field by a factor 100. This is followed by our best-fit (α, ζ) contours for the Vela pulsar, for both cases where $E_\gamma > 100$ GeV, before we compare our results to previous multi-wavelength studies from other works in Section 3.9. Our conclusions follow in Section 3.10. For an alternative and independent implementation of an offset-dipole geometry, see Kundu & Pétri (2017).

3.1 Introduction

The *Fermi*'s Second Pulsar Catalogue (2PC; Abdo et al., 2013) describes the properties of more than 150 pulsars in the energy range 100 MeV to 100 GeV. This catalogue includes the Vela pulsar (Abdo et al., 2009), one of the brightest persistent sources in the GeV sky. A third catalogue is currently in preparation.

Despite the major advances made after nearly 50 years since the discovery of the first pulsar (Hewish et al., 1968), many questions still remain regarding the electrodynamical character of the pulsar magnetosphere, including details of the particle acceleration and pair production, current closure, and radiation of a complex multi-wavelength spectrum. Physical emission models such as the SG (Muslimov & Harding, 2003) and OG (Section 2.5.3; Romani & Yadigaroglu, 1995) fall short of explaining these global magnetospheric characteristics. More recent developments include the global magnetospheric properties. One example is the force-free (FF; see Section 2.6.4) inside and dissipative outside (FIDO; see Section 2.7.1) model (Kalapotharakos & Contopoulos, 2009; Kalapotharakos et al., 2014) that assumes FF electrodynamical conditions (infinite plasma conductivity $\sigma_c \rightarrow \infty$) inside the light cylinder and dissipative conditions (finite σ_c) outside. The wind models of, e.g., Pétri & Dubus (2011) provide an alternative picture where dissipation takes place outside the light cylinder. There is also kinetic / particle-in-cell simulations (PIC; Brambilla et al. 2018; Cerutti et al. 2016b,a, 2020; Kalapotharakos et al. 2018; Philippov & Spitkovsky 2018). See Chapter 2 for a more detailed discussion of these models.

Although much progress has been made using the physical models, geometric light curve modelling still presents a crucial avenue for probing the pulsar magnetosphere in the context of traditional pulsar models, as these emission geometries may be used to constrain the pulsar geometry (inclination angle α and the observer viewing angle ζ with respect to the spin axis $\mathbf{\Omega}$), as well as the γ -ray emission region's location and extent. This may provide vital insight into the boundary conditions and help constrain the accelerator geometry of next-generation full radiation models. Geometric light curve modelling has been performed by, e.g., Dyks et al. (2004a); Venter et al. (2009); Watters et al. (2009); Johnson et al. (2014); Pierbattista et al. (2015) using standard pulsar emission geometries, including a two-pole caustic (TPC, of which the SG is its physical representation; Dyks & Rudak, 2003), OG, and pair-starved polar cap (Harding et al., 2005) geometry.

A notable conclusion from the 2PC was that the spectra and light curves of both the millisecond pulsar (MSP) and young pulsar populations show remarkable similarities, pointing to a common radiation mechanism and emission geometry (tied to the B -field structure). The assumed B -field structure is essential for predicting the light curves seen by the observer using geometric models, since photons are expected to be emitted tangentially to the local B -field lines in the corotating pulsar frame (Daugherty & Harding, 1982). Even a small difference in the magnetospheric structure will therefore have an impact on the light curve predictions. For all of the above geometric models, the most commonly employed B -field has been the retarded vacuum dipole (RVD) solution first obtained by Deutsch (1955). However, other solutions also exist. One example is the static dipole (non-rotating) field (see Section 2.6.3), a special case of the RVD (rotating) field (Dyks & Harding, 2004). Bai & Spitkovsky (2010a) furthermore modelled high-energy (HE) light curves in the context of OG and TPC models using an FF B -field geometry (assuming a plasma-filled magnetosphere), proposing a separatrix layer model close to the last open field line (tangent to the light cylinder at radius $R_{LC} = c/\Omega$ where the corotation speed equals the speed of light c , with Ω the angular speed), which extends from the stellar surface up to and beyond the light cylinder. In addition, the annular gap model of Du et al. (2010), which assumes a static dipole

field, has been successful in reproducing the main characteristics of the γ -ray light curves of three MSPs. This model does, however, not attempt to replicate the nonzero phase offsets between the γ -ray and radio profiles.

The B -field is one of the basic assumptions of the geometric models (others include the gap region's location, and the ϵ_v profile in the gap). Several B -field structures have been studied in this context, including the static dipole (Griffiths, 1995), the RVD (a rotating vacuum magnetosphere which can in principle accelerate particles but do not contain any charges or currents; Deutsch, 1955), the FF (filled with charges and currents, but unable to accelerate particles, since the accelerating E -field is screened everywhere; Contopoulos et al., 1999), and the offset-PC dipole (that analytically mimics deviations from the static dipole near the stellar surface; Harding & Muslimov, 2011a,b). A more realistic pulsar magnetosphere, i.e., a dissipative solution (Kalapotharakos et al., 2012c; Li et al., 2012; Tchekhovskoy et al., 2013; Li, 2014), would be one that is intermediate between the RVD and the FF fields. The dissipative B -field is characterised by the plasma conductivity σ_c (e.g., Lichnerowicz, 1967) which can be chosen in order to alternate between the vacuum ($\sigma_c \rightarrow 0$) and FF ($\sigma_c \rightarrow \infty$) cases (see Li et al., 2012).

We studied the effect of different magnetospheric structures (static dipole, RVD, and offset-PC dipole, further discussed below) and emission geometries (TPC and OG) on pulsar visibility and γ -ray pulse shape, particularly for the case of the Vela pulsar. For the static dipole the field lines are symmetric about the μ -axis, whereas the RVD is distorted due to sweepback of the field lines as the NS rotates. This has implications for the definition of the PC (see Section 3.5).

3.2 Offset-dipole B -field structure

Harding & Muslimov (2011a,b) considered two cases, i.e., symmetric and asymmetric PC offsets. The symmetric case involves an offset of both PCs in the same direction so that the PCs are not antipodal, and applies to NSs with some interior current distortions that produce multipolar components near the stellar surface (see Figure 3.1; Harding & Muslimov, 2011b). The asymmetric case is associated with asymmetric PC offsets in opposite directions and applies to PC offsets due to retardation and/or currents of the global magnetosphere (see Figure 3.2; Harding & Muslimov, 2011b). Both these cases were modelled by introducing an offset parameter ϵ . Thus, as seen in Figure 3.1a the global open field lines of a centred dipole are bent toward the dipole axis on one side and bent away from the dipole axis on the other side of the PC. Therefore, one side of the PC is larger and the PC is effectively shifted from the centre of symmetry (see Figure 3.1b).

The general expression for a symmetric offset-PC dipole B -field in terms of spherical co-ordinates (r', θ', ϕ') in the magnetic frame (indicated by the primed co-ordinates, where $\hat{\mathbf{z}}' \parallel \mu$) is as follows (Harding & Muslimov, 2011b)

$$\mathbf{B}'_{\text{OPCs}}(r', \theta', \phi') \approx \frac{\mu'}{r'^3} \left[\cos \theta' \hat{\mathbf{r}}' + \frac{1}{2}(1+a) \sin \theta' \hat{\boldsymbol{\theta}}' - \epsilon \sin \theta' \cos \theta' \sin(\phi' - \phi'_0) \hat{\boldsymbol{\phi}}' \right], \quad (3.1)$$

where $\mu' = B_0 R^3$ is the magnetic moment, R the stellar radius, B_0 the surface B -field strength at the magnetic pole, ϕ'_0 the magnetic azimuthal angle defining the plane in which the offset occurs, and $a = \epsilon \cos(\phi' - \phi'_0)$ characterises the offset direction in the $x' - z'$ plane. This distortion depends on parameters ϵ (related to the magnitude of the shift of the PC from the magnetic axis) and ϕ'_0 (we choose $\phi'_0 = 0$ in what follows). If $\phi'_0 = 0$ or $\phi'_0 = \pi$ the offset is in the x' direction (i.e., along the x' -axis). If $\phi'_0 = \pi/2$ or $\phi'_0 = 3\pi/2$ the offset is in the y' direction.

The general expression for an asymmetric B -field is as follows (Harding & Muslimov, 2011b)

$$\mathbf{B}'_{\text{OPCa}}(r', \theta', \phi') \approx \frac{\mu'}{r'^3} \left[\cos[\theta'(1+a)] \hat{\mathbf{r}}' + \frac{1}{2} \sin[\theta'(1+a)] \hat{\boldsymbol{\theta}}' - \frac{1}{2} \epsilon (\theta' + \sin \theta' \cos \theta') \sin(\phi' - \phi'_0) \hat{\boldsymbol{\phi}}' \right], \quad (3.2)$$

with the distortion of the field lines also occurring in the $x' - z'$ plane. If we set $\epsilon = 0$ both the symmetric and asymmetric cases reduce to a symmetric static dipole as given in Eq. [(2.47)] with the B -field lines being

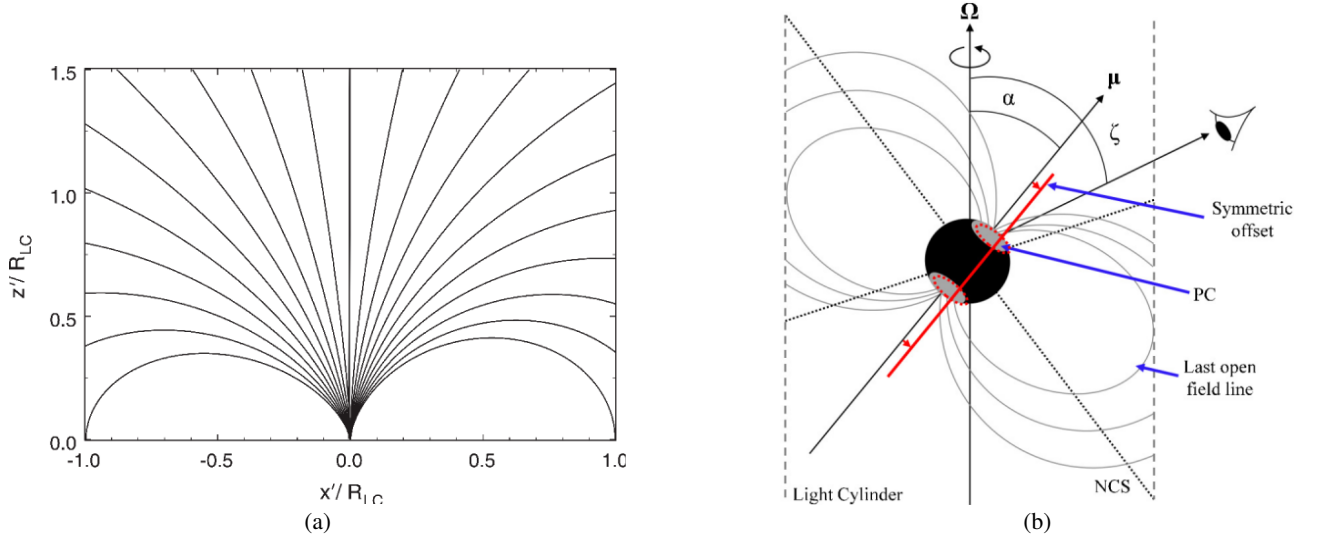


Figure 3.1: In (a) we illustrate the distorted field lines of the offset dipole B -field having symmetrically offset PCs in the $x' - z'$ plane, for an offset $\epsilon = 0.2$ (adapted from Harding & Muslimov 2011b). In (b) we represent the symmetric offset geometrically, where the PCs (grey ovals) are shifted from the magnetic axis in the same direction, resulting in symmetric PC offsets (red dashed circles). The curved arrow around Ω indicates the direction of rotation.

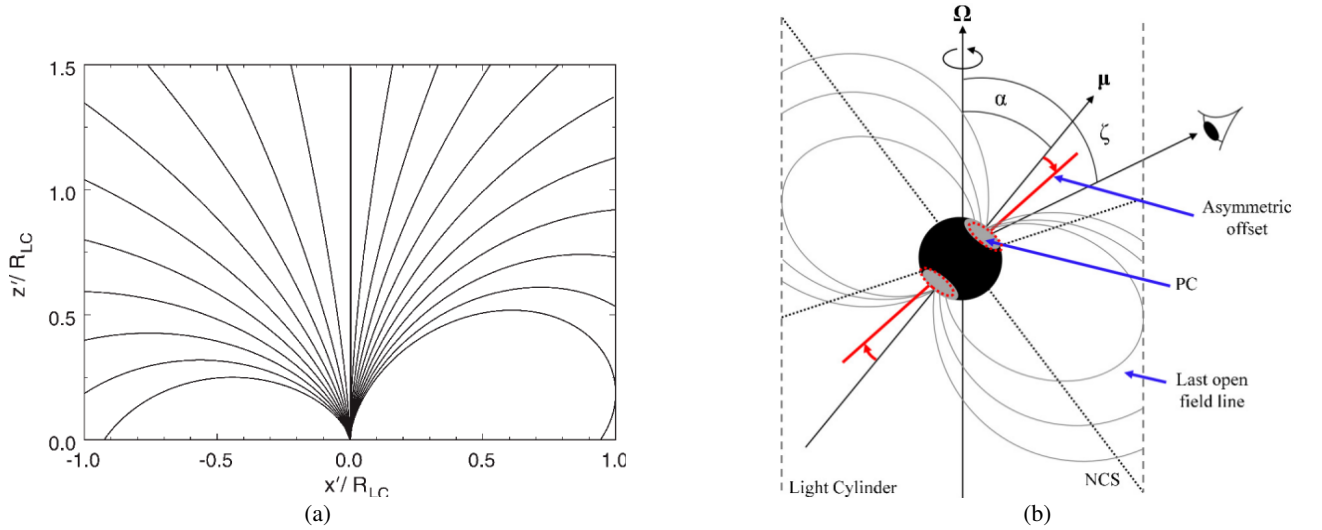


Figure 3.2: In (a) we illustrate the distorted field lines of the offset dipole B -field having asymmetric offset PCs in the $x' - z'$ plane, for an offset $\epsilon = 0.2$ (adapted from Harding & Muslimov 2011b). In (b) we represent the offset geometrically, with the PCs (grey ovals) shifted from the magnetic axis in opposite directions, resulting in asymmetric PC offsets (red dashed circles). The curved arrow around Ω indicates the direction of rotation.

distorted in all directions.

The distance by which the PCs are shifted on the NS surface is given by

$$\Delta r_{\text{PC}} \simeq R \theta_{\text{PC}} \left[1 - \theta_{\text{PC}}^\epsilon \right], \quad (3.3)$$

where $\theta_{\text{PC}} = (\Omega R/c)^{1/2}$ is the standard half-angle of the PC, and Ω the angular speed. This effective shift of the PCs is a fraction of θ_{PC} , therefore it is a larger fraction of R for pulsars with shorter periods (Harding & Muslimov, 2011a). Harding & Muslimov (2011b) found that for the RVD solution, $\epsilon = 0.03 - 0.1$, where offsets as large as 0.1 are associated with MSPs with large θ_{PC} . However, $\epsilon = 0.09 - 0.2$ is expected for FF fields, with the larger offset values related to MSPs (Bai & Spitkovsky, 2010a). One of the main focus points of our study was the implementation of an offset dipole B -field, for the symmetric case only.

The difference between our offset-PC field and a dipole field which is offset with respect to the stellar centre can be most clearly seen by performing a multipolar expansion of these respective fields. Lowrie (2011) gives the scalar potential W for an equatorially offset dipole (EOD) field

$$W'(r', \theta') = \left[\frac{\mu'}{r'^2} \cos \theta' + \frac{\mu' d}{r'^3} \sin \theta' \cos \theta' + \frac{\mu' d}{2r'^3} \sin^2 \theta' \right],$$

with d being the offset parameter, and with the first few leading terms in d/r' listed above. From this potential, we may construct the magnetic field using $B = -\nabla W$:

$$\begin{aligned} \mathbf{B}'_{\text{EOD}}(r', \theta') &= \mathbf{B}'_{\text{dip}}(r', \theta') + \left[\frac{3\mu' d}{r'^4} \sin \theta' \cos \theta' + \frac{3\mu' d}{2r'^4} \sin^2 \theta' \right] \hat{\mathbf{r}} \\ &\quad - \left[\frac{\mu' d}{r'^4} \cos^2 \theta' + \frac{\mu' d}{r'^4} \sin^2 \theta' - \frac{\mu' d}{r'^4} \sin \theta' \cos \theta' \right] \hat{\boldsymbol{\theta}}, \\ &= \mathbf{B}'_{\text{dip}}(r', \theta') + O\left(\frac{1}{r'^4}\right). \end{aligned} \quad (3.4)$$

This means that an offset dipolar field may be expressed (to lowest order) as the sum of a centred dipole and two quadrupolar components. Conversely, our offset-PC field may be written as

$$\mathbf{B}'_{\text{OPCs}}(r', \theta', \phi') \approx \mathbf{B}'_{\text{dip}}(r', \theta') + O\left(\frac{\epsilon}{r'^3}\right). \quad (3.5)$$

Therefore, we can see that the EOD consists of a centred dipole plus quadrupolar and other higher-order components (Eq. [3.4]), while our offset-PC model (Eq. [3.5]) consists of a centred dipole plus terms of order a/r'^3 or ϵ/r'^3 . Since $a \sim 0.2$ and $\epsilon \sim 0.2$, the latter terms present perturbations (e.g., poloidal and toroidal effects) to the centred dipole. Harding & Muslimov (2011a,b) derived these perturbed components of the distorted magnetic field while satisfying the solenoidality condition $\nabla \cdot B = 0$.

In what follows, we decided to study the effect of the simpler symmetric case (which does not mimic field line sweepback of FF, RVD or dissipative magnetospheres) on predicted light curves. These complex B -fields usually only have numerical solutions, which are limited by the resolution of the spatial grid. Hence, it is simpler to investigate the main effects of these structures using analytical approximations such as the offset-PC dipole solution. In future, one can also include the more complex asymmetric case.

3.3 Geometric models

Geometric models assume constant emissivity ϵ_r in the rotational frame. We have also incorporated an SG E -field associated with the offset-PC dipole B -field (making this latter case an *emission* model), which allows

us to calculate the ϵ_v in the acceleration region in the corotating frame from first principles. We have only considered the TPC (assuming uniform ϵ_v) and SG (assuming variable ϵ_v as modulated by the E -field) models for the offset-PC dipole B -field, since we do not have E -field expressions available for the OG model within the context of an offset-PC dipole B -field.

The geometric TPC pulsar model was first introduced by Dyks & Rudak (2003). Muslimov & Harding (2003) revived the physical SG model of Arons (1983), including general relativistic (GR) corrections, and argued that the SG model may be considered a physical representation of the TPC model. This gap geometry has a large radial extent, spanning from the neutron star (NS) surface along the last closed field line up to the light cylinder. The original definition stated that the maximum radial extent reached $R_{\max} \approx 0.8R_{LC}$ (Muslimov & Harding, 2004a). This was later extended to $R_{\max} \approx 1.2R_{LC}$ for improved fits (e.g., Venter et al., 2009, 2012). Typical transverse gap extents of 1 – 5% of the PC angle have been used (Venter et al., 2009; Watters et al., 2009).

The OG model was introduced by Cheng et al. (1986) and elaborated by Romani & Yadigaroglu (1995). They proposed that when the primary current passes through the neutral sheet or null-charge surface (NCS, with a radius of R_{NCS} , i.e., the geometric surface across which the charge density changes sign) the negative charges above this sheet will escape beyond the light cylinder. A vacuum gap region is then formed (in which the E -field parallel to the local B -field, $E_{\parallel} \neq 0$). Analogously, the geometric OG model has a radial extent spanning from the NCS to the light cylinder. We follow Venter et al. (2009) and Johnson et al. (2014) who considered a one-layer model with a transverse extent along the inner edge of the gap.

We performed geometric light curve modelling using the code first developed by Dyks et al. (2004a) which already includes the static dipole and RVD solutions. We extended this code by implementing an offset-PC dipole B -field (for the symmetric case), as well as the SG E_{\parallel} -field corrected for GR effects (see Section 3.6). We solve for the PC rim as explained in Section 3.5. The shape of PC rim depends on the B -field structure at the light cylinder R_{LC} . Once the PC rim has been determined, it is divided into self-similar (interior) rings. These rings are calculated by using open-volume co-ordinates (r_{ovc} and l_{ovc}). After the footpoints of the field lines on a (r_{ovc}, l_{ovc}) grid have been determined, particles are followed along these lines in the corotating frame and emission from them is collected in bins of pulse phase ϕ_L and ζ , i.e., a phase plot is formed by plotting the bin contents (divided by the solid angle subtended by each bin) for a given α , and it is therefore a projection of the radiation beam. To simulate light curves, one chooses a phase plot corresponding to a fixed α , then fix ζ and plot the intensity per solid angle.

The code takes into account the structure/geometry of the B -field (since the photons are emitted tangentially to the local field line), aberration of the photon emission direction (due to rotation, to first order in r/R_{LC}), and time-of-flight delays (due to distinct emission radii) to obtain the caustic emission beam (Morini, 1983; Dyks et al., 2004b). However, Bai & Spitkovsky (2010b) pointed out that previous studies assumed the RVD field to be valid in the instantaneously corotating frame, but actually it is valid in the laboratory frame (implying corrections that are of second-order in r/R_{LC}). This implies a revised aberration formula, which we have implemented in our code.

3.4 Transformation of a B -field from the magnetic to the rotational frame

We implemented an offset dipole B -field for the symmetric case (where the PCs of both hemispheres are offset in the same direction with respect to the magnetic (μ) axis; see Section 3.2) in our geometric code (Section 3.3). Since the offset dipole field is given in terms of magnetic frame co-ordinates ($\hat{z}' \parallel \mu$; Harding & Muslimov, 2011b) it was necessary to transform this solution to the (corotating) rotational frame ($\hat{z} \parallel \Omega$, with Ω the rotation axis). In order to do so, we first performed transformations between the spherical and Cartesian co-ordinates and bases, and then a rotation of the co-ordinate axes to move from the magnetic frame to the rotational frame. We lastly transformed the Cartesian co-ordinates of the position vector from the magnetic to the rotational frame. For a more detailed discussion, we refer the reader to Barnard et al. (2016).

Consider a general B -field specified in the magnetic frame (indicated by the primed co-ordinates), in terms of spherical co-ordinates

$$\mathbf{B}'(r', \theta', \phi') = B'_r(r', \theta', \phi')\hat{\mathbf{r}}' + B'_\theta(r', \theta', \phi')\hat{\boldsymbol{\theta}}' + B'_\phi(r', \theta', \phi')\hat{\boldsymbol{\phi}}'. \quad (3.6)$$

This field may then be transformed to a Cartesian basis and co-ordinate system:

$$\mathbf{B}'(x', y', z') = B'_x(x', y', z')\hat{\mathbf{x}}' + B'_y(x', y', z')\hat{\mathbf{y}}' + B'_z(x', y', z')\hat{\mathbf{z}}'. \quad (3.7)$$

This is done using expressions that specify spherical unit vectors and co-ordinates in terms of Cartesian co-ordinates (see e.g., Griffiths, 1995). Next, one may rotate the B -field components (i.e., the Cartesian frame) through an angle $-\alpha$ (the angle between the $\boldsymbol{\Omega}$ and $\boldsymbol{\mu}$ axes), thereby transforming the B -field from the magnetic to the rotational frame (indicated by the unprimed co-ordinates).

$$\mathbf{B}(x', y', z') = B_x(x', y', z')\hat{\mathbf{x}}' + B_y(x', y', z')\hat{\mathbf{y}}' + B_z(x', y', z')\hat{\mathbf{z}}'. \quad (3.8)$$

Lastly, we transform the magnetic co-ordinates to rotational co-ordinates:

$$\mathbf{B}(x, y, z) = B_x(x, y, z)\hat{\mathbf{x}} + B_y(x, y, z)\hat{\mathbf{y}} + B_z(x, y, z)\hat{\mathbf{z}}. \quad (3.9)$$

3.5 Finding the PC rim and extending the range of ϵ

The object is to find the polar angle θ_* at each azimuthal angle ϕ at the footpoints of the last open B -field lines, lying within a bracket $\theta_{\min} < \theta_* < \theta_{\max}$, such that the field line is tangent to the light cylinder. The PC rim is thus defined. The magnetic structure at the light cylinder therefore determines the PC shape (Dyks & Harding, 2004; Dyks et al., 2004a).

After initial implementation of the offset-PC dipole field in the geometric code, we discovered that we could solve for the PC rim in a similar manner as for the RVD B -field, but only for small values of the offset parameter ϵ ($\epsilon \lesssim 0.05 - 0.1$, depending on α). We improve the range of ϵ by varying the colatitude parameters θ_{\min} and θ_{\max} which delimit a bracket (“solution space”) in colatitude thought to contain the footpoint of last open field line (tangent to the light cylinder R_{LC}). We obtain a progressively larger range of ϵ upon decreasing θ_{\min} and increasing θ_{\max} . We find a maximum $\epsilon = 0.18$ valid for the full range of α . Choosing a maximal solution bracket in colatitude would in principle work, but the code would take much longer to find the PC rim compared to when a smaller bracket (that does contain the correct solution) is used. Therefore, we generalise the search for optimal θ_{\min} and found (by trial and error) that the following linear equation $\theta_{\min} = [(-31/18)\epsilon + 0.6]\theta_{PC}$, for a fixed $\theta_{\max} = 2.0$, resulted in θ_{\min} that yielded maximum values for ϵ .

If the PC rims ($r_{ovc} = 1$) are viewed in the $x' - y'$ plane (in the magnetic frame) as a function of α and ϵ (assuming that the $\boldsymbol{\mu}$ -axis is located perpendicularly to the page at $(x', y') = (0, 0)$ and that ϕ' is measured counterclockwise from the positive x' -axis) we note that the PC shape changes considerably. As α and ϵ are increased the PC offset is larger in the direction of “unfavourably curved” B -field lines (i.e., $-x'$ -axis). For larger α values irrespective of ϵ the PC shape along the x' -axis becomes narrower and irregular. This narrowing effect of the PC is also seen along the y' -axis as ϵ increases. We illustrate the PC shape for a few cases of α and ϵ in Figure 3.3.

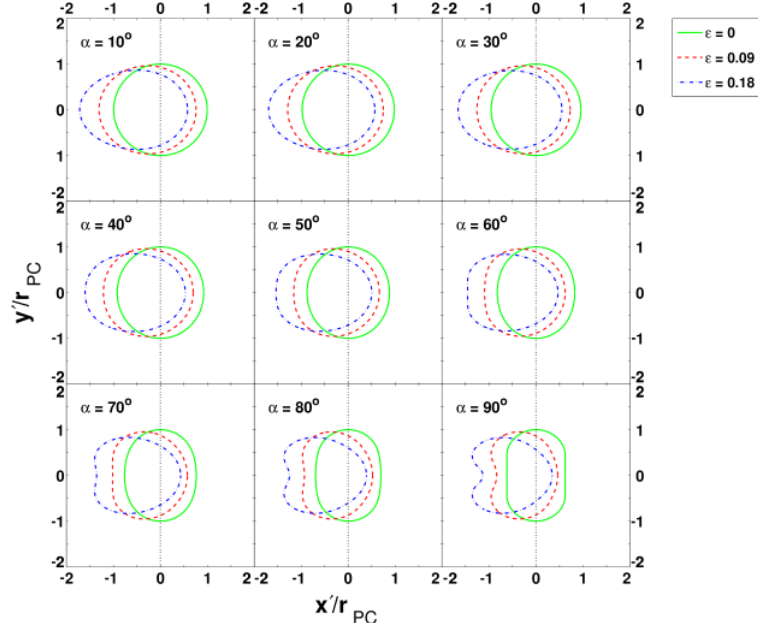


Figure 3.3: PC shapes of the offset-PC dipole B -field for a few cases of α and ϵ in the $x' - y'$ plane assuming that the μ -axis is located perpendicularly to the page at $(x', y') = (0, 0)$ and that ϕ' is measured counterclockwise from the positive x' -axis. Each PC is for a different value of α ranging between 10° and 90° , with 10° resolution. For each α we plot the PC shape for ϵ values of 0 (green solid circle), 0.09 (red dashed circle), and 0.18 (blue dashed-dotted circle). We note that the reference green PCs are for the static centred dipole. The horizontal line at $x' = 0$ (black dotted line) serves as a reference line to show the magnitude and direction of the offset as ϵ is increased.

3.6 Incorporating an SG E -field

3.6.1 Approximate expressions of the associated E -field

It is important to take the accelerating E -field into account when such expressions are available, since this will modulate the emissivity $\epsilon_\nu(s)$ (as a function of arclength s along the B -field line) in the gap as opposed to geometric models where we assume constant ϵ_ν per unit length in the corotating frame. For the SG case, we implemented the full E -field in the rotational frame corrected for GR effects (e.g., Muslimov & Harding, 2003, 2004a). This solution consists of a low-altitude and high-altitude limit which we have to match on each B -field line. The low-altitude solution is given by (Harding, private communication)

$$E_{\parallel, \text{low}} \approx -3\mathcal{E}_0 \nu_{\text{SG}} x^a \left\{ \frac{\kappa}{\eta^4} e_{1A} \cos \alpha + \frac{1}{4} \frac{\theta_{\text{PC}}^{1+a}}{\eta} [e_{2A} \cos \phi_{\text{PC}} + \frac{1}{4} \epsilon \kappa e_{3A} (2 \cos \phi'_0 - \cos(2\phi_{\text{PC}} - \phi'_0))] \sin \alpha \right\} (1 - \xi_*^2), \quad (3.10)$$

with $\mathcal{E}_0 = (\Omega R/c)^2 (B_r/B) B_0$, B_r the radial B -field component, $\nu_{\text{SG}} \equiv (1/4) \Delta \xi_{\text{SG}}^2$, and $\Delta \xi_{\text{SG}}$ the colatitudinal gap width in units of dimensionless colatitude $\xi = \theta/\theta_{\text{PC}}$. Also, $x = r/R_{\text{LC}}$ is the normalised radial distance in units of R_{LC} . Here, $\kappa \approx 0.15 I_{45}/R_6^3$ is a GR compactness parameter characterising the frame-dragging effect near the stellar surface (Muslimov & Harding, 1997), $I_{45} = I/10^{45} \text{ g cm}^2$, I the moment of inertia, $R_6 = R/10^6 \text{ cm}$, $\eta = r/R$ the dimensionless radial co-ordinate in units of R , $e_{1A} = 1 + a(\eta^3 - 1)/3$, $e_{2A} = (1 + 3a)\eta^{(1+a)/2} - 2a$ and $e_{3A} = [(5 - 3a)/\eta^{(5-a)/2}] + 2a$. The magnetic azimuthal angle ϕ_{PC} is defined for usage with the E -field, being π out of phase with ϕ' (one chooses the negative x -axis towards Ω to coincide with $\phi_{\text{PC}} = 0$, labelling

the “favourably curved” B -field lines). We define $\phi' = \arctan(y'/x')$ the magnetic azimuthal angle used when transforming the B -field (Section 3.4). Lastly, ξ_* is the dimensionless colatitude labelling the gap field lines (defined such that $\xi_* = 0$ corresponds to the field line in the middle of the gap and $\xi_* = 1$ at the boundaries; Muslimov & Harding, 2003).

We approximate the high-altitude SG E -field by (Muslimov & Harding, 2004a)

$$E_{\parallel, \text{high}} \approx -\frac{3}{8} \left(\frac{\Omega R}{c} \right)^3 \frac{B_0}{f(1)} v_{\text{SG}} x^a \left[\left(1 + \frac{1}{3} \kappa \left(5 - \frac{8}{\eta_c^3} \right) + 2 \frac{\eta}{\eta_{\text{LC}}} \right) \cos \alpha \right. \\ \left. + \frac{3}{2} \theta_{\text{PC}} H(1) \sin \alpha \cos \phi_{\text{PC}} \right] (1 - \xi_*^2), \quad (3.11)$$

with $f(\eta) \sim 1 + 0.75y + 0.6y^2$ a GR correction factor of order 1 for the dipole component of the magnetic flux through the magnetic hemisphere of radius r in a Schwarzschild metric. The function $H(\eta) \sim 1 - 0.25y - 0.16y^2 - 0.5(\kappa/\epsilon_g^3)y^3(1 - 0.25y - 0.21y^2)$ is also a GR correction factor of order 1, with $y = \epsilon_g/\eta$, $\epsilon_g = r_g/R$, and $r_g = 2GM/c^2$ the gravitational or Schwarzschild radius of the NS (with G the gravitational constant and M the stellar mass). The factors $f(\eta)$ and $H(\eta)$ account for the static part of the curved spacetime metric and have a value of 1 in flat space (Muslimov & Harding, 1997). The critical scaled radius $\eta_c = r_c/R$ is where the high-altitude and low-altitude E -field solutions are matched, with r_c the critical radius, and $\eta_{\text{LC}} = R_{\text{LC}}/R$. This high-altitude solution (excluding the factor x^a) is actually valid for the SG model assuming a static (GR-corrected, non-offset) dipole field. We therefore scale the E -field by a factor x^a to generalise this expression for the offset-PC dipole field. The general E -field valid from R to R_{LC} (i.e., over the entire length of the gap) is constructed as follows (see Eq. [59] of Muslimov & Harding, 2004a)

$$E_{\parallel, \text{SG}} \approx E_{\parallel, \text{low}} \exp[-(\eta - 1)/(\eta_c - 1)] + E_{\parallel, \text{high}}. \quad (3.12)$$

A more detailed discussion of the electrodynamics in the SG geometry may be found in Muslimov & Harding (2003) and Muslimov & Harding (2004a). In the next section, we solve for $\eta_c(P, \dot{P}, \alpha, \epsilon, \xi, \phi_{\text{PC}})$ where P is the period and \dot{P} its time derivative.

3.6.2 Determining the matching parameter η_c

At first, we matched the low-altitude and high-altitude E -field solutions by setting $\eta_c = 1.4$ for simplicity (Breed et al., 2014). However, we realised that η_c may strongly vary for the different parameters. Thus, we had to solve $\eta_c(P, \dot{P}, \alpha, \epsilon, \xi, \phi_{\text{PC}})$ on each B -field line. In what follows we consider electrons to be the radiating particles, and our discussion will therefore generally deal with the negative of the E -field. Since particle orbits approximately coincide with the B -field lines in the corotating frame, it is important to consider the behaviour of the E -field as a function of s rather than η .

We solved the matching parameter in the following way. First, we calculate $E_{\parallel, \text{low}}$, which is independent of η_c , along the B -field. If $-E_{\parallel, \text{low}} < 0$ for all η , it will never intersect with $E_{\parallel, \text{high}}$ and we set $\eta_c = 1.1$, thereby basically using $E_{\parallel, \text{SG}} \approx E_{\parallel, \text{high}}$. Second, we step through η_c (in the range 1.1 – 5.1), calculating $E_{\parallel, \text{SG}}$ and $E_{\parallel, \text{high}}$ as well as the ratio $S_i = S(\eta_i) = E_{\parallel, \text{SG}}(\eta_i)/E_{\parallel, \text{low}}(\eta_i)$ for $i = 1, \dots, N$ at different radii η_i . If $S_i > 1$ we use $1/S_i$. We next calculate a test statistic $T(\eta_c) = \sum_i^N (S_i - 1)^2/N$ using only E -field values where $-E_{\parallel, \text{low}} > -E_{\parallel, \text{high}}$ (i.e., we basically fit $E_{\parallel, \text{SG}}$ to $E_{\parallel, \text{low}}$ when $-E_{\parallel, \text{low}} > -E_{\parallel, \text{high}}$). We then minimise T to find the optimal η_c (similar to what was done in Figure 2 of Venter et al., 2009). In Figure 3.4a, the intersection radius $\eta_{\text{cut}} > \eta_{\text{LC}}$ (i.e., $E_{\parallel, \text{low}}$ and $E_{\parallel, \text{high}}$ do not intersect within the light cylinder) and therefore we impose the restriction that the solution of η_c should lie at or below 5.1. When $-E_{\parallel, \text{low}}$ does not decrease as rapidly (e.g., as in Figure 3.4b) we find reasonable solutions. We note that $E_{\parallel, \text{SG}}$ (referred to as $E_{\parallel, \text{old}}$ in Figure 3.4) produces a bump when $-E_{\parallel, \text{low}}$ decreases more rapidly. To circumvent this problem we test whether $-E_{\parallel, \text{SG}} < -E_{\parallel, \text{high}}$ and in this case we use the intersection radius η_{cut} of $E_{\parallel, \text{low}}$ and $E_{\parallel, \text{high}}$, rather than η_c , to match our solutions (calling this new

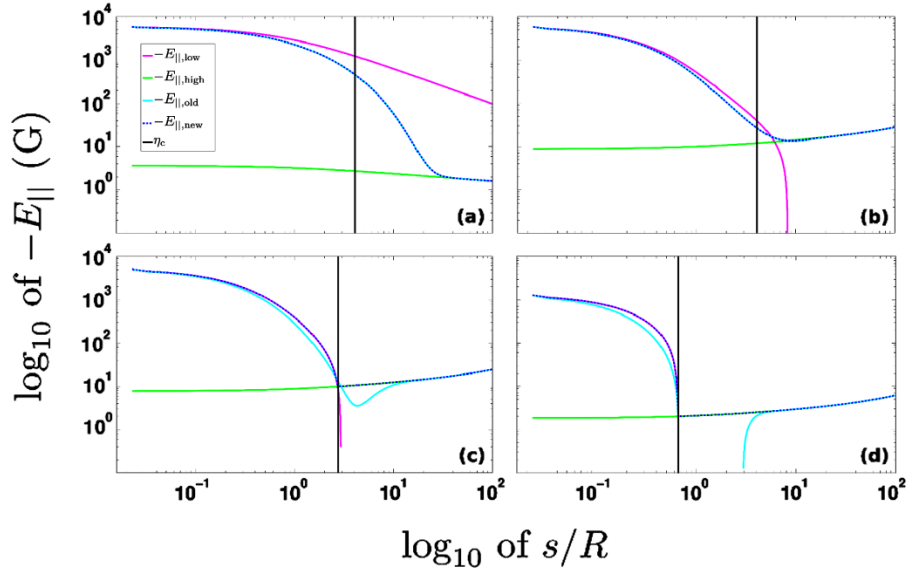


Figure 3.4: Examples of the general SG E -field ($E_{\parallel,\text{new}}$, dashed dark blue line) we obtained by matching $E_{\parallel,\text{low}}$ (magenta line) and $E_{\parallel,\text{high}}$ (green line). We plotted the negative of the various E -fields as functions of the normalised s along the B -field lines, in units of R . We indicated the matching parameter η_c (vertical black line) by using $s_c/R \approx \eta_c - 1$ (which is valid for low altitudes). These plots were obtained for the following parameters: $P = 0.0893$ s, $B_0 = 1.05 \times 10^{13}$ G, $R = 10^6$ cm, $M = 1.4M_\odot$, $\epsilon = 0.18$, and $\xi = 0.975$ (i.e., $\xi_* = 0$). In (a) we chose $\alpha = 90^\circ$, and $\phi_{\text{PC}} = 0$. Here we use $\eta_c = 5.1$ since $\eta_{\text{cut}} > \eta_{\text{LC}}$. In (b) we chose $\alpha = 15^\circ$, $\phi_{\text{PC}} = \pi$. We find a solution of $\eta_c = 5.1$. In (c) we chose $\alpha = 30^\circ$, $\phi_{\text{PC}} = \pi$. If $-E_{\parallel,\text{low}}$ as well as $-E_{\parallel,\text{old}}$ (as defined in Eq. [3.12], light blue line) are below $-E_{\parallel,\text{high}}$ beyond some radius η , we use η_{cut} (in this case $\eta_c = \eta_{\text{cut}} = 3.7$) to match $E_{\parallel,\text{low}}$ and $E_{\parallel,\text{high}}$, resulting in $-E_{\parallel,\text{new}}$ (dashed dark blue). In (d) we chose $\alpha = 75^\circ$, $\phi_{\text{PC}} = \pi$. For large α we observe that $-E_{\parallel,\text{low}}$ changes sign over a small η range. In this case we also use $\eta_c = \eta_{\text{cut}} = 1.7$ to match the solutions.

solution $E_{\parallel,\text{new}}$; see Figure 3.4c). We lastly observe that for $\phi_{\text{PC}} = \pi$ (on “unfavourably curved” field lines) for larger α , $-E_{\parallel,\text{low}}$ field changes sign resulting in a small $\eta_c = \eta_{\text{cut}} = 1.7$ value (Figure 3.4d). We determined η_c (implying $E_{\parallel,\text{new}}$) over the entire ϕ_L and ζ range at and within the SG model boundary, as a function of α . This is necessary for constructing phase plots, i.e., the intensity per solid angle, and light curves, i.e., a constant ζ -cut (refer to as ζ_{cut}) on the phase plot, later on.

Since the E -field solutions have an $x^a = x^{\epsilon \cos(\phi' - \phi'_0)} = x^{-\epsilon \cos \phi_{\text{PC}}}$ factor dependence, a larger (non-zero) offset results in different matching solutions vs. the case for $\epsilon = 0$ (see Figure 3 and 4 in Barnard et al. 2016). In the case of $\alpha = 0$, the first term $\propto \cos \alpha$ is the only contribution to the E -field, with the factor $x^a e_{1A}$ (with an ϵ dependence) being initially larger at low η for $\phi_{\text{PC}} = 0$ than for $\phi_{\text{PC}} = \pi$ (x^a dominates), but rapidly decreasing with η (e_{1A} dominates), leading to a lower value of η_c for $\phi_{\text{PC}} = 0$. One should therefore note that the magnitude of one instance of the E -field with low η_c may initially be higher than another instance with high η_c , but the first will decrease rapidly with η and eventually become lower than the second. Therefore, there is no ϕ_{PC} -dependence for $\alpha = 0$ for $\epsilon = 0$, which is not the case for $\epsilon = 0.18$. For a slightly larger α the second terms in Eq. [3.10] and [3.11] start to contribute to the radiation. This is due to the $\sin \alpha$ term with an ϵ dependence that delivers an extra contribution which is zero in the case for $\epsilon = 0$. At $\alpha = 20^\circ$ the effects of the first and second terms seem to balance each other and therefore we find the same solution of $\eta_c = 5.1$ everywhere except on the SG model boundary (at $\xi \in [0.95, 1.0]$) where $\eta_c = 1.1$, just as in the case of $\epsilon = 0$ and $\alpha = 0^\circ$. For values of $\alpha > 20^\circ$ and $\epsilon = 0.18$ the second term $\sim \cos \phi_{\text{PC}}$ starts to dominate and thus we find solutions of $\eta_c \sim 5.1$ for $\phi_{\text{PC}} \simeq 0$ and systematically smaller solutions for $\phi_{\text{PC}} \simeq \pi$ as α increases and the second term $\propto \sin \alpha$ becomes increasingly important (in both cases of ϵ). At $\alpha = 90^\circ$ we obtain the same solution as in $\epsilon = 0$ case where

the second term dominates (for this case $-E_{\parallel,SG} < 0$ for all η , since the Goldreich-Julian charge density ρ_{GJ} becomes positive). We note that the η_c -distribution reflects two symmetries (one about $\phi_{PC} = \pi$ and one about $\xi = 0.975$, i.e., $\xi_* = 0$, given our gap boundaries): that of the $\cos \phi_{PC}$ term and that of the $(1 - \xi_*^2)$ term in the E_{\parallel} solutions. After solving for η_c , we could solve the particle transport equation along each B -field line (see Section 3.8.1).

3.7 Chi-squared fitting method

We applied a standard χ^2 statistical fitting technique to assist us to objectively find the pulsar geometry (α, ζ) which best describes the observed γ -ray light curve of the Vela pulsar. We use this χ^2 method to determine the best-fit parameters for each of our B -field and geometric model combinations (spanning a large parameter space). The general expression is given by

$$\chi^2 = \sum_{i=1}^{N_{\text{bins}}} \frac{(Y_{d,i} - Y_{m,i})^2}{\sigma_{m,i}^2} \approx \sum_{i=1}^{N_{\text{bins}}} \frac{(Y_{d,i} - Y_{m,i})^2}{Y_{d,i}}, \quad (3.13)$$

where $Y_{d,i}(\phi_{L,i})$ and $Y_{m,i}(\phi_{L,i})$ are the number of counts of the observed and modelled light curves (relative units at phase $\phi_{L,i}$), and $\sigma_{m,i}(\phi_{L,i})$ the uncertainty of the model light curves in each phase bin $i = 1, \dots, N_{\text{bins}}$, with N_{bins} the number of bins. Since we do not know the uncertainty of the model, we approximate the model error by the data error, assuming $\sigma_{m,i}^2(\phi_{L,i}) \approx Y_{d,i}(\phi_{L,i})$ for Poisson statistics. Since we use geometric models, with an uncertainty in the absolute *intensity*, we assume that the *shape* of the light curve is correct. The data possess a background which is also uncertain. Furthermore, *Fermi* has a certain response function that influences the intrinsic shape of the light curve, which reflects the sum of counts from many pulsar rotations. Given all these uncertainties, we incorporate a free amplitude parameter A to allow more freedom in terms of finding the best fit of the model light curves to the data. We normalise the model light curve to range from 0 to the maximum number of observed counts k_2 by using the following expression:

$$Y'_m(\phi_{L,i}) = \frac{Y_m(\phi_{L,i})}{(k_1 + \epsilon_0)} A(k_2 - \text{BG}) + \text{BG} \approx \frac{Y_m(\phi_{L,i})}{k_1} k_2, \quad (3.14)$$

with $k_1 = \max(Y_m(\phi_{L,i}))$, $k_2 = \max(Y_d(\phi_{L,i}))$, ϵ_0 a small value added to ensure that we do not divide by zero, A a free normalisation parameter, and BG the background level of $Y_d(\phi_{L,i})$. We treat the data as being cyclic so we need to ensure that the model light curve is cyclic as well. The model light curve has to be re-binned in order to have the same number of bins in ϕ_L as the data (Abdo et al., 2013). We use a Gaussian Kernel Density Estimator function to rebin and smooth the model light curve (Parzen, 1962). Furthermore, we also introduce the free parameter $\Delta\phi_L$ which represents an arbitrary phase shift of the model light curve so as to align the model and data peaks. We choose the phase shift $\Delta\phi_L$ as a free parameter due to the uncertainty in the definition of $\phi_L = 0$ (see, e.g., Johnson et al., 2014 who also used A and $\Delta\phi_L$). Importantly, we note that we have not changed the relative position (the radio-to- γ phase lag δ), since this is a crucial model prediction. The radio and γ -ray emission regions are tied to the same underlying B -field structure, and δ therefore reflects important physical conditions (or model assumptions) such as a difference in emission heights of the radio and γ -ray beams.

After preparation of the model light curve, we searched for the best-fit solution for each of our B -field and gap combinations over a parameter space of $\alpha \in [0^\circ, 90^\circ]$, $\zeta \in [0^\circ, 90^\circ]$ (both with 1° resolution), $0.5 < A < 1.5$ with 0.1 resolution, and $0 < \Delta\phi_L < 1$ with 0.05 resolution. For a chosen B -field and model geometry we iterate over each set of parameters and search for a local minimum χ^2 value at a particular α and ζ . Once we have iterated over the entire parameter space ($\alpha, \zeta, A, \Delta\phi_L$), we obtain a global minimum value for χ^2 (also called the

optimal χ^2):

$$\chi_{\text{opt}}^2 \approx \sum_{i=1}^{N_{\text{bins}}} \frac{(Y_{\text{d},i} - Y_{\text{opt},i})^2}{Y_{\text{d},i}}. \quad (3.15)$$

If faint pulsars are modelled, Poisson statistics will be sufficient to describe the observations. For the bright Vela, however we assume Gaussian statistics which yields small errors, since the emission characteristics are more significant than those of faint pulsars. However, these small errors on the data yield large values for the reduced optimal χ^2 value $\chi_{\text{opt}}^2/N_{\text{dof}} \gg 1$. We therefore need to rescale (to compensate for the uncertainty in $\sigma_{\text{m},i}$) the χ^2 values by χ_{opt}^2 and multiply by the number of degrees of freedom N_{dof} (the difference between N_{bins} and number of free parameters). The scaled χ^2 is presented by (Pierbattista et al., 2015):

$$\xi^2 = N_{\text{dof}} \frac{\chi^2}{\chi_{\text{opt}}^2}. \quad (3.16)$$

From Eq. [3.16] the ξ^2 for the optimal model are as follows

$$\xi_{\text{opt}}^2 = N_{\text{dof}} \frac{\chi_{\text{opt}}^2}{\chi_{\text{opt}}^2} = N_{\text{dof}}, \quad (3.17)$$

with $\xi_{\text{opt}}^2/N_{\text{dof}} = \xi_{\text{opt},\nu}^2 = 1$ the reduced ξ_{opt}^2 .

If one wishes to compare the optimal model to alternative models, e.g., in our case a B -field combined with several geometric models, confidence contours for 68% (1σ), 95.4% (2σ), and 99.73% (3σ) can be constructed by estimating the difference in the ξ_{opt}^2 and the ξ^2 of the alternative models:

$$\Delta\xi^2 = \xi^2 - \xi_{\text{opt}}^2 = N_{\text{dof}} (\chi^2/\chi_{\text{opt}}^2 - 1). \quad (3.18)$$

The confidence intervals can be estimated by reading the $\Delta\xi^2$ (i.e., $\Delta\xi_{1\sigma,\mu_{\text{dof}}}^2$, $\Delta\xi_{2\sigma,\mu_{\text{dof}}}^2$, and $\Delta\xi_{3\sigma,\mu_{\text{dof}}}^2$) values from a standard χ^2 table for the specified confidence interval at $\mu_{\text{dof}} = 2$ (corresponding to the two-dimensional (α, ζ) grid, Lampton et al., 1976). Using these values for $\Delta\xi^2$ and $\xi_{\text{opt}}^2 = N_{\text{dof}}$, we can determine $\xi^2 = \xi_{\text{opt}}^2 + \Delta\xi^2 = N_{\text{dof}} + \Delta\xi^2$ (i.e., $\xi_{1\sigma}^2$, $\xi_{2\sigma}^2$, and $\xi_{3\sigma}^2$) from Eq. [3.18], which is the value at which we plot each confidence contour. To enhance the contrast of the colours on the filled χ^2 contours, we plot $\log_{10}\xi^2$ on an (α, ζ) grid, with a minimum value of $\log_{10}\xi_{\text{opt}}^2 = \log_{10}(N_{\text{dof}}) = 1.98$ (corresponding to the best-fit solution by construction, i.e., after rescaling, with $N_{\text{dof}} = 100 - 4 = 96$ in our study). The best-fit solution is therefore positioned at $\xi_{\text{opt}}^2 = 96$ and enclosed by the confidence contours with values of $\xi_{1\sigma,\mu_{\text{dof}}}^2 = 96 + 2.30$, $\xi_{2\sigma,\mu_{\text{dof}}}^2 = 96 + 6.17$, and $\xi_{3\sigma,\mu_{\text{dof}}}^2 = 96 + 11.8$ (see Eq. [3.18]; Press et al., 1992). We determine errors on α and ζ for the best-fit solution of each B -field and model combination using the 3σ interval connected contours. We choose errors of 1° for cases when the errors were smaller than one degree (given a model resolution of 1°). See Section 3.8.3 for the best-fit solutions we obtained for the offset-PC dipole B -field and SG model solution for two cases, i.e., the usual E -field, and this same E -field increased by a factor 100.

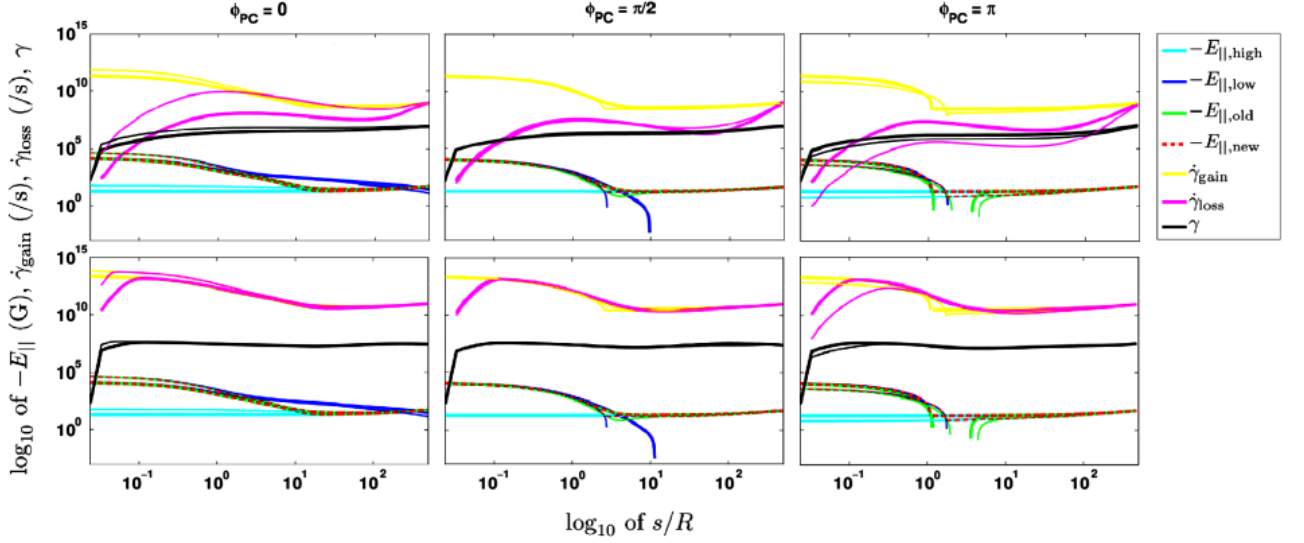


Figure 3.5: Plot of \log_{10} of $-E_{||,high}$ (solid cyan line), $-E_{||,low}$ (solid blue line), the general $-E_{||,SG}$ -field (using η_c as the matching parameter; $-E_{||,old}$, solid green line) and a corrected E -field in cases where a bump was formed using the standard matching procedure (i.e., setting $\eta_c = \eta_{cut}$; $-E_{||,new}$, dashed red line), gain rate $\dot{\gamma}_{gain}$ (solid yellow line), loss rate $\dot{\gamma}_{loss}$ (solid magenta line), and the Lorentz factor γ (solid black line) as a function of s/R . In each case we used $\alpha = 45^\circ$, $P = 0.0893$ s, $B_0 = 1.05 \times 10^{13}$ G (corrected for GR effects), $I = 0.4MR^2 = 1.14 \times 10^{45}$ g cm², and $\xi = 0.975$ (i.e., $\xi_* = 0$). On each panel we represent the curves for $\epsilon = 0$ (thick lines) and $\epsilon = 0.18$ (thin lines). The first row is for the ‘typical’ $E_{||}$ -field whereas the second row represents the $E_{||}$ -field increased by a factor 100. Each column is for a different field line, i.e., the first column for “favourably curved” field lines ($\phi_{PC} = 0$), the middle column for $\phi_{PC} = \pi/2$, and the last panel for “unfavourably curved” field lines ($\phi_{PC} = \pi$). These choices reflect the values of ϕ_{PC} at the stellar surface; they may change as the particle moves along the B -field line, since $B_\phi \neq 0$.

3.8 Results

3.8.1 Particle transport and testing for curvature radiation reaction

Once we solved η_c (see Section 3.6.2), we could calculate the general E -field ($E_{||,new}$) in order to solve the particle transport equation (in the corotating frame) to obtain the particle energy $\gamma(\eta, \phi, \xi_*)$, necessary for determining the CR emissivity. By rewriting Eq. [2.32] we obtain the following

$$\dot{\gamma} = \dot{\gamma}_{gain} + \dot{\gamma}_{loss} = \frac{eE_{||,new}}{m_e c} - \frac{2e^2 \gamma^4}{3\rho_{curv}^2 m_e c} = \frac{1}{m_e c^2} \left[ceE_{||,new} - \frac{2ce^2 \gamma^4}{3\rho_{curv}^2} \right], \quad (3.19)$$

with $\dot{\gamma}_{gain}$ the gain (acceleration) rate, $\dot{\gamma}_{loss}$ the loss rate, e the electron charge, m_e the electron mass, and $m_e c^2$ the rest-mass energy; CRR (taking only CR losses into account) occurs when the energy gain balances the losses and $\dot{\gamma} = 0$.

In Figure 3.5 we plot the \log_{10} of $-E_{||,high}$ (solid cyan line), $-E_{||,low}$ (solid blue line), the general $-E_{||,SG}$ -field (using η_c as the matching parameter; $-E_{||,old}$, solid green line) and a corrected E -field in cases where a bump was formed using the standard matching procedure (see Section 3.6.2, i.e., setting $\eta_c = \eta_{cut}$; $-E_{||,new}$, dashed red line), $\dot{\gamma}_{gain}$ (solid yellow line), $\dot{\gamma}_{loss}$ (solid magenta line), and γ (solid black line) as a function of s/R along the B -field line. The top panels represents the usual SG E -field case and the bottom panels the increased E -field case. For each case we show $\epsilon = 0$ (thick lines) and $\epsilon = 0.18$ (thin lines) on the same plot. As an example we assume $\alpha = 45^\circ$ for both cases in order to compare the two cases. We note that the values for ϕ_{PC} representing

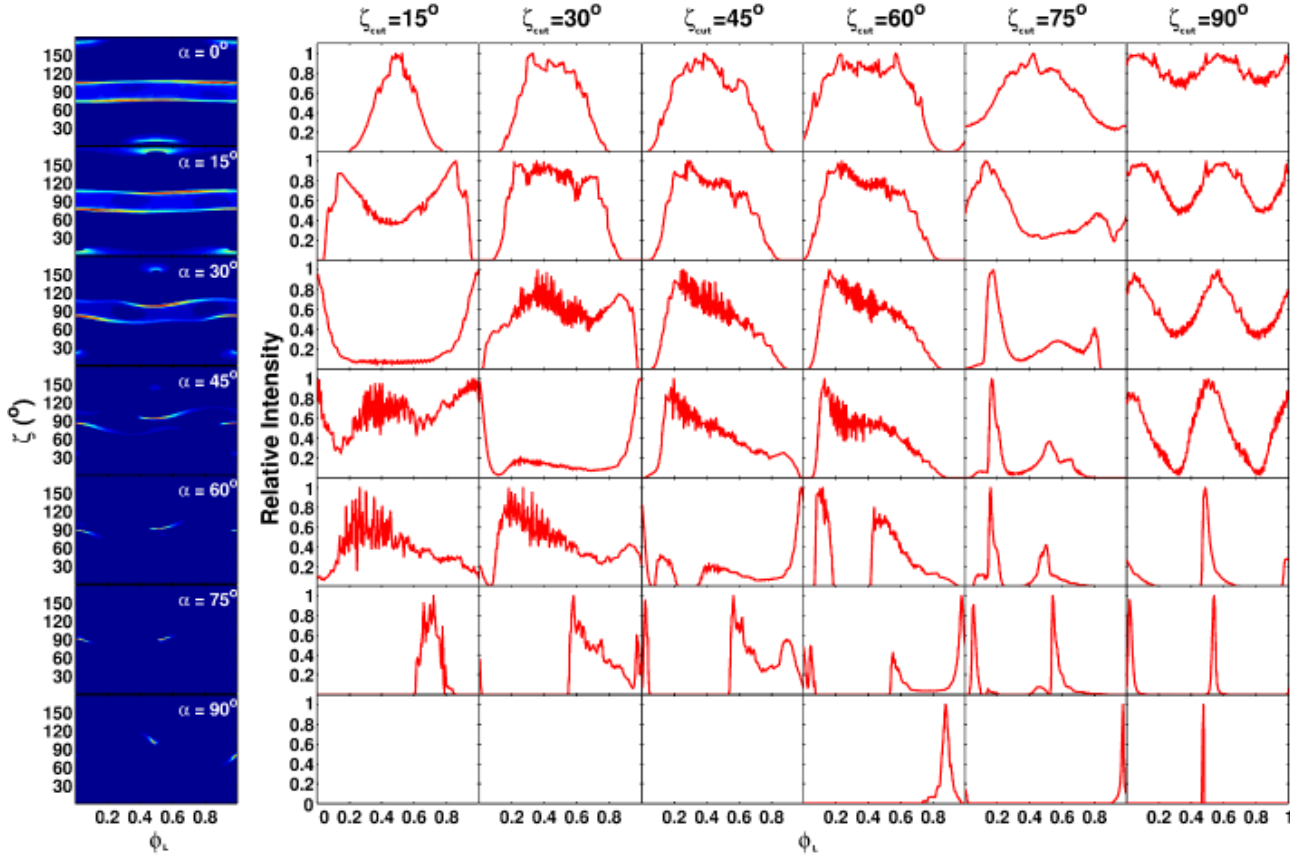
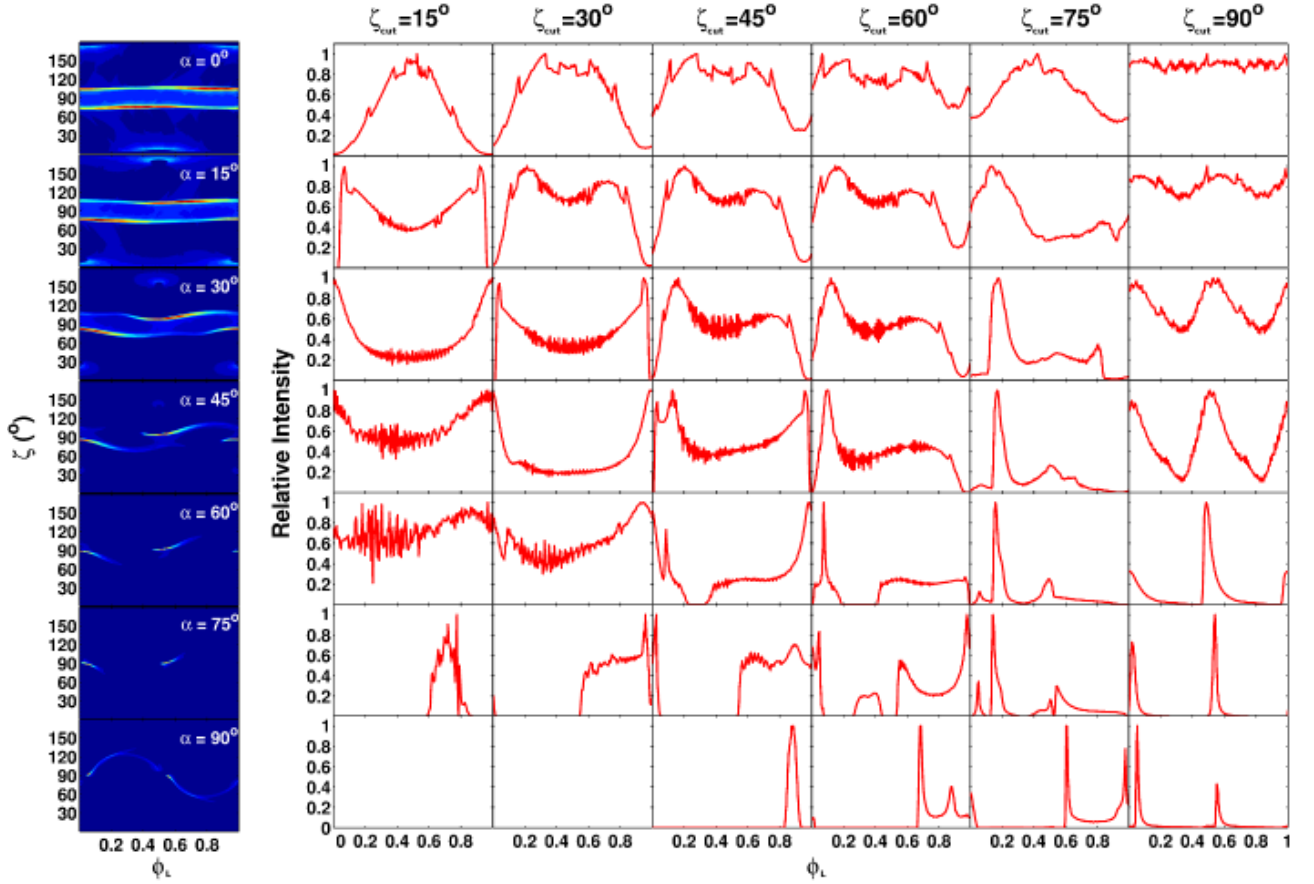


Figure 3.6: Phase plots (first column) and light curves (second column and onward) for the SG model assuming an offset-PC dipole field, for a fixed value of $\epsilon = 0.18$ and variable ϵ_r . Each phase plot is for a different α value ranging from 0° to 90° with a 15° resolution, and their corresponding light curves are denoted by the solid red lines for different ζ_{cut} values, ranging from 15° to 90° , with a 15° resolution.

each column in the figure are actually values on the stellar surface and indicate different B -field lines.

In the top panels of Figure 3.5 we note that $-E_{\parallel, \text{high}}$ displays the following behaviour at low η : for $\phi_{\text{PC}} = 0$, $-E_{\parallel, \text{high}}^{\epsilon \neq 0} > -E_{\parallel, \text{high}}^{\epsilon = 0}$; these are nearly equal for $\phi_{\text{PC}} = \pi/2$, and $-E_{\parallel, \text{high}}^{\epsilon \neq 0} < -E_{\parallel, \text{high}}^{\epsilon = 0}$ for $\phi_{\text{PC}} = \pi$. For $\phi_{\text{PC}} = \pi/2$, the first term of $-E_{\parallel, \text{high}}$ dominates the second, and for $\phi_{\text{PC}} = \pi$, the second term of $-E_{\parallel, \text{high}}$ is always negative, but the positive first term dominates and therefore $-E_{\parallel, \text{high}}$ does not change sign as η increases. Similar behaviour is also seen for $-E_{\parallel, \text{low}}$ (boosted for non-zero ϵ and $\phi_{\text{PC}} = 0$). For $\alpha = 45^\circ$, the second term $\propto \sin \alpha$ now contributes, stopping $-E_{\parallel, \text{low}}$ from changing sign along η for $\phi_{\text{PC}} = 0$ (vs. the case if $\alpha = 0$). The second term of $-E_{\parallel, \text{low}} \sim x^a \cos \phi_{\text{PC}}$ is comparable to the first at low η , but quickly dominates as η increases for $\phi_{\text{PC}} = 0$. The second term of $-E_{\parallel, \text{low}}$ remains positive so that we find $\eta_c = 5.1$ in this case (see Section 3.6.2). For $\phi_{\text{PC}} = \pi/2$ we note that $-E_{\parallel, \text{low}}^{\epsilon \neq 0}$ becomes negative with η . For $\phi_{\text{PC}} = \pi$, the second term of $-E_{\parallel, \text{low}}$ is negative, forcing this field to change sign; this change takes slightly longer to occur when $\epsilon \neq 0$. The fact that $-E_{\parallel, \text{high}}$ is positive leads to a “recovery” of the total E -field, so that it becomes positive again at larger η . The effect of matching the E -field is seen in the evolution of $\gamma(s)$ since γ is determined by E_{\parallel} .

For the usual SG E -field case we notice that the CRR limit is reached in some cases, but only at high altitudes (the yellow and magenta lines reach the same value): e.g., beyond $\eta \approx R_{\text{LC}}$ for $\phi_{\text{PC}} = 0$ and $\alpha = 45^\circ$. We note the importance of actually solving $\eta_c(P, \dot{P}, \alpha, \epsilon, \xi, \phi_{\text{PC}})$ on each B -field line. Previously we set $\eta_c = 1.4$ for all cases and found that the particles did not attain the CRR limit (Breed et al., 2014). Only when we allowed larger values of η_c was $-E_{\parallel, \text{low}}$ boosted and did we find particles reaching the CRR limit in many more cases. The relatively low SG E -field leads to small caustics on the phase plots constructed for photon energies

Figure 3.7: The same as in Figure 3.6, but for a lower E_{\min} of 1 MeV.

> 100 MeV (see Section 3.8.2). Thus, we additionally investigate the effect of *increasing the E-field*.

In the CRR limit we can determine the CR cutoff of the CR photon spectrum as follows, using the formula of Venter & De Jager (2010)

$$E_{\text{CR}} \sim 4E_{\parallel,4}^{3/4} \rho_{\text{curv},8}^{1/2} \text{ GeV}, \quad (3.20)$$

with $\rho_{\text{curv},8} \sim \rho_{\text{curv}}/10^8$ cm the curvature radius of the B -field line and $E_{\parallel,4} \sim E_{\parallel}/10^4$ statvolt cm^{-1} the E -field parallel to the B -field. As a test, we multiply the E -field by a factor 100. Using Eq. [3.20] we estimate the newly implied cutoff energy $E_{\text{CR}} \sim 4$ GeV, which is in the energy range of *Fermi* (>100 MeV). We note that a higher E -field leads to CRR being reached at lower altitudes as seen in the bottom panels of Figure 3.5. This also leads to extended caustic structures on these phase plots, resulting in qualitatively different light curve shapes, as noted below (see Section 3.8.2).

3.8.2 Light curves in different wavebands

In Figure 3.6 we present phase plots and light curves for the offset-PC dipole B -field and $\epsilon = 0.18$, obtaining a variable $\epsilon_v(s)$ due to using an SG E -field solution (with CR the dominating process for emitting γ -rays; see Sections 3.6). The caustic structure and resulting light curves are qualitatively different for various α compared to the constant ϵ_v case (see Figure 7 in Barnard et al. 2016). The caustics appear smaller and less pronounced for larger α values (since E_{\parallel} becomes lower as α increases), and extend over a smaller range in ζ . If we compare Figure 3.6 with the phase plots when $\epsilon = 0$ (see Figure 8 in Barnard et al. 2016), we note a new emission structure close to the PCs for small values of α and $\zeta \approx (0^\circ, 180^\circ)$. This reflects the boosted E_{\parallel} -field on the “favourably curved” B -field lines (with $E_{\parallel} \propto x^a \cos \alpha$, with $a = -\epsilon \cos \phi_{\text{PC}}$ and $\phi_{\text{PC}} = 0$; see Figure 3.5). In

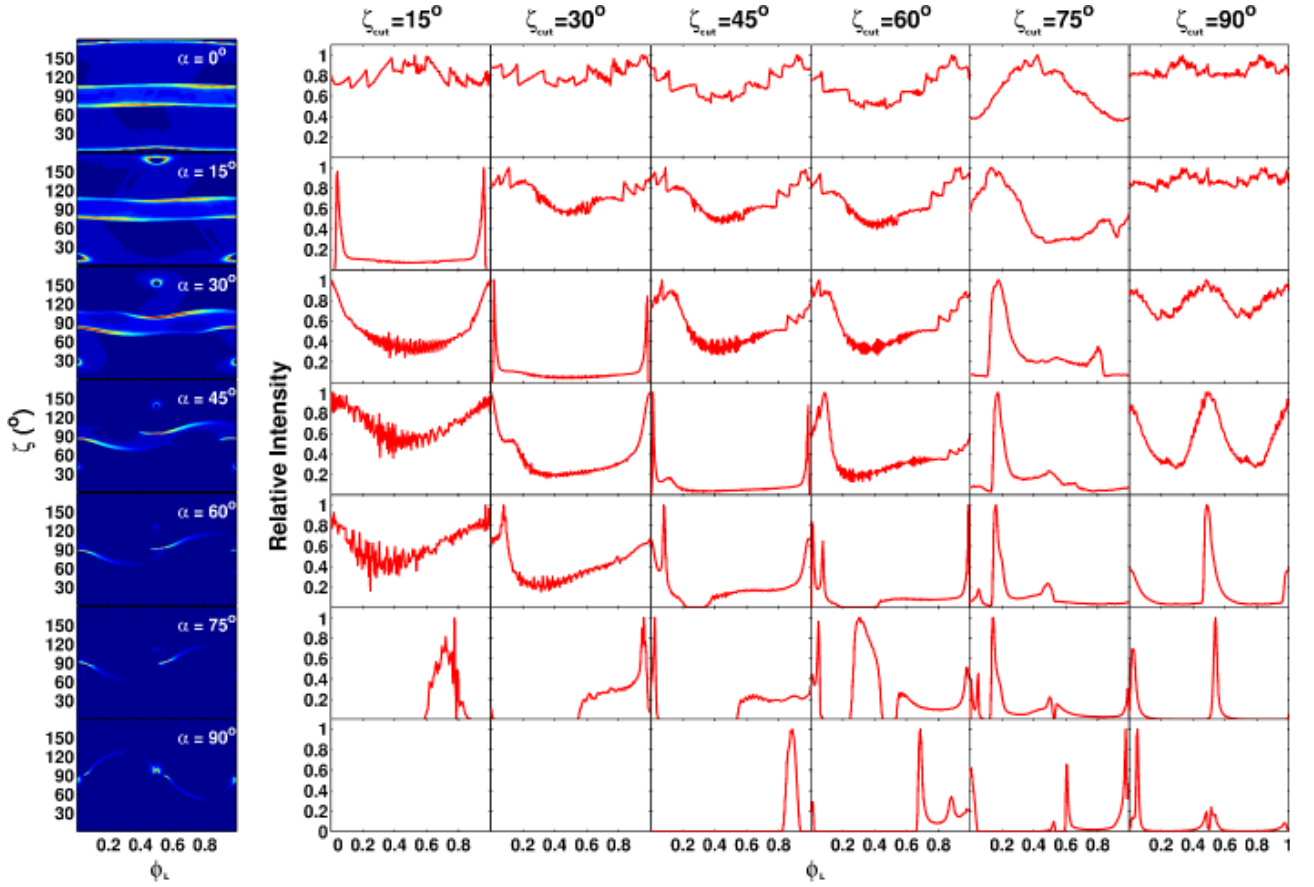


Figure 3.8: The same as in Figure 3.6, but for the case where we multiplied E_{\parallel} by a factor 100, yielding a CR cutoff of $E_{\text{CR}} \sim 4$ GeV.

Figure 3.6 there is also more phase space filled where the light curves generally display only one broad peak with less off-peak emission due to this non-zero ϵ . As α and ζ increase, more peaks become visible, with emission still visible from both poles as seen for larger α and ζ values, e.g., $\alpha = 75^\circ$ and $\zeta = 75^\circ$.

If we compare Figure 3.6 with the case of constant ϵ_v (see Figure 7 in Barnard et al. 2016), we notice that when we take E_{\parallel} into account the phase plots and light curves change considerably. For example, for $\alpha = 90^\circ$ in the constant ϵ_v case a “closed loop” emission pattern is visible in the phase plot, which is different compared to the small “wing-like” emission pattern in the variable ϵ_v case. *Therefore we see that both the B-field and E-field have an impact on the predicted light curves.* This small “wing-like” caustic pattern is due to the fact that we only included photons in the phase plot with energies > 100 MeV. Given the relatively low E -field there are only a few photons with energies exceeding 100 MeV.

Since the SG E -field (see Section 3.6) is low, CRR is reached in most cases but only at high η and small α (Section 3.8.1). This low E -field also causes the phase plots to display small caustics which result in “missing structure”. Therefore, we investigate the effect on the light curves of the offset-PC dipole B -field and SG model combination when we *lower the minimum photon energy* $E_{\gamma, \text{min}}$ from 100 MeV to 1 MeV above which we construct phase plots. For our given SG E -field with a magnitude of $E_{\parallel} \sim 10^2$ statvolt cm^{-1} the estimated cutoff is $E_{\text{CR}} \sim 90$ MeV. This leads to pulsar emission being emitted in the hard X-ray waveband, and can not be compared via χ^2 to *Fermi* (> 100 MeV) data for the Vela pulsar. As an illustration, we present the phase plots and light curves in Figure 3.7 for $\epsilon = 0.18$ and $E_{\gamma, \text{min}} > 1$ MeV. If we compare Figure 3.7 with Figure 3.6 we notice that a larger region of phase space is filled by caustics, especially at larger α , e.g., at $\alpha = 90^\circ$ the visibility is enhanced. The peaks are also wider at low α . Sometimes extra emission features appear, leading to

small changes in the light curve shapes.

We present the phase plots and light curves for this larger E -field (the usual one multiplied by a factor of 100) in Figure 3.8 for the offset-PC dipole and SG model solution with $\epsilon = 0.18$. If we compare Figure 3.8 with Figure 3.6 we notice that more phase space is filled by caustics, especially at larger α . At $\alpha = 90^\circ$ the visibility is again enhanced. The caustic structure becomes wider and more pronounced, with extra emission features arising as seen at larger α and ζ values. This leads to small changes in the light curve shapes. At smaller α values the emission around the PC forms a circular pattern that becomes smaller as α increases. These rings around the PCs become visible since the low E -field is boosted, leading to an increase in bridge emission as well as higher signal to noise. At low α the background becomes feature-rich, but not at significant intensities, though.

3.8.3 $\chi^2(\alpha, \zeta)$ contours and best-fit light curves

In this Section, we present our best-fit solutions of the simulated light curves using the Vela data from *Fermi*. We plot some example contours of $\log_{10}\xi^2$ (colour bar) as well as the optimal (α, ζ) combination. We determine errors on α and ζ for the optimal solution of each B -field and gap model combination using a bounding box delimited by a minimum and maximum value in both α and ζ which surrounds the 3σ contour (see enlargement in bottom left corner of contour). We choose errors of 1° for cases when the errors were smaller than 1° (given our chosen resolution of 1°) and indicate our overall best statistical fit for a certain model combination by a white star.

In Figure 3.9 (top panel left) we present our significance contour $\log_{10}\xi^2$ for an SG model using an offset-PC dipole field, with $\epsilon = 0.15$ and a variable ϵ_v . The corresponding light curve fit of the model (solid red line) for the best-fit geometry to the Vela data (blue histogram) is also shown (Figure 3.9 top panel, right). The observed light curve represents weighted counts per bin as function of normalised phase $\phi_L = [0, 1]$ (Abdo et al., 2013). For this combination, we find a best-fit solution at $\alpha = 76_{-1}^{+3^\circ}$, $\zeta = 48_{-11}^{+15^\circ}$, $A = 0.7$, and $\Delta\phi_L = 0.55$. The model light curve yields a reasonable fit to the Vela data, exhibiting distinct qualitative features including the two main peaks at the same phases, as seen in the Vela data. The peaks are lower than expected (constrained by the low level of off-peak emission, i.e., the χ^2 prefers a small value for A), with the first peak being very broad and a small bump preceding the second peak when compared to the data. We also obtained a better χ^2 best-fit solution for this larger E -field compared to the usual one, for $\epsilon = 0.00$ at $\alpha = 75_{-1}^{+3}$, $\zeta = 51_{-5}^{+2}$, $A = 1.1$, and $\Delta\phi_L = 0.55$. In Figure 3.9 (bottom panels) we show our significance contour $\log_{10}\xi^2$ and its corresponding best-fit light curve. This offset-PC dipole B -field (with $\epsilon = 0$ reduces to the static dipole field) and SG model for an increased E -field therefore provides an overall optimal fit, second only to the RVD and OG model combination (see Figure 3.10).

3.9 Comparison of best-fit parameters for different models

We followed the same approach as Pierbattista et al. (2015) to compare the various optimal solutions of the different models, in two ways: (i) per B -field and model combination, and (ii) overall (for all B -field and model combinations). We determine the difference between the scaled⁵ χ^2 of the optimal model, ξ_{opt}^2 and the other models (ξ^2) using Eq. [3.18], substituting $N_{\text{dof}} = 96$, as summarised in Table 3.1. The best-fit parameters for each B -field and geometric model combination, including the case for $100E_{\parallel}$, are summarised in Table 3.1. The Table includes the different model combinations, the optimal unscaled χ^2 value for each combination, the best-fit free parameters with 3σ -errors on α and ζ , and the comparison between models per B -field ($\Delta\xi_B^2$) and overall ($\Delta\xi_{\text{all}}^2$, with $\Delta\xi^2 = 0$ representing the best-fit solution for each B -field or the overall optimal fit; Pierbattista et al., 2015). We also include several multi-wavelength independent fits (all for the Vela pulsar).

⁵We therefore first scale the χ^2 values using the optimal value obtained for a particular B -field, and second we scale these using the overall optimal value irrespective of B -field.

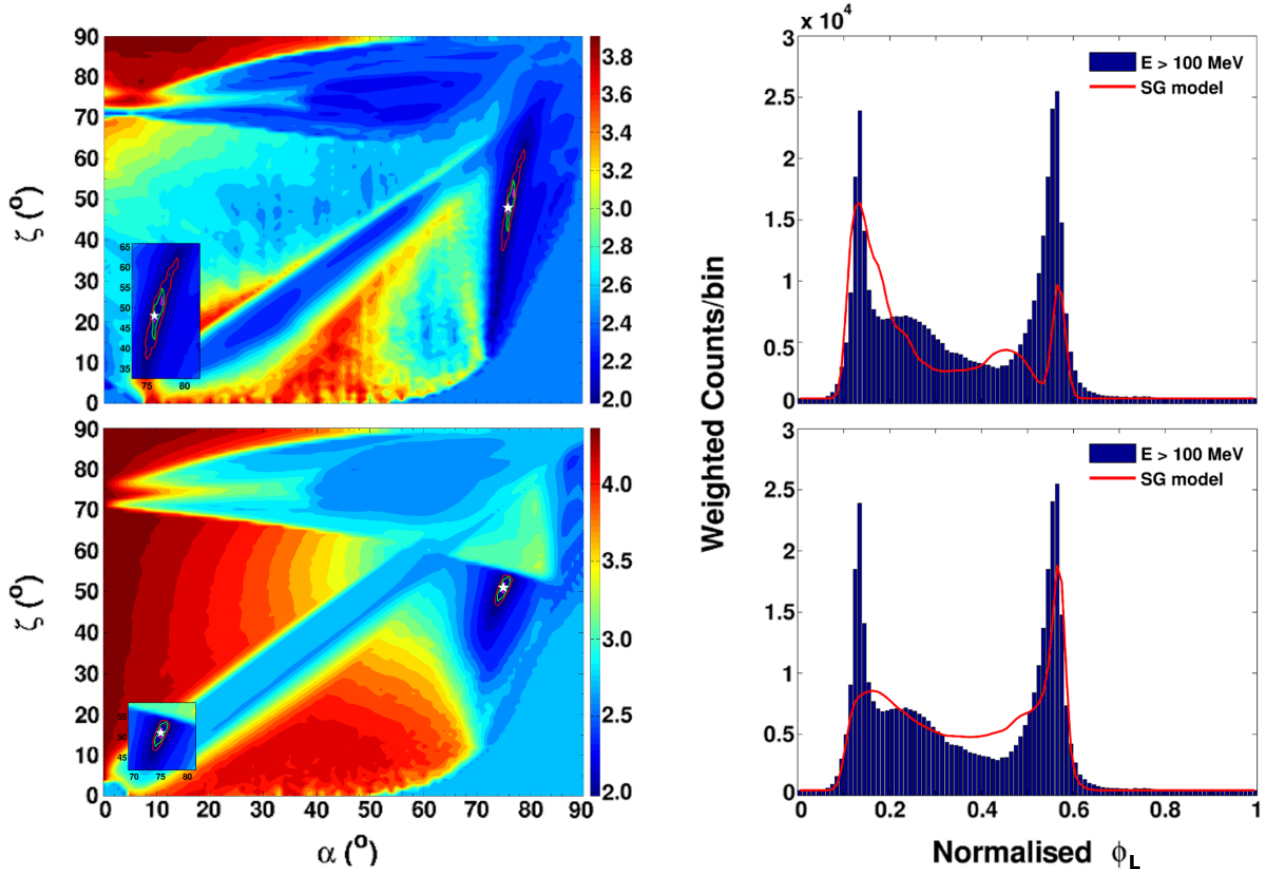


Figure 3.9: Contour plots (left) and the corresponding best-fit light curves (right) for each of the best-fit solutions we obtained for the offset-PC dipole B -field and SG model solution, for the two separate cases: for the usual SG E -field and variable ϵ_v with $\epsilon = 0.15$ (top panels), and for the higher SG E -field and variable ϵ_v with $\epsilon = 0$ when we multiplied the E_{\parallel} by a factor 100 (bottom panels). The contours are on an (α, ζ) grid with the colour bar representing $\log_{10} \xi^2$, with 1.98 corresponding to the best-fit solution, indicated by the white star. The confidence contour for 1 σ (magenta line), 2 σ (green line), and 3 σ (red line) are also shown with an enlargement in the bottom left corner. The blue histogram denotes the observed Vela pulsar profile (for energies $E > 100$ MeV, Abdo et al., 2013) and the red line the model light curve.

In Figure 3.10 we label the different B -field structures assumed in the various models as well as the overall comparison along the x -axis, and plot $\Delta \xi_B^2$ and $\Delta \xi_{\text{all}}^2$ on the y -axis. We represent the TPC geometry with a circle, the OG with a square, and for the offset-PC dipole field we represent the various ϵ values for constant ϵ_v by different coloured stars, for variable ϵ_v by different coloured left pointing triangles, and for the case of $100E_{\parallel}$ by different coloured upright triangles, as indicated in the legend. The dashed horizontal lines indicate our confidence levels we obtained by calculating the expected $\Delta \xi^2$ values using an online χ^2 statistical calculator⁶ for $N_{\text{dof}} = 96$ degrees of freedom⁷, i.e., using p -values of $p_{1\sigma} = 1 - 0.682$, $p_{2\sigma} = 1 - 0.954$, and $p_{3\sigma} = 1 - 0.9973$. We found critical values of $\Delta \xi^2 = 102.06$ (1 σ), 120.60 (2 σ), and 139.05 (3 σ) respectively. These confidence

⁶<http://easycalculation.com/statistics/critical-value-for-chi-square.php>

⁷We note that Pierbattista et al. (2015) assumed that $\Delta \xi^2$ follows a χ^2 distribution with N_{dof} degrees of freedom. We will follow this approximation here, assuming that the best-fit model provides a good fit to the observed light curves. The degrees of freedom may in reality slightly differ, however, and the matter is complicated by the fact that we want to statically compare non-nested models. A Monte Carlo approach would be preferable to find these significance levels. However, our main conclusions will not change for slight changes in these levels (which may be different for each B -field and model combination), and so we do not pursue this matter any further.

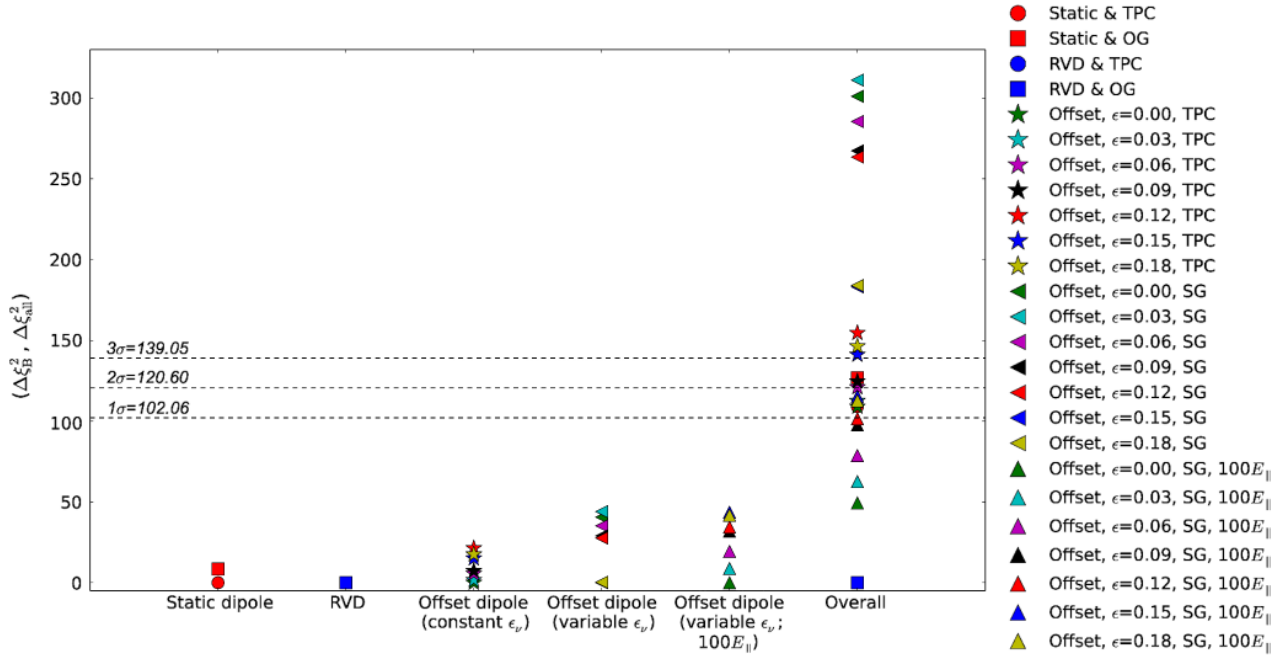


Figure 3.10: Comparison of the relative goodness of the fit of solutions obtained for each B -field and geometric model combination, including the case of $100E_{||}$, as well as all combinations compared to the overall best fit, i.e., RVD B -field and OG model (shown on the x -axis). The difference between the optimum and alternative model for each B -field is expressed as $\Delta\xi_B^2$, and for the overall fit as $\Delta\xi_{\text{all}}^2$ (shown on the y -axis). The horizontal dashed lines indicate the 1σ , 2σ , and 3σ confidence levels. Circles and squares refer to the TPC and OG models for both the static dipole and RVD. The stars refer to the TPC (constant ϵ_v) and the left pointing triangles present the SG (variable ϵ_v) model for the offset-PC dipole field, for the different ϵ values. The upright triangles refer to our SG model and offset-PC dipole case for a larger $E_{||}$ ($100E_{||}$). The last column shows our overall fit comparison (see legend for symbols).

levels are used as indicators of when to reject or accept an alternative fit compared to the optimum fit. The last column represents fits for all models, irrespective of B -field.

For the static dipole field the TPC model gives the optimum fit and the OG model lies within 1σ , implying that the OG geometry may provide an acceptable alternative fit to the data in this case. For the RVD field the TPC model is significantly rejected beyond the 3σ level (not shown on plot), and the OG model is preferred. We show three cases for the offset-PC dipole field, including the TPC model assuming constant ϵ_v , the SG model assuming variable ϵ_v , and the latter with an $E_{||}$ -field increased by a factor 100. The optimal fits for the offset-PC dipole field and TPC model reveal that a smaller offset (ϵ) is generally preferred for constant ϵ_v , while a larger offset is preferred for variable ϵ_v (but not significantly), with all alternative fits falling within 1σ . However, when we increase $E_{||}$, a smaller offset is again preferred for the SG and variable ϵ_v case. When we compare all model and B -field combinations with the overall best fit (i.e., rescaling the χ^2 values of all combinations using the optimal fit involving the RVD B -field and OG model), we notice that the static dipole and TPC model falls within 2σ , whereas the static OG model lies within 3σ . We also note that the usual offset-PC dipole B -field and TPC model combination (for all ϵ values) is above 1σ (with some fits $< 2\sigma$), but the offset-PC dipole B -field and SG model combination (for all ϵ values) is significantly rejected ($> 3\sigma$). However, the case of the offset-PC dipole field and a higher SG $E_{||}$ for all ϵ values leads to a recovery, since all the fits fall within 2σ and delivers an overall optimal fit for $\epsilon = 0$, second only to the RVD and OG model fit.

Several multi-wavelength studies have been performed for Vela, using the radio, X-ray, and γ -ray data, in order to find constraints on α and ζ . We only fit the γ -ray light curve, because we did not want to bias our results

Table 3.1: Best-fit parameters for each B -field and geometric model combination

Combinations Models	ϵ	χ^2	α	ζ	A	$\Delta\phi_L$	$\Delta\xi_B^2$	$\Delta\xi_{\text{all}}^2$
Static dipole B -field:								
TPC	...	0.819	73^{+3}_{-2}	45^{+4}_{-4}	1.3	0.55	0.00	108.75
OG	...	0.891	64^{+5}_{-3}	86^{+1}_{-1}	1.3	0.05	8.44	126.75
RVD B -field:								
TPC	...	3.278	54^{+5}_{-5}	67^{+5}_{-3}	0.5	0.05	723.50	723.50
OG	...	0.384	78^{+1}_{-1}	69^{+2}_{-1}	1.3	0.00	0.00	0.00
Offset-PC dipole B -field for constant ϵ_ν :								
TPC	0.00	0.819	73^{+3}_{-2}	45^{+4}_{-4}	1.3	0.55	0.00	108.75
	0.03	0.834	73^{+2}_{-2}	43^{+4}_{-5}	1.3	0.55	1.76	112.50
	0.06	0.867	73^{+2}_{-2}	42^{+5}_{-5}	1.3	0.55	5.63	120.75
	0.09	0.882	73^{+1}_{-2}	41^{+3}_{-5}	1.3	0.55	7.39	124.50
	0.12	1.000	74^{+1}_{-3}	42^{+3}_{-6}	1.4	0.55	21.22	154.00
	0.15	0.948	73^{+1}_{-2}	39^{+3}_{-5}	1.4	0.55	15.12	141.00
	0.18	0.969	73^{+2}_{-3}	37^{+4}_{-4}	1.3	0.55	17.58	146.25
Offset-PC dipole B -field for variable ϵ_ν :								
SG	0.00	1.587	21^{+3}_{-3}	71^{+1}_{-1}	0.5	0.85	40.52	300.75
	0.03	1.627	73^{+1}_{-1}	17^{+4}_{-3}	0.7	0.55	43.96	310.75
	0.06	1.525	72^{+2}_{-1}	14^{+5}_{-1}	0.5	0.60	35.18	285.25
	0.09	1.452	73^{+1}_{-1}	17^{+3}_{-1}	0.6	0.55	28.90	267.00
	0.12	1.437	74^{+1}_{-1}	27^{+1}_{-7}	0.8	0.55	27.61	263.25
	0.15	1.116	76^{+3}_{-1}	48^{+15}_{-11}	0.7	0.55	0.00	183.00
	0.18	1.119	75^{+2}_{-1}	40^{+6}_{-4}	0.5	0.55	0.26	183.75
Offset-PC dipole B -field for variable ϵ_ν ($100E_\gamma$):								
SG	0.00	0.581	75^{+3}_{-1}	51^{+2}_{-5}	1.1	0.55	0.00	49.27
	0.03	0.634	75^{+2}_{-2}	49^{+5}_{-5}	1.1	0.55	8.73	62.48
	0.06	0.698	75^{+3}_{-3}	49^{+5}_{-6}	1.1	0.55	19.39	78.61
	0.09	0.774	75^{+3}_{-3}	50^{+5}_{-9}	1.1	0.55	31.90	97.54
	0.12	0.789	77^{+2}_{-3}	54^{+2}_{-8}	1.1	0.55	34.42	101.36
	0.15	0.845	77^{+2}_{-4}	55^{+1}_{-14}	0.9	0.55	43.62	115.28
	0.18	0.834	78^{+1}_{-2}	55^{+1}_{-5}	0.8	0.55	41.80	112.51
RVM ¹			53	59.5				
X-ray torus ²				$63.6^{+0.07}_{-0.05}$				
RVD & TPC ³			62–68	64				
RVD & OG ³			75	64				
RVD & Symmetric SG ⁴			44^{+4}_{-1}	54^{+1}_{-5}				
RVD & Asymmetric SG ⁴			65^{+1}_{-2}	65.5^{+2}_{-1}				
RVD & OG ⁴			88^{+2}_{-3}	66.5^{+1}_{-1}				
FF & Symmetric SG ⁴			15^{+1}_{-1}	68.5^{+1}_{-1}				
FF & Asymmetric SG ⁴			55^{+10}_{-20}	54.5^{+4}_{-14}				
FF & OG ⁴			80^{+1}_{-1}	53^{+1}_{-1}				
RVD & PC ⁵			3^{+2}_{-3}	4^{+2}_{-2}				
RVD & SG ⁵			45^{+2}_{-2}	69^{+2}_{-2}				
RVD & OG ⁵			71^{+2}_{-2}	83^{+2}_{-2}				
RVD & OPC ⁵			56^{+2}_{-2}	77^{+2}_{-2}				

Note. The table summarises the best-fit parameters α , ζ , A , and $\Delta\phi_L$, for each model combination, with the errors on α and ζ determined by using the 3σ interval connected contours. We chose a minimum error of 1° if the confidence contour yielded smaller errors. We included the unscaled χ^2 to indicate which geometry yields the optimal fit to the Vela data (i.e., the OG model and RVD B -field). We included other multi-wavelength fits in the second part of the table.

References. ¹ Johnston et al., 2005; ² Ng & Romani, 2008; ³ Watters et al., 2009; ⁴ DeCesar, 2013; and ⁵ Pierbattista et al., 2015.

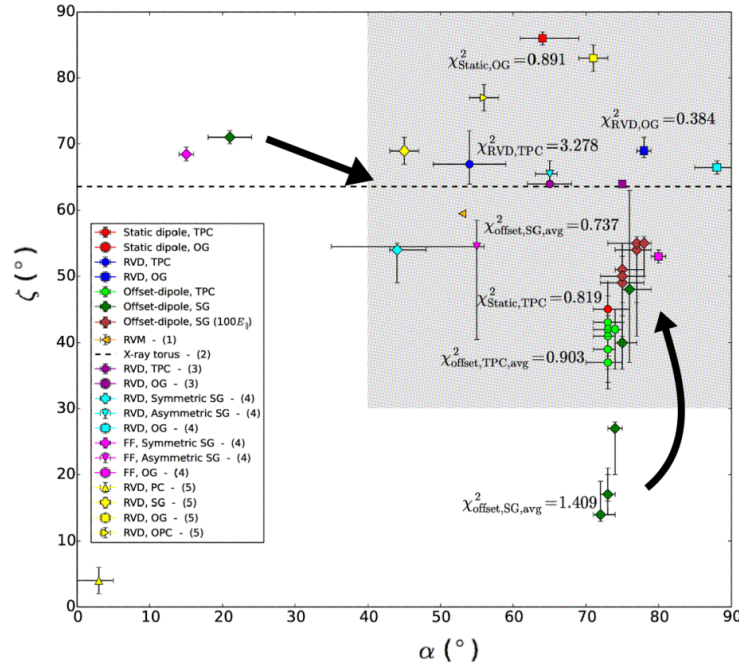


Figure 3.11: Comparison between the best-fit α and ζ , with errors, obtained from this and other multi-wavelength studies. Each marker represents a different case as summarised in Table 3.1, with the unscaled χ^2 ($\times 10^5$) value of our fits indicated. For the offset-PC dipole, for both the TPC and SG models we indicate the average χ^2 value over the range of ϵ . We also show our fits for the offset-PC dipole and SG model case with a larger E_{\parallel} . The two black arrows indicate the shift of the best fits to larger α and ζ if we increase our SG E -field by a factor 100. The shaded region contains all the fits that cluster at larger α and ζ values.

by using a geometric radio emission model (DeCesar, 2013). However, Johnston et al. (2005) determined the radio polarisation position angle from polarisation data by applying a rotating vector model (RVM) fit to the data finding best-fit values of $\alpha = 53^\circ$ and $\zeta = 59.5^\circ$, with an impact angle of $\beta = \zeta - \alpha = 6.5^\circ$. Ng & Romani (2008) applied a torus-fitting technique (Ng & Romani, 2004) to fit the *Chandra* data in order to constrain the Vela X pulsar wind nebula (PWN) geometry, deriving a value of $\zeta = 63.6^{+0.07}_{-0.05}$ represented by the dashed black line in Figure 3.11. Watters et al. (2009) modelled light curves using the PC, TPC, and OG geometries in conjunction with an RVD field, thereby constraining the geometrical parameters α , ζ , and also finding small β in the case of the PC model. They found a good fit for their TPC model at $\alpha = 62^\circ - 68^\circ$ and $\zeta = 64^\circ$, and for the OG geometry at $\alpha = 75^\circ$ and $\zeta = 64^\circ$. We find that our best-fit values for the RVD field, for both the TPC and OG models, are in good agreement with those found by Watters et al. (2009). DeCesar (2013) followed a similar approach to ours, but for the RVD and FF B -fields combined with emission geometries such as the SG (symmetric and asymmetric cases) and OG. They have different free model parameters including α , ζ , w (gap width), and R_{\max} (maximum emission radius), and determined errors on their best fits using the 3σ confidence intervals. They found best-fit solutions for the RVD and OG model at $\alpha = 88^{+2}_{-3}$ and $\zeta = 66.5^{+1}_{-1}$, which is within 10° or less compared to our best-fit solution. Their overall best fit was for the FF B -field and OG geometry, with $\alpha = 80^{+1}_{-1}$ and $\zeta = 53^{+1}_{-1}$. Pierbattista et al. (2015) found a best-fit solution for Vela using the RVD field and OG model combination at $\alpha = 71^{+2}_{-2}$ and $\zeta = 83^{+2}_{-2}$, with ζ exceeding the best-fit solution we found by nearly 15° . However, they fit both the γ -ray and radio light curves, which may explain this discrepancy. We summarise all these multi-wavelength fits and more in Table 3.1.

We graphically summarise the best-fit α and ζ , with errors, from this and other works in Figure 3.11. We notice that the best fits generally prefer a large α or ζ or both. It is encouraging that many of the best-fit solutions lie near the ζ inferred from the PWN torus fitting (Ng & Romani, 2008), notably for the RVD B -

field. A significant fraction of fits furthermore lie near the $\alpha - \zeta$ diagonal, i.e., they prefer a small impact angle, probably due to radio visibility constraints (Johnson et al., 2014). For an isotropic distribution of pulsar viewing angles, one expects ζ values to be distributed as $\sin(\zeta)$ between $\zeta = [0^\circ, 90^\circ]$, i.e., large ζ values are much more likely than small ζ values, which seems to correspond to the large best-fit ζ values we obtain. There seems to be a reasonable correspondence between our results obtained for geometric models and those of other authors, but less so for the offset-PC dipole B -field, and in particular for the SG E -field case. The lone fit near $(20^\circ, 70^\circ)$ may be explained by the fact that a very similar fit, but one with slightly worse χ^2 , is found at $(50^\circ, 80^\circ)$. If we discard the non-optimal TPC / SG fits, we see that the optimal fits will cluster near the other fits at large α and ζ . Although our best fits for the offset-PC dipole B -field are clustered, it seems that increasing ϵ leads to a marginal decrease in ζ for the TPC model (light green) and opposite for SG (dark green), but not significantly (see Table 3.1). For our increased SG E -field case (brown) we note that the fits now cluster inside the grey area above the fits for the static dipole and TPC, and offset-PC dipole for both the TPC and SG geometries.

3.10 Conclusion

We investigated the impact of different magnetospheric structures on predicted γ -ray pulsar light curve characteristics. We extended our code which already included the static dipole and RVD B -fields, by implementing an additional B -field, i.e., the symmetric offset-PC dipole field (Harding & Muslimov, 2011a,b) characterised by an offset ϵ of the magnetic PCs. We also included the full accelerating SG E -field corrected for GR effects up to high altitudes. For the offset-PC dipole field we only considered the TPC (assuming uniform ϵ_v) and SG (modulating the ϵ_v using the E -field) models, since we do not have E -field expressions available for the OG model for this particular B -field. We matched the low-altitude and high-altitude solutions of the SG $E_{||}$ by determining the matching parameter $\eta_c(P, \dot{P}, \alpha, \epsilon, \xi, \phi_{PC})$ on each field line in multivariate space. Once we calculated the general E -field we could solve the particle transport equation. This yielded the particle energy $\gamma(\eta)$, necessary for determining the CR ϵ_v and to test whether the CRR limit is attained. For the case of a variable ϵ_v , we found that the CRR limit is reached for many parameter combinations (of α , ϵ and ϕ_{PC} ; see Figure 3.5), albeit only at large η . A notable exception occurred at large α where the first term of each E -field expression (e.g., Eq. [3.10] and [3.11]) became lower and the second term played a larger role, leading to smaller gain rates and therefore smaller Lorentz factors γ .

We concluded that the magnetospheric structure and emission geometry have an important effect on the predicted γ -ray pulsar light curves. *However, the presence of an E -field may have an even greater effect than small changes in the B -field and emission geometries:* When we included an SG E -field, thereby modulating ϵ_v , the resulting phase plots and light curves became qualitatively different compared to the geometric case.

We fit our model light curves to the observed *Fermi*-measured Vela light curve for each B -field and geometric model combination. We found that the RVD field and OG model combination fit the observed light curve the best for $(\alpha, \zeta, A, \Delta\phi_L) = (78^{+1}_{-1}^\circ, 69^{+2}_{-1}^\circ, 1.3, 0.00)$ and an unscaled $\chi^2 = 3.84 \times 10^4$. As seen in Figure 3.10, for the RVD field an OG model is significantly preferred over the TPC model, given the characteristically low off-peak emission. For the other field and model combinations there was no significantly preferred model (per B -field), since all the alternative models may provide an acceptable alternative fit to the data, within 1σ . The offset-PC dipole field for constant ϵ_v favoured smaller values of ϵ , and for variable ϵ_v larger ϵ values, but not significantly so ($< 1\sigma$). When comparing all cases (i.e., all B -fields), we noted that the offset-PC dipole field for variable ϵ_v was significantly rejected ($> 3\sigma$).

We further investigated the effect which the SG $E_{||}$ had on our predicted light curves in two ways. First, we lowered the minimum photon energy from $E_{\gamma, \min} = 100$ MeV to $E_{\gamma, \min} = 1$ MeV, leading to emission in the hard X-ray waveband. We noted new caustic structures and emission features on the resulting phase plots and light curves that were absent when $E_{\gamma, \min} > 100$ MeV. Since we wanted to compare our model light curves to *Fermi* data we increased the usual low SG E -field by a factor of 100 (with a spectral cutoff $E_{CR} \sim 4$ GeV). When solving the particle transport equation, we noticed that the CRR limit is now reached in most cases at lower

η . The increased E -field also had a great impact on the phase plots, e.g., extended caustic structures and new emission features as well as different light curve shapes emerged. We also compared the best-fit light curves for the offset-PC dipole B -field and $100E_{\parallel}$ combination for each ϵ (Figure 3.10) and noted that a smaller ϵ was again preferred (although not significantly; $< 1\sigma$). However, when we compared this case to the other B -field and model combinations, we found statistically better χ^2 fits for all ϵ values with an optimal fit at $\alpha = 75_{-1}^{+3^\circ}$, $\zeta = 51_{-5}^{+2^\circ}$, $A = 1.1$, and $\Delta\phi_L = 0.55$ for $\epsilon = 0$, being second in quality only to the RVD and OG model fit.

We graphically compared the best-fit α and ζ , with errors, from this and other works in Figure 3.11. We noted that many of the best-fit solutions cluster inside the grey area at larger α and ζ . Some fits lie near the $\alpha - \zeta$ diagonal (possibly due to radio visibility constraints in some cases) as well as near the ζ inferred from the PWN torus fitting (Ng & Romani, 2008), notably for the RVD B -field. There was reasonable correspondence between our results obtained for geometric models and those of other independent studies. When we discarded the non-optimal TPC / SG fits, we saw that the optimal fits clustered near the other fits at large α and ζ . For our increased SG E -field and offset-PC dipole combination (brown) we noted that these fits clustered at larger α and ζ .

There have been several indications that *the SG E -field may be larger than initially thought*. For example, (i) population synthesis studies found that the SG γ -ray luminosity may be too low, pointing to an increased E -field and / or particle current through the gap (e.g., Pierbattista et al., 2015). Furthermore, if the E -field is too low, one is not able to reproduce the (ii) observed spectral cutoffs of a few GeV (Section 3.8.2; Abdo et al., 2013). We found additional indications for an enhanced SG E -field. A larger E -field (increased by a factor of 100) led to (iii) statistically improved χ^2 fits with respect to the light curves. Moreover, the inferred best-fit α and ζ parameters for this E -field (iv) clustered near the best fits of independent studies. We additionally observed that a larger SG E -field also (v) increased the particle energy gain rates and therefore yielded a larger particle energy γ (giving CR that is visible in the *Fermi* band) as well as leading to a CRR regime already close to the stellar surface. These evidences may point to a reconsideration of the boundary conditions assumed by Muslimov & Harding (2004a) which suppressed the E_{\parallel} at high altitudes. They assumed equipotentiality of the SG boundaries as well as the steady state drift of charged particles across the SG B -field lines, implying $E_{\perp} \approx 0$ at high-altitudes, with the flux of charges remaining constant up to high altitudes. One possible way to bring self-consistency may be implementation of the newly developed FIDO model that includes global magnetospheric properties and calculates the B -field and E -field self-consistently.

We envision several future projects that may emanate from this study. One could continue to extend the range of ϵ for which our code finds the PC rim, since more complex field solutions, e.g., the dissipative and FF field structures, may be associated with larger PC offsets. However, the offset-PC dipole solutions have limited applicability to outer magnetosphere emission since they use the static dipole frame and do not model the field line sweep back. Therefore, it would be preferable to investigate the B -fields and E -fields of more complex B -field models (see Sections 2.6 and 2.7) and solve the transport equation to test if the particles reach the CRR limit. The effect of these new fields on the phase plots and light curves can also be studied. There is also potential for multi-wavelength studies, such as light curve modelling in the other energy bands, e.g., combining radio and γ -ray light curves (see Seyffert et al., 2010, 2012; Pierbattista et al., 2015). One could furthermore model energy-dependent light curves, such as those available for Vela and other bright pulsars using *Fermi* data (e.g., Abdo et al., 2009). Lastly, model phase-resolved spectra can be constructed which is an important test of the E_{\parallel} -field magnitude and spatial dependence.

In the next Chapter we will discuss the technical details of the emission modelling code (Harding & Kalapotharakos, 2015; Harding et al., 2018) used in the rest of this study. This emission code is an extension of the geometric code discussed in Section 3.3 and include a FF solution in a SG model scenario. Since we focus on the particle emission from CR (Section 2.4.3), we also refined the radius of curvature of the particle trajectories.

Chapter 4

Model description: code setup and refinements

In this thesis, I modelled pulsar emission by investigating energy-dependent light curves and spectra using a full emission code. In this Chapter, I specifically discuss the technical details of this emission code, the porting and local implementation of it, and how I was able to obtain the results presented in Chapter 5. Additionally, I will give a summary of Harding et al. (2018) in Chapter 6, since those results accompany those in Chapter 5. In Section 4.1, we give a brief description of the pulsar emission code and the calibration thereof follows in Section 4.2. Section 4.3 gives a brief description of the parallelised version of the emission code; this is followed by Section 4.4 where I describe a more accurate computation of the particle trajectories and their radii of curvature ρ_c . Section 4.5 summarises the main conclusions.

4.1 An SSC emission modelling code

Harding et al. (2008) used a 3D optical to γ -ray emission model in an SG scenario including two particle populations, i.e., primaries (leptons) being accelerated from the stellar surface up to altitudes of R_{LC} , as well as non-accelerated electron-positron pairs radiated up to the same altitudes as the primaries. This model is based on the geometric model of Dyks et al. (2004a) that assumed an RVD solution for the B -field (see Section 2.6, 3.3, and 3.5). The open volume coordinates r_{ovc} and l_{ovc} are associated with the radial (i.e., rings) and azimuthal (i.e., arc length along each ring measured in the direction of increasing ϕ_{PC}) coordinates, respectively, as mentioned in Chapter 3. They also explore the geometry of the radio emission in relation to that of the HE emission. They included radiation from a geometric radio emission beam model that consists of a core and a single cone (Rankin, 1993; Gonthier et al., 2004), in order to compute the intensity and angles of radio photons necessary for the cyclotron absorption/synchrotron emission component. The primary particles are injected at the stellar surface and are accelerated along the B -field lines in a SG region bounding the last open field lines via a low and high-altitude SG E -field, that are combined to obtain a total SG E -field over all altitudes (see Section 3.6 and equations therein). In this model, the SG reaches altitudes of R_{LC} . The electron-positron pairs are produced in PC and SG pair cascades following from the accelerated primaries. They investigated the CR from primaries, SR from both primaries and pairs that undergo cyclotron resonant absorption of radio photons and produce significant increases in pitch angle, as well as nonresonant ICS of radio photons (see Section 2.4 for detailed discussions about radiation mechanisms). They followed the same particle dynamics calculation as Harding et al. (2005) but added the CR loss and resonant absorption terms. Due to the large acceleration and SR loss rates the ICS were neglected for the primary particles and the pairs. This resulted in a broadband spectrum ranging from infrared to HE γ -rays. There is no SSC calculation considered in this model, however the model of Harding & Kalapotharakos (2015) does include this radiation component. The model of Harding et al. (2018)

is based on that of Harding & Kalapotharakos (2015), including extended energy ranges.

Using the emission model of Harding & Kalapotharakos (2015), we study the full particle acceleration and focus on the CR emission component. The model assumes a 3D FF B -field as the basic magnetospheric structure. This solution (formally assuming an infinite plasma conductivity, so that the E -field is fully screened) serves as a good approximation to the geometry of field lines implied by the dissipative models that require a high conductivity in order to match observed γ -ray light curves (Kalapotharakos et al., 2012c, 2014; Li et al., 2012). This model is an extended version of the model first used by Harding et al. (2008) with the PC rim (Section 3.5) being determined in a similar fashion for this FF B -field structure. Both primary particles and electron-positron pairs are injected at the stellar surface. The primaries radiate CR and some of these γ -ray photons are converted into pairs in the intense B -fields close to the star. Using an independent code, we calculate a PC pair cascade that develops, since primaries and pairs radiate SR as well as CR that are converted into electron-positron pairs, leading to further generations of particles with lower energies. The primaries are injected with a low initial speed and are further accelerated along the B -field lines by a constant parallel E -field E_{\parallel} that is parallel to the local B -field lines (used as a free parameter in this model) in an extended SG and current sheet scenario near the last open field lines. In this model, the SG extends beyond R_{LC} into the current sheet, reaching altitudes of up to $r = 2R_{LC}$. All calculations are performed in the laboratory frame. In order to explain the VHE emission seen from pulsars they included an SSC component (involving energetic primaries and pair SR) which could reproduce the spectral flux level as observed by MAGIC and VERITAS (see Section 1.1).

Harding et al. (2018) adapted the emission code of Harding & Kalapotharakos (2015) further by updating the CR component to a SC radiation component, as well as a two step accelerating E -field, i.e., E_{\parallel} inside the light cylinder and E_{\parallel} beyond the light cylinder and into the current sheet, as motivated by results of global MHD and PIC pulsar models. Our contribution was an improved calculation of the particle trajectories and their ρ_c 's. They presented the broadband spectrum of Vela ranging from infrared (IR) to beyond 10 TeV energies, thereby explaining the TeV emission recently observed by *H.E.S.S.* (see Chapter 6 for more details). In Chapter 5 I focus on the GeV spectrum and energy-dependent CR light curves from the primary particles using the model of Harding & Kalapotharakos (2015). Additionally, we included the two-step E_{\parallel} to study the effect thereof on the light curves and spectra. In Chapter 6 I will give a short summary of my contribution to the work published in Harding et al. (2018), which includes the refined ρ_c discussed in Section 4.4.

4.2 Calibration of the code

Before the implementation of a refined ρ_c , I first calibrated the emission code, since it is an essential component of evaluating and excluding any uncertainties in the predictions and estimates. I investigated the spectral output obtained by comparing it with the original data (from our collaborators), using the same version of the code paired with different compilers. The different choices of compilers produced variations in the model simulations.

As a test case, I studied the variations in spectra, for the Crab pulsar, for two calculations of the observer angle ζ . Using the z -component ($z'(s)$) of the velocity of the particle as a function of s , we calculated $\zeta = \arccos(z'(s))$, and second, we used a linear calculation $\zeta = (-\pi/2z' + \pi/2)$. Later, I made a cut on ζ so that the predictions would be observer-specific (characterised by ζ_{cut}). Thus, different implementations of the emission direction of individual photons would influence what a particular observer at a constant ζ would see. This was to test whether the implementation of the inverse cosine had any impact on the predicted spectrum.

The impact of the compiler choice is illustrated in Figure 4.1 showing the phase-averaged CR spectra for different compilers assuming $\alpha = 45^\circ$, $\zeta_{\text{cut}} = 50^\circ$, as well as that the emission originates from primary particles only. In Figure 4.1 I choose compilers such as GCC, ICC, MVS, and CLANG, for both colatitude calculations. Additionally, I considered for some compilers the optimised and non-optimised cases to further investigate the effect thereof on the calculations. The legend indicates our combination choices, where no letter denotes the simulations done by us and letters A and Z those done by two collaborators. The spectra for the two colatitude

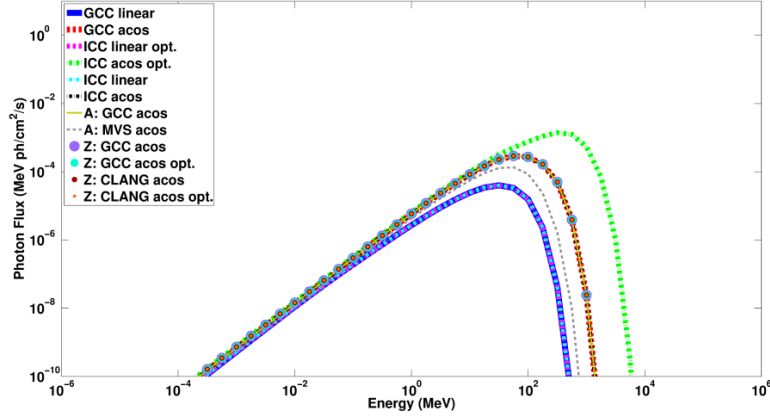


Figure 4.1: An example of the phase-averaged CR spectra for the Crab pulsar assuming $\alpha = 45^\circ$ and $\zeta_{\text{cut}} = 50^\circ$. Each curve represents a combination of a compiler with a different calculation of the colatitude, i.e., linear and inverse cosine. The letters A and Z refer to the results obtained by our collaborators using other compilers.

calculations, regardless of the compiler choice, are distinctively different. However, two exceptions are the MVS and the optimised ICC compilers, both for the inverse cosine case. For the linear case, the photon flux is lower than that of the inverse cosine case. Since the emission code uses the inverse cosine calculation and the output for the majority of compilers agree, I opted for the compiler that yielded results consistent with those of our collaborators, i.e., GCC.

Another element of calibration is the resolution of the simulations. This is especially important when constructing results since the emission is followed along each B -field line. Thus the more field line footpoints there are on the PC, the more emission there is, resulting in better quality phase plots, light curves, and spectra. To investigate the effect the resolution of the model has on its accuracy, I constructed phase plots for different grid sizes of azimuthal divisions and the number of rings (self-similar to the PC rim; see Section 3.5). As an example I illustrate the phase plots for Vela assuming $\alpha = 75^\circ$, $\zeta_{\text{cut}} = 65^\circ$, and a constant accelerating E_{\parallel} -field, i.e., $eE_{\parallel}/m_e c^2 = 0.25 \text{ cm}^{-1}$. In Figure 4.2 I illustrate the effect on the phase plots for four different resolutions. The top panels are for a fixed amount of azimuthal divisions, but different amount of rings. The bottom panels are for a different amount of azimuthal divisions, but fixed amount of rings. If more rings are added there is more emission that accumulates to form the caustics, thus they appear brighter. This is also the case when adding more azimuthal bins, although the effect is not as prominent as in the former case. We set the resolution to 360 azimuthal bins and 7 rings for the results in the Chapter 5, since the shape as well as the emission quality are reasonable for these choices.

4.3 Running the code on a cluster

The emission code described in Section 4.1 is available in both a serial and parallelised version, with a major difference in the structure of each code. The parallelised code (hereafter referred to as the parallel code) consists of several parts to ensure it is computationally effective. Thus, the radiation by particles injected on different field lines were computed in a distributed and independent fashion, and only later is the emission from all particles accumulated in a phase plot.

We calibrated the serial and parallel codes to minimise differences in the separate codes and to ensure that new implementations were not missed. We made some alterations to the parallel code in order to generate simulations on our local cluster, i.e., at the NWU, Potchefstroom. These modifications include

- The compiler needed for the code is mpiicpc, however the local cluster uses the intel/ mpi compiler. Thus, the code was slightly adapted, but the outputs were carefully calibrated against the original code.

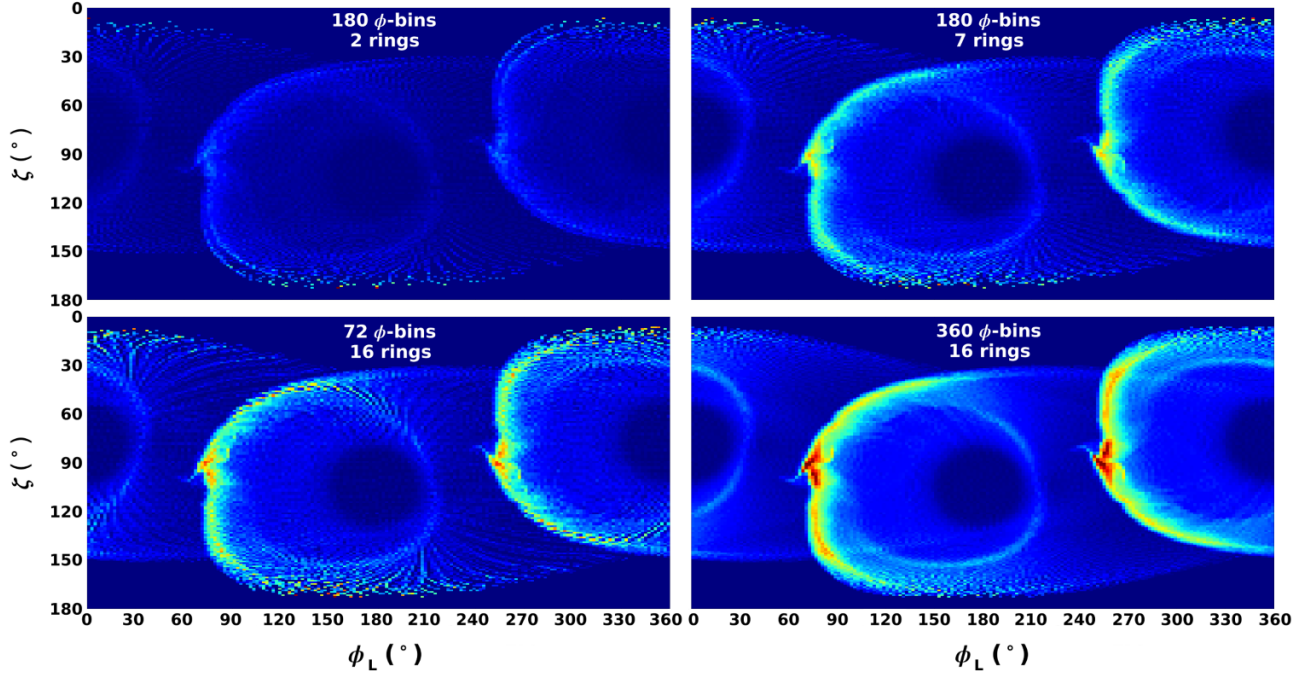


Figure 4.2: An example of the phase plots for the Vela pulsar assuming $\alpha = 75^\circ$ and $\zeta_{\text{cut}} = 65^\circ$. Each phase plot is for a different resolution, i.e., number of azimuthal divisions and number of rings. Top panels are for same amount azimuthal divisions, but increasing number of rings. Bottom panels are for different azimuthal divisions but same amount of rings.

- The original job script uses a Portable Batch System scheduler, i.e., computer software that performs job scheduling with the primary responsibility to allocate computational tasks on a high-performance computer. However, the local cluster uses a different job scheduler namely the Sun Grid Engine. The main difference between the two schedulers is the operation of each.
- We encountered memory issues caused by large dimensional arrays. We reduced the memory consumption significantly and this will be discussed below.

The parallel code uses the mpiicpc compiler on the Discover¹ cluster. The serial code is split up in parts and then parallelised. The *.sh files are needed to submit and run the job on the system. The script and code need to be tailored to each system. However, several of the parameters like $r_{\text{ovc}}^{\text{min}}$, $r_{\text{ovc}}^{\text{max}}$, the number of azimuthal divisions, and the number of rings are set in this file and override what is set in the main code. The code apportion subcalculations to the number of processors one specifies when you submit the job.

The parallelisation of the code involved splitting the serial code into different parts and then using a Makefile to compile and create the executable file. All these different parts of code, each serving a specific purpose, are called in the main code. The local cluster has two different directories. The *home* directory handles smaller files such as the source code and sample job script, whereas the *scratch* directory handles large amounts of data.

In the parallel code the emission of an electron is calculated and then distributed to all frequency bins, requiring write access to all frequency bins. Since it is binning emission in E_γ , ϕ_L , and ζ bins, huge ‘sky cubes’ are produced from which the light curves and spectra are constructed. We take the pair spectrum as an input (calculated by another code) and then focus on the emission properties. In principle this should allow us to parallelise the code more easily, since we can distribute the individual B -field lines (spatial parts of the grid, i.e., stellar surface). Basically, the emission code distributes B -field lines among cores. Particles are transported along B -field lines and radiate emission that is then binned in a “master matrix” (therefore the need of global

¹<https://www.nccs.nasa.gov/>

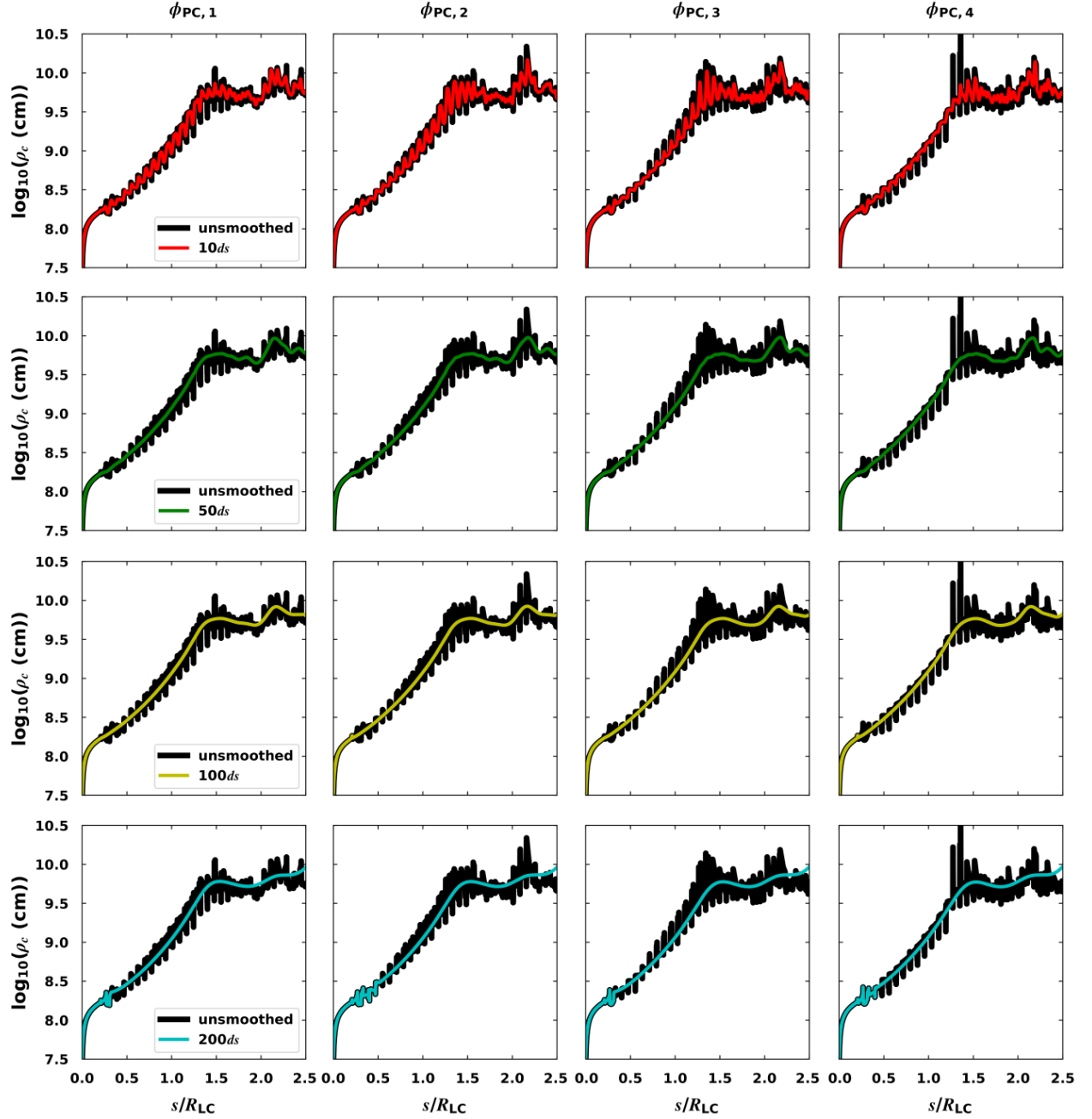


Figure 4.3: An example of the newly calculated ρ_c as a function of normalised arclength s/R_{LC} before (solid black line) and after (coloured lines) smoothing and matching. Each column represents an arbitrary B -field line, and each row corresponds to different smoothing parameters, i.e., $h = [10ds, 50ds, 100ds, 200ds]$, increasing from top to bottom as indicated in the legend.

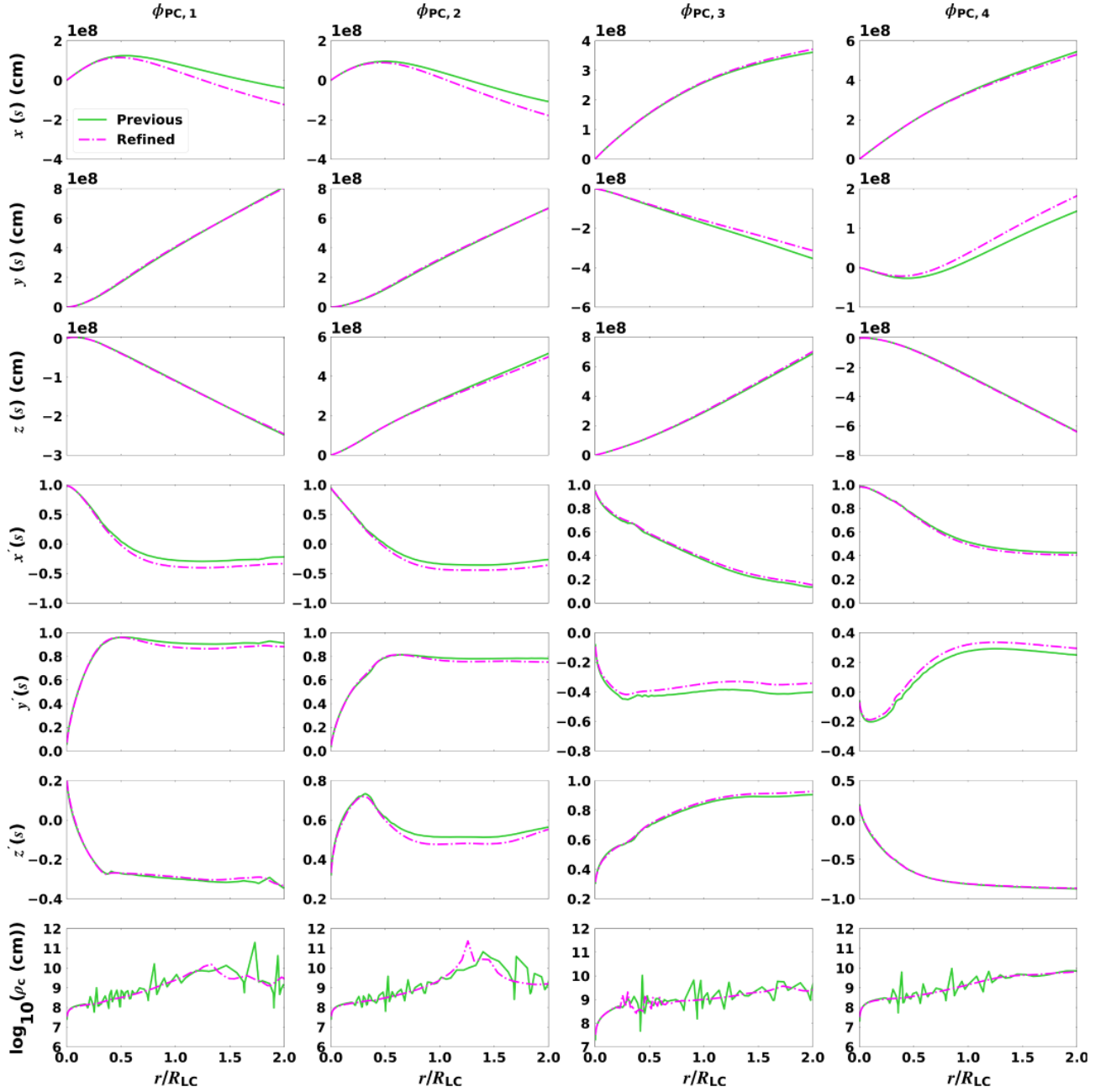


Figure 4.4: A comparison of electron position $x(s)$, $y(s)$, $z(s)$, trajectory direction $x'(s)$, $y'(s)$, $z'(s)$ and $\log_{10}(\rho_c)$, as calculated previously (lime green) and now being refined (magenta), for $\alpha = 75^\circ$, along four arbitrary B -field lines (i.e., field line footpoints with $\phi_{PC,1} = 45^\circ$, $\phi_{PC,2} = 135^\circ$, $\phi_{PC,3} = 225^\circ$ and $\phi_{PC,4} = 315^\circ$) on the outer ring of the PC.

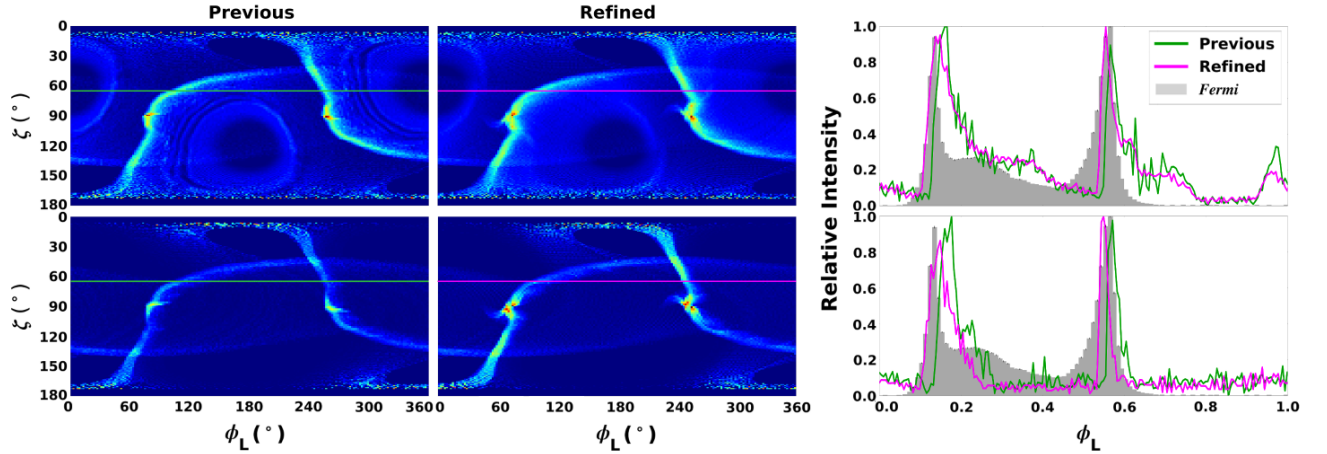


Figure 4.5: Phase plots and pulse profiles for $\alpha = 60^\circ$, $\zeta_{\text{cut}} = 65^\circ$, and $0.1 < E_\gamma < 50.0$ GeV. This figure serves as a comparison between phase plots for the previous (left column) and refined (centre column) ρ_c calculation, and their associated light curves (right column). The top row is for a constant E_\parallel (scenario 1), and the bottom row is for a two-step E_\parallel (scenario 2). We shifted the resulting γ -ray model light curves by -0.14 in normalised phase to fit the *Fermi* LAT (Abdo et al. 2010d, 2013, http://fermi.gsfc.nasa.gov/ssc/data/access/lat/2nd_PSR_catalog/) data points.

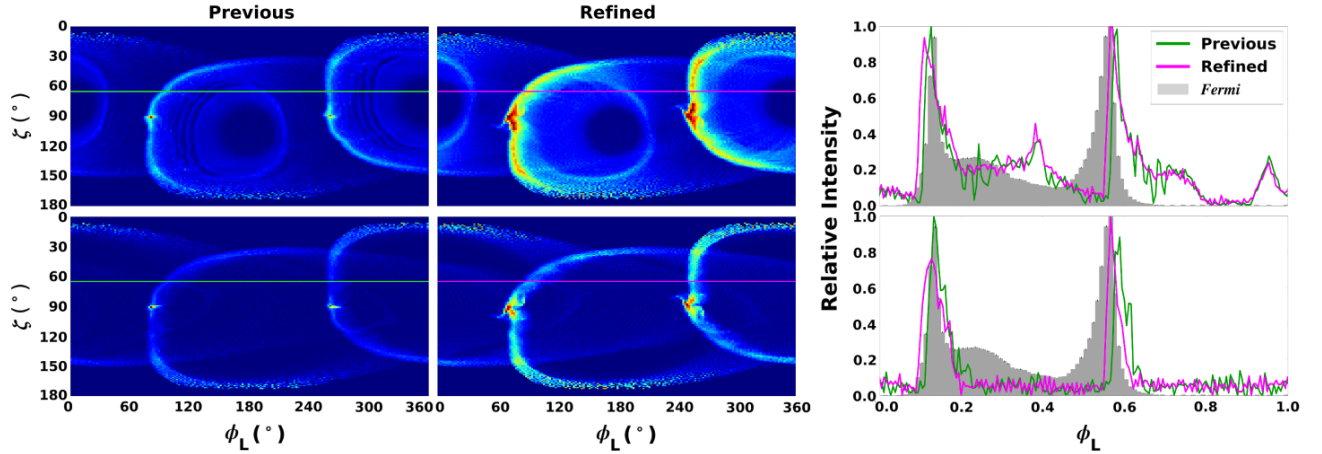
memory structures). We have to investigate if this can potentially cause problems. For the serial code, the ‘sky cubes’ are filled by running field lines sequentially. On the cluster, we of course assume that lines are independent and emission from them can be superposed.

The parallel code calculates the same broadband spectrum expected from a pulsar as the serial code. However, with the parallel code we experienced memory issues caused by seven-dimensional arrays. We reduced the memory consumption significantly by allocating the memory dynamically, however it did not fully address our problems. The dynamic allocation did speed up the code on the other hand, because the compiler did not optimise the code with the static allocation as done initially. We also encountered errors that explicitly state “ran out of memory” as well. We solved this by distributing a number of threads over additional nodes, to get access to more memory.

Since we were limited on time and the modifications needed for the parallel code would be time consuming we opted to use the serial code. This is acceptable since we only attempted to isolate the first to second peak (P1/P2) effect seen in the observations assuming that particles emit CR (see Chapter 5 for details). However, when additional radiation mechanisms are considered such as in Harding & Kalapotharakos (2015) and Harding et al. (2018) the parallel code is necessary since it saves computational time, and solves more complicated problems.

4.4 Recalculating the curvature radius ρ_c

We refine the previous first-order calculation of ρ_c along the electron (or positron) trajectory, assuming that all particles injected at the footpoint of a particular B -field line follow the same trajectory, independent of their energy, since these are quickly accelerated to relativistic energies by the unscreened E -field. This independence of ρ_c on energy also reduces computational time significantly, since the calculation is done beforehand. We furthermore assume that the B -field is strong enough to constrain the movement of the electrons so they will move parallel to the field line in the co-rotating frame. Thus, there will be no perpendicular motion in the co-rotating frame, since the perpendicular particle energy is nearly instantly expended via SR. We thus take into account the perpendicular $\mathbf{E} \times \mathbf{B}$ drift in the lab frame.

Figure 4.6: Same as Figure 4.5, but for $\alpha = 75^\circ$.

To calculate the electron's trajectory as well as its associated ρ_c in the lab frame, we used a small, fixed step size ds (where s is the arclength) along the B -field line. The first derivative along the trajectory (i.e., direction) is equivalent to the normalised B -field components as a function of s . Next, we smooth the directions using s as the independent variable, to counteract numerical noise. Second, we match the unsmoothed and smoothed directions of the electron trajectory at particular s values to get rid of unwanted “tails” at low and high altitudes, introduced by the use of a Gaussian kernel density estimator (KDE) smoothing procedure. Third, we use a second-order method involving interpolation by a Lagrange polynomial to obtain the second-order derivatives of the positions along the trajectory as a function of s (Faires & Burden, 2002). This accuracy is necessary since ρ_c is a function of second-order derivatives of the electron position, and instabilities may be exacerbated if not dealt with carefully. Lastly, we match ρ_c calculated using smoothed and unsmoothed directions to get rid of “tails” in ρ_c at low and high altitudes, as before.

In Figure 4.3 we illustrate ρ_c (measured in cm) as a function of s/R_{LC} , to show the impact of the smoothing parameter h on the ρ_c calculation. This is shown for four arbitrary B -field lines with footpoints along the outer ring (rim) on the PC, as indicated by different values of the PC azimuthal coordinate ϕ_{PC} . For too small an h value, e.g., $10ds$, there is not a significant amount of smoothing and therefore the ρ_c vs. s curve is undersmoothed, and still noisy. As we increase h , the ρ_c becomes smoother, however for $h = 100ds$ there are some small instabilities introduced at $s/R_{LC} < 0.5$. This is due to the tolerance we chose when matching the unsmoothed and smoothed ρ_c 's to get rid of the “tails”.

Having a pre-calculated ρ_c in hand, for a fine division in s along any particular B -field line, I then interpolate ρ_c in my particle transport calculations to accommodate an adaptive, variable- ds approach that is used to speed up the transport calculations, without losing accuracy of the trajectory. In Figure 4.4 the parameters describing the particle trajectory are compared for the previous and the newly calculated ρ_c . These include the particle positions $x(s)$, $y(s)$, $z(s)$ in cm, dimensionless directions or spatial derivatives $x'(s)$, $y'(s)$, $z'(s)$, and \log_{10} of ρ_c . This comparison is shown for four arbitrary B -field lines with footpoints along the outer ring (rim) on the PC, as indicated by different values of ϕ_{PC} . The changes in position and direction are rather minor. However, the improved calculation smooths out some instabilities in $\rho_c(s)$. See Appendix A for a more detailed discussion and calculations.

We present phase plots and light curves for $\alpha = 60^\circ$ and $\alpha = 75^\circ$ in Figure 4.5 and 4.6, assuming $\zeta_{cut} = 65^\circ$, $r_{ovc} = [0.90, 0.96]$. We illustrate the effect of the previous and refined ρ_c calculation on the predicted phase plots and light curves. In Figure 4.5 and 4.6 the phase plots and light curves associated with the previous and refined ρ_c are compared for a constant $E_{||}$ -field and a two-step constant $E_{||}$ -field (hereafter scenario 1 and scenario 2, respectively), for two different values of α . The photon energy E_γ extends over a wide GeV range from 100 MeV to 50 GeV. For scenario 2, I chose a constant $E_{||}$ inside the light cylinder ($R_{acc,low}$; the

acceleration per unit length) and a constant E_{\parallel} outside the light cylinder and into the current sheet ($R_{\text{acc,high}}$). For scenario 1 (top panels) there appears inter-peak bridge emission at lower energies near the PCs (dark circles). This is not the case for scenario 2 (bottom panels), since $R_{\text{acc,low}}$ is too low at altitudes inside R_{LC} , resulting in suppression of the emission as well as lowering the first peak's intensity. The caustics on the phase plots for the refined ρ_c calculation, regardless of our choice of α , appear smoother and brighter than for the previous ρ_c calculation, although their shape is largely maintained between the two calculations. A small, additional feature becomes visible near the emission caustic (indicated by a red colour) when using the refined calculation. The caustics are also generally wider, and appear fuller (more filled out with radiation). The caustic shape furthermore depends strongly on the choice of α . For $\alpha = 60^\circ$ the caustic is more spread out in an S-curve shape, whereas for $\alpha = 75^\circ$ it is rounded and concentrated around the PCs. The respective light curves for the two calculations are very similar, although they tend to be smoother for the refined calculation. The model light curves appear later in phase than the data and therefore we shifted the model with -0.14 in phase to fit the *Fermi* data. In Figure 4.5 and 4.6 I chose a the same resolution than what will be used in Chapter 5. If I compare these to Figure 4.2 I notice that our resolution choice is fairly good.

4.5 Conclusion

The full emission code is a complex code that required us to first do a calibration to understand the output. This calibration included choosing and comparing compilers used between the different systems. Another important factor was the resolution of the simulations, since higher resolution resulted in better quality light curves and spectra. Particles that are accelerated tangentially along the curved B -field emit CR. The curvature of the field lines is characterised by ρ_c . Thus, I refined the ρ_c to improve the transport calculation. The need for this will be discussed in Chapter 5 and 6.

The serial emission code does run for solving simple problems involving single radiation mechanisms. However, for more complex problems, e.g., simulating emission from primaries and pairs for additional radiation mechanisms, the serial code needs to be parallelised. Due to the complex nature of this code and for it to work on our local cluster, future updates will be necessary. There are multiple helpful tools available that will enable us to eliminate problems, e.g., *Valgrind* and *blitz++* that we will investigate in future.

In Chapter 5, we will present the results that we obtained using the serial version of the code described in Section 4.1. We will investigate the observed light curve trends via energy-dependent light curves and spectra in the CR regime. I will demonstrate that most of the trends seen in the energy-dependent light curves can be reproduced using our code, in a CR framework.

Chapter 5

Probing the γ -ray pulsar emission mechanism via energy-dependent light curve modelling

In this Chapter, I will be focusing on emission from the Vela pulsar in the GeV band. I use a steady-state emission model (see Section 4.1) to predict E_γ -dependent light curves and spectra that result from primary particles emitting CR; this model includes my refined calculation of ρ_c of the particle trajectory (see Section 4.4). In Section 5.2, I will discuss a “reverse mapping” method used to isolate the spatial origin of the light curve peaks, and in Section 5.3.1 I performed a small parameter study to find optimal values for the model’s free parameters. In Section 5.3, I present sample light curves and spectra, showing the behaviour of the peaks as a function of ρ_c , as applied to the Vela pulsar. For the optimal light curve and spectral fits, I study the local environment of the peaks’ emission regions, finding a systematic difference in ρ_c , γ , and $E_{\gamma,CR}$ for the two peaks. Concluding remarks follow in Section 5.4. This Chapter is a summary of an article in preparation (Barnard et al., in press) the results of which accompany those of Harding et al. (2018).

5.1 Introduction

The field of pulsar science has been revolutionised by the detection of pulsed emission by ground-based telescopes. In the VHE band, MAGIC detected pulsations from the Crab pulsar at energies up to 1 TeV (Ansoldi et al., 2016), and H.E.S.S. II detected pulsed emission from the Vela pulsar in the sub-20 GeV to 100 GeV range (Abdalla et al., 2018). New observations by H.E.S.S. reveal pulsed emission from Vela at a few TeV (H.E.S.S. Collaboration, in preparation). H.E.S.S. II furthermore detected pulsed emission from PSR B1706–44 in the sub-100 GeV energy range (Spir-Jacob et al., 2019). Pulsed emission from the Geminga pulsar between 15 GeV and 75 GeV at a significance of 6.3σ was recently detected by MAGIC, although only the second light curve peak is visible at these energies. The MAGIC spectrum is an extension of the *Fermi* LAT spectrum, ruling out the possibility of a sub-exponential cut-off in the same energy range at the 3.6σ level (Acciari et al., 2020).

Interestingly, as the photon energy E_γ is increased (above several GeV), the main light curve peaks of Crab, Vela and Geminga seem to remain at the same phase positions, the intensity ratio of the first to second peak (P1/P2) decreases for Vela and Geminga, the inter-peak “bridge” emission evolves for Vela, and the peak widths decrease for Crab (Aliu et al., 2011), Vela (Abdo et al., 2010d) and Geminga (Abdo et al., 2010b). The P1/P2 vs. E_γ effect was also seen by *Fermi* for a number of pulsars (Abdo et al., 2010c, 2013). In general, multi-wavelength pulsar light curves exhibit an intricate structure that evolves with E_γ (e.g., Bühler & Blandford, 2014), reflecting the various underlying emitting particle populations and spectral radiation components that contribute to this emission, as well as the local B -field geometry and E -field spatial distribution.

Some traditional physical emission models invoke CR from extended regions within the magnetosphere to explain the HE spectra and light curves. These include the SG (Arons, 1983; Harding & Muslimov, 2003) and

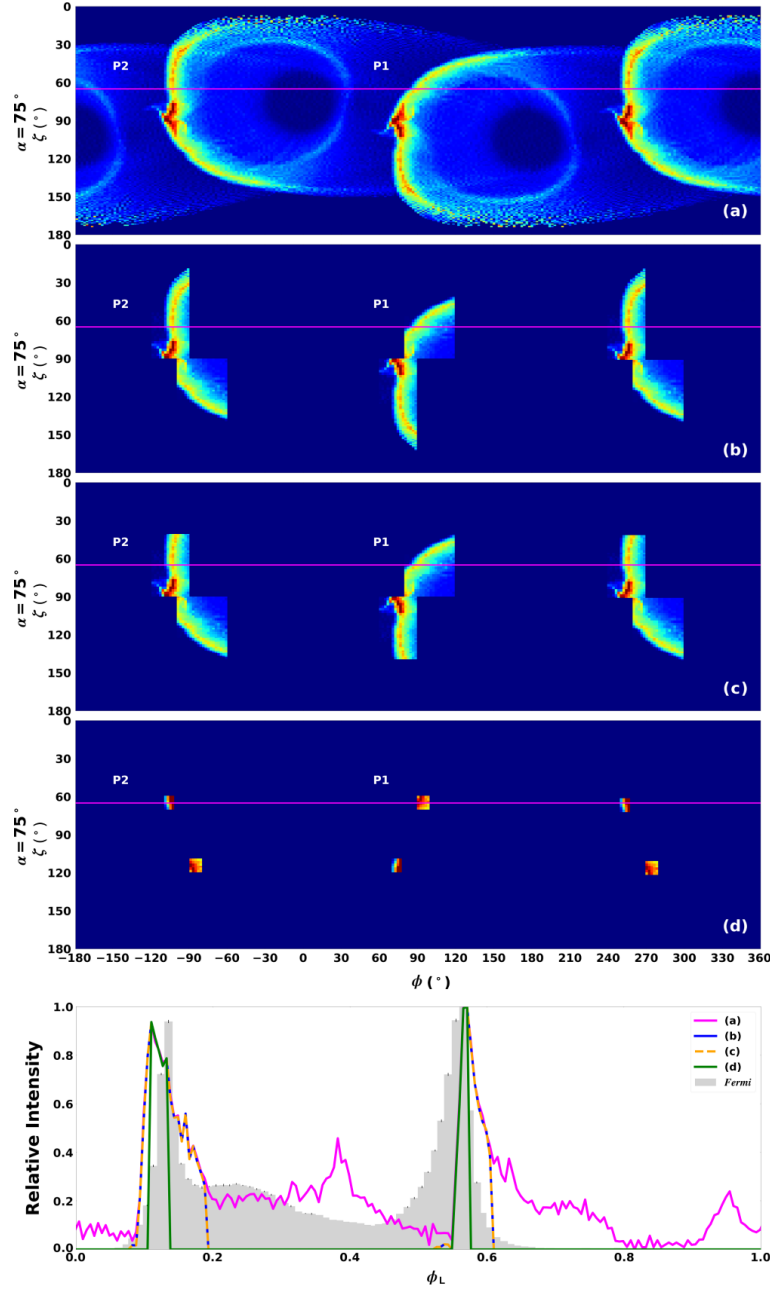


Figure 5.1: Example phase plots with (ϕ_L, ζ) -“blocks”(or 2D bins) and their associated light curves for $\alpha = 75^\circ$, $\zeta_{\text{cut}} = 65^\circ$, $R_{\text{acc}} = 0.25 \text{ cm}^{-1}$, and $0.1 < E_\gamma < 50 \text{ GeV}$. In order to indicate how we isolated the first and second light curve peaks (labelled ‘P1’ and ‘P2’), we made cuts in (ϕ_L, ζ) as follows: (a) no cut, (b) $\phi_{L,P1} = [-100^\circ, -60^\circ]$ and $\phi_{L,P2} = [-120^\circ, -90^\circ]$ for all ζ , (c) $\zeta_{P1} = [90^\circ, 160^\circ]$ and $\zeta_{P2} = [40^\circ, 90^\circ]$ for same ϕ_L as in (b), and (d) $\phi_{L,P1} = [-90^\circ, -81^\circ]$, $\zeta_{P1} = [110^\circ, 120^\circ]$, $\phi_{L,P2} = [-109^\circ, -103^\circ]$, and $\zeta_{P2} = [60^\circ, 70^\circ]$. The light curve legend in the lower panel refers to each associated phase plot, for increasingly smaller (ϕ_L, ζ) bins. The *Fermi* data for Vela are indicated by a grey histogram (Abdo et al. 2013, http://fermi.gsfc.nasa.gov/ssc/data/access/lat/2nd_PSR_catalog/). We shifted the resulting γ -ray model light curves by -0.14 in normalised phase to fit the data. This reflects the degeneracy of $\phi_L=0$ in the data (reflecting the main radio peak) and $\phi_L=0$ (the phase of the μ -axis).

OG (Romani & Yadigaroglu, 1995; Cheng et al., 1986) models. However, they fall short of fully addressing global magnetospheric characteristics, e.g., the particle acceleration and pair production, current closure, and radiation of a complex multi-wavelength spectrum.

Geometric light curve modelling (Dyks et al., 2004a; Venter et al., 2009; Watters et al., 2009; Johnson et al., 2014; Pierbattista et al., 2015) presented an important interim avenue for probing the pulsar magnetosphere in the context of traditional pulsar models, focusing on the spatial rather than physical origin of HE photons. More recent developments include global magnetospheric models such as the FIDO model (Brambilla et al., 2015; Kalapotharakos & Contopoulos, 2009; Kalapotharakos et al., 2014), equatorial current sheet models (e.g., Bai & Spitkovsky 2010a; Pétri 2012), the striped-wind models (e.g., Pétri & Dubus 2011), and PIC (Brambilla et al., 2018; Cerutti et al., 2016a,b, 2020; Kalapotharakos et al., 2018; Philippov & Spitkovsky, 2018). Some studies using the FIDO models assume that particles are accelerated by induced E -fields in dissipative magnetospheres and produces GeV emission via CR (e.g., Kalapotharakos et al. 2014). Conversely, in some of the wind or current-sheet models, HE emission originates beyond the light cylinder via synchrotron radiation (SR) by relativistic, hot particles that have been accelerated via magnetic reconnection inside the current sheet (e.g., Pétri & Dubus, 2011; Philippov & Spitkovsky, 2018). Given the ongoing debate between the emission mechanisms of HE emission, our motivation in this study is to explain the GeV spectrum and light curves of Vela as measured by *Fermi* and H.E.S.S. Specifically, by modelling the E_γ -dependent light curves (and P1/P2 signature) in the CR regime of SC radiation, we hope to probe whether this effect can serve as a potential discriminator between emission mechanisms and models (see also the reviews of Harding 2016; Venter 2016; Venter et al. 2017 on using pulsar light curves to scrutinise magnetospheric structure and emission distribution).

5.2 Isolating the origin of emission for each of the light curve peaks

Using the model described in Section 4.1, and for a given magnetic inclination angle $\alpha = 75^\circ$, we generated phase plots (observer angle ζ vs. rotation phase ϕ_L ; Figure 5.1). We inject the primaries into a roughly annular slot gap situated between $r_{\text{ovc}} = 0.90$ and $r_{\text{ovc}} = 0.96$ (Dyks et al., 2004a; Harding et al., 2018), and divide the surface projection of the slot gap situated near the rim of the PC into 7 rings, with each ring having 360 azimuthal segments. We additionally set $ds = 10^{-3}R_{\text{LC}}$ with a corresponding $h = 50ds$. The phase plots are emitted photon fluxes \dot{N}_γ that have been normalised using the primary particle flux (the appropriate Goldreich-Julian injection rate at the stellar surface); \dot{N}_γ is collected in bins of ζ and ϕ_L . The photon directions have been corrected for the Special Relativistic effects of rotation and time-of-flight delays. Lastly, \dot{N}_γ per bin is divided by the solid angle subtended by each phase plot bin, i.e., $\delta\Omega = (\cos\zeta - \cos(\zeta + \delta\zeta))\delta\phi_L \approx \sin\zeta\delta\zeta\delta\phi_L$. To generate light curves, a constant- ζ cut (ζ_{cut}) is made through the respective phase plot (see lower panel of Figure 5.1).

As mentioned in Section 5.1, the relative fading of peak 1 vs. peak 2 with E_γ seems to be a common characteristic of HE light curves. We have also been able to reproduce this with the code. In order to probe the origin of this effect, it is necessary to isolate the spatial origin of each light curve peak. We start by isolating each peak on the phase plot (using increasingly smaller (ζ, ϕ_L) bins) and then apply “reverse mapping” to uncover the emission’s spatial position. This can be compared to developing a “reverse dictionary” that translate a chosen (ϕ_L, ζ) range into a spatial range within the magnetosphere. In our code, we calculate only the emission from the northern rotational hemisphere. The contribution of the emission from the southern hemisphere is obtained taking into account the symmetry with respect to the centre of the star (i.e., $\dot{S}_\gamma/d\Omega(\phi_L, \zeta) = \dot{N}_\gamma/d\Omega(\phi_L + 180^\circ, 180^\circ - \zeta)$), where \dot{S}_γ and \dot{N}_γ indicate the contribution of the southern and northern rotational hemispheres, respectively. This symmetry exploitation saved computational time, and the corresponding full sky map is shown in the first panel of Figure 5.1. The implication is that one has to carefully keep track of the (ϕ_L, ζ) coordinates of each peak, and map them back onto the northern-hemisphere caustic (e.g., mapping P1 onto the northern-hemisphere caustic where $\zeta > 90^\circ$). Using the latter, one can perform the reverse mapping to find the

spatial coordinates of this emission.

This reverse mapping procedure is illustrated in Figure 5.1 for a constant acceleration “rate” (acceleration per unit length) $R_{\text{acc}} = eE_{\parallel}/m_e c^2 \text{ cm}^{-1}$, with e the electron charge, m_e the electron mass, and $m_e c^2$ the rest-mass energy. The first panel is for the full phase space, whereas panels (b), (c), and (d) are for different (ϕ_L, ζ) -“blocks” or bins. In panel (b), we make a cut in ϕ_L for both peaks but keep ζ fixed and see that only the peaks remain on the corresponding light curve (see bottom panel). If we then narrow the range in ζ for a fixed ϕ_L interval (same as in (b)), we note that the light curve remains the same. Lastly, we make ϕ_L and ζ small enough so that only the maximum of each peak is included in the (ϕ_L, ζ) range, as seen in panel (d). These ranges in ϕ_L and ζ are referred to as the “optimal bins” for both peaks and are necessary for constructing the phase-resolved spectra of each peak. We chose the ζ -range for each peak with width of $\pm 5^\circ$ around $\zeta_{\text{cut}} = 65^\circ$, to include the ζ inferred from the pulsar wind nebula torus fit of Vela (Ng & Romani, 2008).

5.3 Results

5.3.1 Finding optimal fitting parameters

After having isolated the spatial origin of the emission of each light curve peak as described in the previous section, we first perform joint light curve and spectral fitting to find optimal model parameters; subsequently, we will consider the local environments where the respective light curve peaks originate (Section 5.3), given these optimal parameters. We consider two cases throughout this paper, based on either a constant or a two-step parametric accelerating E_{\parallel} -field, independent of the ϕ_{PC} , ζ and r . Thus, we choose (and subsequently refer to this as scenario 1 and scenario 2): (1) a constant R_{acc} from the stellar surface and into the current sheet (see Harding & Kalapotharakos 2015), and (2) a two-valued R_{acc} , where $R_{\text{acc,low}}$ occurs inside, and $R_{\text{acc,high}}$ outside the light cylinder (see Harding et al. 2018). The two-step function for the accelerating E_{\parallel} is motivated by global dissipative models (Kalapotharakos et al., 2014, 2017; Brambilla et al., 2015) and kinetic PIC models (Cerutti et al., 2016b; Kalapotharakos et al., 2018), that indicate that the particle acceleration takes place primarily near the current sheet, outside the light cylinder.

I performed a preliminary parameter study to search for an optimal combination of α , ζ_{cut} , and R_{acc} (for both scenarios, respectively), calibrated against *both* the observed HE light curves *and* spectra measured by *Fermi* and H.E.S.S. II. We start by fixing ζ_{cut} and testing different values of R_{acc} ; later, we fix R_{acc} and free ζ_{cut} ¹.

Figure 5.2 shows the E_{γ} -dependent light curves for scenario 1 (left column) and scenario 2 (right column). For scenario 1, we choose four arbitrary constant R_{acc} values, and for scenario 2, seven arbitrary $R_{\text{acc,low}}$ and $R_{\text{acc,high}}$ combinations, as indicated in the legends. We also indicate different energy ranges (with the minimum E_{γ} increasing from top to bottom), with the first panel showing light curves for a full HE range $E_{\gamma} \in (100 \text{ MeV}, 50 \text{ GeV})$. The E_{γ} ranges correspond to those of the *Fermi* light curves in Figure 2 in Abdo et al. (2010d), and Abdo et al. (2013), as well as $E_{\gamma} > 20 \text{ GeV}$ to match the H.E.S.S. II data (Abdalla et al., 2018). The light curves for scenario 1 display bridge emission at $\phi_L \geq 0.25$ that diminishes as E_{γ} increases. For scenario 2, bridge emission develops when $R_{\text{acc,low}} \geq 0.10 \text{ cm}^{-1}$ and $R_{\text{acc,high}} = 0.25 \text{ cm}^{-1}$. For $R_{\text{acc,low}} = 0.3 \text{ cm}^{-1}$ and $R_{\text{acc,high}} = 0.25 \text{ cm}^{-1}$ the light curve almost mimics our fit in scenario 1 for $R_{\text{acc}} = 0.25 \text{ cm}^{-1}$ (since these respective values are so close). If both $R_{\text{acc,low}}$ and $R_{\text{acc,high}}$ are small, we obtain light curve shapes that are contrary to what is expected (probably because the particles do not reach radiation reaction limit), e.g., choosing $R_{\text{acc,low}} = 0.04 \text{ cm}^{-1}$ and $R_{\text{acc,high}} = 0.1 \text{ cm}^{-1}$, yields an increase of P1/P2 for at $E_{\gamma} > 8.0 \text{ GeV}$, contrary to what is observed. For combinations where $R_{\text{acc,low}}$ is small and $R_{\text{acc,high}} \geq 1.0 \text{ cm}^{-1}$, we see that P1 remains relatively high for $E_{\gamma} > 8.0 \text{ GeV}$, instead of following the observed trend. The optimal choice in terms of reproducing

¹Given how computationally expensive this exercise is, we only considered a few values of the free parameters. In future, a more robust method may be considered where parameter space of several free parameters may be searched for optimal joint light curve and spectral fits. Given the disparate nature of these data, and the complexity of such a joint fit, here we perform a pilot study to indicate the effect of the different parameters, and to find a reasonable joint fit by eye.

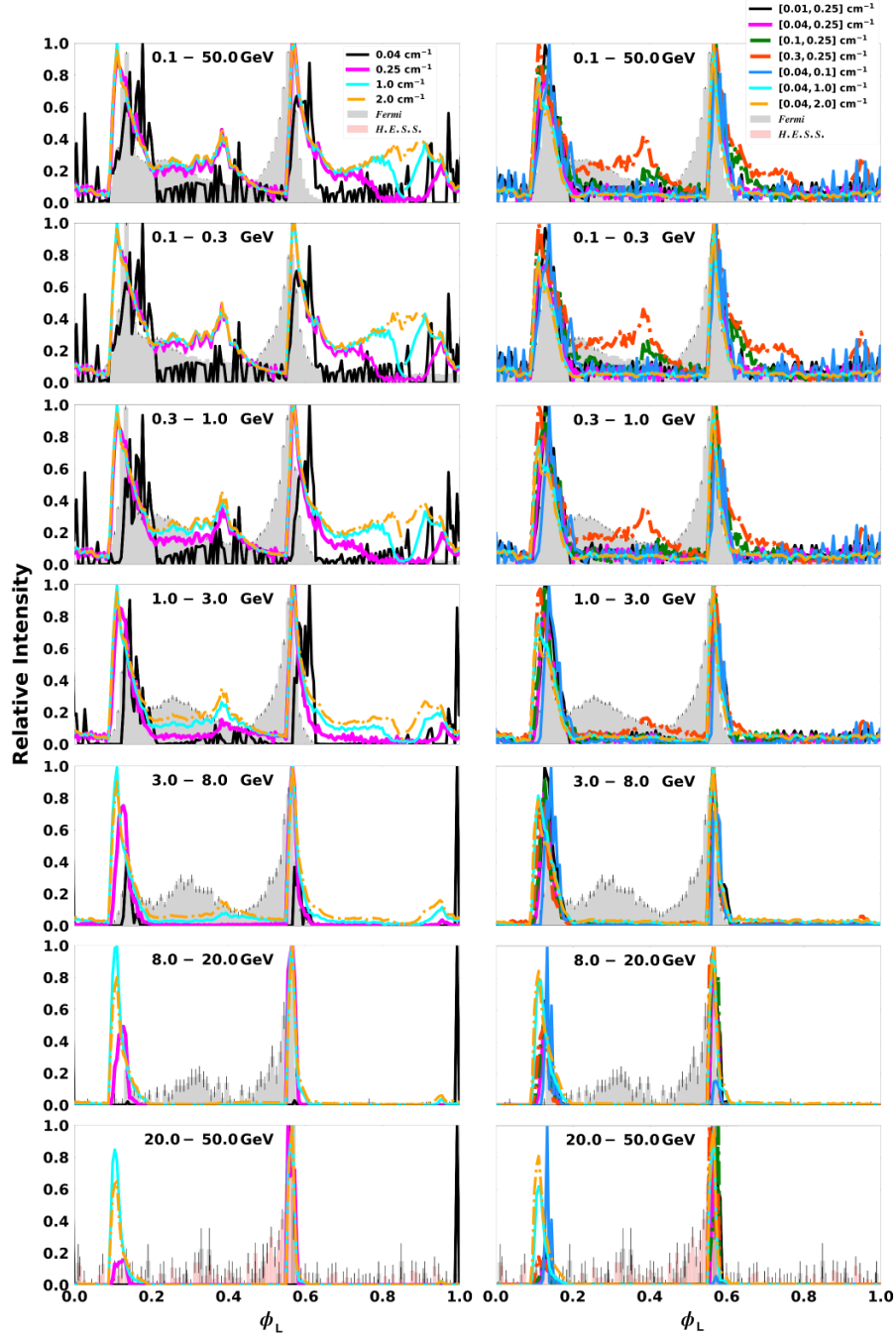


Figure 5.2: Energy-dependent light curves for $\alpha = 75^\circ$ and $\zeta_{\text{cut}} = 65^\circ$ for several different combinations of R_{acc} for both the constant E_{\parallel} (left column) and two-valued E_{\parallel} (right column) case. The top panels are for the full E_{γ} -range, and for each panel thereafter, the minimum E_{γ} is increased as indicated. We are fitting the model light curves to the *Fermi* (Abdo et al. 2010d, 2013, http://fermi.gsfc.nasa.gov/ssc/data/access/lat/2nd_PSR_catalog/), and H.E.S.S. (at $E_{\gamma} > 20$ GeV; Abdalla et al. 2018) data points. We shifted the predicted light curves by $\delta = 0.14$ in normalised phase. One observes that for some choices of E_{\parallel} , the P1/P2 decrease with E_{γ} is more apparent than for others.

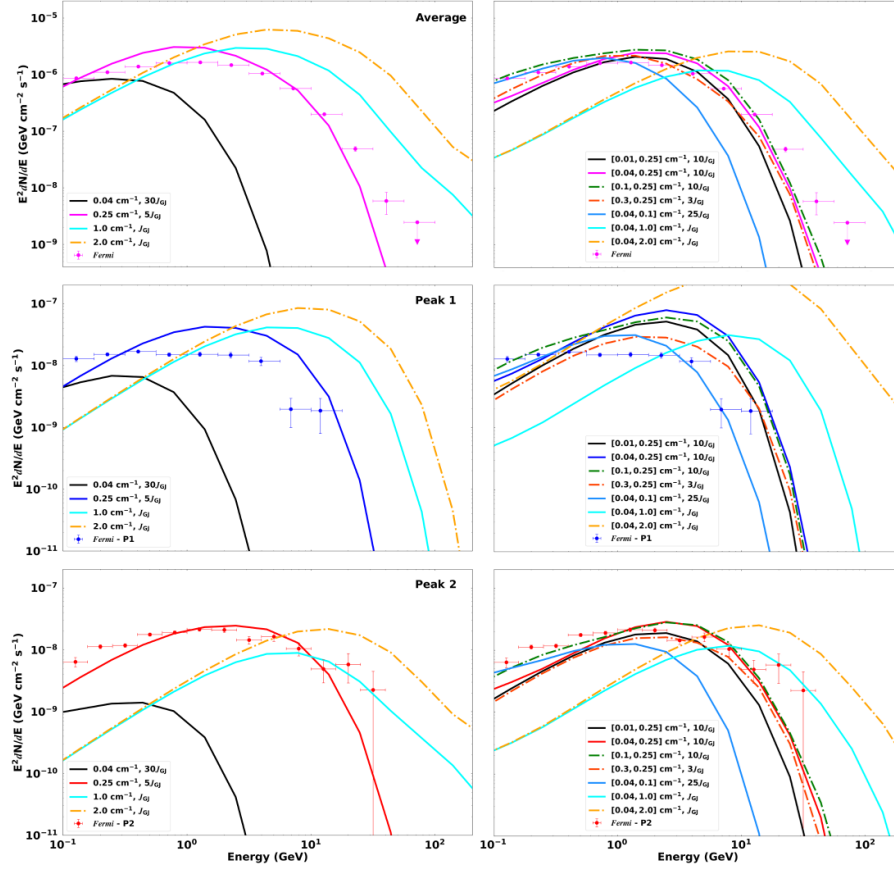


Figure 5.3: Model phase-averaged and phase-resolved spectra associated with Figure 5.2 for the same for α , ζ_{cut} and R_{acc} -field combinations, for both scenario 1 (left column) and scenario 2 (right column). In each E_{\parallel} case the legend indicate the chosen values for R_{acc} , $R_{\text{acc,low}}$, $R_{\text{acc,high}}$, and the flux normalisation factor. The data points for the phase-average spectra are from Abdo et al. (2013) (see http://fermi.gsfc.nasa.gov/ssc/data/access/lat/2nd_PSR_catalog/), and the phase-resolved spectra are updated data to those published in Abdo et al. (2010d)

the P1/P2 effect seems to be $(R_{\text{acc,low}}, R_{\text{acc,high}}) = (0.04, 0.25) \text{ cm}^{-1}$, although the bridge emission is somewhat underpredicted.

In both scenarios, four main trends are evident in our optimal fits to the light curves as they evolve with E_{γ} . First, the model peaks remain at the same phase, i.e., P1 at $\phi_L = [0.10, 0.18]$ and P2 at $\phi_L = [0.57, 0.60]$, after we shifted the model in phase to fit the data. Second, the intensity ratio of P1 relative to P2 decreases as E_{γ} increases in some cases, where the peaks are nearly equal in height at lower E_{γ} . Third, the bridge emission fades at higher energies, possibly reflecting its softer spectrum and its origin at lower altitudes, where acceleration is suppressed as compared to the current sheet environment. Lastly, the pulse width decreases with an increase in E_{γ} . It is encouraging that the model can broadly reproduce these observational trends. We also note that a two-step E_{\parallel} -field provides more reasonable light curve shapes, especially at lower photon energies.

The observed phase-averaged CR spectra are characterised by a power law with an (sub)exponential cutoff. In our model, this spectrum is calculated as the observed \dot{N}_{γ} at a particular viewing angle ζ_{cut} , summing the fluxes (originating in different parts of the magnetosphere) over ϕ_L and dividing by $2\pi d^2$, where d (in cm) is the distance to the source. To calculate the phase-resolved spectra associated with each peak, we limit the ϕ_L -range to include the specific fraction of the emission we want to study. We scaled the phase-resolved flux with the ratio of the difference in each peak's ϕ_L -range of the *Fermi* data to the model range. Figure 5.3 shows the

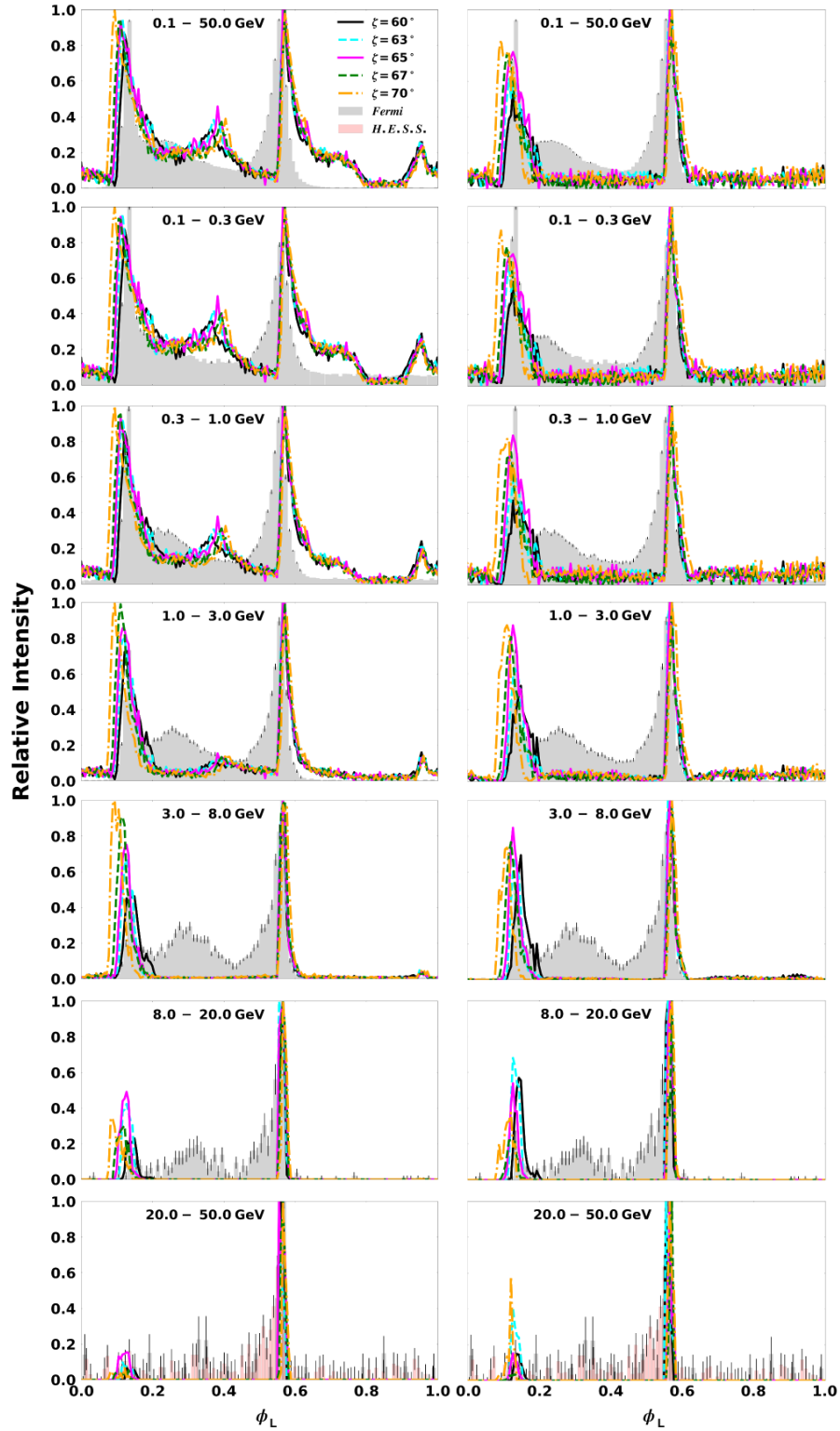


Figure 5.4: Energy-dependent light curves for $\alpha = 75^\circ$ and different ζ_{cut} for the optimal values of E_{\parallel} -field for both scenario 1 (left) and scenario 2 (right). In each R_{acc} case, the legend indicates the chosen values for ζ_{cut} . The first row are for the full E_{γ} -range, and each panel thereafter is for an increase in the minimum E_{γ} . We are fitting the model light curves to the *Fermi* (Abdo et al. 2010d, 2013, http://fermi.gsfc.nasa.gov/ssc/data/access/lat/2nd_PSR_catalog/) and to the H.E.S.S. (at $E_{\gamma} > 20$ GeV; Abdalla et al. 2018) data points, with $\delta = -0.14$.

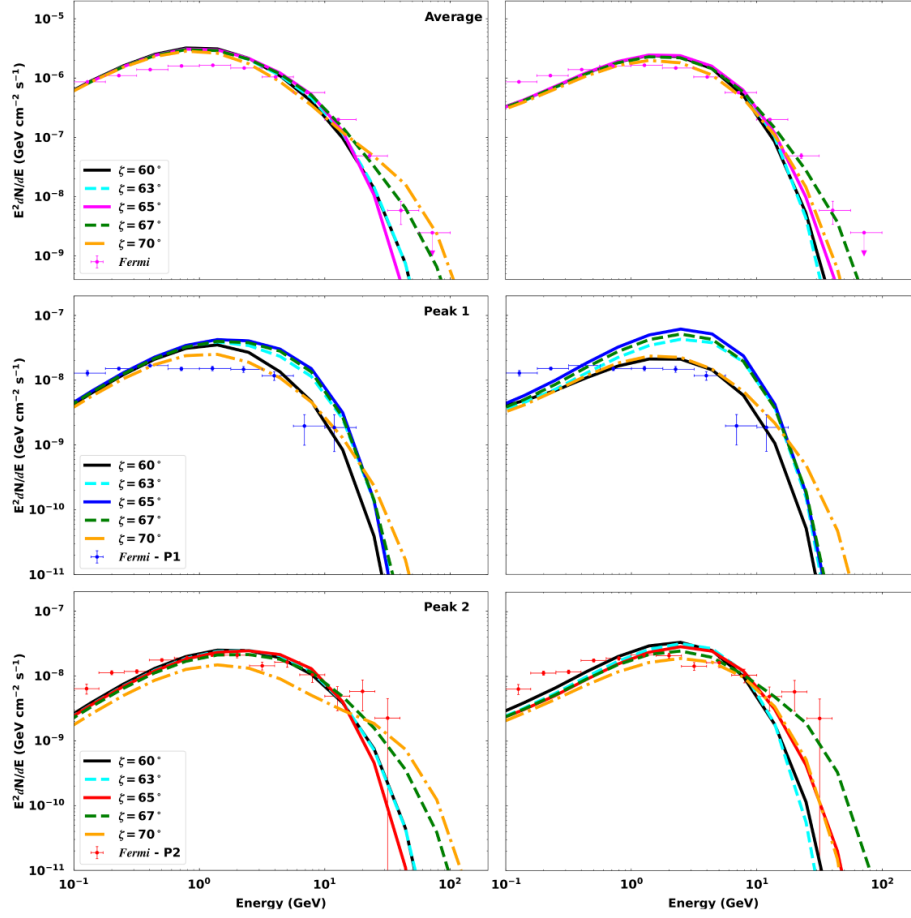


Figure 5.5: Model phase-averaged and phase-resolved spectra associated with Figure 5.4 for the same α , ζ_{cut} and optimal R_{acc} choices, for both scenario 1 (left) and scenario 2 (right). In each case, the legend indicates the chosen values for ζ_{cut} . The flux normalisation factor is $5J_{\text{GJ}}$ for the first case and $10J_{\text{GJ}}$ for the second. The data points for the phase-average spectra are from Abdo et al. (2013) (see http://fermi.gsfc.nasa.gov/ssc/data/access/lat/2nd_PSR_catalog/), and the phase-resolved spectra are updated data to those published in Abdo et al. (2010d).

phase-averaged and phase-resolved (for both P1 and P2) spectra per row. These are associated with the light curves in Figure 5.2, for both scenarios and the same parameter values as in Figure 5.2. The phase-resolved spectra are taken from Abdo et al. (2010d), but we have removed an incorrect exposure correction that led to spectral points in the peaks being higher than the phase-averaged spectrum. Since the predicted CR \dot{N}_γ are lower than the *Fermi* data points (Abdo et al. 2010d, 2013, http://fermi.gsfc.nasa.gov/ssc/data/access/lat/2nd_PSR_catalog/), we scaled the model with a flux normalisation factor in terms of J_{GJ} . The flux normalisation factor is a multiple of the Goldreich-Julian current density $J_{\text{GJ}} = \rho_{\text{GJ}}c$ (with $\rho_{\text{GJ}} = -\mathbf{\Omega} \cdot \mathbf{B}/2\pi c$ the corresponding charge density; Goldreich & Julian 1969). This spectrum normalisation has some freedom, since the actual multiplicity of HE particles in the pulsar magnetosphere is not absolutely certain. In the figure legend, we indicate $[R_{\text{acc}}, J_{\text{GJ}}]$ for scenario 1 and $[R_{\text{acc,low}}, R_{\text{acc,high}}, J_{\text{GJ}}]$ for scenario 2.

For scenario 1, at small R_{acc} the model does not fit the data, and the flux is too low, even with a large flux normalisation factor. This may be addressed in future by invoking SC emission, rather than pure CR (Harding et al., 2018). As R_{acc} increases, the model better fits the data; however, when it becomes too large, it shifts the spectra to larger E_γ 's and the spectral shape changes and deviates from the data points. This reflects the fact that a larger accelerating E -field is implied, leading to a larger particle energy and spectral cutoff. Also, for

larger R_{acc} the flux normalisation factor becomes smaller. This flux factor should in principle be constant for the phase-averaged and phase-resolved spectra, but the flux level is not consistent between the different predicted spectra, e.g., at $R_{\text{acc}} = 0.25$ P1's model spectra overestimates the data, but not for P2 or the phase-averaged spectra. This may point to the need for a spatially-dependent normalisation of the current in future.

For scenario 2, most combinations of $R_{\text{acc,low}}$ and $R_{\text{acc,high}}$ yield a good fit to the data, except when both $R_{\text{acc,low}}$ and $R_{\text{acc,high}}$ are small, e.g., $R_{\text{acc}} = [0.04, 0.1] \text{ cm}^{-1}$, or $R_{\text{acc,high}}$ is high, e.g., $R_{\text{acc}} = [0.04, 2.0] \text{ cm}^{-1}$. When $R_{\text{acc,low}}$ is small and $R_{\text{acc,high}}$ is very high, the spectra extend to unreasonably high E_γ . For $R_{\text{acc,low}} = 0.3 \text{ cm}^{-1}$ and $R_{\text{acc,high}} = 0.25 \text{ cm}^{-1}$ the spectral fits almost mimic our fits in scenario 1 for $R_{\text{acc}} = 0.25 \text{ cm}^{-1}$, although the flux normalisation is a bit lower for scenario 2. In both scenarios, $E_{\gamma,\text{CR}}$ varies significantly as we change the parameters, so that for certain choices of R_{acc} , P1 may have a larger cutoff than P2, contrary to what is observed. Thus, we settle on $R_{\text{acc}} = 0.25 \text{ cm}^{-1}$ for scenario 1, and $R_{\text{acc,low}} = 0.04 \text{ cm}^{-1}$ and $R_{\text{acc,high}} = 0.25 \text{ cm}^{-1}$ for scenario 2 as optimal values for this paper.

Next, I consider the impact of different values of ζ_{cut} on the predicted light curves and spectra, for the optimal values of R_{acc} . I study the energy-dependent light curves for $\alpha = 75^\circ$ and $\zeta_{\text{cut}} = [60^\circ, 63^\circ, 65^\circ, 67^\circ, 70^\circ]$ (Figure 5.4). One notices that P1/P2 decreases with energy at different rates. For larger ζ_{cut} (i.e., 67° and 70°), P1 is relatively higher at lower E_γ . In scenario 2, the same happens at larger ζ_{cut} but only at $E_\gamma \geq 20 \text{ GeV}$. Also, the level of bridge emission depends on the choice of ζ_{cut} . Figure 5.5 indicates spectra for the same optimal R_{acc} parameters, but for different ζ_{cut} values. For smaller ζ_{cut} , the model spectra fit the data well, but for larger ζ_{cut} , the model spectral cutoffs extend to higher E_γ , sometimes overshooting the data. Also, these spectra are lower in flux than those for the smaller ζ_{cut} fits (we fixed the flux normalisation for all values of ζ_{cut}). In scenario 2, $E_{\gamma,\text{CR}}$ varies significantly, so that for certain choices of ζ_{cut} , P1 has a larger cutoff than P2. If we analyse Figure 5.4 and 5.5 concurrently, our optimal fit for both scenarios is for $\zeta_{\text{cut}} = 65^\circ$.

5.3.2 Optimal model fit

We perform simulations for the Vela pulsar for the following parameters²: spin period $P = 0.089 \text{ ms}$, its time-derivative $\dot{P} = 1.25 \times 10^{-13} \text{ s}^{-1}$, and $d = 0.29 \text{ kpc}$. We construct all subsequent figures, e.g., phase plots, light curves, and spectra for optimal values of $\alpha = 75^\circ$, and $\zeta_{\text{cut}} = 65^\circ$ (we indicate spectra for $\alpha = 60^\circ$ for comparison). Additional optimal values are $R_{\text{acc}} = 0.25 \text{ cm}^{-1}$ and a flux normalisation factor of $5J_{\text{GJ}}$ for scenario 1, and $R_{\text{acc,low}} = 0.04 \text{ cm}^{-1}$, $R_{\text{acc,high}} = 0.25 \text{ cm}^{-1}$, and $10J_{\text{GJ}}$ for scenario 2. These values produce good fits to the *Fermi* and H.E.S.S. II data.

In Figure 5.6 we show the energy-dependent phase plots and accompanying light curves for our optimal fit, for both scenarios. For scenario 1 (left phase plot) the bridge and most of the off-peak emission disappears with increasing E_γ , although the light curve peak positions for both scenarios remain roughly stable. The other light curve trends mentioned in Section 5.3.1 are also visible here, i.e., the decrease of P1/P2 and a decrease in peak width with E_γ .

To test the robustness of the P1/P2 vs. E_γ effect, we studied the light curves at $\zeta_{\text{cut}} = 40^\circ$ to obtain a counter-example. These light curves have a different emission structure than those in Figure 5.6, due to a different spatial origin of the emission. In Figure 5.7 the observer misses the bridge emission, since emission radiated at $\zeta_{\text{cut}} = 40^\circ$ is farther from the PCs than emission at $\zeta_{\text{cut}} = 65^\circ$. The phase plots for scenario 1 remains brighter than for the second scenario. As the energy increases, the relative flux of P1 becomes larger than that of P2. A similar study was done by Brambilla et al. (2015) assuming a FIDO model to show that the P1/P2 effect is common, but not universal, since a change in geometry can reverse the effect. Figure 5.7 supports this finding. We shifted the model light curves by -0.2 in phase to fit the *Fermi* and H.E.S.S. data. This indicates the effect of ζ on the degeneracy of $\phi_L=0$ in the data (reflecting the main radio peak) and $\phi_L=0$ (the phase of the μ -axis).

In Figure 5.8, the phase-averaged and phase-resolved spectra are shown for $\alpha = 60^\circ$ and $\zeta_{\text{cut}} = 65^\circ$. The model spectra fit the *Fermi* LAT points for both R_{acc} cases fairly well. In the first scenario, the phase-resolved

²Manchester et al. (2005).

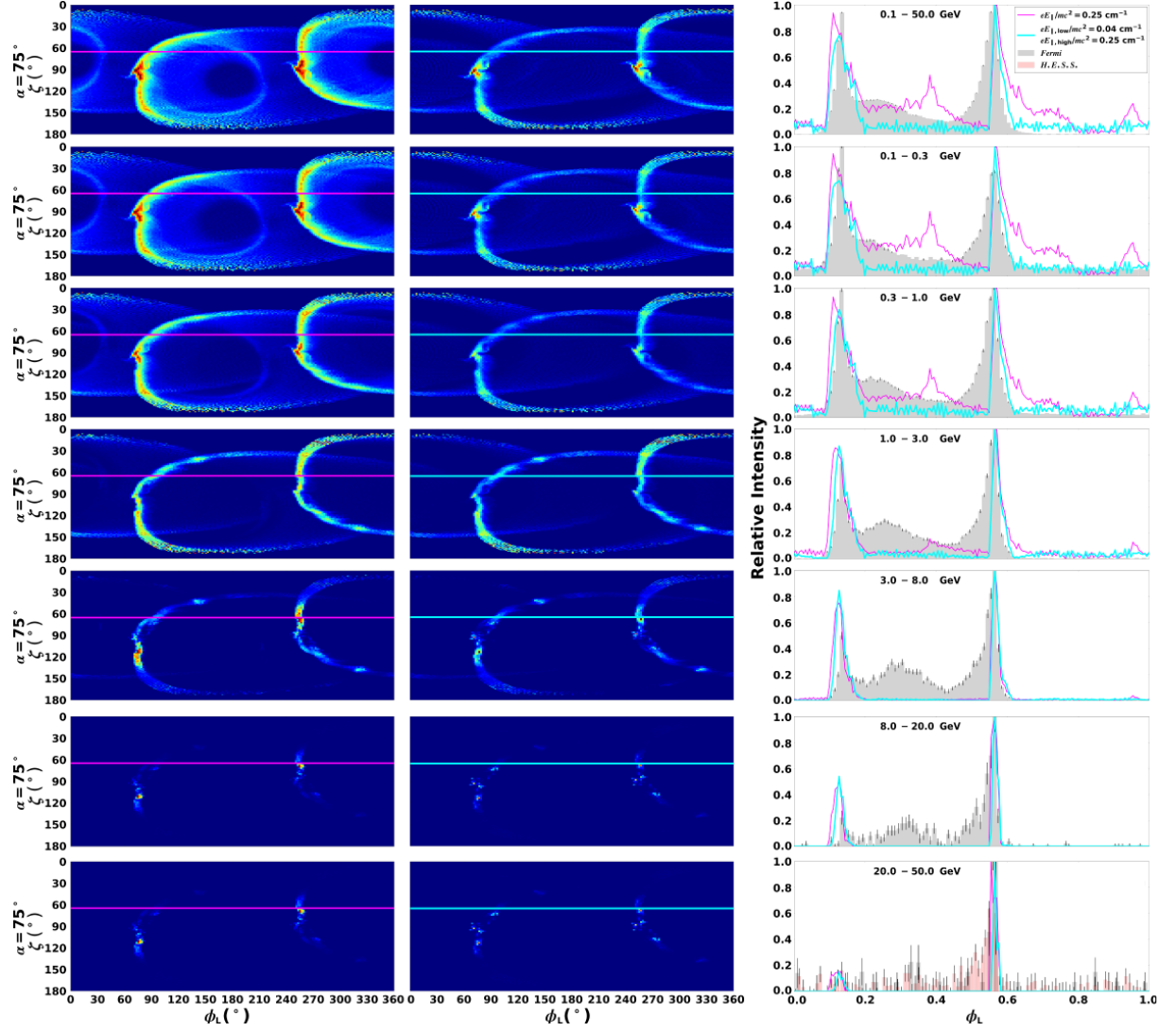


Figure 5.6: Energy-dependent phase plots and light curves for $\alpha = 75^\circ$ and $\zeta_{\text{cut}} = 65^\circ$ and for the optimal R_{acc} for both the first (left column) and second (centre column) scenarios, plus their associated light curves (right column). The top panels are for the full E_γ -range, and each panel thereafter is for a different sub-band, as indicated by the labels in the light curve panels. Peaks were shifted by -0.14 to fit the *Fermi* LAT and H.E.S.S. data.

spectra of P1 has a higher flux than that of P2, although the latter has a tail extending to higher E_γ and a slightly larger $E_{\gamma,\text{CR}}$. In Figure 5.9, the phase-averaged and phase-resolved spectra are shown for the optimal parameters. The model spectra fit the data for both scenarios fairly well. In the first scenario, the phase-resolved spectra of P1 has a higher flux than that of P2, although smaller than the flux of P1 seen in Figure 5.8. For P2, the high- E_γ tail extends not as far in E_γ as in Figure 5.8, but $E_{\gamma,\text{CR}}$ remains larger for P2, with the predicted cutoff being $E_{\gamma,\text{CR}} \sim 1$ GeV. A larger cutoff for P2 than P1 is expected for this ζ_{cut} value, since the second light curve peak survives longer than P1 as E_γ increases (see Figure 5.2). This may not always be the case, as pointed out in Figure 5.4 where the P1 remains larger than P2 depending on the choice of ζ_{cut} .

5.3.3 Testing the attainment of the CRR limit

We solved the transport equation of a particle as it moves along a B -field line, focusing on CR (e.g., Daugherty & Harding, 1982; Harding et al., 2005):

$$\dot{\gamma} = \dot{\gamma}_{\text{gain}} + \dot{\gamma}_{\text{loss}} = \frac{1}{m_e c^2} \left[c e E_{\parallel} - \frac{2 c e^2 \gamma^4}{3 \rho_c^2} \right], \quad (5.1)$$

with $\dot{\gamma}$ the time-derivative of γ , $\dot{\gamma}_{\text{gain}}$ the acceleration rate, and $\dot{\gamma}_{\text{loss}}$ the loss rate. From Eq. (5.1), it is clear that the $\dot{\gamma}_{\text{gain}}$ is dependent on R_{acc} , and $\dot{\gamma}_{\text{loss}}$ is directly proportional to γ^4 and ρ_c^{-2} . Eq. (5.1) may be recast in spatial terms by dividing by c (assuming relativistic outflow of particles):

$$\frac{d\gamma}{dl} = R_{\text{acc}} - \frac{2 e^2 \gamma^4}{3 m_e c^2 \rho_c^2}. \quad (5.2)$$

The CR spectral energy cutoff is defined as follows (e.g., Daugherty & Harding, 1982; Cheng & Zhang, 1996):

$$E_{\gamma,\text{CR}} = \frac{3 \lambda_c \gamma^3}{2 \rho_c} m_e c^2, \quad (5.3)$$

where $\lambda_c = \hbar/(m_e c)$ is the Compton wavelength, and \hbar the reduced Planck's constant. The curvature radiation reaction (CRR) limit is attained when the acceleration rate equals the loss rate. In this limit, the Lorentz factor is (e.g., Luo et al., 2000)

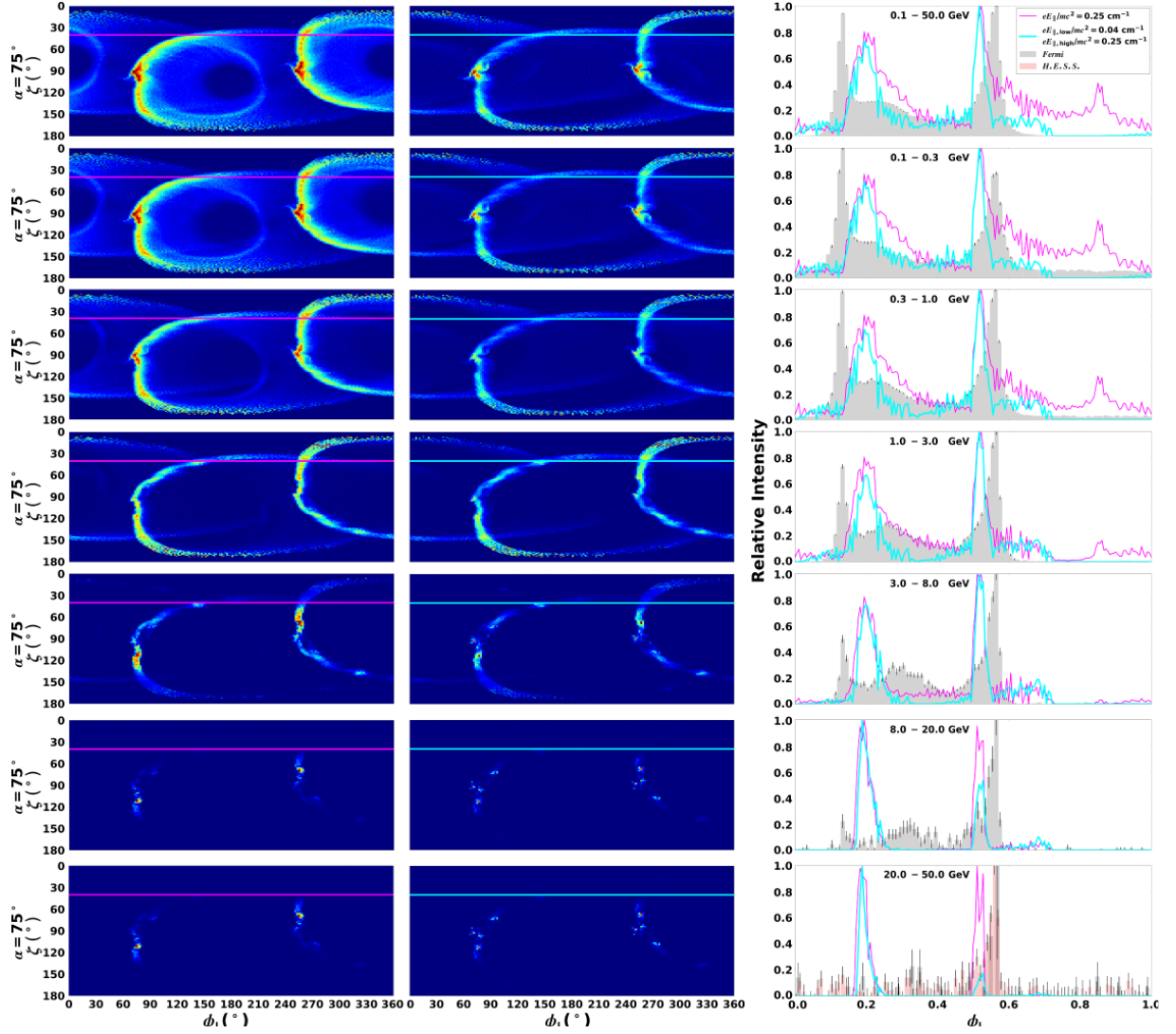
$$\gamma_{\text{CRR}} = \left(\frac{3 E_{\parallel} \rho_c^2}{2 e} \right)^{1/4}. \quad (5.4)$$

Substituting Eq. (5.4) into Eq. (5.3), we obtain for a constant E -field (Venter & De Jager, 2010)

$$E_{\gamma,\text{CR}} \sim 4 \left(\frac{E_{\parallel}}{10^4 \text{ statvolt cm}^{-1}} \right)^{3/4} \left(\frac{\rho_c}{10^8 \text{ cm}} \right)^{1/2}, \quad (5.5)$$

measured in GeV. We generally test if the CRR limit is attained in both scenarios by plotting the \log_{10} of ρ_c , γ , $\dot{\gamma}_{\text{gain}}$, and $\dot{\gamma}_{\text{loss}}$ along the same field lines chosen in Figure 4.4, checking if the acceleration and loss rates become equal at large distances. The particle dynamics depend on the ρ_c , therefore an improved calculation yielding a smoother ρ_c has an impact on the particle transport and thus the energy-dependent light curves and spectra.

In Figure 5.10, the CRR limit is almost immediately attained in the first scenario, since the E_{\parallel} is large enough to supply the primaries with ample energy at lower altitudes. The rapid rise of $\gamma \rightarrow \sim 5 \times 10^7$ leads to a rapid increase in $\dot{\gamma}_{\text{loss}}$, and then the CRR limit is reached around $0.2 R_{\text{LC}}$. However, since ρ_c oscillates or dips along some of the field lines, this limit is disturbed (since the loss rate is anti-correlated with ρ_c) and in some

Figure 5.7: The same as Figure 5.6 but for $\zeta_{\text{cut}} = 40^\circ$ and $\delta = -0.2$.

cases only recovered later on at higher altitudes. Indeed, instabilities in ρ_c cause similar but anti-correlated oscillations in $\dot{\gamma}_{\text{loss}}$. If the E_{\parallel} is lower inside the light cylinder, as in the second scenario, the acceleration of the primaries is initially suppressed, as is $\dot{\gamma}_{\text{loss}}$. However, beyond $r \sim R_{\text{LC}}$, where a higher E_{\parallel} is assumed, the particles accelerate efficiently, and the CRR limit may be reached around $r \sim 1.5R_{\text{LC}}$.

5.3.4 Local environment of emission regions connected to each light curve peak

In order to isolate and understand the P1/P2 vs. E_{γ} effect seen in the light curves of Vela, we investigated the values of $E_{\gamma, \text{CR}}$ (Eq. [5.3]), ρ_c , and γ in the spatial regions where each model peak originates, for the set of optimal parameters we found as described in Section 5.3.2. Thus, as explained in Section 5.2, we performed “reverse mapping” and accumulated the range of values that these three quantities assume in the regions where the photons originate that make up P1 and P2. These binned quantities are presented as E_{γ} -dependent histograms below, where we scaled the frequency of occurrence of the quantities using the emitted \dot{N}_{γ} to obtain a true relative probability for each chosen energy range.

In Figure 5.11 we show histograms for $\log_{10}(E_{\gamma, \text{CR}}/\text{GeV})$, for different energy ranges. This quantity is calculated using Eq. (5.3), specifically involving ρ_c and γ . These quantities are in principle calculated for all

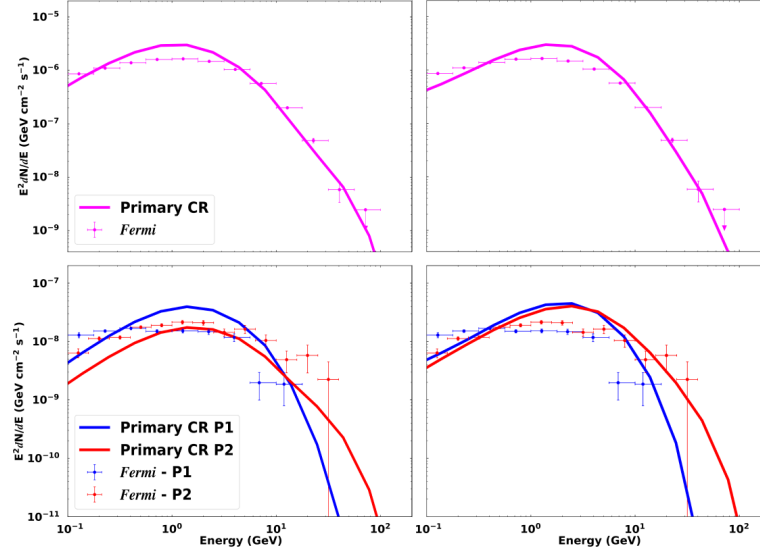


Figure 5.8: Phase-averaged (top panel) and phase-resolved (bottom panel) spectra for the refined ρ_c calculation, for $\alpha = 60^\circ$ and $\zeta_{\text{cut}} = 65^\circ$. For the first scenario (left column), the flux is normalised using $2J_{\text{GJ}}$ and for the second case (right column), it is normalised using $5J_{\text{GJ}}$. The data points for the phase-average spectra are from Abdo et al. (2013) (see http://fermi.gsfc.nasa.gov/ssc/data/access/lat/2nd_PSR_catalog/), and the phase-resolved spectra are updated data to those published in Abdo et al. (2010d).

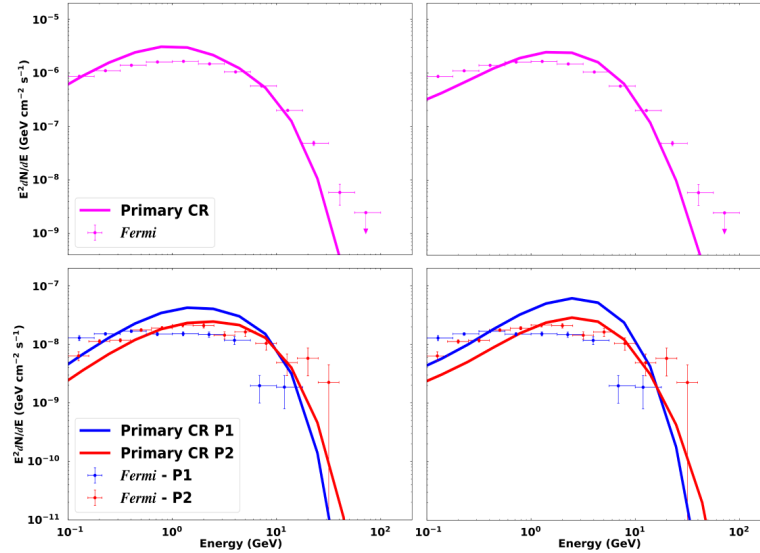


Figure 5.9: The same as Figure 5.8, but for $\alpha = 75^\circ$ and $\zeta_{\text{cut}} = 65^\circ$. For the first scenario (left column), the flux normalisation factor is $5J_{\text{GJ}}$ and for the second scenario (right column), it is $10J_{\text{GJ}}$.

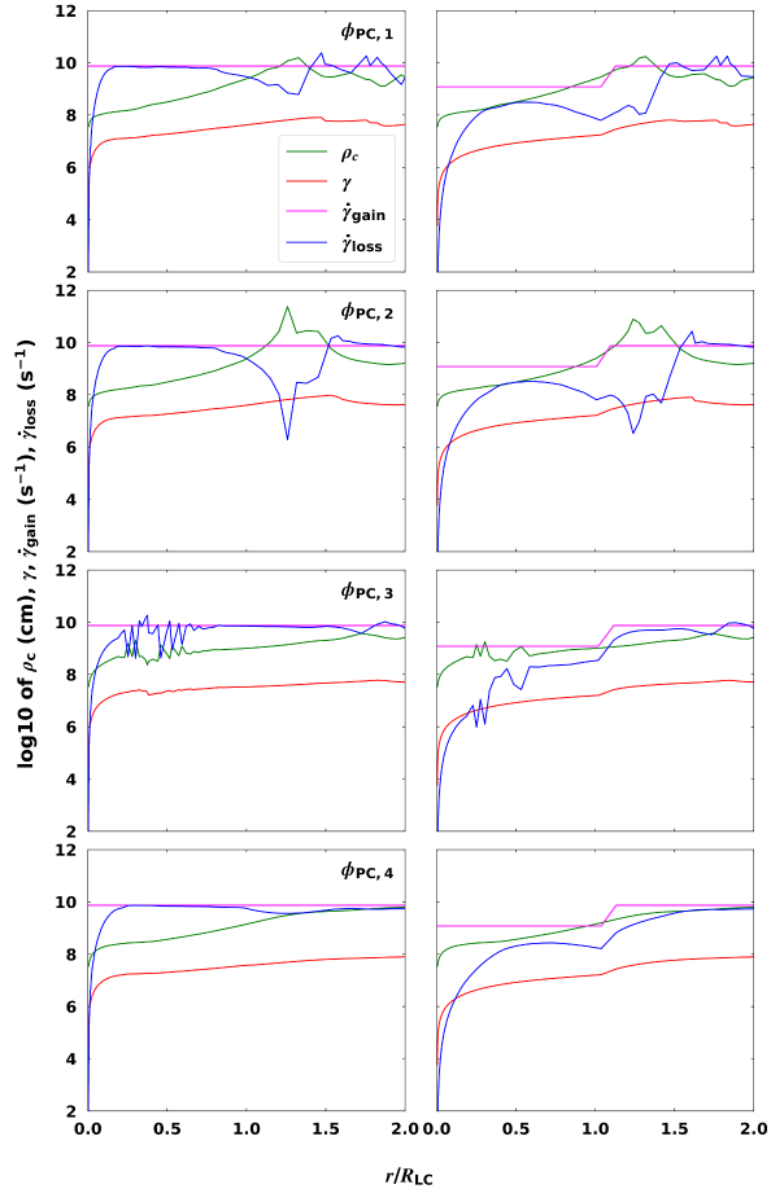


Figure 5.10: The particle dynamics, along the same B -field lines as in Figure 4.4, are shown for the refined ρ_c calculation, for $\alpha = 75^\circ$. The quantities plotted are the \log_{10} of ρ_c (green), γ (red), $\dot{\gamma}_{\text{gain}}$ (magenta), and $\dot{\gamma}_{\text{loss}}$ (blue), for both scenario 1 (left column) and scenario 2 (right column).

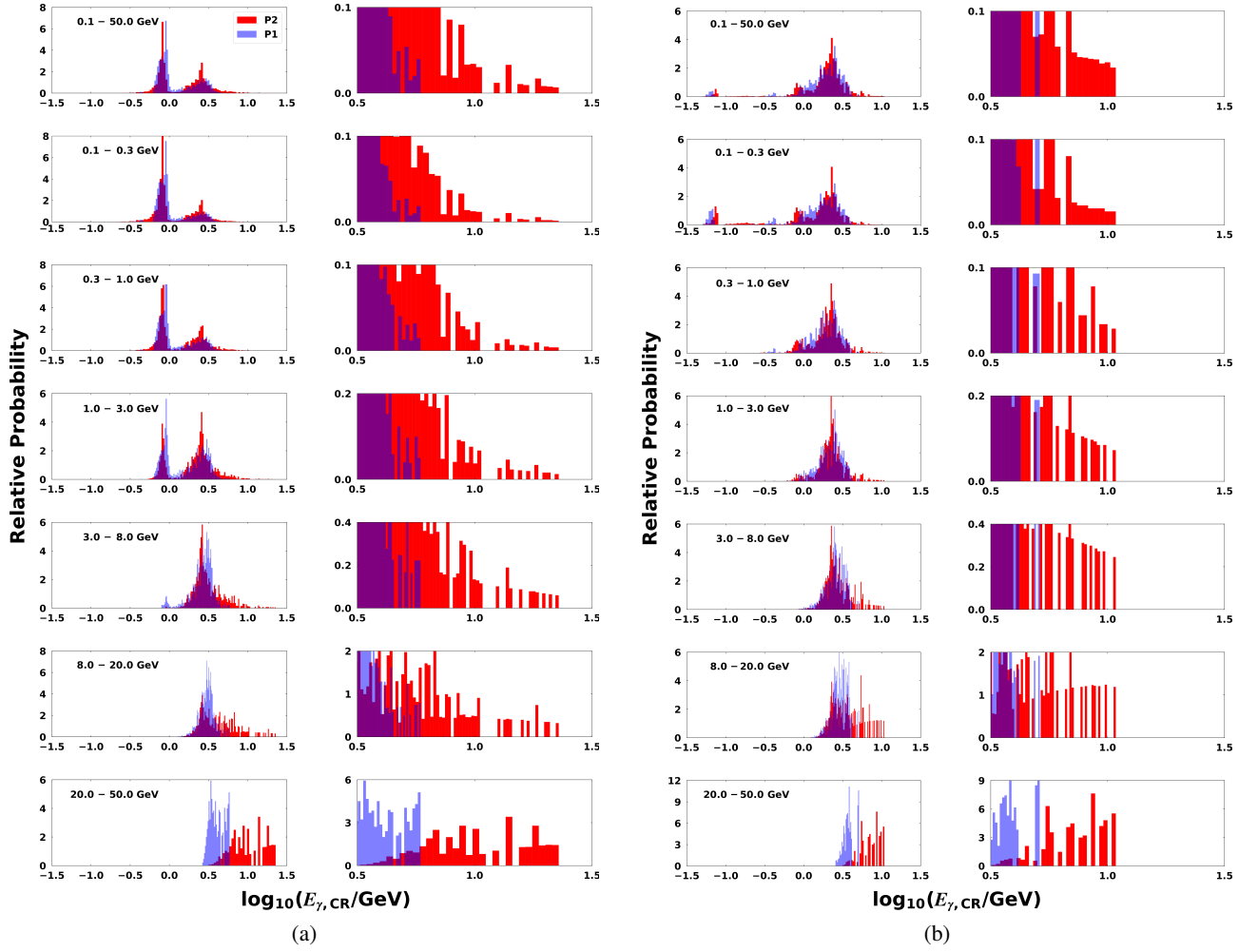
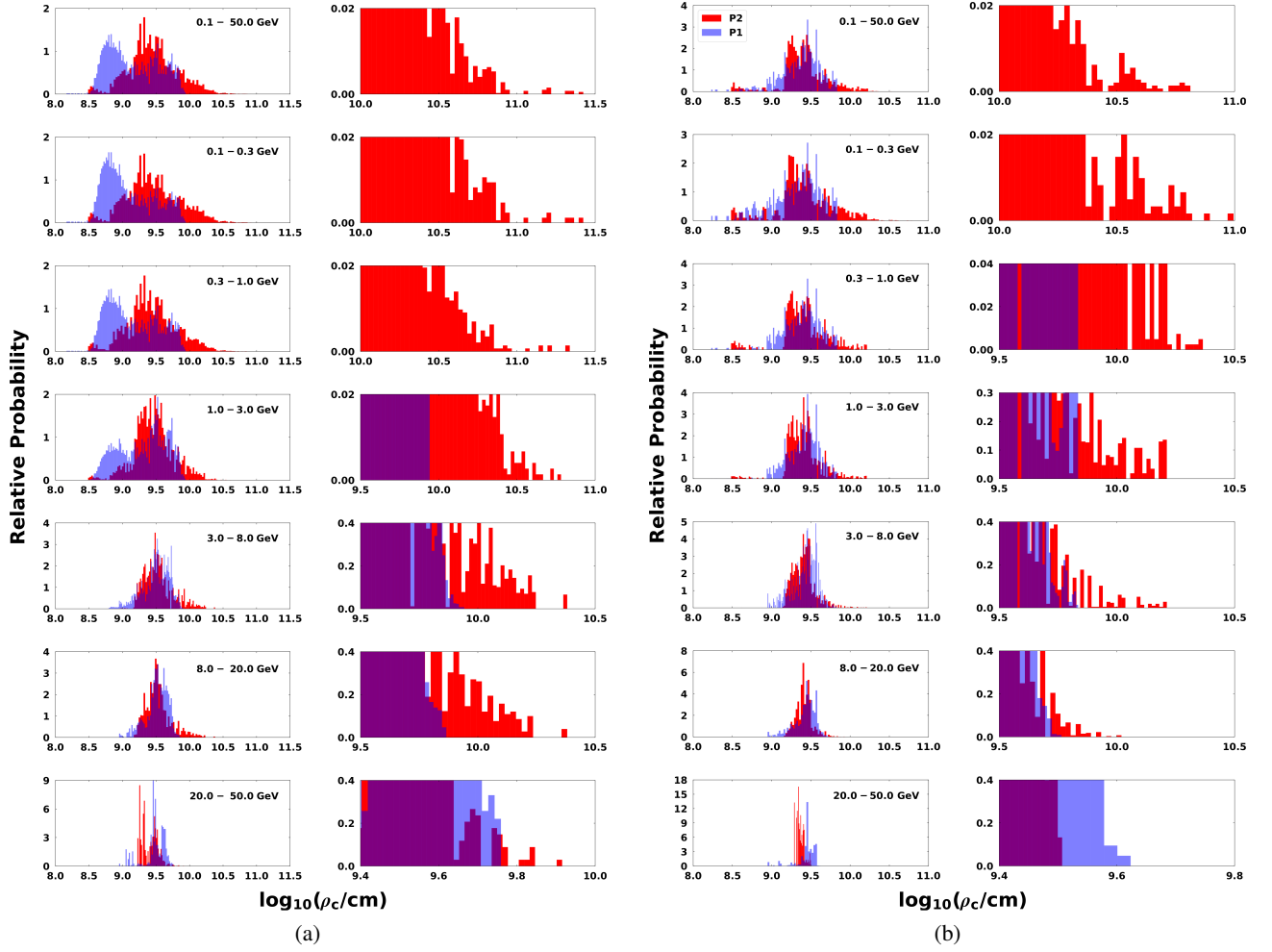


Figure 5.11: Energy-dependent histograms for $\log_{10}(E_{\gamma,\text{CR}}/\text{GeV})$ for P1 (blue curve) and P2 (red curve), where (a) represents scenario 1 and (b) scenario 2. The respective energy bands are indicated as labels in each panel. The second column in each case represents a zoom-in of the tails of the distributions for large values of $\log_{10}(E_{\gamma,\text{cut}}/\text{GeV})$.

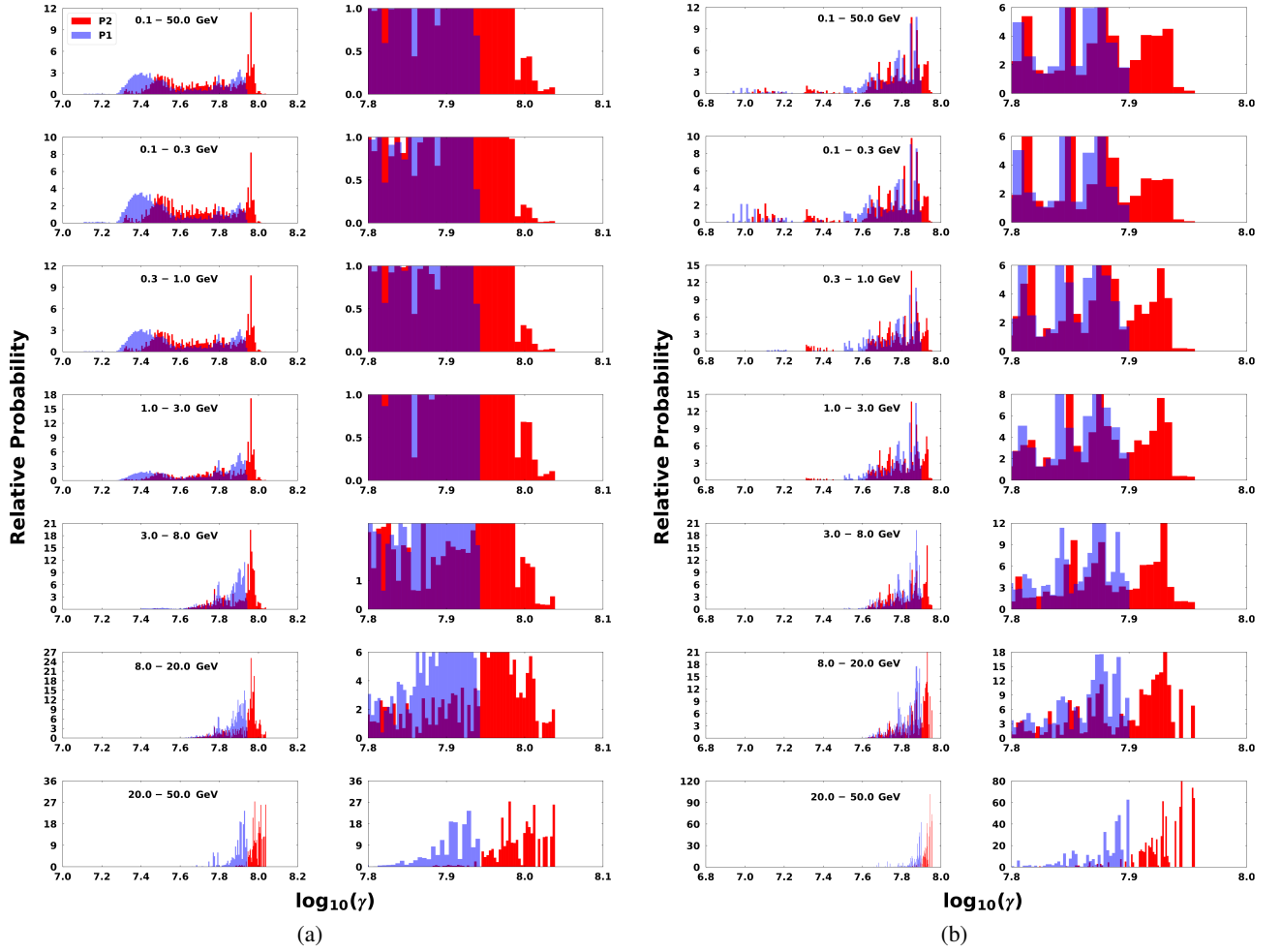
E_γ , but we subsequently apply cuts in E_γ and then study the resulting distributions of the ρ_c and γ associated with photons in a particular chosen band. In the first scenario (left column), there appears two bumps, for both peaks, at lower E_γ (up to ~ 5 GeV), situated around $\log_{10}(E_{\gamma,\text{CR}}/\text{GeV}) \approx -0.2$ and 0.4 . The lower bump disappears with increasing E_γ . In (b), we show scenario 2 where there is a small low- E_γ bump (up to ~ 0.3 GeV) at even smaller values of $\log_{10}(E_{\gamma,\text{CR}}/\text{GeV}) \approx -1.2$. The existence of this bump is probably because of the lower value of R_{acc} inside the light cylinder that suppresses the low-altitude acceleration and emission in this scenario. Also, the lower-energy bump disappears as the E_γ is increased, since only photons from individually-radiated spectra (that make up the cumulative spectrum seen by the observer) with higher cutoffs are then visible. The $\log_{10}(E_{\gamma,\text{CR}}/\text{GeV})$ of P2 is relatively larger than that of P1 for both scenarios, as seen in the zoom-ins. This confirms what has already been seen in the light curves in Figure 5.6 and spectra in Figure 5.9: P2 survives with an increase in energy, since its spectral cutoff is relatively higher than that of P1. The $\log_{10}(E_{\gamma,\text{CR}}/\text{GeV})$ of P2 reaches values as high as $\sim 10^{1.0} - 10^{1.4}$, with larger values reached in the first scenario, given the higher E -field. In Figure 5.12 we show histograms of the relative probability as a function of $\log_{10}\rho_c$ for P1 (blue) and P2 (red). For the first scenario in (a), with a zoom-in of the tail of the distributions (right column), there appears a bump around $\log_{10}\rho_c \approx 8.5$ to 9.0 for P1 at lower E_γ (up to ~ 3 GeV), which

Figure 5.12: The same as Figure 5.11 but for $\log_{10}(\rho_c)$.

disappears with increasing E_γ . In (b) we show scenario 2, where there is no low- E_γ bump at smaller values of $\log_{10}\rho_c$ as in the first scenario. This is due to the fact that in the first scenario, the accelerating E -field is relatively larger at lower altitudes, so that the particles can radiate in the GeV band from these lower altitudes characterised by lower values of $\log_{10}\rho_c$. In the second scenario, however, the small value of $R_{\text{acc,low}}$ inside the light cylinder suppresses emission in the GeV band originating from lower altitudes, hence the missing bump. Importantly, the $\log_{10}\rho_c$ of P2 is relatively larger than that of P1 for both scenarios, as seen in the zoom-ins, with P2's associated ρ_c reaching values as high as $\sim 10^{9.8} - 10^{11.5}$ cm (indicating relatively less curved orbits). The ρ_c values reached in scenario 1 for P2 are also relatively larger than those in scenario 2 for the same peak. Thus, for sustained acceleration, particles radiating at high energies are moving along slightly straighter orbits (and radiating from farther out, see Figure 5.14). It is only at energies above 20 GeV that the values of $\log_{10}\rho_c$ associated with P1 becomes comparable or larger than those associated with P2.

Similar to Figure 5.11 and Figure 5.12, we show histograms of $\log_{10}(\gamma)$ in Figure 5.13 for different energy ranges. In the first scenario indicated in (a), there appears a bump around $\log_{10}(\gamma) \approx 7.3 - 7.5$ for both peaks at lower E_γ (up to ~ 3 GeV), which disappears with increasing E_γ . In (b) we show scenario 2 where there is no low- E_γ bump at smaller values of $\log_{10}(\gamma)$. There is also a peak in $\log_{10}(\gamma) \sim 8$ for P2 in scenario 1, while $\log_{10}(\gamma)$ is relatively smaller in scenario 2, given the fact that particles experienced less acceleration in that case. The $\log_{10}(\gamma)$ of P2 is relatively larger than that of P1 as seen in the zoom-ins for both scenarios.

In Figure 5.14(a), (b), and (c) we limit the emission radius r to altitudes at and beyond R_{LC} to investigate the

Figure 5.13: The same as Figure 5.11 but for $\log_{10}(\gamma)$.

change in the range of values for the pertinent quantities as compared to the previous cases where we considered emission from all altitudes. We show histograms for \log_{10} of $E_{\gamma,CR}$, ρ_c , and γ , respectively, for the first scenario. At lower E_γ (up to ~ 3 GeV), the P1 bumps at lower values that we first noticed in Figure 5.11a, 5.12a, and 5.13a are suppressed. This indicates that photons originating inside the light cylinder come from regions that are characterised by lower values of $E_{\gamma,CR}$, ρ_c , and γ . This effect of limiting the emission altitudes is not as noticeable in the second scenario in Figure 5.15(a), (b), and (c). For $E_{\gamma,CR}$ the slight bump (including P1 and P2 emission) at low values of $E_{\gamma,CR}$ disappears at lower E_γ (up to ~ 0.3 GeV). For ρ_c and γ the difference is insignificant, given the fact that the low-altitude E -field already suppresses the emission.

5.4 Conclusion

There is an ongoing debate regarding the origin of the GeV emission detected from pulsars, it being attributed either to CR or SR (or even IC; see Lyutikov et al. 2012; Lyutikov 2013). One way in which to possibly discriminate between these options is to model the energy-dependent light curves of several bright pulsars.

We modelled E_γ -dependent light curves and spectra of the Vela pulsar in the HE regime assuming CR from primaries to see if we can explain the origin of the decreasing ratio of P1/P2 vs. E_γ , expecting that the answer may lie in a combination of the values of geometric and physical parameters associated with each peak.

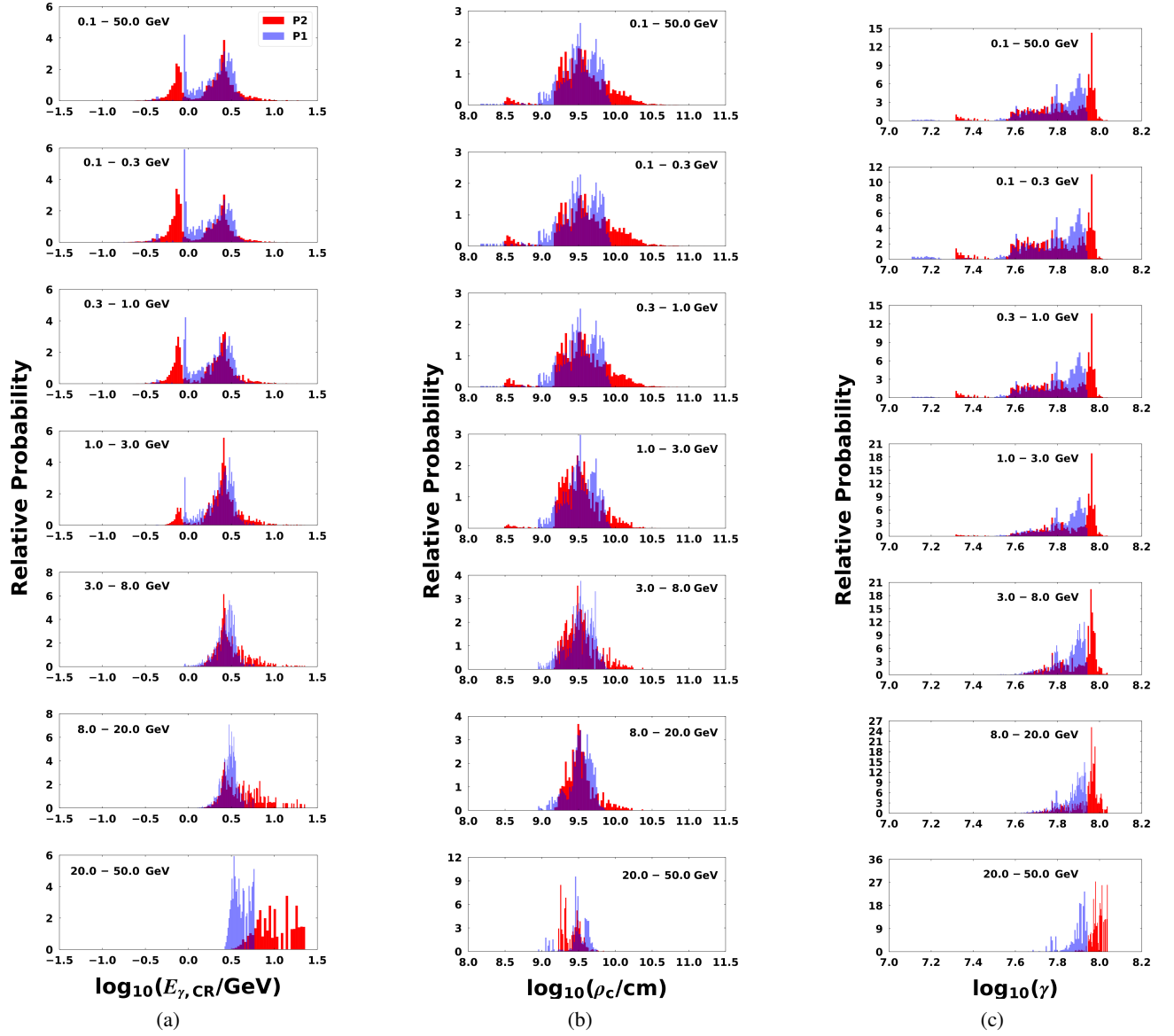


Figure 5.14: Energy-dependent histograms of (a) $\log_{10}(E_{\gamma,CR}/\text{GeV})$, (b) $\log_{10}(\rho_c)$, and (c) $\log_{10}(\gamma)$, for P1 (blue curve) and P2 (red curve). All three cases are for the first scenario at altitudes equal to and beyond R_{LC} , into the current sheet.

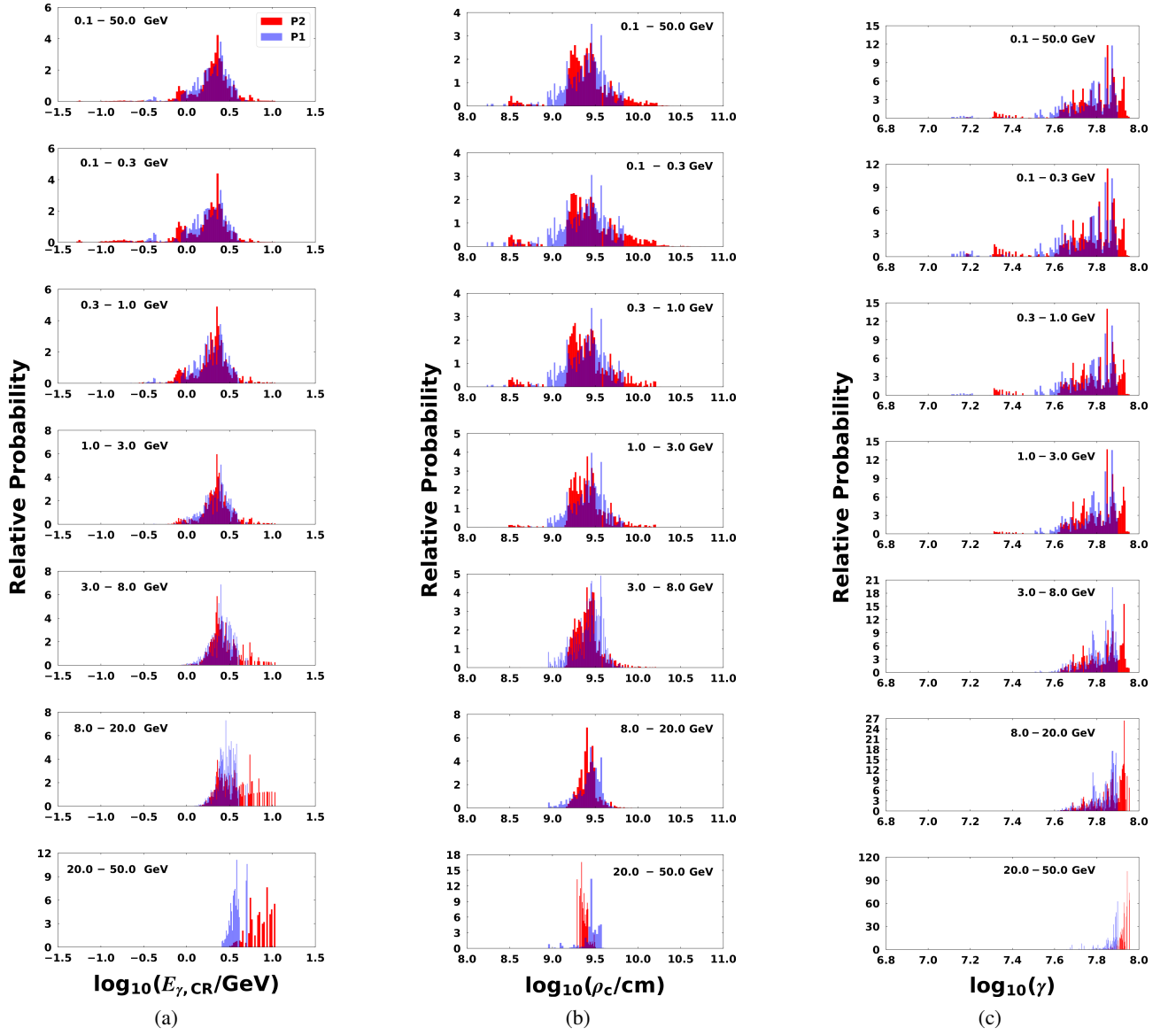


Figure 5.15: The same as in Figure 5.14 but for the second scenario.

Since the light curves probe geometry, e.g., α , ζ and emission gap position and extent, and the spectrum probes both the energetics and geometry, we simultaneously fit these data with our model to obtain optimal fitting parameters.

We presented a refined calculation of the ρ_c of particle trajectories, impacting the CR loss rate and leading to smoother phase plots and light curves. However, this refinement had a rather small impact, as the broad structure of caustics and light curves remained similar to what was found previously. We assumed a FF magnetosphere (implying zero E -fields) as a good first approximation of the true B -field structure, yet considered both a constant and two-step accelerating E -field. We also found that the CRR limit was easily reached in the first scenario, and sometimes also in the second. We proceeded to isolate the P1/P2 effect by selecting photons that make up these two light curve peaks, and investigating the range of associated values of ρ_c , $E_{\gamma,CR}$ and γ . We found that the phase-resolved spectra associated with each peak indicated a slightly larger spectral cutoff for P2, confirming that P2 survives with an increase in energy, given its larger spectral cutoff. This was also seen in energy-dependent histograms of $E_{\gamma,CR}$, confirming that this quantity was systematically larger for P2. The reason for this became more clear upon discovery that both the ρ_c and γ were systematically larger for P2, for both scenarios. If CRR is reached, one expects $E_{\gamma,CR} \propto \rho_c^{1/2}$ for a constant E -field, so the larger ρ_c would explain the larger spectral cutoff for P2. Conversely, even if CRR is not attained, $E_{\gamma,CR} \propto \gamma^3 \rho_c^{-1}$. Given the systematic dominance of γ for P2, and the strong dependence of the third power, the larger spectral cutoff of P2 is thus explained by the larger γ . We also found that the values of ρ_c and γ remained larger for P2 when only considering emission beyond the light cylinder; in particular, the largest values of these quantities occurred there, pointing to dominant emission from that region to make up the GeV light curves.

We thus found reasonable fits to the energy-dependent light curves and spectra of Vela, and our model that assumes CR as the mechanism responsible for the GeV emission captures the general trends of the decrease of P1/P2 vs. E_γ , evolution / depression of the inter-peak bridge emission, plus stable peak positions and a decrease in the peak widths as E_γ is increased. However, an unknown azimuthal dependence of the E -field as well as uncertainty in the precise spatial origin of the emission preclude a simplistic discrimination of emission mechanisms. Similar future modelling of energy-dependent light curves and spectra within a striped-wind context that assumes SR to be the relevant GeV mechanism will be necessary to see if those models can also reproduce and explain these salient features in the case of Vela and other pulsars.

We note that the drop in P1/P2 vs. E_γ may not be universal, as also found by (Brambilla et al., 2015). We found a counter-example for a different choice of ζ_{cut} , where P1/P2 increases with E_γ . This was also the case for specific choices of the two-step acceleration E -field. There may also be other parameter combinations that can yield this behaviour. However, this effect seems prevalent and has been seen in both HE and VHE data of bright pulsars.

In the next Chapter we will discuss the study done by Harding et al. (2018) to explain the pulsed VHE emission observed by H.E.S.S. from the Vela pulsar, and our contribution. I will give a summary of their study, the parameter values assumed, and the implications of our improved calculation of ρ_c (see Section 4.4) on their results.

Chapter 6

Modelling the emission from the Vela pulsar in the TeV band

In this Chapter, I will briefly discuss the work published in Harding et al. (2018). In Section 6.1 an overview of the study is given that includes the motivation thereof, the refinements made to their SSC emission code, the assumptions made, as well as the results obtained. Section 6.2 highlights my contribution to the study which is mainly the refined calculation of ρ_c of the particle trajectories, as well as its effect on the model light curves and spectra for different wavebands and radiation components. This is followed by our concluding remarks in Section 6.3.

6.1 Overview

The Vela pulsar is the first pulsar detected in the VHE range by H.E.S.S. up to energies of a few TeV (Djannati-Ataï et al., 2017). The pulsed emission at such extreme energies might be either connected to the GeV emission of *Fermi*'s spectra or it could be a new radiation component. More details as to the measured spectrum will be given in a forthcoming paper by the H.E.S.S. Collaboration. The study by Harding et al. (2018) treated it to be a separate component that is radiated by particles that have been accelerated up to energies of several TeV.

Some studies attempted to model the VHE pulsed emission detected from the Crab pulsar as ICS (Du et al., 2012; Lyutikov et al., 2012; Harding & Kalapotharakos, 2015). Others modelled the emission from this same pulsar as cyclotron-self-Compton emission from electron-positron pairs in an OG model, where the pairs scatter their own SR radiation. Harding & Kalapotharakos (2015) modelled the emission observed from Crab, Vela and two bright MSPs (i.e., PSR B1937+21 and PSR B1821–24) in the optical-to-TeV energy range with an SSC model, where pairs from the PC scatter their own SR in the outer magnetosphere (see Section 4.1). Other studies have proposed that SR from particles accelerated via reconnection in the current sheet could reach TeV energies through Doppler boosting (Uzdensky & Spitkovsky, 2014; Mochol & Pétri, 2015). Rudak & Dyks (2017) modelled Vela's measured VHE emission in an OG scenario, where primary particles are accelerated inside this gap and scatter the observed IR to optical emission, that are placed along the inner edge of the gap and believed to come from SR emitted by pairs also produced in this gap. They showed that primaries, whose CR spectrum match the *Fermi* measured GeV spectrum, produce a significant ICS emission component reaching energies up to ~ 10 TeV.

A basic description of the pulsar model has been given in Chapter 4. For more details, see Harding et al. (2008); Harding & Kalapotharakos (2015); Harding et al. (2018).

Harding et al. (2018) extended the SSC emission code of Harding & Kalapotharakos (2015) To summarise, the main refinements include the following:

- The spectral energy range for the radiation calculation was extended to span from IR (10^{-3} eV) to VHE (100 TeV) energies. This expanded range is necessary, since it includes more soft photons whose scattering is in the Thompson limit, and for modelling the SSC emission at the highest energies.
- A more accurate calculation of the particle trajectories and their ρ_c 's. This in turn gives a more precise determination of the energy of the accelerated particles and of their emitted radiation spectrum. This improved trajectory calculation is discussed in Section 4.4 and will appear in a forthcoming paper (Barnard et al. 2020, in preparation).
- The accelerating E_{\parallel} is divided into a two-step E_{\parallel} , i.e., a lower E_{\parallel} inside the light cylinder (mostly SR emission), and a higher E_{\parallel} at and beyond the light cylinder (into the current sheet, with the GeV emission mostly from CR). This two-step E -field is utilised in Chapter 5. In Harding & Kalapotharakos (2015), the E_{\parallel} was set to one constant high value extending from the NS surface to $2 R_{LC}$. This change provides better agreement with recent global MHD and PIC pulsar models showing that the particle acceleration takes place primarily near the current sheet outside of the light cylinder in near-FF magnetospheres of young and middle-aged pulsars.
- Another update was the injection of electron–positron pairs only above the PC in regions where the global FF current density enables pair cascades. Injection was thus only done at selected azimuthal PC angles (see Harding et al. (2018) for more details).
- The last improvement to the model of Harding & Kalapotharakos (2015) is that the MeV to GeV radiation from accelerated / relativistic particles inside and outside of the light cylinder are emitted via SC radiation, although their radiation at GeV energies is mostly in the CR limit. In Harding & Kalapotharakos (2015), both the accelerating primary particles (as well as the pairs) could acquire pitch angles at low altitudes through cyclotron-resonant absorption of radio photons (as in the 2018 model), but their SR and CR were treated separately.

Harding et al. (2018) assumed the same parameter values as those used in Chapter 5, except that their $R_{acc} = 0.2 \text{ cm}^{-1}$ is slightly lower than what we used. This also impacts the spectral normalisation factor that shifts the spectral flux up or down to fit the GeV data points (see Chapter 5 and Harding et al. (2018) for the explanation thereof). Our normalisation factor for the two-step E_{\parallel} is slightly larger than theirs of $10J_{GJ}$. Figure 6.1 and Figure 6.2 show the first results obtained with the improved code. In Figure 6.1 the E_{γ} -dependent model light curves for Vela are illustrated, assuming $\alpha = 75^\circ$ and $\zeta_{cut} = 65^\circ$, for the IR/optical (0.1 – 1 eV) band and three other γ -ray bands ranging between 0.05 GeV and 100 TeV. In Figure 6.2 the phase-averaged spectrum is represented and includes all the radiation components produced by this model. The primaries and pairs respectively produce these components via emission mechanisms as discussed in Chapter 2. The TeV component is specifically produced by primary particles (that produce the GeV component via SC) that upscatter the pair SR.

6.2 The effect of the refined ρ_c on the model output

The equations of motion for the Lorentz factor, γ , and perpendicular momentum, p_{\perp} (in units of mc), of a particle as it moves along a B -field line are as follow (Harding et al., 2005)

$$\frac{d\gamma}{dt} = \frac{eE_{\parallel}}{mc} - \frac{2e^4}{3m^3c^5} B^2 p_{\perp}^2 - \frac{2e^2\gamma^4}{3\rho_c^2} + \left(\frac{d\gamma}{dt}\right)^{abs} - \left(\frac{d\gamma}{dt}\right)^{SSC}, \quad (6.1)$$

$$\frac{dp_{\perp}}{dt} = -\frac{3c}{2r} p_{\perp} - \frac{2e^4}{3m^3c^5} B^2 \frac{p_{\perp}^3}{\gamma} + \left(\frac{dp_{\perp}(\gamma)}{dt}\right)^{abs}. \quad (6.2)$$

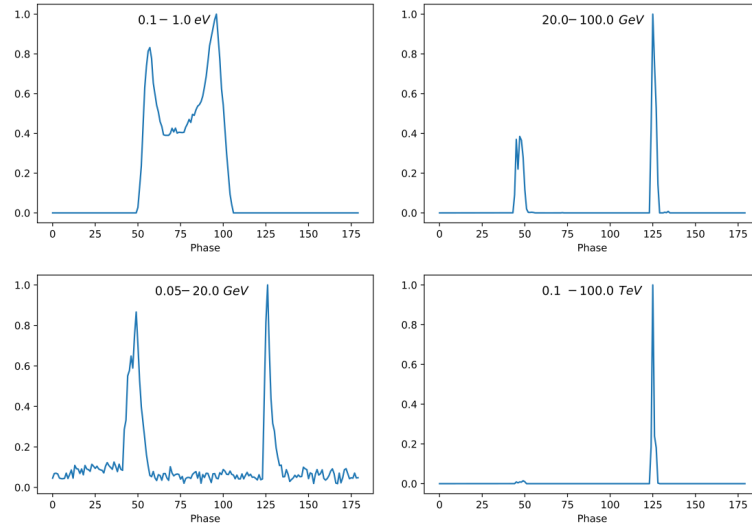


Figure 6.1: E_γ -dependent light curves for emission from Vela in the IR/optical band ($0.1 - 1$ eV), and three different γ -ray energy bands (ranging between 0.05 GeV- 100 TeV), assuming $\alpha = 75^\circ$ and $\zeta_{\text{cut}} = 65^\circ$. The phase is in degrees. One notices the relatively small peak separation in the optical; this increases with energy, and the relative intensity of P1 decreases with an increase in energy. From Harding et al. (2018).

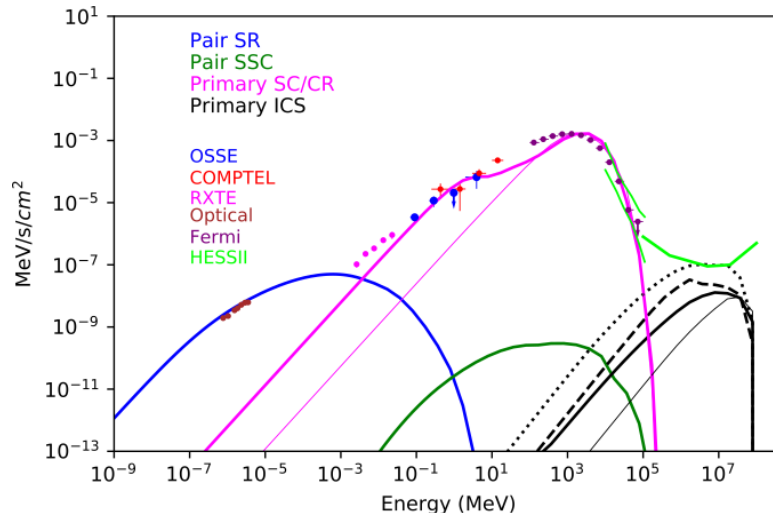


Figure 6.2: Model phase-averaged spectra for the Vela pulsar assuming $\alpha = 75^\circ$ and $\zeta_{\text{cut}} = 65^\circ$. The emission from primaries and pairs are included (as labelled). The solid black lines represent the ICS components from accelerated SC-emitting (thick line) or CR-emitting (thin line) primaries scattering the pair SR component (blue solid line), while the dashed and dotted black lines are the spectra from SC-emitting primaries scattering toy-model soft IR/optical photons with energy range ($0.5 - 4$ eV) and ($0.005 - 4$ eV), respectively. The model spectra are fit to the data points from Abdo et al. (2013) (http://fermi.gsfc.nasa.gov/ssc/data/access/lat/2nd_PSR_catalog/), Shibano et al. (2003), and Harding et al. (2002b). The H.E.S.S. II detection (Abdalla et al., 2018) and HE sensitivity are also shown. From Harding et al. (2018).

In Eq. (6.1), the different terms on the right-hand side are the CR acceleration rate, SR losses, CR losses, cyclotron/synchrotron absorption, and IC losses. In Eq. (6.2), the various terms on the right-hand side are adiabatic momentum change along the field line, SR losses, and cyclotron/synchrotron resonant absorption. The SSC losses are negligible for p_{\perp} .

The refined calculation of ρ_c is needed to improve the calculation of the particle dynamics that form the basis to describe the emission from the particles. The particles can emit radiation via CR, SC, SSC and ICS with a detailed calculation of these processes and their emission directions described in Harding et al. (2008); Harding & Kalapotharakos (2015); Torres (2018). The CR loss term (see Eq. (6.1) is strongly dependent on γ and ρ_c . This loss term influences the particle dynamics due to the coupling between this term and the particle γ (i.e., the $\gamma(s)$ at the next step in arclength s along the B -field line is determined by the losses suffered by the particle at the previous step, in particular the CR loss term). This in turn influences the other radiation mechanisms' loss terms, as they also depend on $\gamma(s)$. The dynamical equations are solved step by step for each radiation mechanism, so using a refined $\gamma(s)$ will improve the radiation calculations, i.e., from primary particles that emit SR, IC, SSC, etc. This also improves spectral calculations, specifically the CR component which depends on both γ and ρ_c .

As seen in Figure 4.4 the particle trajectories and ρ_c calculated previously and now via a refined calculation deviate slightly from each other. This implies that particles may move “off” the B -field lines in the old calculation (i.e., the adaptive step length sometimes sampled a particular B -line crudely, especially at high altitudes, and this led to particles numerically ‘jumping’ to an adjacent field line). Thus, the new calculation impacts the emission directions (both of the primaries and the pairs), since the new trajectories that are calculated using fixed but small steps in arclength are slightly different. Therefore, a more accurate calculation of the particle trajectories and their ρ_c 's leads to refined phase plots, i.e., the caustic structure is more pronounced, although the structure remains roughly the same. The respective light curves are also somewhat smoother and occur at slightly different phase, as shown in Figure 4.6 in Chapter 4. Also, as the E_{γ} increases the light curve trends investigated in Chapter 5, in the CR regime, are still present at TeV energies. A different trajectory will influence the pair dynamics as well to some extent, since it probes a slightly different B -field and radio photon distribution. It was thus necessary to refine the trajectory and ρ_c calculation, given the interconnectedness and dependence of the particle dynamics and emission calculations on these basic spatial calculations.

6.3 Conclusion

This study's motivation was to explain the TeV emission observed from the Vela pulsar by H.E.S.S. This observation provided a fundamental lower limit to the relativistic particles of a few TeV. They claimed that in order to obtain this measurement of several TeV, accelerated particles are needed that obtain such high energies. These particles will radiate CR at GeV energies, and also give rise to SC, SSC and ICS emission, where the primary ICS (i.e., SSC by primaries involving the pair SR) component is close to the H.E.S.S. sensitivity. Thus, the TeV spectrum can be explained within this framework that invokes CR to explain the GeV emission. This also supports our argument and findings in Chapter 5.

It is important to keep on refining the model calculations, e.g., of particle trajectories. If one can refine these calculations to get a more accurate model, then data can more directly be used to constrain the unknown assumptions (radio emission height, pair spectra parameters, etc.), since discrepancies with respect to the data will more likely be due to model assumptions, and not the model implementation. This is especially important since upcoming ground-based telescopes such as CTA should be able to detect more VHE pulsars with its higher sensitivity than current telescopes.

In Chapter 7 we will give a summary of the aims, the process of achieving them, and the findings from the study as a whole. I will lastly also give a future outlook on what can still be done.

Chapter 7

Conclusions

Pulsars are dense NSs that spin rapidly and contain strong B -fields, E -fields, and gravitational fields (e.g., Abdo et al. 2010c). These compact stars emit pulsed emission across the entire electromagnetic spectrum, injecting HE particles into the local environment. The *Fermi* LAT has revolutionised the field of pulsar science with the number of γ -ray pulsar detections increasing from 7 pre-*Fermi* to 117 (in 2013) to over 250. The ongoing detections of pulsed VHE emission from pulsars by ground-based telescopes paved the way to explore a new region of this γ -ray energy range. Light curve profiles in different energy bands and spectral properties from these pulsars have been studied in great detail. Therefore, energy-dependent light curve and spectral modelling served as useful tools to constrain the B -field structure, pulsar geometry (α and ζ), constrain the GeV emission region's location and extent (i.e., within and beyond the light cylinder), and this may also help to discriminate between different emission mechanisms (e.g., Dyks et al. 2004a; Venter et al. 2009; Watters et al. 2009; Johnson et al. 2014; Pierbattista et al. 2015). In this study, I focused on HE and VHE γ -ray emission from the Vela pulsar, one of the brightest sources detected by *Fermi*.

7.1 Significant contributions and results

7.1.1 Offset-dipole studies

The first aim of this study was to investigate the impact of different assumed magnetospheric structures on the predicted HE γ -ray pulsar light curve features of the Vela pulsar as observed by *Fermi*. I adopted a geometric pulsar modelling code (Dyks et al., 2004a) that already included the static dipole and RVD B -fields. I implemented a symmetric offset-PC dipole field (Harding & Muslimov, 2011a,b) characterised by an offset ϵ from the magnetic PCs. This included transforming the B -field from the co-rotating to the lab frame. For each B -field, I considered both the TPC and OG models, assuming uniform ϵ_v . Additionally, I implemented the full accelerating SG E -field corrected for GR effects up to high altitudes, which modulated ϵ_v . For the offset-PC dipole field I only considered the TPC and SG models, since there are no OG E -field expressions available for this particular B -field solution. I obtained a general SG $E_{||}$ -field by matching the low-altitude and high-altitude solutions of this $E_{||}$ -field by determining the matching parameter $\eta_c(P, \dot{P}, \alpha, \epsilon, \xi, \phi_{PC})$ on each field line in multivariate space.

After the general SG E -field was calculated I could solve the particle transport equation, which yielded the particle energy $\gamma(\eta)$, necessary for determining the CR ϵ_v and to test whether the CRR limit was attained. I found that the CRR limit was reached (see Figure 3.5), albeit only at large η . Thus, the SG E -field is relatively low, therefore the particle energy only becomes large enough to yield significant CR at large altitudes above the stellar surface and thus particles do not always attain the CRR limit. Given this low SG E -field, I further investigated the effect that the SG $E_{||}$ had on the predicted light curves in two ways. First, the minimum

photon energy was lowered from $E_{\gamma,\min} = 100$ MeV to $E_{\gamma,\min} = 1$ MeV, leading to radiation in the hard X-ray waveband. Second, since I wanted to compare our model light curves to *Fermi* data the usual low SG E -field was increased by a factor of 100 (with a spectral cutoff now at $E_{\gamma,\text{CR}} \sim 4$ GeV).

We fit our model light curves to the observed *Fermi*-measured Vela light curve for each B -field and geometric model combination. We found that our overall optimal light curve fit to the data was for the RVD field and OG model as seen in Figure 3.10. For the other B -field and model combinations there were no significantly preferred model (per B -field), since all the alternative models may provide an acceptable alternative fit to the data, within 1σ . The offset-PC dipole field preferred smaller values of PC offsets when assuming constant ϵ_v , and larger values for variable ϵ_v , but not significantly so ($< 1\sigma$). When comparing all cases (i.e., all B -field and model combinations), we found that the offset-PC dipole field for variable ϵ_v was significantly rejected. When I lowered E_γ we noted new caustic structures and emission features on the resulting phase plots and light curves that were absent when $E_{\gamma,\min} > 100$ MeV. When I increased the SG E -field by a factor of 100, we found improved phase plots and light curve fits, e.g., extended caustic structures and new emission features as well as different light curve shapes emerged, as well as CRR being now reached in most cases at lower η . I also compared the best-fit light curves for the offset-PC dipole B -field and $100E_\parallel$ combination for each ϵ (Figure 3.10) and noted that a smaller ϵ was again preferred (although not significantly; $< 1\sigma$). In particular, when I compared this case to the other B -field and model combinations, we found statistically better fits for all ϵ values with this combination being second in quality only to the RVD and OG model fit.

I compared the best-fit α and ζ , with errors, from this and other independent studies (Figure 3.11) and noted that many of the best-fit solutions cluster inside the grey area at larger α and ζ . Some fits lie near the $\alpha - \zeta$ diagonal (possibly due to radio visibility constraints in some cases) as well as near the ζ inferred from the PWN torus fitting (Ng & Romani, 2008), notably for the RVD B -field. Therefore, there was reasonable correspondence between my results and those of other studies. However, when I discarded the non-optimal TPC / SG fits, I saw that the optimal fits clustered near the other fits at large α and ζ . For the increased SG E -field and offset-PC dipole combination, I noted that these fits also clustered at larger α and ζ .

7.1.2 Energy-dependent CR light curves and spectral modelling

The second aim of this study was to investigate the HE light curve trends as a function of E_γ as well as the phase-resolved spectra so as to contribute to the debate of whether CR or SR is responsible for the HE emission. As a first approach, I modelled the E_γ -dependent light curves and phase-resolved spectra of the Vela pulsar in the HE regime assuming CR from primary particles in order to explain the origin of the decreasing ratio of P1/P2 vs. E_γ as seen in the observations, expecting that it is due to the combination of the values of geometric and physical parameters associated with each peak. Since the light curves probe geometry, e.g., α , ζ and emission gap position and extent, and the spectrum probes both the energetics and geometry, I simultaneously fit our model to the *Fermi* and H.E.S.S. data points to obtain optimal fitting parameters.

We used a full emission code (Harding & Kalapotharakos, 2015), but only assumed CR, and implemented a refined calculation of the ρ_c of particle trajectories, impacting the CR loss rate and leading to smoother phase plots and light curves. However, this improved ρ_c had a rather small effect on the spatial distribution of the emissivity, as the broad structure of caustics and light curves remained similar to what was found previously. I assumed an SG and current sheet model in an FF magnetosphere (implying an E -field that is fully screened) as a good first approximation of the true B -field structure, yet I considered both a constant and two-step accelerating E -field. I solved the particle transport for both cases and found that the CRR limit was easily reached in the first scenario, but not always in the second. In order to isolate the P1/P2 effect, I selected photons that make up these two light curve peaks, and investigated the range of associated values of ρ_c , $E_{\gamma,\text{CR}}$ and γ for each peak. I found that the phase-resolved spectra associated with each peak indicated a slightly larger spectral cutoff for P2, confirming that P2 survives longer with an increase in E_γ , given its larger spectral cutoff. This behaviour is also seen in the spectral observations by *Fermi* and other ground-based Cherenkov detectors. This was also seen in energy-dependent histograms of $E_{\gamma,\text{CR}}$, confirming that this quantity was systematically larger for P2.

The reason for this became more clear upon discovery that both the ρ_c and γ were systematically larger for P2, for both E -field scenarios. If CRR is reached, one expects $E_{\gamma,CR} \propto \rho_c^{1/2}$ for a constant E -field, so the larger ρ_c would explain the larger spectral cutoff for P2. Conversely, even if CRR is not attained, $E_{\gamma,CR} \propto \gamma^3 \rho_c^{-1}$. Given the systematic dominance of γ for P2, and the strong dependence of the third power, the larger spectral cutoff of P2 is thus explained by the larger γ . I also found that the values of ρ_c and γ remained larger for P2 when only considering emission beyond the light cylinder into the current sheet. In particular, the largest values of these quantities occurred there, pointing to dominant emission from that region to make up the GeV light curves.

7.1.3 SSC modelling

The aim of the study done by Harding et al. (2018) was to explain the pulsed emission observed by H.E.S.S. from the Vela pulsar up to energies of a few TeV (Djannati-Ataï et al., 2017). The pulsed emission at such extreme energies might be either connected to the GeV emission of *Fermi*'s spectra or it could be a new radiation component. This study by Harding et al. (2018) viewed it to be a separate emission component, i.e., SSC emission, that is radiated by particles that have been accelerated up to energies of several TeV.

Rudak & Dyks (2017) modelled Vela's measured VHE emission in an OG scenario, where primary particles are accelerated inside this gap and scatter the observed IR to optical emission that are placed along the inner edge of the gap and believed to come from SR emitted by pairs also produced in this gap. They showed that primaries, whose CR spectrum match the *Fermi* measured GeV spectrum, produce a significant ICS emission component reaching energies up to ~ 10 TeV.

We contributed to the study done by Harding et al. (2018). Harding et al. (2018) expanded the SSC emission code of Harding & Kalapotharakos (2015) and included the following refinements: (1) extension of the spectral energy range (spanning from IR to VHE energies) in order to include more soft photons, the scattering of which is in the Thompson limit, and for modelling the SSC emission at the VHE energies, (2) a more accurate calculation of the particle trajectories and their radii of curvature, giving a more precise determination of the accelerating particle energy and of their emitted radiation spectrum, (3) a two-step accelerating $E_{||}$, i.e., a lower $E_{||}$ inside the light cylinder, and a higher $E_{||}$ at and beyond the light cylinder (this is in agreement with recent global MHD and PIC pulsar models), (4) the injection spectrum of electron–positron pairs only above the PC in regions, (5) the MeV to GeV radiation from accelerated/relativistic particles inside and outside of the light cylinder are emitted via SC radiation, although their radiation at GeV energies is mostly in the CR limit.

Our contribution to the above mentioned study was the refined calculation of the particle trajectories and ρ_c as noted in point 2, and was needed to improve the calculation of the particle dynamics that was necessary to describe the emission from the particles.

7.2 Research implications

7.2.1 Offset-dipole studies

I conclude that the magnetospheric structure and emission geometry have an important effect on the predicted γ -ray pulsar light curves. *However, the presence of an E -field may have an even greater impact than small changes in the B -field structure and emission geometries:* When we included an SG E -field, thereby modulating ϵ_v , the resulting phase plots and light curves became qualitatively different compared to the geometric case.

There have been several indications that *the SG E -field may be larger than initially thought*. For example,

- Population synthesis studies found that the SG γ -ray luminosity may be too low, and therefore an increased E -field and / or particle current through the gap are necessary (e.g., Pierbattista et al. 2015).
- If the $E_{||}$ -field is too low the observed spectral cutoffs of a few GeV are not obtained (Section 3.8.2; Abdo et al., 2013).

- We found additional indications for an enhanced SG E -field. An increased E -field (multiplied by a factor of 100) led to statistically improved fits with respect to the light curves. This also yielded the second-best fit, next to the RVD and OG combination.
- Moreover, the inferred best-fit α and ζ parameters for this increased E -field clustered near the best fits of independent studies.
- We observed that a larger SG E -field also increased the particle energy gain rates and therefore yielded a larger particle energy γ , leading to particles reaching the CRR regime at altitudes close to the stellar surface.

The above mentioned arguments may point to a reconsideration of the boundary conditions assumed by Muslimov & Harding (2004a) that suppressed the E_{\parallel} at high altitudes, or of the current distribution in the gap. One possible way to bring self-consistency between B -field and E -field calculations may be to implement the newly developed FIDO model or PIC models that include global magnetospheric properties.

7.2.2 Energy-dependent CR light curves and spectral modelling

We found reasonable fits to the E_{γ} -dependent light curves and spectra of Vela as measured by *Fermi* and H.E.S.S. and our model that assumes CR as the mechanism responsible for the GeV emission captures the four general observed trends: (i) the decrease of P1/P2 vs. E_{γ} , (ii) evolution / depression of the inter-peak bridge emission, (iii) peak positions remaining at constant phases, and (iv) a decrease in the peak widths with an increase in E_{γ} . However, an unknown azimuthal dependence of the E -field as well as uncertainty in the precise spatial origin of the emission preclude a simplistic discrimination of the emission mechanism responsible for the GeV emission inside and beyond the light cylinder. Similar future modelling of energy-dependent light curves and spectra within a striped-wind context that assumes SR to be the relevant GeV mechanism will be necessary to see if those models can also reproduce and explain these prominent features in the case of Vela and other pulsars. We note that the drop in P1/P2 vs. E_{γ} may not be universal, as a study by Brambilla et al. (2015) points out. We found a counter-example for a different choice of ζ_{cut} (where P1/P2 increases with E_{γ}) as well as for specific choices of the two-step acceleration E -field. There may also be other parameter combinations that can yield this behaviour. However, this effect seems prevalent and has been seen in both HE and VHE data of bright pulsars.

7.2.3 SSC modelling

Harding et al. (2018) modelled the emission from particles that emit radiation via CR, SC, SSC and ICS. Upon solving the particle dynamics the refined ρ_c significantly impacted the calculation of $\gamma(s)$. The CR loss term strongly depends on $\gamma(s)$ and ρ_c and in return influences the particle dynamics due to the coupling between this term and the particle $\gamma(s)$. An improved $\gamma(s)$ would in turn influence other emission mechanisms' loss terms, as they also depend on $\gamma(s)$. Therefore, if the dynamical equations are solved for each emission mechanism (using a refined $\gamma(s)$) the radiation calculations (from primary particles) would also be more accurate. This also improved spectral calculations, specifically the CR component.

I found that the inclusion of the refined ρ_c and more accurate particle trajectories led to refined phase plots, i.e., the caustic structure was more pronounced, although the shape remained roughly the same. Also, the respective light curves were also slightly smoother and occurred at a different phase (but not significantly different). As E_{γ} was increased the light curve trends remained at TeV energies.

7.3 Future prospects

There are several future projects that may emerge from this study. The projects related to the study of the impact of the B -field structure on the light curves include extending the range of ϵ for which our code finds the PC rim, since more complex field solutions, such as the dissipative and FF field structures, may be associated with larger PC offsets. However, the offset-PC dipole solutions may be more applicable to MSPs discovered by *NICER*. It would still be preferable to investigate the self-consistent B -fields and E -fields of the dissipative models and solve the transport equation to test if the particles reach the CRR limit. The effect of these new fields on the phase plots and light curves can also be studied.

The VHE pulsed emission from pulsars depends strongly on the electrodynamics and the magnetospheric structure. Therefore, one could extend the SSC emission code by implementing more realistic B -field structures and their associated E -field distributions, thereby constraining the magnetospheric physics. One could use global dissipative magnetosphere models that represent solutions where a finite conductivity is specified on B -field lines above the stellar surface. These dissipative solutions fill the gap between the RVD (assuming zero conductivity) and the FF (assuming infinite conductivity) solutions (see Kalapotharakos et al. 2012b; Li et al. 2012). In future, an SC radiation mechanism can be incorporated as done by Harding et al. (2018). This mechanism seems to be able to produce spectra that are relatively higher at lower MeV energies, and that may provide better fits to the light curve and spectral data. Study the effects of different (azimuthally-dependent) injection spectra on TeV component.

There is also potential for multi-wavelength studies, such as light curve modelling in other energy bands, e.g., combining radio and γ -ray light curves (see Seyffert et al., 2010, 2012; Pierbattista et al., 2015). One could furthermore continue to model energy-dependent light curves, such as those available for other bright pulsars using data from *Fermi* and ground-based telescopes (e.g., Abdo et al., 2010a,b). Lastly, model phase-resolved spectra can be constructed, which will be an important test of the E_{\parallel} -field magnitude and its spatial dependence. This multi-wavelength study would assist in studying the evolution of P1/P2 with E_{γ} in more depth and could shed some more light on the underlying emission geometry and radiation mechanisms responsible for the HE and VHE emission. For example, modelling of the VHE pulsed emission could scrutinise the general emission framework of any particular model, as well as constraining particle energetics. Once the model has been thus tested, we will apply it to future detections of VHE pulsars (expected from the list of potential VHE sources released by *Fermi*; Ackermann et al., 2013).

Lastly, the application of the code to jointly fit light curve, spectral, and polarisation data may yield further constraints. Attempting to reproduce HE phase-resolved spectra, i.e., behaviour of spectral index / cutoff with phase, may yield important constraints.

Appendix A

Refined calculation of the curvature radius ρ_c

In this Appendix, I describe the updated procedure to calculate the radius of curvature of particle trajectories in the lab frame.

We refine the previous first-order calculation of ρ_c along the electron¹ trajectory in the lab frame, assuming that all particles injected at the footpoint of a particular B -field line on the stellar surface follow the same trajectory, independent of their energy, since these are quickly accelerated to relativistic energies by the unscreened E -field. We furthermore assume that the B -field is strong enough to constrain the movement of the electrons so they will move parallel to the field line in the co-rotating frame. Thus, we do not consider any perpendicular motion in this frame, since the perpendicular particle energy is nearly instantly expended via SR. We thus take into account the perpendicular $\mathbf{E} \times \mathbf{B}$ drift in the lab frame in which our new calculation for ρ_c takes place.

To calculate the electron's trajectory as well as its associated ρ_c , we first use a small, fixed step size ds (arclength interval) along the B -field line in the lab frame. The particle is injected at the stellar surface, and we trace its motion using this step length. Since we are using a numerical solution of the FF B -field at a particular magnetic inclination angle α , the three Cartesian components of the local first-order derivative of the position are available at any specified position (albeit that they may have to be interpolated, given the set resolution of the numerical solution of the FF field). One can thus use this information to map out a particle's trajectory for a given step length ds . The particle positions (x, y, z) as well as the local first derivatives (x', y', z') along the trajectory (i.e., the normalised velocity or the direction of motion), which is equivalent to the normalised B -field components, as a function of the cumulative arclength s are used to compute both the full particle trajectory and its $\rho_c(s)$.

The calculation involves three positions (previous, current, and next, denoted by indices $i - 1$, i and $i + 1$, respectively). At injection, let the particle position be (x_0, y_0, z_0) . Viewing this position as being at the 'previous' step, let us denote this as $(x_{i-1}, y_{i-1}, z_{i-1})$. The first-order derivatives at this position is also available: $(x'_{i-1}, y'_{i-1}, z'_{i-1})$. We next step along the field line, updating the arclength s . The position was then updated according to the Euler method:

$$x_i = x_{i-1} + x'_{i-1} \cdot ds, \quad (\text{A.1})$$

and similar for the other two coordinates. The current position and derivative (x'_i, y'_i, z'_i) were then saved. We similarly moved to the next position

$$x_{i+1} = x_i + x'_i \cdot ds, \quad (\text{A.2})$$

also for y and z . We thus have position and local direction components at three adjacent points with which we start the process.

We step along the particle trajectory (this stepping procedure is repeated until some large radius is reached), so that the x_{i+1} becomes the current position, and similar for the first-order derivative.

¹We use "electron" to collectively refer to electrons and positrons.

First, at the current position, we smooth the three spatial coordinates (x, y, z) using s as the independent variable to counteract numerical noise or uncertainties that may be present in the numerical calculation of the global B -field structure (and also taking into account the spatial grid on which this B -field was calculated). The smoothing is performed using a Gaussian Kernel Density Estimator (KDE; Parzen 1962) smoothing procedure. We choose the smoothing parameter h as a fraction of R_{LC} ; this needs to be adapted when increasing or decreasing the step size. The smoothing parameter used in the KDE procedure sets the level of smoothing (i.e., the spatial range in s over which smoothing occurs), and needs to be connected to ds to avoid under- or over-smoothing. After some testing, we set $h = 50ds$.

Second, we noticed that the our use of a KDE smoothing procedure on the position coordinates introduced some artificial “tails” at low and high altitudes, thus, the procedure is failing at the edges of the position range. We thus piecewise match (using some small tolerance on the allowed fraction that the smoothed and unsmoothed positions may differ) the unsmoothed and smoothed spatial positions of the electron trajectory at particular s values to get rid of these unwanted “tails” and to end up with the most satisfactory set of positions that constitute three smooth but realistic functions of arclength (i.e., a combination of the smoothed and unsmoothed positions as functions of s).

Third, we also smooth and then piecewise match the unsmoothed and smoothed directions of the electron trajectory at particular s values to get rid of these unwanted “tails”, as was done with the position coordinates.

Fourth, we use a second-order method involving interpolation by a Lagrange polynomial to obtain the second-order derivatives of the positions along the trajectory as a function of s , based on the (smoothed and matched) first derivatives (Faires & Burden, 2002):

$$x''(s) = \frac{(-3x'_{i-1} + 4x'_i - x'_{i+1})}{2ds}, \quad (\text{A.3})$$

and similar for y and z . This increased accuracy is necessary since ρ_c is a function of second-order derivatives (acceleration) of the electron position, and instabilities may be exacerbated if not dealt with carefully. We do this both for the smoothed and unsmoothed first-order derivatives of the position. Fifth, with the second-order derivatives in hand, we calculate two instances of ρ_c , one involving the unsmoothed (‘us’) and one involving the smoothed (‘s’) accelerations:

$$\rho_{c,us}(s) = \frac{1}{\sqrt{x''_{us}(s)^2 + y''_{us}(s)^2 + z''_{us}(s)^2}}, \quad (\text{A.4})$$

$$\rho_{c,s}(s) = \frac{1}{\sqrt{x''_s(s)^2 + y''_s(s)^2 + z''_s(s)^2}}. \quad (\text{A.5})$$

Finally, we piecewise match these two results for $\rho_c(s)$ to get rid of “tails” in ρ_c at low and high altitudes, as before.

Having a pre-calculated ρ_c in hand, as well as a particle trajectory (particle positions), for a fine division in arclength along any particular B -field line, we then interpolate ρ_c in our particle transport calculations to accommodate an adaptive, variable- ds approach that is used to speed up the transport calculations, without losing accuracy of the trajectory.

Bibliography

- Abdalla, H., Aharonian, F., Ait Benkhali, F., et al. 2018, *A&A*, 620, A66
- Abdo, A. A., Ackermann, M., Ajello, M., et al. 2010a, *ApJ*, 708, 1254
- . 2010b, *ApJ*, 720, 272
- . 2010c, *ApJS*, 187, 460
- . 2010d, *ApJ*, 713, 154
- Abdo, A. A., Ackermann, M., Atwood, W. B., et al. 2009, *ApJ*, 696, 1084
- Abdo, A. A., Ajello, M., Allafort, A., et al. 2013, *ApJS*, 208, 17
- Acciari, V. A., Ansoldi, S., Antonelli, L. A., et al. 2020, *A&A*, 643, L14
- Ackermann, M., Ajello, M., Allafort, A., et al. 2013, *ApJS*, 209, 34
- Aleksić, J., Alvarez, E. A., Antonelli, L. A., et al. 2011, *ApJ*, 742, 43
- . 2012, *A&A*, 540, A69
- Aleksić, J., Ansoldi, S., Antonelli, L. A., et al. 2015, *Journal of High Energy Astrophysics*, 5, 30
- Aliu, E., Anderhub, H., Antonelli, L. A., et al. 2008, *Science*, 322, 1221
- Aliu, E., Archambault, S., Archer, A., et al. 2015, *ApJ*, 800, 61
- Aliu, E., Arlen, T., Aune, T., et al. 2011, *Science*, 334, 69
- Alpar, M. A., Cheng, A. F., Ruderman, M. A., & Shaham, J. 1982, *Nature*, 300, 728
- Ansoldi, S., Antonelli, L. A., Antoranz, P., et al. 2016, *A&A*, 585, A133
- Antoniadis, J., Freire, P. C. C., Wex, N., et al. 2013, *Science*, 340, 448
- Arendt, P. N., J. & Eilek, J. A. 1998, *arXiv e-prints*, arXiv:9801257
- Arons, J. 1983, *ApJ*, 266, 215
- Arons, J. & Scharlemann, E. T. 1979, *ApJ*, 231, 854
- Asseo, E. & Khechinashvili, D. 2002, *MNRAS*, 334, 743
- Atwood, W. B., Abdo, A. A., Ackermann, M., et al. 2009, *ApJ*, 697, 1071
- Baade, W. & Zwicky, F. 1934a, *Proc. Nat. Acad. Sci.* 20, 259

- . 1934b, *Proc. Nat. Acad. Sci.* 20, 254
- Backer, D. C., Kulkarni, S. R., Heiles, C., et al. 1982, *Nature*, 300, 615
- Bai, X.-N. & Spitkovsky, A. 2010a, *ApJ*, 715, 1282
- . 2010b, *ApJ*, 715, 1270
- Barnard, M., Venter, C., & Harding, A. K. 2016, *ApJ*, 832, 107
- Becker, W. & Pavlov, G. G. 2002, arXiv e-prints, arXiv:0208356
- Belyaev, M. A. 2015, *New Astron.* 36, 37
- Beskin, V. S., Gurevich, A. V., & Istomin, I. N. 1983, *Zhurnal Eksperimentalnoi i Teoreticheskoi Fiziki*, 85, 401
- Beskin, V. S., Kuznetsova, I. V., & Rafikov, R. R. 1998, *MNRAS*, 299, 341
- Bilous, A. V., Watts, A. L., Harding, A. K., et al. 2019, *ApJ*, 887, L23
- Blumenthal, G. R. & Gould, R. J. 1970, *Rev. Mod. Phys.*, 42, 237
- Bogdanov, S. & Grindlay, J. E. 2009, *ApJ*, 703, 1557
- Bogdanov, S., Rybicki, G. B., & Grindlay, J. E. 2007, *ApJ*, 670, 668
- Bowers, R. L. & Deeming, T. 1984, *Astrophysics I - Stars* (Boston: Jones & Bartlett Publishers, Inc.)
- Bowyer, S., Byram, E. T., Chubb, T. A., & Friedman, H. 1964, *Nature*, 201, 1307
- Bradt, H., Rappaport, S., & Mayer, W. 1969, *Nature*, 222, 728
- Brambilla, G., Kalapotharakos, C., Harding, A. K., & Kazanas, D. 2015, *ApJ*, 804, 84
- Brambilla, G., Kalapotharakos, C., Timokhin, A. N., et al. 2018, *ApJ*, 858, 81
- Breed, M. 2015, PhD thesis, North-West University
- Breed, M., Venter, C., Harding, A. K., & Johnson, T. J. 2014, arXiv e-prints, arXiv:1411.1835
- Bühler, R. & Blandford, R. 2014, *Reports on Progress in Physics*, 77, 066901
- Bulik, T., Rudak, B., & Dyks, J. 2000, *MNRAS*, 317, 97
- Burns, M. L. & Harding, A. K. 1984, *ApJ*, 285, 747
- Cerutti, B., Mortier, J., & Philippov, A. A. 2016a, *MNRAS*, 463, L89
- Cerutti, B., Philippov, A., & Dubus, G. 2020, arXiv e-prints, arXiv:2008.11462
- Cerutti, B. & Philippov, A. A. 2017, *A&A*, 607, A134
- Cerutti, B., Philippov, A. A., & Spitkovsky, A. 2016b, *MNRAS*, 457, 2401
- Chadwick, J. 1932, *Nature*, 129, 312
- Chaisson, E. J. & McMillan, S. 2002, *Astronomy Today* (4th ed.; New Jersey: Prentice Hall)

- Chandrasekhar, S. 1931, *ApJ*, 74, 81
- Chen, A. Y., Yuan, Y., & Vasilopoulos, G. 2020, *ApJ*, 893, L38
- Chen, K. & Ruderman, M. 1993, *ApJ*, 402, 264
- Cheng, K. S. 2011, in *High-Energy Emission from Pulsars and their Systems: Proc. of the First Session of the Sant Cugat Forum on Astrophysics*, ed. D. F. Torres & N. Rea (Springer: Springer-Verlag Berlin Heidelberg), 79
- Cheng, K. S., Ho, C., & Ruderman, M. 1986, *ApJ*, 300, 500
- Cheng, K. S., Ruderman, M., & Zhang, L. 2000, *ApJ*, 537, 964
- Cheng, K. S. & Zhang, J. L. 1996, *ApJ*, 463, 271
- Chiu, H.-Y. & Salpeter, E. E. 1964, *Phys. Rev. Lett.*, 12, 413
- Cocke, W. J., Disney, M. J., & Taylor, D. J. 1969, *Nature*, 221, 525
- Contopoulos, I. & Kalapotharakos, C. 2010, *MNRAS*, 404, 767
- Contopoulos, I., Kazanas, D., & Fendt, C. 1999, *ApJ*, 511, 351
- Coroniti, F. V. 1990, *ApJ*, 349, 538
- Daugherty, J. K. & Harding, A. K. 1982, *ApJ*, 252, 337
- . 1983, *ApJ*, 273, 761
- De Jager, O. C., Harding, A. K., Sreekumar, P., & Strickman, M. 1996, *A&A Suppl.*, 120, C441
- DeCesar, M. E. 2013, PhD thesis, University of Maryland, College Park
- Deutsch, A. J. 1955, *Ann. d'Astrophys.*, 18, 1
- Djannati-Ataï, A., Giavitto, G., Holler, M., Rudak, B., Venter, C., & H. E. S. S. Collaboration. 2017, in *American Institute of Physics Conference Series*, Vol. 1792, 6th International Symposium on High Energy Gamma-Ray Astronomy, 040028
- Dodson, R., Legge, D., Reynolds, J. E., & McCulloch, P. M. 2003, *ApJ*, 596, 1137
- Du, Y. J., Qiao, G. J., Han, J. L., et al. 2010, *MNRAS*, 406, 2671
- Du, Y. J., Qiao, G. J., & Wang, W. 2012, *ApJ*, 748, 84
- Duncan, R. C. & Thompson, C. 1992, *ApJL*, 392, L9
- Dyks, J. & Harding, A. K. 2004, *ApJ*, 614, 869
- Dyks, J., Harding, A. K., & Rudak, B. 2004a, *ApJ*, 606, 1125
- Dyks, J. & Rudak, B. 2003, *ApJ*, 598, 1201
- Dyks, J., Rudak, B., & Harding, A. K. 2004b, *ApJ*, 607, 939
- Erber, T. 1966, *Rev. of Modern Phys.* 38, 626
- Faires, J. D. & Burden, R. L. 2002, *Numerical Methods* (3th ed.; Brooks Cole)

- Fichtel, C. E., Hartman, R. C., Kniffen, D. A., et al. 1975, *ApJ*, 198, 163
- Fierro, J. M., Michelson, P. F., Nolan, P. L., & Thompson, D. J. 1998, *ApJ*, 494, 734
- Frąckowiak, M. & Rudak, B. 2005, *Adv. Space Res.*, 35, 1152
- Fritz, G., Henry, R. C., Meekins, J. F., et al. 1969, *Science*, 164, 709
- Gendreau, K. C., Arzoumanian, Z., Adkins, P. W., et al. 2016, in *Society of Photo-Optical Instrumentation Engineers (SPIE) Conference Series*, Vol. 9905, *Space Telescopes and Instrumentation 2016: Ultraviolet to Gamma Ray*, ed. J.-W. A. den Herder, T. Takahashi, & M. Bautz, 99051H
- Giacconi, R., Gursky, H., Paolini, F. R., & Rossi, B. B. 1962, *Phys. Rev. Lett.*, 9, 439
- Gold, T. 1968, *Nature*, 218, 731
- . 1969, *Nature*, 221, 25
- Goldreich, P. & Julian, W. H. 1969, *ApJ*, 157, 869
- Gonthier, P. L., Van Guilder, R., & Harding, A. K. 2004, *ApJ*, 604, 775
- Grenier, I. A., Hermsen, W., & Clear, J. 1988, *A&A*, 204, 117
- Griffiths, D. J. 1995, *Introduction to Electrodynamics* (3rd ed.; San Francisco: Pearson Benjamin Cummings)
- Haensel, P., Potekhin, A. Y., & Yakovlev, D. G. 2007, in *Astrophysics and Space Science Library*, ed. P. Haensel, A. Y. Potekhin, & D. G. Yakovlev, Vol. 326 (New York: Springer)
- Halpern, J. P. & Holt, S. S. 1992, *Nature*, 357, 222
- Harding, A. K. 2005, in *22nd Texas Symposium on Relativistic Astrophysics*, ed. P. Chen, E. Bloom, G. Madejski, & V. Patrosian, 149
- Harding, A. K. 2007, *ArXiv Astrophysics e-prints* (astro-ph/0710.3517)
- . 2016, *J. Plasma Phys.* 82, 635820306
- Harding, A. K. & Grenier, I. A. 2011, in *High-Energy Emission from Pulsars and their Systems: Proc. of the First Session of the Sant Cugat Forum on Astrophysics*, ed. D. F. Torres & N. Rea (Springer: Springer-Verlag Berlin Heidelberg), 79
- Harding, A. K. & Kalapotharakos, C. 2015, *ApJ*, 811, 63
- Harding, A. K., Kalapotharakos, C., Barnard, M., & Venter, C. 2018, *ApJL*, 869, L18
- Harding, A. K. & Lai, D. 2006, *Rep. Prog. Phys.*, 69, 2631
- Harding, A. K. & Muslimov, A. G. 1998, *ApJ*, 508, 328
- Harding, A. K. & Muslimov, A. G. 2003, in *Pulsars, AXPs and SGRs Observed with BeppoSAX and Other Observatories*, ed. G. Cusumano, E. Massaro, & T. Mineo, 121
- . 2011a, *ApJL*, 726, L10
- . 2011b, *ApJ*, 743, 181
- Harding, A. K., Muslimov, A. G., & Zhang, B. 2002a, *ApJ*, 576, 366

- Harding, A. K. & Preece, R. 1987, *ApJ*, 319, 939
- Harding, A. K., Stern, J. V., Dyks, J., & Frackowiak, M. 2008, *ApJ*, 680, 1378
- Harding, A. K., Strickman, M. S., Gwinn, C., et al. 2002b, *ApJ*, 576, 376
- Harding, A. K., Usov, V. V., & Muslimov, A. G. 2005, *ApJ*, 622, 531
- Hewish, A. 1975, *Rev. of Modern Phys.* 47, 567
- Hewish, A., Bell, S. J., Pilkington, J. D. H., et al. 1968, *Nature*, 217, 709
- Hillier, R. R., Jackson, W. R., Murray, A., et al. 1970, *ApJL*, 162, L177
- Hirofani, K. 2001, *ApJ*, 549, 495
- . 2006, *ApJ*, 652, 1475
- . 2008a, *ArXiv Astrophysics e-prints* (astro-ph/0809.1283)
- . 2008b, *ApJL*, 688, L25
- Hoyle, F., Narlikar, J. V., & Wheeler, J. A. 1964, *Nature*, 203, 914
- Jackson, J. D. 1999, *Classical Electrodynamics* (3rd ed.; New York: John Wiley and Sons, Inc.)
- Johnson, T. J., Venter, C., Harding, A. K., et al. 2014, *ApJS*, 213, 6
- Johnston, S., Hobbs, G., Vigeland, S., et al. 2005, *MNRAS*, 364, 1397
- Kalapotharakos, C., Brambilla, G., Timokhin, A., et al. 2018, *ApJ*, 857, 44
- Kalapotharakos, C. & Contopoulos, I. 2009, *A&A*, 496, 495
- Kalapotharakos, C., Contopoulos, I., & Kazanas, D. 2012a, *MNRAS*, 420, 2793
- Kalapotharakos, C., Harding, A. K., & Kazanas, D. 2014, *ApJ*, 793, 97
- Kalapotharakos, C., Harding, A. K., Kazanas, D., & Brambilla, G. 2017, *ApJ*, 842, 80
- Kalapotharakos, C., Harding, A. K., Kazanas, D., & Contopoulos, I. 2012b, *ApJL*, 754, L1
- Kalapotharakos, C., Kazanas, D., Harding, A., & Contopoulos, I. 2012c, *ApJ*, 749, 2
- Kalapotharakos, C., Wadiasingh, Z., Harding, A. K., & Kazanas, D. 2020, *arXiv e-prints*, arXiv:2009.08567
- Kanbach, G. 2001, in *The Universe in Gamma Rays*, ed. V. Schönfelder, 127–158
- Kanbach, G., Arzoumanian, Z., Bertsch, D. L., et al. 1994, *A&A*, 289, 855
- Keane, E. F., Kramer, M., Lyne, A. G., et al. 2011, *MNRAS*, 415, 3065
- Kniffen, D. A., Hartman, R. C., Thompson, D. J., et al. 1974, *Nature*, 251, 397
- Kundu, A. & Pétri, J. 2017, *MNRAS*, 471, 3359
- Lamb, F. K., Boutloukos, S., Van Wassenhove, S., et al. 2009, *ApJ*, 706, 417
- Lampton, M., Margon, B., & Bowyer, S. 1976, *ApJ*, 208, 177

- Landau, L. D. 1932, *Phys. Z. Sowjetunion*, 1, 285
- Large, M. I., Vaughan, A. E., & Mills, B. Y. 1968, *Nature*, 220, 340
- Leung, G. C. K., Takata, J., Ng, C. W., et al. 2014, *ApJL*, 797, L13
- Li, J., Spitkovsky, A., & Tchekhovskoy, A. 2012, *ApJ*, 746, 60
- Li, J. G. 2014, PhD thesis, Princeton Univ.
- Lichnerowicz, A. 1967, *Relativistic Hydrodynamics and Magnetohydrodynamics* (New York: Benjamin)
- Limyansky, B. 2019, in *AAS/High Energy Astrophysics Division*, Vol. 17, *AAS/High Energy Astrophysics Division*, 109.32
- Lockhart, W., Gralla, S. E., Özel, F., & Psaltis, D. 2019, *MNRAS*, 490, 1774
- Lowrie, W. 2011, *A Student's Guide to Geophysical Equations* (1st ed.; Cambridge University Press)
- Luo, Q., Shibata, S., & Melrose, D. B. 2000, *MNRAS*, 318, 943
- Lyubarskii, Y. E. 1996, *A&A*, 311, 172
- Lyutikov, M. 2013, *MNRAS*, 431, 2580
- Lyutikov, M., Otte, N., & McCann, A. 2012, *ApJ*, 754, 33
- Manchester, R. N., Hobbs, G. B., Teoh, A., & Hobbs, M. 2005, *Astron. J.*, 129, 1993
- Manchester, R. N. & Taylor, J. H. 1977, *Pulsars* (San Francisco: W. H. Freeman)
- Mattox, J. R., Bertsch, D. L., Fichtel, C. E., et al. 1992, *ApJL*, 401, L23
- McCann, A. 2015, *ApJ*, 804, 86
- McEnery, J., van der Horst, A., Dominguez, A., et al. 2019, in *Bulletin of the American Astronomical Society*, Vol. 51, 245
- McLaughlin, M. A., Lyne, A. G., Lorimer, D. R., et al. 2006, *Nature*, 439, 817
- Medin, Z. & Lai, D. 2007, *MNRAS*, 382, 1833
- Mereghetti, S. 2008, *Astron. Astrophys. Rev.* 15, 225
- Mészáros, P. 1992, *High-energy radiation from magnetized neutron stars*. (Chicago: The Univ. of Chicago Press)
- Michel, F. C. 1973a, *ApJ*, 180, 207
- . 1973b, *ApJL*, 180, L133
- . 1982, *Rev. of Modern Phys.* 54, 1
- . 1994, *ApJ*, 431, 397
- Miller, M. C., Lamb, F. K., Dittmann, A. J., et al. 2019, *ApJL*, 887, L24
- Minkowski, R. 1942, *ApJ*, 96, 199

- Mochol, I. & Pétri, J. 2015, MNRAS, 449, L51
- Montgomery, H. 1999, European Journal of Physics, 20, 271
- Morini, M. 1983, MNRAS, 202, 495
- Morrison, P. 1958, Il Nuovo Cimento, 7, 858
- Morrison, P., Olbert, S., & Rossi, B. 1954, Phys. Rev., 94, 440
- Muslimov, A. & Harding, A. K. 1997, ApJ, 485, 735
- Muslimov, A. G. & Harding, A. K. 2003, ApJ, 588, 430
- . 2004a, ApJ, 606, 1143
- . 2004b, ApJ, 617, 471
- Muslimov, A. G. & Tsygan, A. I. 1992, MNRAS, 255, 61
- Ng, C. & Romani, R. W. 2008, ApJ, 673, 411
- Ng, C. Y. & Romani, R. W. 2004, ApJ, 601, 479
- Ostriker, J. P. & Gunn, J. E. 1969, ApJ, 157, 1395
- Pacini, F. 1967, Nature, 216, 567
- Padmanabhan, T. 2000, Theoretical Astrophysics - Volume 1, Astrophysical Processes (Cambridge: Cambridge Univ. Press)
- . 2001, Theoretical Astrophysics - Volume 2, Stars and Stellar Systems (Cambridge: Cambridge Univ. Press)
- Palen, S. E. 2002, Shaum's Outline of Theory and Problems of Astronomy (New York: McGRAW-HILL)
- Parzen, E. 1962, Ann. Math. Stat., 33, 1065
- Pellizzoni, A., Pilia, M., Possenti, A., et al. 2009, ApJ, 691, 1618
- Pétri, J. 2012, MNRAS, 424, 2023
- . 2016, J. Plasma Phys. 82, 635820502
- Pétri, J. & Dubus, G. 2011, MNRAS, 417, 532
- Petrova, S. A. 2016, arXiv e-prints, arXiv:1608.07998
- . 2017, J. Cosmol. Astropart. Phys. 2017, 041
- Philippov, A. A. & Spitkovsky, A. 2014, ApJL, 785, L33
- . 2018, ApJ, 855, 94
- Pierbattista, M., Harding, A. K., Grenier, I. A., et al. 2015, A&A, 575, A3
- Press, W. H., Teukolsky, S. A., Vetterling, W. T., & Flannery, B. P. 1992, Numerical recipes in C. The art of scientific computing
- Ramana Murthy, P. V. & Wolfendale, A. W. 1986, Gamma-ray astronomy (Cambridge: Cambridge Univ. Press)

- Rankin, J. M. 1993, *ApJ*, 405, 285
- Rea, N. & Esposito, P. 2011, in *High-Energy Emission from Pulsars and their Systems: Proc. of the First Session of the Sant Cugat Forum on Astrophysics*, ed. D. F. Torres & N. Rea (Springer: Springer-Verlag Berlin Heidelberg)
- Riley, T. E., Watts, A. L., Bogdanov, S., et al. 2019, *ApJL*, 887, L21
- Romani, R. W. 1996, *ApJ*, 470, 469
- Romani, R. W. & Watters, K. P. 2010, *ApJ*, 714, 810
- Romani, R. W. & Yadigaroglu, I.-A. 1995, *ApJ*, 438, 314
- Rudak, B. & Dyks, J. 2017, in *International Cosmic Ray Conference*, Vol. 301, 35th International Cosmic Ray Conference (ICRC2017), 680
- Rudak, B., Dyks, J., & Bulik, T. 2002, in *Neutron Stars, Pulsars, and Supernova Remnants*, ed. W. Becker, H. Lesch, & J. Trümper, 142
- Ruderman, M. A. & Sutherland, P. G. 1975, *ApJ*, 196, 51
- Rybicki, G. B. & Lightman, A. P. 1979, *Radiative processes in astrophysics* (New York: John Wiley and Sons, Inc.)
- Schönfelder, V. 2001, in *The Universe in Gamma Rays*, ed. V. Schönfelder, *A&A Library*, 1
- Seyffert, A., Venter, C., de Jager, O. C., & Harding, A. K. 2010, in *25th Texas Symposium on Relativistic Astrophysics*, 130
- Seyffert, A. S., Venter, C., Johnson, T. J., & Harding, A. K. 2012, *arXiv e-prints*, arXiv:1201.4272
- Shibanov, Y. A., Koptsevich, A. B., Sollerman, J., & Lundqvist, P. 2003, *A&A*, 406, 645
- Sokolov, A. A. & Ternov, I. M. 1968, *Synchrotron radiation* (1st ed.; Oxford, NY: Pergamon Press)
- Spir-Jacob, M., Djannati-Ataï, A., Mohrmann, L., et al. 2019, *arXiv e-prints*, arXiv:1908.06464
- Spitkovsky, A. 2006, *ApJL*, 648, L51
- . 2011, *Astrophys. and Space Science Proc.* 21, 139
- Staelin, D. H. & Reifstein, III, E. C. 1968, *Science*, 162, 1481
- Story, S. A., Gonthier, P. L., & Harding, A. K. 2007, *ApJ*, 671, 713
- Sturrock, P. A. 1971, *ApJ*, 164, 529
- Svensson, R. 1982, *ApJ*, 258, 335
- Takata, J., Shibata, S., & Hirokuni, K. 2004, *MNRAS*, 354, 1120
- Tananbaum, H., Gursky, H., Kellogg, E. M., et al. 1972, *ApJL*, 174, L143
- Tang, A. P. S., Takata, J., Jia, J. J., & Cheng, K. S. 2008, *ApJ*, 676, 562
- Taylor, R. J. 1994, *The Stars, Their Structure and Evolution* (Cambridge: Cambridge University Press)

- Tchekhovskoy, A., Spitkovsky, A., & Li, J. G. 2013, *MNRAS*, 435, L1
- Thompson, D. J., Fichtel, C. E., Kniffen, D. A., & Ogelman, H. B. 1975, *ApJL*, 200, L79
- Thompson, D. J., Harding, A. K., Hermsen, W., & Ulmer, M. P. 1997, in *American Institute of Physics Conference Series*, Vol. 410, *Proceedings of the Fourth Compton Symposium*, ed. C. D. Dermer, M. S. Strickman, & J. D. Kurfess, 39–56
- Timokhin, A. N. 2006, *MNRAS*, 368, 1055
- . 2010, *MNRAS*, 408, 2092
- Timokhin, A. N. & Arons, J. 2013, *MNRAS*, 429, 20
- Torres, D. F. 2018, *Nature Astronomy*, 2, 247
- Truemper, J., Pietsch, W., Reppin, C., et al. 1978, *ApJL*, 219, L105
- Usov, V. V. & Melrose, D. B. 1995, *Austr. J. Phys.*, 48, 571
- Uzdensky, D. A. & Spitkovsky, A. 2014, *ApJ*, 780, 3
- Venter, C. 2016, in *The 4th Annual Conference on High Energy Astrophysics in Southern Africa (HEASA 2016)*, 40
- Venter, C. & De Jager, O. C. 2005, *ApJL*, 619, L167
- . 2010, *ApJ*, 725, 1903
- Venter, C., Harding, A. K., & Grenier, I. 2017, in *XII Multifrequency Behaviour of High Energy Cosmic Sources Workshop (MULTIF2017)*, 38
- Venter, C., Harding, A. K., & Guillemot, L. 2009, *ApJ*, 707, 800
- Venter, C., Johnson, T. J., & Harding, A. K. 2012, *ApJ*, 744, 34
- Watters, K. P., Romani, R. W., Weltevrede, P., & Johnston, S. 2009, *ApJ*, 695, 1289
- Wheeler, J. A. 1966, *Ann. Rev. Astron. Astrophys.*, 4, 393
- Will, C. M. 1994, *Phys. Usp.*, 37, 697
- Yadigaroglu, I. A. G. 1997, PhD thesis, Stanford University
- Zavlin, V. E., Pavlov, G. G., Sanwal, D., et al. 2002, *ApJ*, 569, 894